

**UCLA**

**UCLA Electronic Theses and Dissertations**

**Title**

Non-invasive monitoring of hematopoietic reconstitution and immune cell function through Positron Emission Tomography

**Permalink**

<https://escholarship.org/uc/item/8z9618sg>

**Author**

McCracken, Melissa Nicole

**Publication Date**

2014

Peer reviewed|Thesis/dissertation

UNIVERSITY OF CALIFORNIA

Los Angeles

**Non-invasive monitoring of hematopoietic reconstitution and immune cell function  
through Positron Emission Tomography**

A dissertation submitted in partial satisfaction of the  
requirements for the degree Doctor of Philosophy  
in Molecular and Medical Pharmacology

by

Melissa Nicole McCracken

2014



## ABSTRACT OF THE DISSERTATION

### **Non-invasive monitoring of hematopoietic reconstitution and immune cell function through Positron Emission Tomography**

By

Melissa Nicole McCracken

Doctor of Philosophy in

Molecular and Medical Pharmacology

University of California, Los Angeles, 2014

Professor Owen N. Witte, Chair

Multiple diseases including blood disorders, autoimmunity, infections, and cancer result from defects in proper hematopoiesis or immune cell function. Hematopoietic stem cell (HSC) transplants or genetic modification of these cells can be used as a therapy to correct the observed deficiencies. Engineering antigen specific T cell receptors (TCR) in T cells, or in HSCs, has provided new targeted therapies against cancer by arming the host's immune system to specifically recognize the cancer of interest. The standard method to monitor immune cells is peripheral blood samples that cannot provide whole-body measurements of cell locations. Positron emission tomography (PET) allows non-invasive and repetitive *in vivo* visualization of positron-emitting probes. Here we use two PET imaging techniques to monitor the immune system. PET reporter genes are applied to detect only the specific, engineered immune cell

populations, and immunoPET is used for the detection of total endogenous CD8 cells by radiolabeling an antibody fragment.

We demonstrated that HSC transplants expressing PET reporter genes could be tracked for total cell engraftment, location, expansion, and elimination. The dual PET reporter/suicide gene sr39TK was expressed in a humanized mouse model of HSC transplant. Cells were detected through PET reporter imaging and then selectively eliminated through sr39TK suicide gene function validating its use for cell tracking and, if needed, ablation.

We then developed a new PET reporter with human deoxycytidine kinase containing three point mutations within the active site (hdCK3mut) in combination with the PET probe [<sup>18</sup>F]-L-FMAU (1-(2-deoxy-2-<sup>18</sup>fluoro-β-L-arabinofuranosyl)-5-methyluracil). Comparison of hdCK3mut and sr39TK established that hdCK3mut was approximately two fold more sensitive for in vivo detection. hdCK3mut was capable of tracking HSC engraftment, expansion, and the intratumor trafficking of engineered T cells. Expression of hdCK3mut was inert with no effect on cell longevity or function.

For detection of endogenous CD8 cells, a minibody (2.43 Mb) was engineered and radiolabeled with <sup>64</sup>Cu. 2.43 Mb retained the ability to detect CD8 cells within the spleen and lymph nodes but did not cause antibody dependent cell depletion.

PET is a powerful imaging modality that can be adapted to track lymphoid cells *in vivo*. Our work demonstrates three applications of how PET imaging can be applied for whole-body, selective detection of hematopoietic cells.

The dissertation for Melissa Nicole McCracken is approved.

Heather Christofk

Donald Kohn

Caius Radu

Michael Teitell

Owen N. Witte, Committee Chair

University of California, Los Angeles

2014

## **DEDICATION**

This dissertation is dedicated to my grandpa Doc Morse and my parents  
Michael and Sharon McCracken.

## TABLE OF CONTENTS

<b>Abstract of Dissertation</b>	<b>ii</b>
<b>Committee Page</b>	<b>iv</b>
<b>Dedication Page</b>	<b>v</b>
<b>List of Figures</b>	<b>viii</b>
<b>List of Tables</b>	<b>xiv</b>
<b>Acknowledgements</b>	<b>xv</b>
<b>Vita</b>	<b>xviii</b>
<b>Chapter 1:</b> PET imaging in immunology research. Small Animal Imaging - Basics and Practical Guide 2 <sup>nd</sup> Edition Chapter 35	1
References:	52
<b>Chapter 2:</b> Application of a Rapid, Simple, and Accurate Adenovirus- Based Method to Compare PET Reporter Gene/PET Reporter Probe Systems. <i>Mol Imaging Biol</i> , <b>15</b> , 273-281 (2012).	62
References	71
<b>Chapter 3:</b> Long-term in vivo monitoring of mouse and human hematopoietic stem cell engraftment with a human positron emission tomography reporter gene. <i>Proc Natl Acad Sci U S A</i> <b>110</b> , 1857-1862 (2013).	81
References	87
<b>Chapter 4:</b> Non-invasive detection of tumor infiltrating engineered T cells by human PET reporter imaging. Submitted	95
References	132
<b>Chapter 5:</b> In vivo HSV-sr39TK positron emission tomography and suicide gene elimination of human hematopoietic stem cells and their progeny in humanized mice. Submitted	139



References	173
<b>Chapter 6:</b> Engineered antibody fragments for immunoPET imaging of endogenous CD8 <sup>+</sup> T cells <i>in vivo</i> . <i>Proc Natl Acad Sci U S A</i> <b>111</b> , 1108-1113 (2014).	180
References	186
<b>Chapter 7:</b> Conclusion and future studies	192
References	199

## LIST OF FIGURES

<b>Chapter 1:</b>		<b>1</b>
Figure 1-1	Principles and classes of PET imaging.	41
Figure 1-2	Glucose consumption in immune cells measured by [ <sup>18</sup> F]-FDG.	42
Figure 1-3	Nucleoside Salvage in PET imaging of immune cells with [ <sup>18</sup> F]-FAC.	43
Figure 1-4	Detection of lymphocytes with 2-[ <sup>18</sup> F]fludarabine PET imaging.	45
Figure 1-5	Ex vivo labeling of T cells with [ <sup>64</sup> Cu]-PTSM.	46
Figure 1-6	ImmunoPET by antibody engineering and radiolabeling.	47
Figure 1-7	Targeting hCD20 with <sup>64</sup> Cu labeled proteins.	48
Figure 1-8	Subclasses of PET reporter genes.	49
Figure 1-9	Tracking CTLs with HSV-TK PET reporter imaging.	50
Figure 1-10	hdCK3mut PET reporter gene imaging of hematopoietic reconstitution.	51
<b>Chapter 2:</b>		<b>62</b>
Figure 2-1	Cloning and production of adenovirus vectors.	67
Figure 2-2	Viral titers, measured as infectious genome units for the adenovirus vectors.	67

Figure 2-3	Titration of Ad.HL.sr39TK for microPET/microCT quantification.	68
Figure 2-4	TK2 and dCK PRG efficacies with L-FMAU as the PRP.	69
Figure S2-1	Time course for hepatic adenovirus reporter gene expression.	79
Figure S2-2	Comparative efficacy of dCK-DM and dCKA100VTM as PRGs, with <sup>18</sup> F-L-FMAU as PRP.	80
<b>Chapter 3:</b>		<b>81</b>
Figure 3-1	Development of a human thymidine selective PET reporter gene hdCK3mut.	83
Figure 3-2	hdCK3mut and [ <sup>18</sup> F]-L-FMAU PET can track reporter-labeled mouse hematopoietic cells during early engraftment and expansion in bone marrow chimera mice.	83
Figure 3-3	hdCK3mut mouse HSCs persist in vivo allowing long-term monitoring of therapeutic cell transplantation.	84
Figure 3-4	hdCK3mut allows for noninvasive detection of human HSC engraftment.	85
Figure 3-5	Overlapping integration sites in hdCK3mut-labeled human hematopoietic cells defines a common cell of origin with multipotent lineage capacity in vivo.	86

Figure S3-1	Vector maps of viruses used.	90
Figure S3-2	Biodistribution of removed grafts after [ <sup>18</sup> F]-L-FMAU imaging.	90
Figure S3-3	Additional [ <sup>18</sup> F]-L-FMAU MicroPET scans at 4 wk post mouse BMT in reporter chimeric mice.	91
Figure S3-4	Quantification of flow cytometry from hdCK3mut and YFP mHSC recipient mice.	91
Figure S3-5	IHC of mHSC recipient animals of YFP and hdCK3mut at 8 wk post-BMT.	92
Figure S3-6	Methylcellulose assay for hdCK3mut or YFP recipient mice.	93
Figure S3-7	Sequential scans of hdCK3mut recipient mice at 15 and 27 wk post-BMT.	94
Figure S3-8	IHC of hdCK3mut recipient hHSC recipient animal.	94
<b>Chapter 4:</b>		<b>95</b>
Figure 4-1	Establishment of humanized mice harboring F5 TCR against MART-1.	123
Figure 4-2	Engraftment and hematopoiesis of human cells in BLT mice.	124
Figure 4-3	hdCK3mut expressing T cells developed in vivo are capable of cytokine production.	125
Figure 4-4	In vitro function of MART-1 specific T cells	126

	developed <i>in vivo</i> .	
Figure 4-5	Immunohistochemistry of immune infiltrates from xenografts removed from F5/hdCK3mut animals.	127
Figure 4-6	Detection of hdCK3mut engineered TILs by [ <sup>18</sup> F]-L-FMAU PET reporter imaging.	128
Figure 4-7	Visualization of engrafted stem and progenitor cells expressing the hdCK3mut PET reporter gene.	129
Figure S4-1	IHC of M202 and M207 Tumors from hdCK3mut recipient animals.	130
Figure S4-2	Additional IHC of M202 and M207 Tumors from F5/hdCK3mut recipient animals.	130
Figure S4-3	Additional [ <sup>18</sup> F]-FDG scans of BLT animals.	131
Figure S4-4	Additional [ <sup>18</sup> F]-L-FMAU scans of BLT animals.	131
<b>Chapter 5:</b>		<b>139</b>
Figure 5-1	Experimental system to test ESO/TK PET reporter and suicide gene function <i>in vivo</i> .	164
Figure 5-2	Human cells develop in NSG-A2.1 mice transplanted with PBSCs.	165
Figure 5-3	Effector function of <i>in vivo</i> derived NY-ESO-1-TCR bearing cells from HSCs.	166
Figure 5-4	High-resolution sr39TK PET reporter imaging of gene-modified cells <i>in vivo</i> .	167

Figure 5-5	GCV ablates gene modified cells hematopoietic niches.	168
Figure 5-6	Immunophenotyping and VCN analysis after drug treatment.	169
Figure S5-1	Validation of sr39TK function in Jurkat cells.	170
Figure S5-2	ROI Analysis.	171
Figure S5-3	Chimerism, vector marking, and PET probe signal in vertebrae.	172
<b>Chapter 6:</b>		<b>180</b>
Figure 6-1	Mb construction and epitope specificity are shown.	182
Figure 6-2	The 2.43 Mb retains Lyt2.2 <sup>+</sup> antigen specificity.	182
Figure 6-3	Anti-CD8 Mb does not deplete CD8-expressing cells in vivo.	183
Figure 6-4	Immuno-PET imaging of <sup>64</sup> Cu-NOTA-2.43 Mb 4 h p.i. is shown.	183
Figure 6-5	Immuno-PET imaging of <sup>64</sup> Cu-NOTA-2.43 Mb and <sup>64</sup> Cu-NOTA-YTS169 Mb shows in vivo specificity of the 2.43 Mb to Lyt2.2 <sup>+</sup> mice.	184
Figure 6-6	Immuno-PET imaging of <sup>64</sup> Cu-NOTA-2.43 Mb in antigen-blocked and antigen-depleted B/6 mice is shown.	185
Figure S6-1	Purification and characterization of 2.43 and YTS169 Mbs are shown.	189

Figure S6-2	Purification of the sCD $\alpha\beta$ antigen in two steps.	190
Figure S6-3	Solution phase binding of 2.43 and YTS169 Mbs to sCD8 $\alpha\beta$ is demonstrated by SEC.	190
Figure S6-4	Kinetic analysis of Mb binding to sCD8 $\alpha\beta$ antigen using SPR Biacore 3000 is shown.	191

## LIST OF TABLES

<b>Chapter 2:</b>		<b>62</b>
Table 2-1	Plasmids and adenoviral vectors used in this study	65
Table 2-2	Primers used in this study	65
<b>Chapter 3:</b>		<b>81</b>
Table S3-1	Enzyme kinetics for hdCK3mut and hdCKDM with L-FMAU	94
<b>Chapter 5:</b>		<b>139</b>
Table S5-1	Total human chimerism and lymphoid composition in NSG recipients of ESO/TK-transduced or non-transduced PBSC.	160
<b>Chapter 6:</b>		<b>180</b>
Table 6-1	Ex vivo biodistribution analysis of $^{64}\text{Cu}$ -NOTA-2.43 Mb 4 h p.i. in Lyt2.2 <sup>+</sup> B/6 mice, Lyt2.1 <sup>+</sup> C3H mice, NSG SCID mice, antigen-blocked B/6 mice, and antigen-depleted B/6 mice.	184
Table 6-2	Ex vivo biodistribution analysis of $^{64}\text{Cu}$ -NOTA-YTS169 Mb 4 h p.i. in Lyt2.2 <sup>+</sup> B/6 mice and Lyt2.1 <sup>+</sup> C3H mice.	185



## ACKNOWLEDGEMENTS

I would like to first thank my mentor Dr. Owen Witte for his outstanding support and mentorship over the last five years. Owen is an exceptional mentor, scientist, and an inspiration. My time in graduate school in Owen's laboratory has been incredible, and I am so thankful for the unparalleled opportunities he has provided me. His guidance has helped me to think critically, independently, and above all has provided all training necessary for me to succeed in my future scientific career.

I would like to thank the members of my doctoral committee; Heather Christofk, Donald Kohn, Caius Radu and Mike Tietell. Their guidance and support during my training has been vital. Each member has provided direction, advice, and their expertise to help me succeed.

Thank you to all of my collaborators who have made my thesis project possible. I am especially thankful to have had the opportunity to work with Eric Gschweng. Eric has been instrumental in completing chapters 3 and 5. I look forward to continued collaborations as each of us move on into postdoctoral positions. Thank you to Richard Tavare who has been highly collaborative and has broadened my imaging expertise by teaching me immunoPET, resulting in the completion of Chapter 6. Thank you to Jose Gil for leading the PET reporter gene comparison studies resulting in the completion of Chapter 2.

I am so thankful to have worked with such wonderful and talented individuals within the Witte lab. Evan Nair-Gill helped me in planning experiments, presentations, and writing. Jami Witte taught me so many lab skills and has helped me complete all of my projects. Donghui Cheng

who stayed late to finish my sorts and taught me flow cytometry. Peter Clark for the helpful discussions and edits of grants and manuscripts. Tanya Stoyanova and Andrew Goldstein for always supporting me, and helping me with anything I need. Stephanie Wiltzus and Howard Mak for teaching me all of my animal handling skills. Barbara Anderson for keeping everything organized and helping me coordinate submissions and meetings. All other members of the Witte lab who have helped me along the way. Thank you all for supporting and encouraging me over the last five years.

My thesis has been highly collaborative and has depended on the outstanding resources available within the department of Pharmacology at UCLA. A special thank you to members who have directly helped me. Michael Phelps for creating a fun and collaborative department. Johannes Czernin for helping teach me about clinical PET and providing outstanding support. Harvey Hershman for all of his help with writing and grant revisions. The staff at the Crump Institute for Molecular Imaging for helping in my imaging studies.

Thank you to my funding sources that have supported me throughout my time here, the California Institute for Regenerative Medicine Pre-doctoral Training Grant for funding support from 2011-2013, the Graduate Division Dissertation year Fellowship from 2013-2014, and the ICMIC Career Development award in 2014.

A version of Chapter 1 will be reproduced in *Small Animal Imaging-Basics and Practical Guide* 2nd Edition by Springer Publishing.

Chapter 2 is reproduced with permission of *Molecular Imaging and Biology*.

Chapter 3 and 6 are reproduced with permission from the Proceedings of the National Academy.

Chapter 4 was submitted to the Journal of Clinical Investigation for review on May 30, 2014.

Chapter 5 was submitted to Cancer Research.

Finally, a huge thank you to my friends and family for their constant support of me. Especially to my mom and dad who have always believed in me and have been proud of anything I do. You have all been so amazing and I am so blessed to have you in my life.

## VITA

- 2009 B.S., Biochemistry and Molecular Biology  
University of California, Davis  
Davis, California
- 2009 Graduate Student  
Department of Molecular and Medical Pharmacology  
David Geffen School of Medicine  
University of California, Los Angeles
- 2011-2013 Award Recipient/Graduate Trainee  
California Institute for Regenerative Medicine Training  
Grant  
University of California, Los Angeles
- 2013-2014 Award Recipient/Graduate Trainee  
Graduate Division Dissertation Year Fellowship  
Training Grant  
University of California, Los Angeles
- 2014 Award Recipient  
*In vivo* Cellular and Molecular Imaging Center  
(ICMIC) Career Development Awardee  
University of California, Los Angeles

## PUBLICATIONS

- Mason, B.D., **McCracken, M.**, Bures, E.J. & Kerwin, B.A. Oxidation of free L-histidine by tert-Butylhydroperoxide. *Pharm Res* **27**, 447-456 (2010). PMID: 20127149
- Gil, J.S., Machado, H.B., Campbell, D.O., **McCracken, M.N.**, Radu, C., Witte, O.N., Herschman, H.R. Application of a Rapid, Simple, and Accurate Adenovirus-Based Method to Compare PET Reporter Gene/PET Reporter Probe Systems. *Mol Imaging Biol* **15**, 273-281 (2012). PMID: 23054556
- McCracken, M.N.**, Gschweng, E.H., Nair-Gill, E., McLaughlin, J., Cooper, A.R., Riedinger, M., Cheng, D., Nosala, C., Kohn, D.B., Witte, O.N. Long-term in vivo monitoring of

mouse and human hematopoietic stem cell engraftment with a human positron emission tomography reporter gene. *Proc Natl Acad Sci U S A* **110**, 1857-1862 (2013). PMID: 23319634

Tavaré, R., **McCracken, M.N.**, Zettlitt, K.A., Knowles, S.M., Salazar, F.B., Olafsen, T., Witte, O.N., Wu, A.M. Engineered antibody fragments for immunoPET imaging of endogenous CD8<sup>+</sup> T cells *in vivo*. *Proc Natl Acad Sci U S A* **111**, 1108-1113 (2014). PMID: 24390540

Gschweng, E.H., **McCracken, M.N.**, Kaufman, M.L., Ho, M., Hollis, R.P., Wang, X., Saini, N., Koya, R., Chodon, T., Ribas, A., Witte, O.N., Kohn, D.B. In vivo HSV-sr39TK positron emission tomography and suicide gene elimination of human hematopoietic stem cells and their progeny in humanized mice. *Cancer Research* (Submitted).

Bunimovich, Y.L., Nair-Gill, E., Riedinger, M., **McCracken, M.N.**, Cheng, D., McLaughlin, J., Radu, C.G., Witte, O.N. Deoxycytidine kinase augments ATM-mediated DNA repair and contributes to radiation resistance. *PLOS One* (Submitted)

Clark, P.M., Flores, G., Evdokimov, N.M., **McCracken, M.N.**, Nair-Gill, E., Chai, T., Faull, K.F., Phelps, M.E., Jung, M.E., Witte, O.N. A novel positron emission tomography probe demonstrates a striking concentration of ribose salvage in the liver. *Proc Natl Acad Sci U S A* (2014) In Press.

**McCracken, M.N.**, Vatakis, D.N., Dhaval, D., McLaughlin, J., Zack, J.A., Witte, O.N. Non-invasive detection of tumor infiltrating engineered T cells by human PET reporter imaging. *Journal of Clinical Investigation* (Submitted).

## PRESENTATIONS

### *Oral Presentations:*

Pharmacology Floor Meeting	2010 – 2012
UCLA Stem Cell Club	2012, 2013
Joint Center for Translational Research Retreat	2012
UCLA-CalTech Engineered Immunity Consortium	2010 – 2013
UCLA BSCRC Faculty Meeting	2013
World Molecular Imaging Congress	2013

Molecular and Medical Pharmacology Department Retreat  
“Best Graduate Student Talk”

2013

***Poster Presentation:***

*2010:*

Pharmacology Department Retreat

*2011:*

UCLA BSCRC Conference

Joint Center for Translational Medicine Retreat

Pharmacology Department Retreat

California Institute for Regenerative Medicine Grantee Meeting

*2012:*

UCLA BSCRC Conference

HHMI Science Meeting

Broad Tri-Institutional Stem Cell Meeting

Joint Center for Translational Medicine Retreat

International Society for Stem Cell Research- Yokohama

*2013:*

UCLA BSCRC Conference

California Institute for Regenerative Medicine Grantee Meeting

*2014:*

UCLA BSCRC Conference

## **CHAPTER 1:**

PET imaging in immunology research.

## **PET Imaging in Immunology:**

### **1. Introduction to PET imaging in immunology**

The immune system is dynamic and continually adapts to maintain the health of the whole-body. Innate immune cells survey tissues for abnormalities and are able to detect and infiltrate infected and/or abnormal tissues. Signals from the initial infiltrating antigen-presenting immune cells lead to activation of the adaptive immune system including: 1. recruitment of adaptive immune cells, 2. activation and rapid expansion of antigen specific adaptive immune cells, 3. differentiation into antigen specific effector cells and 4. homing to the abnormal tissue if activated in lymphatic organs such as the spleen or lymph nodes [1]. Once the infected tissue is cleared, there is a rapid decline in effector cells and a small number of adaptive immune cells will remain as memory T or B cells that quickly expand upon repeat exposure to the antigen. Defects in proper immune responses can cause complications that include autoimmunity, persistent infection, or malignancies [2]. Monitoring the response of the immune system can provide insight into proper diagnosis and therapeutic management of these diseases.

Methods used to monitor the immune system can be limited and biased. Most frequently a peripheral blood sample is taken to monitor changes in cell abundance, phenotype, or cytokine levels. On occasion, a tissue biopsy can be obtained for additional analysis of immune cell infiltrates outside of the periphery. Biopsies are invasive, difficult to collect, and suffer from the bias of site specificity. Together these methods provide information on the state of the immune system at a single static time point but are subjective towards the sampled sites and limited in evaluating the state of the immune system across the whole body. This poses a clinical challenge for current immune based therapies. For example, in order to determine the success of a



hematopoietic stem cell transplant requires mature cells to be detected within the periphery, which can take up to 8 weeks. A non-invasive method to detect engraftment and expansion within the marrow and thymus at an earlier time point could reduce transplant complications by earlier detection of marrow failure. Alternatively, cancer immunotherapies that rely on the expansion and infiltration of anti-tumor cells have limited methods to track cells *in vivo*. Clinicians are unable to detect the location of on-target/off-tumor cellular cytotoxicity of the infused therapeutic cell product prior to complications, and cannot determine the quantity of successful tumor infiltrating cells without biopsy [3]. Non-invasive, whole-body techniques to monitor immune cell function can complement and improve the current clinical and pre-clinical methods.

Clinical imaging technologies such as X-ray, computed tomography (CT), magnetic resonance imaging (MRI), and positron emission tomography (PET) are used as routine diagnostic tools for a wide range of diseases but have had limited immunological applications. Small animal pre-clinical studies have utilized strategies restricted to small animals such as 2 photon microscopy, fluorescent, and bioluminescent imaging (BLI) or have adapted clinical modalities such as single-photon emission computed tomography (SPECT), PET, CT and MRI as methods for measuring changes in the immune system [4]. Each technology is relevant and in certain instances will be the most appropriate to use, but we have chosen to focus on PET imaging in pre-clinical studies of immunology due to the diversity of applications. One advantage of PET is that technologies developed pre-clinically can be applied directly to clinical problems, allowing for imaging agents to go from bench-top to bedside.

## The use of PET imaging in immunology

PET allows non-invasive, quantitative, and repetitive *in vivo* visualization of the biodistribution of positron-emitting probes specific for a wide variety of biological processes [5-6]. Released positrons from the probe annihilate with an electron in nearby tissue and emit two anti-parallel 511 keV high energy gamma photons. PET detectors measure the co-detection of both events and determine the location, creating a 3-dimensional image [6](Figure 1A). Pre-clinical microPET has a resolution of 1-2mm which is sufficient to detect lymph nodes more accurately than both BLI and SPECT. For immunology studies evaluating alterations in lymph nodes, a co-registered PET/CT scan can be most accurate in determining size, location, and probe accumulation while other imaging modalities are limited due to tissue penetrance and sensitivity. Tissue, including bone, does not scatter the high energy photons causing no attenuation problems allowing direct scaling from pre-clinical to clinical studies.

PET scans measure different biological processes based on the probe's design [7]. Positron emitting probes include short-lived isotopes (Half lives:  $^{18}\text{F}$ -110 min,  $^{11}\text{C}$ -20 min,  $^{68}\text{Ga}$ -68 min) that are commonly engineered into metabolites, or PET reporter probes. A fluorinated glucose analog, 2-deoxy-2- $(^{18}\text{F})$ fluoro-D-glucose ( $[^{18}\text{F}]$ -FDG), measures glucose consumption and is the most commonly used PET probe[8]. In the clinic,  $[^{18}\text{F}]$ -FDG is widely used for cancer diagnosis, staging, and response to therapy. Recently, investigators have begun to test whether  $[^{18}\text{F}]$ -FDG can be used to monitor immune cell function in cases of autoimmunity and blood malignancies [8]. Long-lived positron emitting nuclides (half-lives:  $^{124}\text{I}$ - 4.1 days,  $^{131}\text{I}$ - 8 days,  $^{64}\text{Cu}$ - 12.7 hours,  $^{89}\text{Zr}$ - 3.3 days) are more commonly used in antibody or peptide labeling.

Imaging via direct labeling of an antibody can be used for biomarker diagnostics and potentially theranostics [9-10].

Pre-clinical studies using microPET for in vivo visualization of immune responses in animal models is expanding. Sections will be divided into the four major sub-classes of PET imaging: 1. metabolic- radiolabeling a metabolite to study the utilization of a biochemical compound, 2. labeling- ex vivo labeling of cells with a radioisotope prior to infusion, 3. direct targeting- engineering radiolabeled peptides or antibodies to detect a protein of interest, 4. reporter imaging- engineering cells to express a unique protein that can be specifically detected through a cognate probe (Figure 1B).

## **2. Metabolic probes for monitoring changes in the immune system.**

The most broadly used PET sub-class is metabolic imaging. Metabolite mimetics are designed and radiolabeled to monitor a specific biochemical process in vivo. These probes can mimic sugars, nucleosides, amino acids, hormones or neurotransmitters [6]. The distribution of the probe demonstrates where an increased consumption of the metabolite is in comparison to other tissues within the body. Identifying changes in the metabolism of hematopoietic cells in response to an infection, cancer, or autoimmunity can identify key metabolites needed for proper immunity.

During an immune response, innate immunity is the first line of defense followed by an adaptive immune response [11]. Each immune cell lineage has different functional abilities that require certain biochemical substrates. During an immune response, cells will adapt their accumulation and metabolism of certain substrates depending on their activation state or

location. Macrophages and granulocytes will increase the expression of glucose transporters and glycolytic enzymes to generate the energy required for phagocytosis and cytokine secretion when located within inflamed tissue [12]. PET measurements of differentially regulated metabolic pathways may enable more thorough evaluation of immune cell function in vivo.

**Probe design and isotope utilization:** During the administration of the radiolabeled probe the biodistribution mimics how the body naturally accumulates the metabolite of interest. Metabolites are radiolabeled at a high specific activity and administered at concentrations of pico to femtomole per gram of tissue [5-6]. This low concentration allows most probes to function with no biological or pharmacological effect due to the low concentration of the metabolite [5, 7]. The probe is then excreted with the majority of probes cleared from circulation through renal filtration and hepatic clearance in some instances. The total radiation exposure from the probe is usually highest in the bladder and is the limiting organ for determining the dose based on radiation limits and not on concentrations of the substrate [8].

The distribution, accumulation, and clearance of most metabolites are short in comparison to peptides or antibodies. For synthesis and radiochemistry, choosing an isotope with a short half-life is best suited for these studies allowing fast detection and decay of the probe in vivo [5]. Most PET probes incorporate  $^{18}\text{F}$  because of its relatively short half-life (110 minutes), which is permissive for radiochemical synthesis, transport, application and imaging, yet undergoes decay rapidly enough to render it harmless within half a day [13].  $^{18}\text{F}$  chemistry typically replaces a hydrogen or hydroxyl group with a  $^{18}\text{F}$  isotope and allows for a metabolite mimetic. In cases where  $^{18}\text{F}$  cannot be used, other radiolabeled metabolites such as  $^{11}\text{C}$  and rarely  $^{15}\text{O}$  and  $^{13}\text{N}$  can

be used [5, 13].  $^{11}\text{C}$  has a 20 minute half-life. In order to complete a synthesis and purification with enough activity for imaging, the starting  $^{11}\text{C}$  activity will be much higher than  $^{18}\text{F}$  due to the rapid decay.

To date, thousands of unique PET probes have been made (The Radiosynthesis Database of PET Probes (RaDaP)). We will cover key studies that have applied metabolic probes to address issues in immunology.

**Glucose consumption by 2-deoxy-2-( $^{18}\text{F}$ )fluoro-D-glucose ( $^{18}\text{F}$ )-FDG):** [ $^{18}\text{F}$ ]-FDG is the most commonly used PET probe for pre-clinical and clinical studies [8]. It mimics glucose and can be used as an indication of the glycolytic rate of cells (Figure 2A). Most cancer cells will switch their metabolism towards a highly glycolytic state and the total glucose consumption is increased. [ $^{18}\text{F}$ ]-FDG imaging has exploited this phenotype of cancer by using the accumulation of [ $^{18}\text{F}$ ]-FDG as a method of diagnosis, staging, and response to therapy [8]. Normal tissues with a natural high glucose consumption will also accumulate [ $^{18}\text{F}$ ]-FDG including the heart and brain. Most hematopoietic tissues have weak glucose accumulation at a basal resting state and because of this [ $^{18}\text{F}$ ]-FDG has only been applied to studies with an activated or abnormal immune system [4].

**Cancer:** Lymphoma and leukemia have higher glucose consumption in comparison to non-malignant hematopoietic cells. [ $^{18}\text{F}$ ]-FDG accumulation is used as a method for staging and identifying cancerous cells in clinical diagnosis [8]. In one study, B cell leukemia cell lines were

engineered to express C/EBP $\alpha$ , causing cells to transdifferentiate towards a non-malignant macrophage phenotype. Total tumor burden after transplantation of parental or transdifferentiated cells was assessed by [ $^{18}\text{F}$ ]-FDG imaging. In animals receiving C/EBP $\alpha$  expressing cells, a decreased tumor burden and reduction in [ $^{18}\text{F}$ ]-FDG imaging was observed [14]. This study identified that glucose consumption is correlated with malignancy and that as cells transdifferentiate their metabolic requirements change. Future studies that aim to target cells to transdifferentiate in vivo can apply [ $^{18}\text{F}$ ]-FDG imaging for tracking total disease.

The relative accumulation of [ $^{18}\text{F}$ ]-FDG can also vary depending on the metabolic state of leukemic cells. The activation of the phosphatidylinositol 3-kinase (PI3K) pathway is known to increase glucose consumption and is partially regulated by PTEN. In an experimental mouse model, silencing of PTEN by shRNA led to the development of a T cell acute lymphoblastic leukemia (T-ALL). The shRNA construct was a “Tet-off” system and addition of doxycycline reactivated PTEN testing whether loss of PTEN is needed for disease maintenance. PTEN activation in T-ALL caused a decrease in the PI3K pathway and as a result the reduced the [ $^{18}\text{F}$ ]-FDG accumulation in specific organs in vivo [15] (Figure 2B). Although PTEN was activated systemically in a clonal leukemia, the change in accumulation of [ $^{18}\text{F}$ ]-FDG was heterogeneous suggesting that the regulation of the PI3K pathway can be affected by different factors within the tissue microenvironment.

**Autoimmunity:** Experimental models of autoimmunity including multiple sclerosis (experimental autoimmune encephalitis, EAE) [16] and rheumatoid arthritis [17-18] have been monitored through [ $^{18}\text{F}$ ]-FDG imaging.

The EAE model demonstrated that [ $^{18}\text{F}$ ]-FDG accumulation is not a strong indicator of immune infiltrates prior to disease onset, but as mild clinical symptoms are detectable an increase in glycolysis is seen [16] (Figure 2C). The rates of glycolysis by [ $^{18}\text{F}$ ]-FDG signal in the spinal column were not correlated with the severity of the disease, however when immune cell numbers decreased due to treatment with an immunosuppressive drug, a decrease in [ $^{18}\text{F}$ ]-FDG signal was observed. The limitation with [ $^{18}\text{F}$ ]-FDG was that disease could not be identified prior to clinical manifestation. For autoimmune diseases, [ $^{18}\text{F}$ ]-FDG may not be appropriate for staging of disease but could be useful in monitoring treatment and reduction of immune cells.

**Inflammation:** Inflammation in diseases such as atherosclerosis [19], liver damage [20] or colitis [21] have been measured with [ $^{18}\text{F}$ ]-FDG scans. Mice treated with concanavalin A had a significant increase in [ $^{18}\text{F}$ ]-FDG accumulation within the spleen and liver while severe combined immunodeficient (SCID) mice had no change between treatment and control [20]. The enhanced [ $^{18}\text{F}$ ]-FDG accumulation was due to the activation of T cells in the spleen and the infiltration of activated immune cells within the liver. SCID mice lack lymphocytes and [ $^{18}\text{F}$ ]-FDG accumulation was unchanged after concanavalin A treatment. Short-term experimental models like this can help identify when [ $^{18}\text{F}$ ]-FDG can be useful in monitoring multiple sites of inflammation.

**Cell proliferation by 3'-deoxy-3'-[ $^{18}\text{F}$ ]fluorothymidine ([ $^{18}\text{F}$ ]-FLT) accumulation:** [ $^{18}\text{F}$ ]-FLT is a substrate for thymidine kinase 1 (TK1) which is active in cells during S phase and can be used as a marker for cell proliferation [22-23]. Experimental models have looked at [ $^{18}\text{F}$ ]-FLT

accumulation in normal tissue and in cancers such as lymphoma. Accumulation of [ $^{18}\text{F}$ ]-FLT is seen within the spleen and bone marrow in healthy animals identifying sites of high cellular proliferation [23]. In lymphoma, the accumulation of [ $^{18}\text{F}$ ]-FLT is increased due to a significant increase in the percentage of replicating cells and in their division rate [23]. Accumulation of [ $^{18}\text{F}$ ]-FLT can also vary depending on serum and tumor levels of thymidine [24-25]. Mouse and rats have high serum thymidine levels and can dilute the accumulation of [ $^{18}\text{F}$ ]-FLT. Human serum has thymidine at concentrations 100 times lower than mice [26]. The average [ $^{18}\text{F}$ ]-FLT dose in humans is still administered with endogenous thymidine in greater than 150 fold excess potentially explaining the lack of signal in some hyperproliferative cells [25]. Deciphering tumor from immune cell infiltrates may be difficult with [ $^{18}\text{F}$ ]-FLT imaging, but in inflammation or infection models, the proliferation of immune cell infiltrates may be detected.

**Nucleoside salvage pathway measured by fluorinated nucleoside analogs:** [ $^{18}\text{F}$ ]-FLT is used as a marker of general cell proliferation and cannot be used to distinguish between the proliferation of immune versus non-immune cells. Recently, Radu and colleagues have developed nucleoside analog PET probes that target deoxycytidine kinase (dCK) [27]. dCK is the rate limiting enzyme in the nucleoside salvage pathway and is known to have high expression in lymphocytes. By targeting a metabolic pathway increased in T cells, the detection of active immune responses can be identified more accurately than with [ $^{18}\text{F}$ ]-FDG or [ $^{18}\text{F}$ ]-FLT alone.

**[ $^{18}\text{F}$ ]-FAC (1-(2'-deoxy-2'-[ $^{18}\text{F}$ ]fluoroarabinofuranosyl) cytosine):** dCK is the rate limiting enzyme in the accumulation and phosphorylation of the DNA terminating drug Gemcitabine



(dFdC). Accumulation of dFdC was highest in activated T cells, but due to the two fluorine atoms was not amenable for  $^{18}\text{F}$  radiochemistry [27].  $^{18}\text{F}$ -FAC is a similar compound to dFdC differing only by a hydrogen atom replacing the second fluorine (Figure 3A).

$^{18}\text{F}$ -FAC had strong retention in the spleen, thymus, and bone marrow of wild type mice [27]. A reduction in  $^{18}\text{F}$ -FAC signal was observed when animals were treated with the systemic immunosuppressive drug dexamethasone, which is toxic to lymphocytes [27]. In a genetic knockout of dCK a complete loss of  $^{18}\text{F}$ -FAC signal in all lymphoid organs was seen, with a dramatic reduction in the total number of mature T and B cells [28-29] (Figure 3B). Together these studies demonstrate the specificity of  $^{18}\text{F}$ -FAC for lymphoid tissues and the requirement of dCK for normal lymphopoiesis.

In models of immune cell expansion such as a viral induced tumor or autoimmunity, an increased  $^{18}\text{F}$ -FAC accumulation was seen in the thymus, lymph nodes and spleen [24, 27] (Figure 3C). Analysis of isolated immune cells identified that activated effector CD8 T cells from the draining lymph node had the highest accumulation of  $^{18}\text{F}$ -FAC with other lymphoid cells accumulating  $^{18}\text{F}$ -FAC at lower rates. The authors found that the accumulation of  $^{18}\text{F}$ -FAC was correlated with proliferation, and activated CD8 cells have the highest percentage of cells in S-G<sub>2</sub>-M phases (Figure 3D). Tumor infiltrated T cells have lower accumulation which may be due to a reduction in the proliferation/cell cycling rates [24].  $^{18}\text{F}$ -FAC is more selective for lymphocytes than other metabolic probes but has limited capacity in detecting tumor infiltrating T cells, identifying the need to develop additional T cell specific probes.

**2'-deoxy-2'-[<sup>18</sup>F]fluoro-9-β-D-arabinofuranosylguanine ([<sup>18</sup>F]F-AraG):** In a preliminary study, a radiolabeled AraG was synthesized and incubated with primary, activated or lymphoblastic T cells [30]. Accumulation of [<sup>18</sup>F]F-AraG was increased in activated T cells and in the leukemic cell line. Although animal studies using [<sup>18</sup>F]F-AraG are limited, the promising preliminary data suggests that [<sup>18</sup>F]F-AraG may be useful in detecting T cell malignancies in vivo.

**2-[<sup>18</sup>F]fludarabine:** Fludarabine is phosphorylated by dCK into Fludarabine phosphate (2-fluoro-ara-adenosine monophosphate [2-F-ara-AMP]) that is a nucleoside analog resistant to adenosine deaminase. This drug has been used successfully to treat lymphoid malignancies. In wild-type animals the accumulation of 2-[<sup>18</sup>F]fludarabine is seen in the spleen while in SCID animals that signal is lost [31] (Figure 4A,B). Subcutaneous B cell lymphomas were also detected by 2-[<sup>18</sup>F]fludarabine demonstrating the selectivity for lymphoid cells in vivo. The lack of thymus signal and high accumulation in B cell lymphomas suggest that 2-[<sup>18</sup>F]fludarabine may be useful in monitoring B cell locations and malignancies.

**Advantages and limitations of metabolic PET:** The advantage of metabolic PET is that measurements of cell function and metabolism can be obtained in vivo. When cell populations are isolated, their metabolism may change and not represent the true metabolic demands of the cells. For some myeloid derived cells, isolation can be difficult and can cause cell apoptosis prior to analysis. Measuring the accumulation of a radiolabeled metabolite in vivo can provide information of the whole-body metabolic demands of cells.

Probe synthesis can be a limiting step in metabolic PET. Some probes have multiple synthetic steps, low radiochemical yield, or require long tedious incubations [13]. When scaling from pre-clinical to clinical studies, this consideration can pose a significant hurdle in obtaining sufficient yield of the chemically pure product.

The major disadvantage for imaging immune cell function with metabolic PET is the lack of specificity for immune cells only. As seen in [ $^{18}\text{F}$ ]-FDG imaging, other tissues such as the brain and heart will accumulate the metabolic probe. When applying metabolic PET to immunology it is important to validate that the signal observed is due to changes in immune cell function rather than an experimental artifact or signal from non-immune cells.

**Future applications of metabolic PET:** T cell metabolism is complex and changes based on the activation state and location of cells [32]. As discussed, probes that measure nucleoside salvage are capable of detecting lymphoid cells, and activated T cells increase their accumulation of [ $^{18}\text{F}$ ]-FAC [27]. Intratumor T cells have low accumulation of [ $^{18}\text{F}$ ]-FAC probe and may switch their metabolic requirements. New probes that can measure the metabolic requirements of intratumoral T cells are needed as they could have broad applicability to monitor models of cancer immunotherapy.

Identifying unique metabolic states of immune cell subsets will also improve our understanding of the kinetics of an immune response. Probes that distinguish macrophages from dendritic cells, or CD4 from CD8 cells could help identify the quantity and location of individual lineages.

Similar to the work of Nair-Gill and colleagues [24] more studies may use a comparison and combination of multiple metabolic PET probes to identify the kinetics of how metabolism changes after a disruption in immune perturbation from drug therapy, infection, or cancer.

### **3. Visualization of targeted cell populations by pre-labeling ex vivo**

Ex vivo labeling of isolated hematopoietic cells has been utilized to track a range of immune cell subsets. Monocytes [33], engineered T cells [34], bulk lymphocytes, natural killer cells [35] and lymphoma cells have all been successfully monitored for their distribution and location by pre-labeling cells prior to infusion in SPECT and PET studies [36].

**$^{64}\text{Cu}$  direct cell labeling technologies:** Cell based immunotherapies are currently being developed to treat a broad range of diseases with an emphasis on treating cancer. Some therapies require an ex vivo expansion and culture of these immune cells prior to treatment. This ex vivo expansion can lead to the terminal differentiation of these cells, which are then expected to have a finite life span in vivo. Robust assays to monitor these cells short-term would enable investigators to serially track the location and distribution of transplanted cells. Ex vivo incubation of the therapeutic cells with a residualizing probe can provide a simple and consistent method to track cells. The most widely used direct cell label is  $^{64}\text{Cu}$ -pyruvaldehyde-bis(*N*-methylthiosemicarbazone) ( $^{64}\text{Cu}$ -PTSM) [37].

$^{64}\text{Cu}$ -PTSM acts as a lipophilic, redox-active transporter of  $\text{Cu(II)}$  ions that passively diffuses across the cell membrane and delivers copper into the cells. Once inside, the  $^{64}\text{Cu}$  and

PTSM complex can dissociate but the  $^{64}\text{Cu}$  is retained inside the cell due to the charge while the neutral PTSM can freely diffuse out of the cell (Figure 5A, B) [37].

The first demonstration of this labeling technique was with total isolated splenocytes labeled for 55min with  $^{64}\text{Cu}$ -PTSM. Cells were injected intravenously and imaged at 10 minutes and 20 hours after infusion. Lymphocytes trafficked from the lungs to the liver and spleen [37].

One concern of pre-labeling lymphocytes has been the documented sensitivity and cell death after exposure to radiation. New methods have been developed to minimize the inhibitory effects of  $^{64}\text{Cu}$ -PTSM on T cells in mouse models of T cell trafficking [34]. Isolated OVA  $\text{T}_\text{h}1$  were labeled using an optimized method and tested for cell viability, IFN- $\gamma$  production, proliferation, apoptosis, and DNA double-strand breaks. Although the optimized parameters were better than previous, defects in total T cell function were still observed. FACS analysis of phosphorylated histones of the H2AX family ( $\gamma$ -H2AX) was determined as a marker of radiation-induced DNA double-strand breaks. Three hours after  $^{64}\text{Cu}$ -PTSM labeling the relative  $\gamma$ -H2AX expression was approximately 9-fold higher than that of unlabeled OVA- $\text{T}_\text{h}1$  cells. While labeled cells retained similar viability to their unlabeled counterparts, a significant decrease in IFN-gamma production was observed indicating the probe caused defects in immune cell function.

For imaging purposes, the transplanted cells were tracked for up to 48 hours and cell locations were detected even within single lymph nodes. The homing and localization of cells was dependent upon injection route and whether or not the animal was activated by OVA peptide (Figure 5B). Labeled cells retained an equivalent homing capacity in comparison to non-labeled

cells and demonstrated the efficacy in utilizing  $^{64}\text{Cu}$ -PTSM for short consecutive scans of T cell homing in vivo.

**Limitations in imaging:** The biggest limitation in PET applications with direct labeling is the potential radiotoxicity from the isotope used [34]. Isotopes with long decay times have continued exposure increasing the damage. Another concern in using radiometals for PET imaging is that only a fraction of the decay is beta emissions that create the 511KeV events detected by PET [38]. The other emissions can be high energy gamma rays that can cause DNA damage [39-40]. Additional emissions can cause noise and background within the scans, reducing the image quality [9, 40-41].

#### **4. Targeted imaging by antibody and peptide engineering.**

Detecting a selective subset of cells can be achieved by multiple PET modalities. Investigators often look for methods that allow for tracking a specific cell population without manipulating the cells via expression of exogenous DNA. These methods can include pre-labeling as previously discussed or the use of radiolabeled antibodies and peptides [7, 42].

To target specific cell populations in vivo with a high specificity antibody and peptides for PET imaging have been used. Pre-clinical and recent clinical studies have tested these agents for detecting tumor associated cancer antigens or lineage specific cell surface proteins [42]. These proteins have high binding affinities allowing for signal accumulation based on binding to the target protein.

**Antibody and antibody fragments:** ImmunoPET uses targeted antibodies for monitoring the expression and distribution of subsets of cells in vivo [10, 38, 42]. Full length antibodies are the most commonly used but can be unfavorable for imaging.

An Immunoglobulin G (IgG) antibody is typically 150 kDa and is above the glomerular filtration threshold, which extends the blood half-life. The liver removes circulating antibodies, making this the dose limiting organ in imaging. High retention of circulating antibody within the blood also prevents imaging at early time points. Reducing the antibody size can reduce the half-life, and antibody fragments under 70kDa can be filtered through the kidney, reducing the radiation dose exposure to the liver.

Antibodies contain their specificity within the Fv portion, while domains of the Fc region contain the components for inducing antibody dependent cellular cytotoxicity (ADCC), complement-dependent cytotoxicity (CDC), FcRn salvage receptor binding to keep the antibody in circulation, or to activate additional immune cells. Modulating or removing portions of the antibody can alter and remove these biological effects.

Radiolabeling antibodies and peptides can be done by site-specific modification or by modifying exposed protein residues. For antibodies or fragments that lose affinity after non-specific radiolabeling, investigators can engineer free cysteines away from the binding site for site-specific modification [38, 43-44].

Antibody fragments from largest to smallest are intact (150kDa), sc-Fv-Fc (105kDa), minibody (80kDa), diabody (50kDa), and sc-Fv (25kDa) (Figure 6A). The most commonly used

antibody fragments for imaging are minibodies and diabodies. Minibody fragments contain a covalent dimer of scFv-C<sub>H</sub>3. The removal of the C<sub>H</sub>2 domain on minibody fragments removes ADCC, CDC, and FcRn salvage receptor binding functions. This also reduces a minibodies half-life in the blood to 5-11 hours in comparison to 12 days for intact antibodies. Diabody fragments are dimers of the scFv and retain the high avidity from the bivalency but are under the kidney filtration cut-off allowing a half-life of 3-7 hours. Depending on the assay and selected target an antibody can be engineered for optimal imaging *in vivo*.

**Targeted Peptides:** Lower molecular weight peptides have also been developed for PET imaging that are smaller than the 25kDa scFv antibody fragment. Small peptides such as the Pegylated Arg-Gly-Asp has been used to measure binding to brain tumor integrins [45]. Cystine knot peptides (knottins) are approximately 3kDa, non-immunogenic and can be engineered to bind a protein of interests [46]. Affibodies are engineered proteins with 58-amino acid residues that contain a binding surface similar to IgG antibodies [47]. Nanobodies, which are natural 15kDa antibodies from camels [48]. Most recently, the use of the 10th type III domain of human fibronectin (FN3) [49]. Current immunology applications have focused on nanobodies and on FN3 domains [48-49].

Nanobodies are a unique antibody format from camels. Nanobodies contain a single variable region of the heavy-chain-only (V<sub>HH</sub>) and are attractive proteins for therapy and imaging applications due to their small size (15kDa) and nanomolar affinity [48]. Due to the fast clearance and high targeting capacity, short-lived isotopes (<sup>18</sup>F, <sup>68</sup>Ga) can be applied,



significantly reducing the total radiation exposure. For lymphocytes which are especially sensitive to radiation, reducing the total radiation dose can improve cell viability.

FN3 is a protein that is less than 10 kDa, comprised of a  $\beta$ -sandwich, and has been engineered for high binding affinity to many targets including the B cell marker CD20 [49]. The FN3<sub>CD20</sub> has high stability and a single lysine for site specific amine conjugation of radioisotopes (Figure 7A). Improvements in tissue perfusion and a short blood half-life make the FN3 proteins attractive for applications in immunology.

**Selection of isotopes and methods of radiolabeling:** The most common radioisotopes applicable for PET that have been used in labeling proteins have been  $^{18}\text{F}$ ,  $^{64}\text{Cu}$ ,  $^{89}\text{Zr}$ ,  $^{68}\text{Ga}$ , and  $^{124}\text{I}$ . These can be added to the protein of interest through direct conjugation or by a linker that connects the radioisotope to the protein. For metal groups, a chelating agent is typically used as the linker providing a reproducible method to label the protein of interest. Linkers can be conjugated to amino acids in proteins such as lysines, tyrosines, or cysteines.

A radioisotope is selected based on the desired imaging time point and half-life of the engineered protein. For larger proteins including antibodies, minibodies, and diabodies imaging time points are typically 4 hours to 4 days after injection and require longer-lived isotopes  $^{64}\text{Cu}$  (12.7 hr),  $^{89}\text{Zr}$  (78.4 hr), and  $^{124}\text{I}$  (100.2 hr)[41].

A simple and robust labeling method has used direct radioiodination of  $^{124}\text{I}$  on antibodies, minibodies and diabodies modifying the exposed tyrosine residues [41]. The limitation is if the target is endocytosed then the  $^{124}\text{I}$  will efflux out of the cell and free  $^{124}\text{I}$  accumulates within the

thyroid and stomach. Residualizing probes should be used instead to allow accumulation of radioactivity such as  $^{64}\text{Cu}$ ,  $^{89}\text{Zr}$ , or  $^{68}\text{Ga}$ . These probes remain within the lysosome after the target protein is degraded increasing signal overtime [38, 41].

Excluding direct radioiodination, a linker is needed to anchor the isotope to the protein. Reactive cysteines are optimal targets and are usually engineered into the peptide or protein for site specific labeling [9-10, 41]. By engineering free cysteines conjugation is consistent with 1-2 radioisotopes added per protein keeping a relatively consistent specific activity. Without engineering cysteines, exposed lysines can be targeted with radiometal bound chelates [41, 48-50]. For small peptides including the nanobodies and FN3 proteins lysine conjugation is most commonly used. Macrocyclic chelators that bind the radioisotope and target the free amine group are derivatives of (1,4,7,10-tetraazacyclododecane-1,4,7,10-tetraacetic acid) (DOTA) and 2-[4,7-bis(carboxymethyl)-1,4,7-triazonan-1-yl]acetic acid (NOTA) (Figure 6B, 7A). These chelators are discussed below in the specific examples of peptide imaging in immunology.

**Tracking T cell locations with anti-CD8:** CD8 is an extracellular marker almost exclusively seen on cytotoxic T cells. CD8 cells can directly target and lyse cells through T cell receptor (TCR) / major histocompatibility (MHC) engagement. Pre-clinical models of T cell location, development, and function have improved our understanding of how the CD8 cells can clear infections or cancer. Two mouse specific CD8 minibodies (Mb) were made to target CD8 T cells in vivo [51]. The 2.43 Mb reacts with lyt 2.2, an isoform of CD8, in mouse strains such as C57Bl/6, but not in C3H. Radiolabeling of 2.43 by  $^{64}\text{Cu}$ -NOTA enabled imaging by microPET and detection of endogenous mouse CD8 cells which were seen predominantly in the spleen and

lymph nodes, with minimal signal seen in the bone marrow (Figure 6C). Signal was observed in the liver and is believed to be scavenged  $^{64}\text{Cu}$  and protein clearance of the radiolabeled minibody. The high signal seen within the lymph nodes is indicative of the sensitivity of the 2.43 Mb for detecting CD8. It is estimated that a naïve mouse lymph node contains 1 million cells with 7-12% being CD8. This estimates that between 70,000 – 120,000 CD8 cells can be detected with 2.43 Mb immunoPET [51]. Follow up studies should investigate the tracking and kinetics of CD8 cells after immunotherapies that stimulate T cell expansion and tumor infiltration in mouse models of cancer.

**Tracking B cell locations with anti-CD20:** CD20 is a pan B cell marker that has been a successful target in treating lymphomas with antibody therapy. Rituximab, the anti-CD20 antibody has had clinical success and has been extensively studied pre-clinically. A transgenic mouse was made to express human CD20 enabling investigators to study the human therapy in a mouse models.

A preliminary study demonstrated that  $^{64}\text{Cu}$ -DOTA-Rituxumab can target all transgenic CD20 B cells allowing investigators to monitor the location of total B cells in mice [52]. This study demonstrated the efficacy of using intact antibody imaging to identify primary sites of lymphoma. Signal was predominantly seen within the spleen and was blocked when animals were pretreated with cold Rituximab. Biodistribution determined that the highest dose was seen within the spleen and liver. When dose values from the mouse were estimated for human scans, the total exposure was below the safety limits. Together these validated that an intact

radiolabeled antibody could be effective in monitoring CD20 expressing lymphoma for staging and response to therapy.

As an alternative to intact antibody imaging, a CD20 specific FN3 protein of less than 10kDa was developed as an imaging agent. FN3<sub>CD20</sub> is made and isolated from E. coli, and can be lyophilized until needed. The ability to produce and store the FN3<sub>CD20</sub> is advantageous over antibodies or antibody fragments which can be difficult to produce in large quantities, purify and store. FN3<sub>CD20</sub> was labeled the same as <sup>64</sup>Cu-DOTA-Rituxumab, by <sup>64</sup>Cu bound to the DOTA linker conjugated at a free lysine (Figure 7A) [49]. Using the transgenic mice expressing human CD20, the <sup>64</sup>Cu-DOTA-FN3<sub>CD20</sub> was able to target the spleen with a faster and 10x higher accumulation measured as target tissue-to-blood ratio. The other organs with residual signal were the liver and kidneys. The liver signal is most likely due to free <sup>64</sup>Cu that dissociated from the DOTA label. The kidney signal is due to renal clearance of small peptides. Signals in these organs are lower than the spleen and lower than that seen with <sup>64</sup>Cu-DOTA-Rituxumab. In xenograft studies the <sup>64</sup>Cu-DOTA-FN3<sub>CD20</sub> had the highest tumor:liver ratio compared to the antibody and a minibody (Figure 7B). The success with adapting the FN3<sub>CD20</sub> as an imaging agent will hopefully lead to the development of FN3 imaging agents towards alternate immune markers.

### **Limitations in imaging:**

Protein size and quantity of the protein used can be a limitation in imaging. Proteins too large cannot easily target tumors or tissue with low permeability or perfusion [48]. Engineering smaller fragments can improve this defect but smaller proteins may have a faster blood

clearance, or lower avidity towards the target [10, 38, 53]. Nanobodies retain the affinity but can potentially be immunogenic and will need to be tested further [48].

**Future directions in immunoPET:** Improvements in  $^{18}\text{F}$  chemistry for labeling can solve current issues with protein imaging such as the radiotoxicity and the long incubation times required prior to scanning. The short half-life and ease in attaining  $^{18}\text{F}$  isotope can allow for faster scans with reduced radiotoxicity. As scientists design peptides with optimal blood half-life and biodistribution,  $^{18}\text{F}$  radiolabeling can become a more relevant isotope for these studies.

## **5. PET reporter genes for tracking engineered cells in vivo.**

**PET reporter gene overview:** Reporter genes allow investigators to detect a subset of specific genetically labeled cells in vivo by scanning with the corresponding reporter probe. Applications with PET reporter genes have been used in preclinical PET studies since 1996 with a large portion of studies investigating lymphocyte tracking after immunotherapies [54-55].

Reporter genes are ideal for preclinical studies that need to monitor the fate of transplanted immune cells[54]. An exogenous protein is expressed in the selected cells as a PET reporter and is then monitored for location, quantity, and distribution by the corresponding PET probe. Studies have tracked total hematopoietic cells, engineered T cells, dendritic cells, and other phagocytic cells in vivo.

PET reporter genes have utilized three unique subclasses of proteins (Figure 8) [54]. Expression of an extracellular protein such as a receptor or transmembrane protein allows for

direct targeting by the radiolabeled probe. PET reporters can also be membrane transporters. These allow for detection by active transport and accumulation of their probe intracellular. The most widely used PET reporters are enzymatic kinase reporters, which phosphorylate specific radio-labeled PET probes. Phosphorylated molecules are trapped within cells that express the enzyme reporter. In cells that do not express the reporter, the PET probe can freely efflux from the cell [54]. We will cover the applications of PET reporter genes only in immunology, although applications such as stem cell based therapies have also been tested.

**Advantages and disadvantages of PET reporter imaging:** The advantages of PET reporter gene imaging over metabolic or direct targeting are: 1. the ability to monitor subsets of cells (i.e. only the engineered T cells expressing a CAR), 2. unlike metabolic probes, the ideal PET reporter probe should have no accumulation in non-modified cells allowing for whole-body detection of reporter cells. 3. PET reporters expression is stable and should overcome the variability of cellular metabolism and expression/detection can be more consistent regardless of tissue location. 4. some PET reporter genes have also been demonstrated as effective suicide genes allowing for selective cell elimination if needed.

The major disadvantage of PET reporter gene imaging is the need to manipulate the cell either ex vivo or through targeted vector delivery in vivo. Cells can only express the PET reporter gene after the addition of exogenous DNA. Expression of foreign proteins can be immunogenic, deleterious, or oncogenic to the reporter labeled cells [56]. Although this is a potential risk, pre-clinical studies have tested whether the expression of a PET reporter gene will

alter function [57]. Expression of a human based enzymatic reporter did not affect hematopoiesis or T cell function [57-58].

Methods for transiently expressing a reporter gene have included transfection, adenoviral infection, or lipid molecule targeting [54, 59]. These methods are ideal for short term assays, for cells with limited replication potential so the transient DNA is not diluted, or for cell populations with short finite life-spans. Examples of pre-clinical studies that have used transient expression are dendritic cell vaccine trafficking and in vivo targeting of macrophages [4, 54, 56].

Viral infection by lenti- or retroviruses allow for lasting expression by genomic integration. Genomic insertion of a PET reporter gene is ideal for tracking hematopoietic stem cell progeny or activated T cells. These cells both have high replication rates and the relative expression of the PET reporter will remain constant with the integrated DNA being passed to daughter cells. The major disadvantage to viral gene delivery is the risk of insertional oncogenesis, vector splicing, or vector silencing [56]. Insertional oncogenesis happens when the viral integration is within a tumor suppressor, or there is transactivation or enhancement of an oncogene near the vector integration site [60]. In a model of insertional oncogenesis, the dual PET reporter/suicide gene HSV-TK was used [61]. After treatment of mice with ganciclovir to induce suicide function in HSV-TK cells, escaped leukemic clones due to vector splicing were observed [61].

**Enzymatic PET reporter genes:** Kinase PET reporter genes have been the most widely used in immunology studies. One reason for utilizing an enzymatic PET reporter is that even with low enzyme expression, the signal is amplified due to the enzymatic turnover rate of the reporter [54]. One limitation of enzymatic PET reporter genes is that the probe must be delivered into

cells by endogenous transporters [55, 57, 62-63]. Expression of these transporters is not regulated by the PET reporter gene and may vary depending on cell state or location [16, 64-65]. This may result in inconsistent signal regardless of the expression of the PET reporter gene. Yet one advantage of kinase reporter genes over transporters or some extracellular reporters is that the enzymatic reporters studied to date are relatively small (about 1kb, hNET is approximately 1.9kb) [54]. In therapeutic vectors with limitations on total vector size, minimizing the PET reporter can help improve viral titer, and protein expression.

**HSV-TK:** Herpes simplex virus type 1 thymidine kinase (HSV-TK) was first demonstrated as a suicide gene in vitro with selective elimination of expressing cells by acycloguanosine compounds such as Ganciclovir (GCV) [66]. In clinical studies the expression of HSV-TK was immunogenic when expressed in adoptively transferred T cells for graft versus leukemia [67-68]. Immune responses were from CD8 cells against the HSV-TK gene and were rapid, most likely due to memory T cell responses. No pre-clinical studies have reported immunogenicity from HSV-TK in mice. The lack of prior exposure to HSV infection may prevent mice from developing immunogenicity to this PET reporter making it a useful pre-clinical tool. To validate HSV-TK as a PET reporter, investigators first tested whether SPECT ( $^{131}\text{I}$ ) and PET ( $^{124}\text{I}$ ,  $^{18}\text{F}$ ) probes of acycloguanosine like compounds could visualize HSV-TK expressing xenografts in mice [55].

In 2002, a mutant form of HSV-TK with improved  $V_{\max}/K_m$  for GCV (sr39TK, described by [62]) was used in the first immunology based application of monitoring tumor burden in Bcr-Abl leukemia [69]. Sequential scans with a radiolabeled penciclovir analog, 9-(4- $^{18}\text{F}$ )-fluoro-3



hydroxymethylbutyl) guanine ( $[^{18}\text{F}]$ -FHBG), were obtained from animals with BCR-ABL leukemia or BCR-ABL leukemia with G protein-coupled receptor 132 (G2A) knockout. Total tumor burden was visualized within the bone marrow and lymph nodes. Animals with a genetic loss of G2A had significantly elevated signal, which corresponded to increased tumor burden and shorter life-expectancy. This study demonstrated the feasibility of PET reporter imaging of HSV-TK as a tool to monitor the location of leukemogenic or normal immune cells in vivo.

HSV-TK was then applied to monitor the location and migration of Epstein Bar Virus (EBV) reactive human T cells [70]. Signal was observed in the spleen and in the EBV<sup>+</sup> HLA matched tumors 24 hours after lymphocyte infusion with peak signal seen at 48 hours ( $[^{124}\text{I}]$ -FIAU probe was administered 4 hours prior to scan) (Figure 9). Infused cells could be monitored by PET imaging for up to 15 days post infusion, while in contrast, when cells were pre-labeled with  $[^{124}\text{I}]$ -FIAU in vitro, signal was only maintained up to 8 days post-infusion. This demonstrates the capacity of being able to pre-label or image cells at distinct time points as needed when cells express the HSV-TK reporter gene.

Additional studies have utilized HSV-TK as a tool to monitor immune responses. The locations and infiltration of tumor reactive T cells has been detected by  $[^{18}\text{F}]$ -FHBG in mouse and human models of immunotherapy. These have included engineered T cell receptors (TCRs), chimeric antigen receptors (CARs), and tumor reactive T cells from viral induced sarcomas [71-73]. Animals that received a bone marrow transplant with cells engineered to express HSV-TK were challenged with a viral induced sarcoma and this allowed for the detection of a primary anti-tumor response in vivo [74].

By incorporating HSV-TK, PET reporter gene cells are detected with a 3D image of the location of engineered cells. This has enabled investigators to decipher tumor draining lymph nodes signal from tumor signal because of the improved resolution of PET in comparison to alternate imaging modalities.

**Next generation enzymatic PET reporter genes:** Due to the observed clinical immunogenicity with HSV-TK, alternate enzymatic PET reporters were developed. Homologous to HSV-TK, the human nucleoside kinases were tested in PET reporter applications. Two mutant forms of human deoxycytidine kinase (hdCK) have been successful in monitoring engineered hematopoietic cells [57-58].

Expression of hdCKDM (point mutations of R104M and D133A) when probed with 2'-[<sup>18</sup>F]-fluoro-2'-deoxyarabinofuranosyl-5-ethyluracil ([<sup>18</sup>F]-FEAU) was able to track tumor infiltrated CAR modified T cells in a model of metastatic prostate cancer [58]. Human T cells were engineered to express hdCKDM and the Pz-1 CAR that is targeted to prostate-specific membrane antigen (PSMA). T cells were transplanted and imaged 6 hours post infusion with [<sup>18</sup>F]-FEAU. Signal accumulated in the lung tumors of animals given the hdCKDM expressing T cells. This study demonstrates that hdCKDM could be used in monitoring cellular adoptive immunotherapy to track the location of engineered cells within metastatic tumors.

A separate study evaluated the expression of hdCK3mut (three point mutations within the active site) with [<sup>18</sup>F]-L-FMAU to monitor long-term hematopoietic stem cell engraftment and expansion [57] (Figure 10A). Expression of hdCK3mut allowed for serial detection of reporter cells up to 32 weeks after a bone marrow transplantation (Figure 10B). Importantly, long-term

expression of hdCK3mut was inert in hematopoietic stem cells with the hdCK3mut progeny cells having comparable engraftment, expansion, and longevity to non-reporter labeled cells (Figure 10C).

These studies show that hdCK-based PET reporter genes can be applied to current immunological difficulties in monitoring the location and longevity of transplanted engineered cells. Examples include tracking HSC transplants, engineered T cell therapies, or monitoring experimental GvHD. Expression of a hdCK based reporter gene is maintained and does not alter the cells function in vivo. To overcome the immunogenicity problem that HSV-TK faces, hdCKDM and hdCK3mut are human enzymes with minimal mutations, and should thus not be immunogenic if translated into clinical studies.

**Transporter PET reporter:** In a mouse model of adoptive immunotherapy the human norepinephrine transporter (hNET) was expressed as a PET reporter gene and detected by  $^{124}\text{I}$ -metaiodobenzylguanidine ( $^{124}\text{I}$ -MIBG) [75]. To test the sensitivity of hNET as a PET reporter, T cells were injected intratumorally and imaging after 4 hours detected as little as  $10^4$  cells. To track tumor infiltration of T cells, EBV reactive CD8 cells were transduced to express hNET and injected intravenous. On day 1, 8 and 28, animals were scanned with  $^{124}\text{I}$ -MIBG which showed a progressive increase in signal from the tumor infiltrating lymphocytes at each time point. Although hNET is a human enzyme and should reduce the immunogenicity seen with HSV-TK in human applications, comparative analysis determined that HSV-TK was more sensitive.

**Receptor/ligand PET reporter:** Although several receptor PET reporter genes have been developed, their applications to immunology have been limited. The recombinant carcinoembryonic antigen (CEA) was tested as a potential PET reporter gene by expression in the T cell leukemia line Jurkat. Anti-CEA minibody imaging detected CEA positive Jurkats, thereby demonstrating the potential applications of receptor or extracellular PET reporter genes [76-77].

**Future directions of PET reporter genes:** Only one study has been reported which uses PET reporter imaging for monitoring T cell activation by turning on the expression of HSV-TK [78]. Although all Jurkat cells were transduced with the inducible HSV-TK construct, the reporter was only activated and detected in those animals treated with anti-CD3 and anti-CD28. Similar inducible reporter systems may also be helpful in addressing the behavior of immune cells after immunotherapies (e.g. anti-PD1, DC vaccine, anti-CTLA4, or engineered T cells with TCRs or CARs) are given. In particular, if signal is weak or absent, one might be able to predict treatment failure or poor response to therapy.

Improvements in lineage specific reporters could also broaden the use of PET reporter genes. For instance, using lineage induced reporters would enable tracking of the development/fate of lymphoid lineages post HSC transplant. However, current lineage reporters can be weak, but new methods for amplification of expression will most likely improve these lineage inducible systems [4].

Improvements in the PET reporter gene and probe combination can also allow PET reporter genes to be used in additional immunology applications. The higher the sensitivity of the

reporter and specificity of the probe, the less cells that are then needed for detection in a selected area. For studies that are tracking a small number of cells, this could provide a new method of detection. Applications could include monitoring the location of lymphocytes intratumor or detecting alloreactive cells that cause autoimmune disorders. For enzymatic reporters, improving the enzymatic activity for the probe to lower the  $K_m$  and increase the turnover rate will allow for increased probe sequestration. Current PET reporter probes have seen non-specific clearance in the gallbladder, intestines, liver, kidneys, and bladder [57, 62, 79]. Metabolism and clearance of ideal PET reporter probes will be through renal filtration, with minimal signal seen in the kidneys and excretion through the bladder.

HSV-TK has been a successful reporter due to its sensitivity, small size, and broad applicability. One key feature of HSV-TK is the dual functionality of being a reporter and suicide gene. When given pharmacological doses of acycloguanosine compounds (e.g. Ganciclovir) the HSV-TK expressing cells are selectively eliminated [66]. Current literature on novel reporters has discussed the potential of utilizing the human PET reporters as suicide genes [57-58], or targeting the receptor reporters with a therapeutic antibody for selective elimination. Development of the suicide gene function will allow investigators to remove reporter cells in case of an adverse event, improving the safety of cell based therapies.

## **6. Scanner and quantification limitations**

**Resolution limitations:** The resolution of microPET scanners is approximately 1mm. The resolution of a PET scanner is determined by the size of the scintillator crystals. In some instruments a continuous sheet of scintillator is used and the resolution is adjusted based on the

thickness of the sheet and the size of the photomultiplier tubes reading out [5]. It is difficult to improve the resolution of the image due to the reconstruction, and scanner sensitivity depending on the isotope used [5]. The slight scatter in signal between positron release and annihilation and total sensitivity can be problematic for small areas such as mouse lymph nodes that are at the limit of detection for microPET scanners. To date, the maximum predicted resolution is about 0.5mm for a microPET scan [5]. A strategy to more accurately detect lymph nodes is to include the co-registration of a CT scan that can provide improved anatomical information at a higher resolution (typically 50-250um) allowing for ROIs drawn on the CT to be applied to the PET scan for quantification.

**Scanner Sensitivity:** The total sensitivity of scanners is actively being investigated to improve current technologies. MicroPET scanners can detect from 4–15 % of total signal [80]. For experimental probes, the total counts or coincidence events needed for an accurate image reconstruction can be limiting when synthesis and production has low yields. For peptide or antibody fragments, the specific activity after radiolabeling can also vary depending on conjugation conditions and concentration of isotope. By utilizing scanners with enhanced sensitivity, less isotope and lower specific activity is needed. Conversely, investigators can choose to conjugate at the same or higher specificity to reduce the total amount of peptide needed per scan. The reduction in radioactivity improves safety, and reduces the cost per study. Improved sensitivity also allows sequential scans of the same animal to be extended to longer time points. To increase the sensitivity of the scanner and improve preclinical instrumentation new technology focuses on utilizing different types of detectors (planar versus cylindrical, material of detector, and range of detectable energy) [80].

**Scanner quantification limitations:** Partial volume effect can be problematic in immunology studies because it may underestimate the total activity in a small area on the scan[81-82] . In particular, ROIs over areas such as the lymph nodes may be quantified with lower values in comparison to ex vivo biodistribution values. This issue/occurrence can be explained by the imaging software that keeps the minimum size of ROIs during analysis to 1 voxel (approximately 1mm). Due to partial signal scatter and the actual lymph node size being smaller than 1mm in some cases the quantified signal by PET analysis will be lower than actual values creating a partial volume effect. This limitation in accuracy below 1mM makes quantification not completely accurate for small ROIs due to current image analysis techniques. If possible, biodistribution by gamma counting lymph nodes is the most accurate measurement of total activity per gram.

**Low signal in microPET imaging:** Low signal can be missed in organs adjacent to sites of probe metabolism due to the bleed over in signal and difficulty in scaling the scan appropriately[81]. For example, with most small molecule probes, clearance occurs in the kidneys and bladder. The prostate, located next to the bladder, can be difficult to detect in both pre-clinical and clinical scans. Adjusting the imaging protocol to allow a longer conscious uptake including excretion of extra probe through the bladder can help to reduce this issue.

Low cell densities may also dilute the accumulated signal making it hard to register over background in certain studies. Immune cells located intratumor, and in other immune organs may not be detected depending on the cell state and the sensitivity of the probe. In a recent study no signal was observed from PET reporter labeled human cells located within the mouse spleen

[57]. For this experiment, the human cells comprised less than 5% of total spleen cells. Potential explanations are due to the low metabolic state of cells or the weak signal to noise ratio.

Intratumor cells have also been difficult to detect in some studies. For metabolic probes, the background tumor metabolism can affect signal. As shown by Radu et al., cells can also change metabolic states intratumor altering the signal accumulation [24, 27]. Tumors also exhibit the enhanced permeability and retention effect (EPR) causing non-specific accumulation of some probes [83-84]. For pre-clinical studies, ex vivo analysis and biodistribution studies can complement the PET scan and accurately determine the percent injected dose in each isolated organ.

## **7. Concluding remarks and future directions of PET in pre-clinical/clinical immunology applications.**

PET is a powerful imaging tool for pre-clinical studies due to the sensitivity, resolution, and wide array of applications and probes. We have covered key PET studies in immunology and emphasized the areas where improvements and future research should be focused. Advancing pre-clinical PET imaging will not only improve our understanding of disease processes and therapeutics, but also translate into beneficial clinical applications.



**Acknowledgements:** We acknowledge all colleagues who contributed to the work presented here. Melissa N. McCracken was supported by the CIRM training grant (TG2-01169) and the UCLA Graduate Division Dissertation Year Fellowship. Owen N. Witte is an investigator of the Howard Hughes Medical Institute and partially support by the Eli and Edythe Broad Center of Regenerative Medicine and Stem Cell Research.

## Figure Legends:

**Figure 1: Principles and classes of PET imaging.** A) Accumulated probe will emit positrons. Positrons will annihilate with a nearby electron and create two opposing 511keV gamma rays. The paired 511keV gamma rays are detected as coincident events in the detector and a 3D image is reconstructed. B) PET images can detect multiple biological processes. Metabolism of a specific substrate can be measured by radiolabeling a mimetic and monitoring the accumulation of the probe. Ex vivo labeling of cells by residualizing isotopes can allow for tracking cells once transplanted in vivo. Antibody or peptides can be used to detect the expression of extracellular proteins. PET reporter genes allow specific detection by exogenous expression of a unique protein that can be targeted with a reporter specific probe.

**Figure 2: Glucose consumption in immune cells measured by [<sup>18</sup>F]-FDG.** A) Chemical structure of [<sup>18</sup>F]-FDG. B) T-ALL mice initiated by shRNA Pten silencing. Addition of Dox will turn on Pten and reduce PI3K signaling. [<sup>18</sup>F]-FDG signal seen in Pten off mice is within the liver and spleen. Pten on reduces total tumor burden and removes majority of the liver signal previously observed. (Adapted from Miething et al. 2014) C) [<sup>18</sup>F]-FDG in EAE mice. In mice with clinical EAE scores an increase in [<sup>18</sup>F]-FDG is seen in the spinal column. (Adapted from Radu et al. 2007 Copyright (2007) National Academy of Sciences, USA.)

**Figure 3: Nucleoside Salvage in PET imaging of immune cells with [<sup>18</sup>F]-FAC.** A) Gemcitabine (dFdC) and [<sup>18</sup>F]-FAC chemical structure. B) [<sup>18</sup>F]-FAC imaging of WT and dCK

KO mice. (Adapted from Toy et al. 2010) C) [ $^{18}\text{F}$ ]-FAC imaging of MSV development in wild-type mice. Signal is observed in the: Thy- thymus, Sp-spleen, GI- gastrointestinal track, Bl- bladder, BM- bone marrow, DLN- draining lymph node, T- tumor. (Adapted from Nair-Gill et al. 2010) D) [ $^3\text{H}$ ]-FAC uptake from sorted cells. Cells were fixed and stained with propidium iodide. The percentage in S-G<sub>2</sub>-M was plotted against the accumulation of [ $^3\text{H}$ ]-FAC. Open, filled, and half-filled symbols represent 3 experiments. Shapes were assigned according to cell type: squares- B cells, triangles- CD4<sup>+</sup> T cells, circles- CD8<sup>+</sup> T cells, diamonds- CD11b<sup>hi</sup> myeloid cells. Colors were assigned based on the tissues from which a cell population was isolated: blue- spleen, green- DLN, red- tumor, gray- naive lymph nodes. A positive correlation between [ $^3\text{H}$ ]-FAC accumulation and percent in S-G<sub>2</sub>-M was observed ( $r^2 = 0.68$ ,  $P < 0.0001$ ). (Adapted from Nair-Gill et al., Republished with permission of J Clin Invest, from “PET probes for distinct metabolic pathways have different cell specificities during immune responses in mice.”, Nair-Gill et al., 120, 6, 2010; permission conveyed through Copyright Clearance Center, Inc.)

**Figure 4: Detection of lymphocytes with 2-[ $^{18}\text{F}$ ]fludarabine PET imaging.** A) Chemical structure of 2-[ $^{18}\text{F}$ ]fludarabine. B) Wild-type or SCID mice were scanned with 2-[ $^{18}\text{F}$ ]fludarabine. In wild-type mice, signal was observed within the spleen. (Adapted from Dhilly et al. 2014, with kind permission from Springer Science and Business Media)

**Figure 5: Ex vivo labeling of T cells with [ $^{64}\text{Cu}$ ]-PTSM.** A) [ $^{64}\text{Cu}$ ]-PTSM bound and free PTSM. B) Schematic of how [ $^{64}\text{Cu}$ ]-PTSM labels cells ex vivo. (Adapted from Adonai et al.

2002 Copyright (2002) National Academy of Sciences, USA.) C) Different administration routes of  $^{64}\text{Cu}$ -PTSM-labeled OVA-Th1 cells resulted in distinct homing patterns. Representative PET/CT images at 7 h (left) and 27 h (right), with focus on perithymic LNs, lung, and spleen (indicated by arrows). i.p. = intraperitoneal; i.v. = intravenous. (Adapted from Griessinger et al. This research was originally published in *JNM*. Christoph M. Griessinger, et al. In Vivo Tracking of Th1 Cells by PET Reveals Quantitative and Temporal Distribution and Specific Homing in Lymphatic Tissue. *J Nucl Med*. 2014;55:301-307. © by the Society of Nuclear Medicine and Molecular Imaging, Inc.)

**Figure 6: ImmunoPET by antibody engineering and radiolabeling.** A) Antibody and antibody fragments. Top- structure and domains of the antibody fragment and size. Bottom- Representative biodistribution (%ID/g ) over time of a tumor targeted antibody fragment. Tumor is plotted in yellow, blood is plotted in blue. (Adapted from Knowles at al. Reprinted with permission. © (2012) American Society of Clinical Oncology. All rights reserved.) B) Chelating agents used for radiolabeling antibodies and peptides. DOTA and NOTA are capable of binding a charged metal isotope within the center ring structure. C)  $^{64}\text{Cu}$ -NOTA-2.43 Mb imaging of mice. Bl6 are lyt 2.2 and signal is seen within the spleen and lymph nodes. Spleen and lymph node signal is lost in C3H and NSG. C3H are lyt 2.1 and the 2.43 Mb cannot detect the CD8 cells in vivo. NSG are immunodeficient and contain no endogenous CD8 cells. (Adapted from Taváre et al. 2014)

**Figure 7: Targeting hCD20 with  $^{64}\text{Cu}$  labeled proteins.** A) Structure of the [ $^{64}\text{Cu}$ ]-DOTA-FN3<sub>CD20</sub> peptide used. B) Subcutaneous xenografts expressing hCD20 were detected by [ $^{64}\text{Cu}$ ]-DOTA-FN3<sub>CD20</sub> (left) or [ $^{64}\text{Cu}$ ]-DOTA-Rituximab (right). Yellow arrow indicates tumor. L-liver, K-kidneys, BP-blood pool. (Adapted from Natarajan et al. 2013)

**Figure 8: Subclasses of PET reporter genes.** PET reporter genes can be one of three subclasses of proteins. Receptor PET reporter genes are a transmembrane protein that allows for reporter imaging by binding a radiolabeled ligand or targeted peptide to the protein. Transporter PET reporter genes work by transporting a PET reporter probe intracellular. Enzyme or kinase PET reporter genes work by phosphorylating their cognate probe trapping the probe intracellular.

**Figure 9: Tracking CTLs with HSV-TK PET reporter imaging.** Sequential oblique projections of summed coronal images at a 45° angle to visualize the Sp-spleen, targeted tumors, K-kidneys, St-stomach, Bl-bladder, H-heart 4 h after [ $^{124}\text{I}$ ]FIAU injections on days 1, 8, and 15 after infusion of CTL-TKGFP. Tumors implanted are autologous and *HLA-A0201*<sup>+</sup> EBV<sup>+</sup> tumors. (Reprinted by permission from Macmillan Publishers Ltd: Nature Biotechnology (Koehne et al.), copyright (2003))

**Figure 10: hdCK3mut PET reporter gene imaging of hematopoietic reconstitution.** A) Recipient mice received a BMT with either hdCK3mut expressing cells or YFP, scan was obtained 4 weeks after transplant. Signal was observed in the T-thymus, S-Spleen, BM-bone

marrow of hdCK3mut. Clearance of the probe was seen in both recipients in the GI-gastrointestinal tract, K-kidney, Bl-bladder. B) Persistent reporter signal was observed in the BM- bone marrow and Sp-spleen of reporter mice up to 32 weeks post BMT. C) No defect in longevity or life expectancy was observed between hdCK3mut and YFP recipients. (Adapted from McCracken et al. 2013)

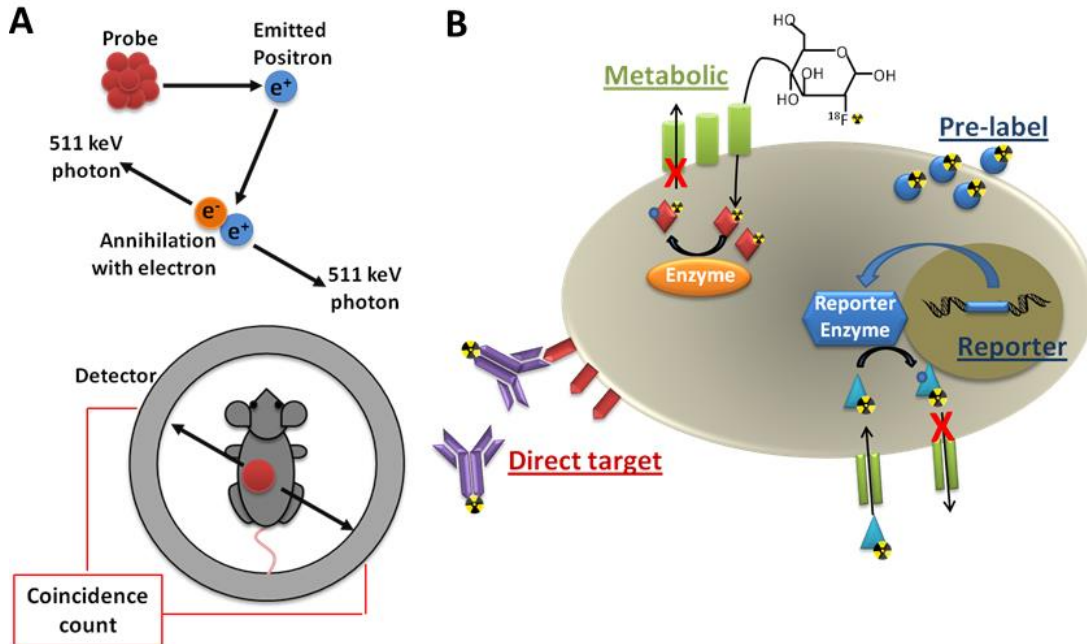


**Figure 1: Principles and classes of PET imaging.** A) Accumulated probe will emit positrons. Positrons will annihilate with a nearby electron and create two opposing 511keV gamma rays. The paired 511keV gamma rays are detected as coincident events in the detector and a 3D image is reconstructed. B) PET images can detect multiple biological processes. Metabolism of a specific substrate can be measured by radiolabeling a mimetic and monitoring the accumulation of the probe. Ex vivo labeling of cells by residualizing isotopes can allow for tracking cells once transplanted in vivo. Antibody or peptides can be used to detect the expression of extracellular proteins. PET reporter genes allow specific detection by exogenous expression of a unique protein that can be targeted with a reporter specific probe.

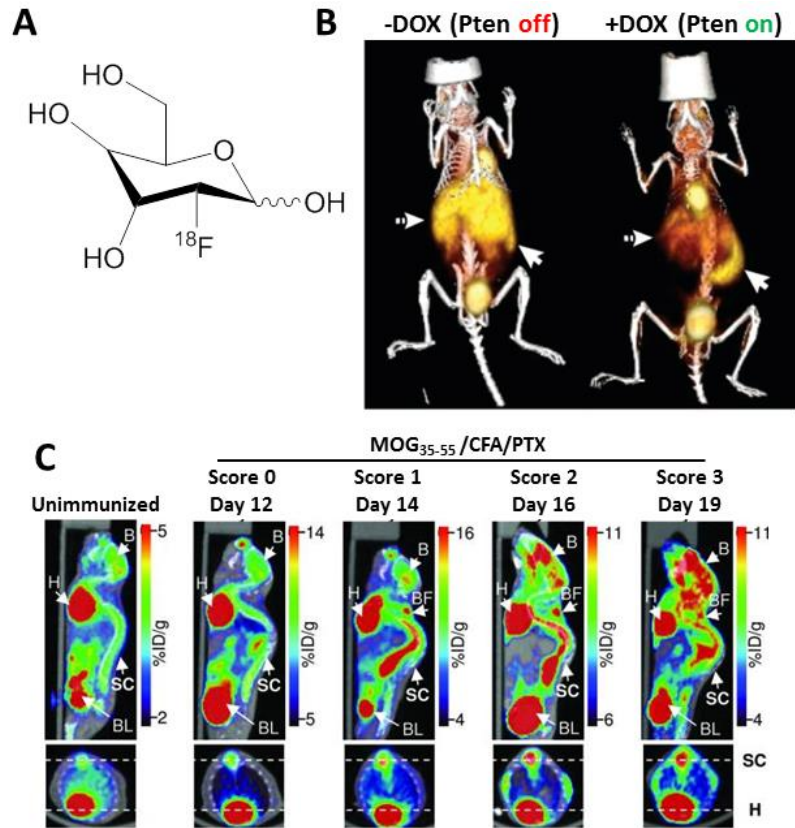


**Figure 2: Glucose consumption in immune cells measured by [<sup>18</sup>F]-FDG.** A) Chemical structure of [<sup>18</sup>F]-FDG. B) T-ALL mice initiated by shRNA Pten silencing. Addition of Dox will turn on Pten and reduce PI3K signaling. [<sup>18</sup>F]-FDG signal seen in Pten off mice is within the liver and spleen. Pten on reduces total tumor burden and removes majority of the liver signal previously observed. (Adapted from Miething et al. 2014) C) [<sup>18</sup>F]-FDG in EAE mice. In mice with clinical EAE scores an increase in [<sup>18</sup>F]-FDG is seen in the spinal column. (Adapted from Radu et al. 2007 Copyright (2007) National Academy of Sciences, USA.)



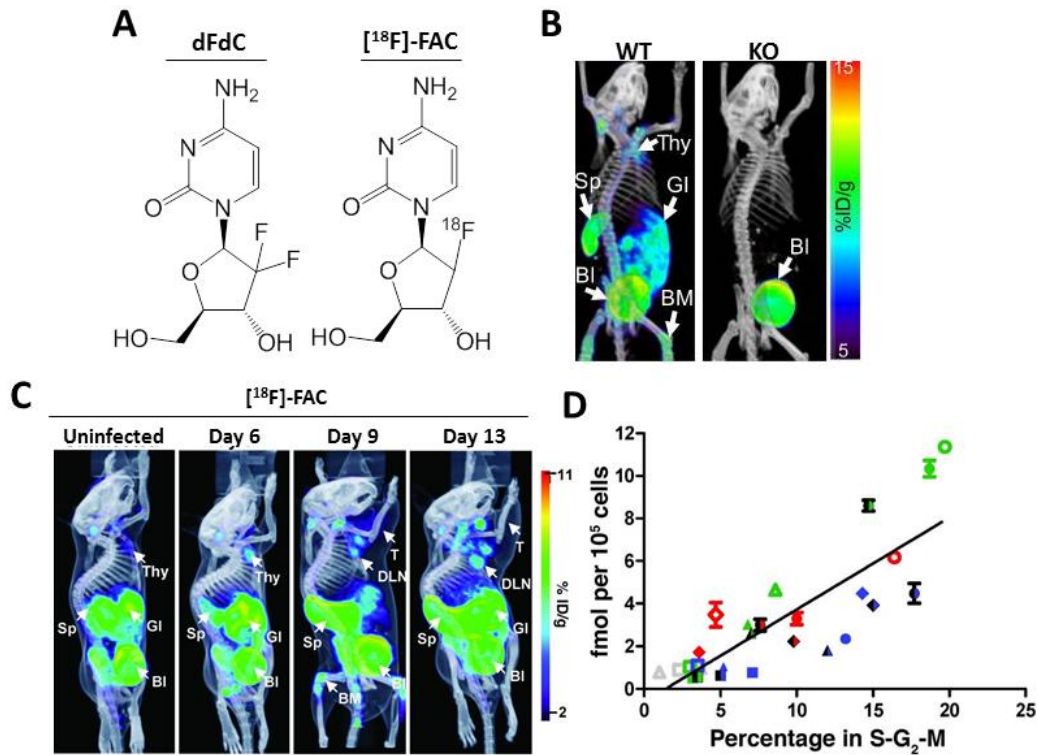


**Figure 3: Nucleoside Salvage in PET imaging of immune cells with  $[^{18}\text{F}]\text{-FAC}$ .** A) Gemcitabine (dFdC) and  $[^{18}\text{F}]\text{-FAC}$  chemical structure. B)  $[^{18}\text{F}]\text{-FAC}$  imaging of WT and dCK KO mice. (Adapted from Toy et al. 2010) C)  $[^{18}\text{F}]\text{-FAC}$  imaging of MSV development in wild-type mice. Signal is observed in the: Thy- thymus, Sp-spleen, GI- gastrointestinal track, Bl- bladder, BM- bone marrow, DLN- draining lymph node, T- tumor. (Adapted from Nair-Gill et al. 2010) D)  $[^3\text{H}]\text{-FAC}$  uptake from sorted cells. Cells were fixed and stained with propidium iodide. The percentage in S-G<sub>2</sub>-M was plotted against the accumulation of  $[^3\text{H}]\text{-FAC}$ . Open, filled, and half-filled symbols represent 3 experiments. Shapes were assigned according to cell type: squares- B cells, triangles- CD4<sup>+</sup> T cells, circles- CD8<sup>+</sup> T cells, diamonds- CD11b<sup>hi</sup> myeloid cells. Colors were assigned based on the tissues from which a cell population was isolated: blue- spleen, green- DLN, red- tumor, gray- naive lymph nodes. A positive correlation between  $[^3\text{H}]\text{-FAC}$  accumulation and percent in S-G<sub>2</sub>-M was observed ( $r^2 = 0.68$ ,  $P < 0.0001$ ).

(Adapted from Nair-Gill et al., Republished with permission of J Clin Invest, from “PET probes for distinct metabolic pathways have different cell specificities during immune responses in mice.”, Nair-Gill et al., 120, 6, 2010; permission conveyed through Copyright Clearance Center, Inc.)

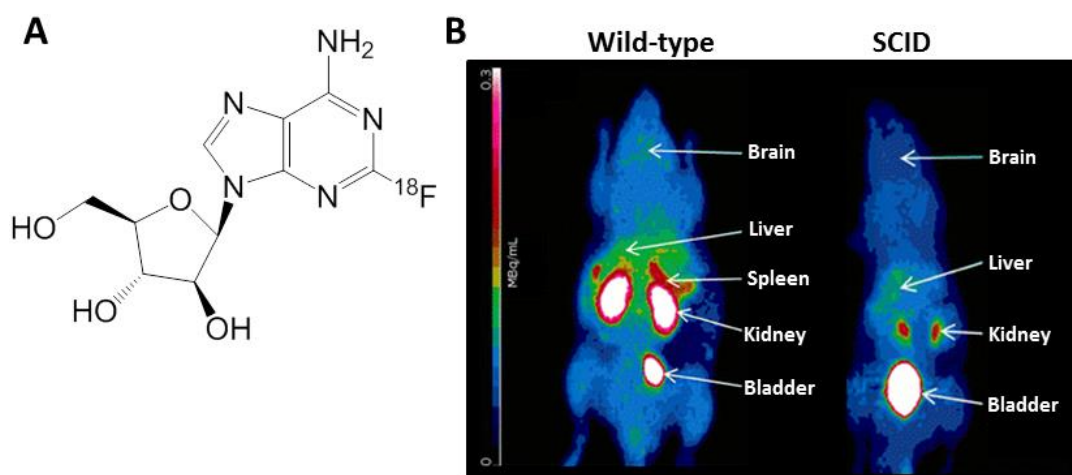


**Figure 4: Detection of lymphocytes with 2-[<sup>18</sup>F]fludarabine PET imaging.** A) Chemical structure of 2-[<sup>18</sup>F]fludarabine. B) Wild-type or SCID mice were scanned with 2-[<sup>18</sup>F]fludarabine. In wild-type mice, signal was observed within the spleen. (Adapted from Dhilly et al. 2014, with kind permission from Springer Science and Business Media)

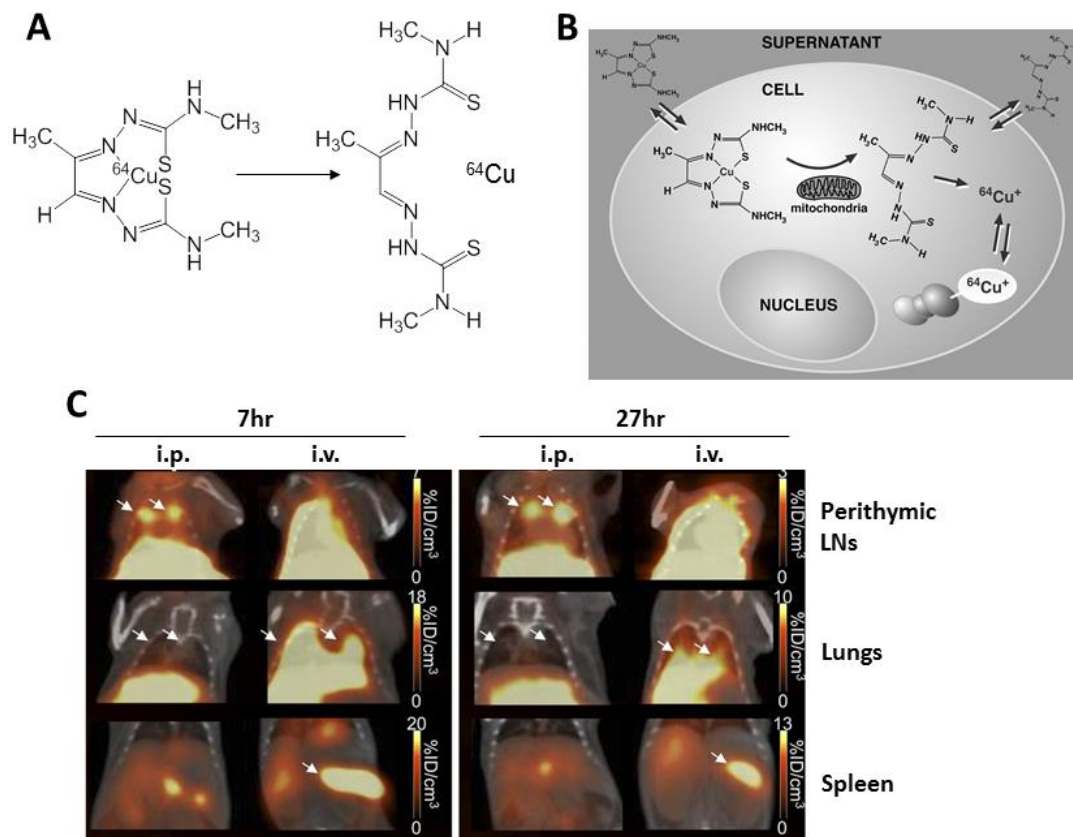


**Figure 5: Ex vivo labeling of T cells with  $[^{64}\text{Cu}]\text{-PTSM}$ .** A)  $[^{64}\text{Cu}]\text{-PTSM}$  bound and free PTSM. B) Schematic of how  $[^{64}\text{Cu}]\text{-PTSM}$  labels cells ex vivo. (Adapted from Adonai et al. 2002 Copyright (2002) National Academy of Sciences, USA.) C) Different administration routes of  $^{64}\text{Cu}\text{-PTSM}$ -labeled OVA-Th1 cells resulted in distinct homing patterns. Representative PET/CT images at 7 h (left) and 27 h (right), with focus on perithymic LNs, lung, and spleen (indicated by arrows). i.p. = intraperitoneal; i.v. = intravenous. (Adapted from Griessinger et al. This research was originally published in *JNM*. Christoph M. Griessinger, et al. In Vivo Tracking of Th1 Cells by PET Reveals Quantitative and Temporal Distribution and Specific Homing in Lymphatic Tissue. *J Nucl Med*. 2014;55:301-307. © by the Society of Nuclear Medicine and Molecular Imaging, Inc.)

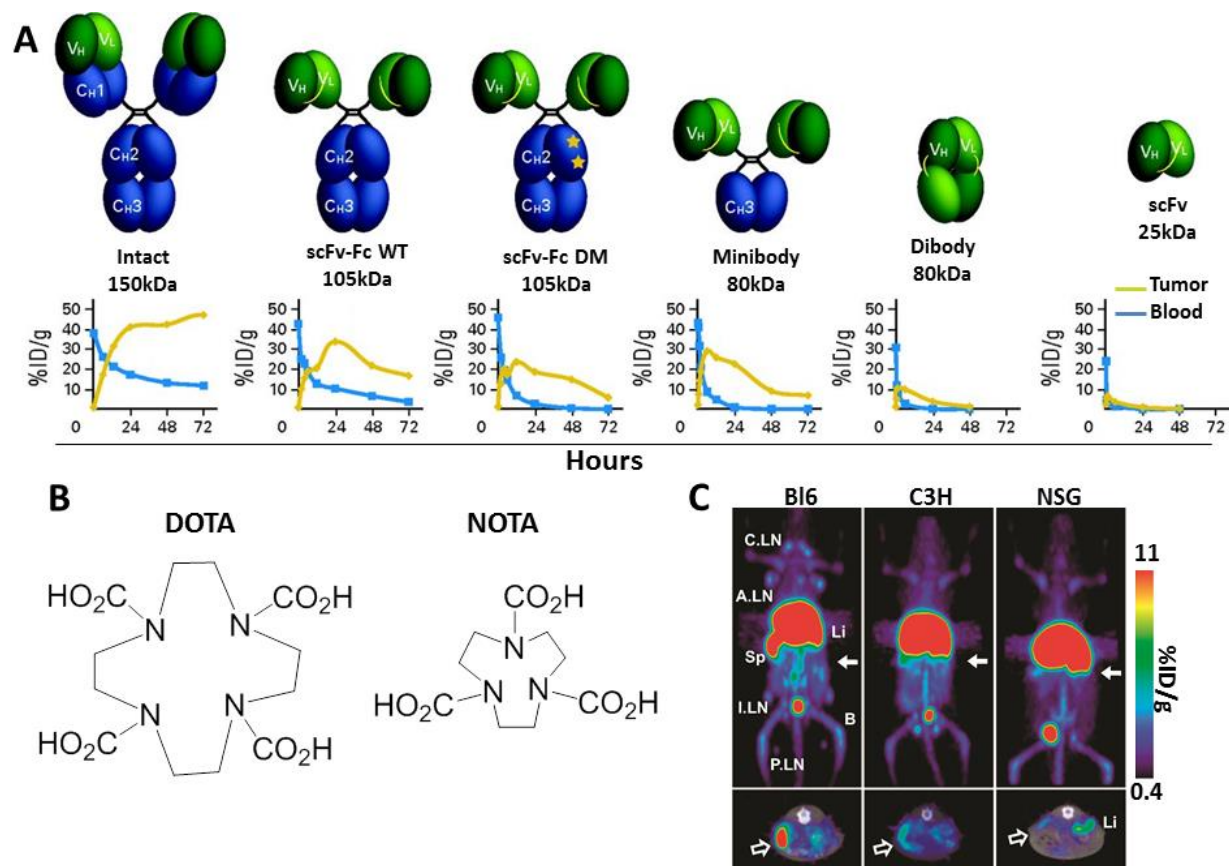


**Figure 6: ImmunoPET by antibody engineering and radiolabeling.** A) Antibody and antibody fragments. Top- structure and domains of the antibody fragment and size. Bottom- Representative biodistribution (%ID/g ) over time of a tumor targeted antibody fragment. Tumor is plotted in yellow, blood is plotted in blue. (Adapted from Knowles at al. Reprinted with permission. © (2012) American Society of Clinical Oncology. All rights reserved.) B) Chelating agents used for radiolabeling antibodies and peptides. DOTA and NOTA are capable of binding a charged metal isotope within the center ring structure. C)  $^{64}\text{Cu}$ -NOTA-2.43 Mb imaging of mice. Bl6 are lyt 2.2 and signal is seen within the spleen and lymph nodes. Spleen and lymph node signal is lost in C3H and NSG. C3H are lyt 2.1 and the 2.43 Mb cannot detect the CD8 cells in vivo. NSG are immunodeficient and contain no endogenous CD8 cells. (Adapted from Taváre et al. 2014)

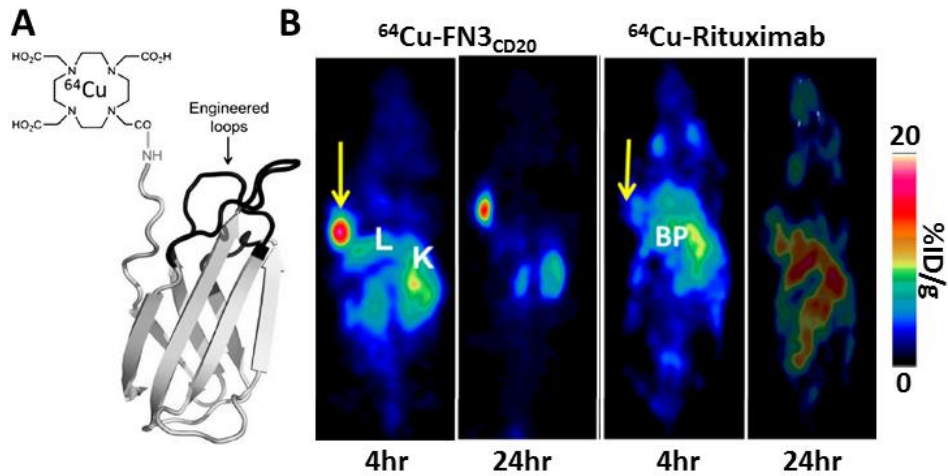


**Figure 7: Targeting hCD20 with  $^{64}\text{Cu}$  labeled proteins.** A) Structure of the  $^{64}\text{Cu}$ -DOTA-FN3<sub>CD20</sub> peptide used. B) Subcutaneous xenografts expressing hCD20 were detected by  $^{64}\text{Cu}$ -DOTA-FN3<sub>CD20</sub> (left) or  $^{64}\text{Cu}$ -DOTA-Rituximab (right). Yellow arrow indicates tumor. L-liver, K-kidneys, BP-blood pool. (Adapted from Natarajan et al. 2013)

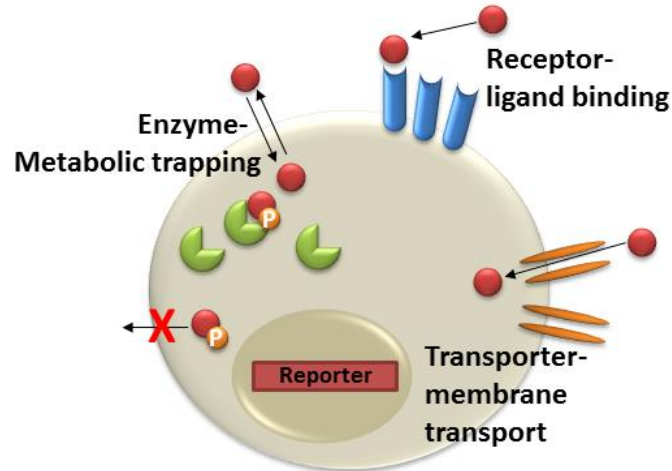


**Figure 8: Subclasses of PET reporter genes.** PET reporter genes can be one of three subclasses of proteins. Receptor PET reporter genes are a transmembrane protein that allows for reporter imaging by binding a radiolabeled ligand or targeted peptide to the protein. Transporter PET reporter genes work by transporting a PET reporter probe intracellular. Enzyme or kinase PET reporter genes work by phosphorylating their cognate probe trapping the probe intracellular.

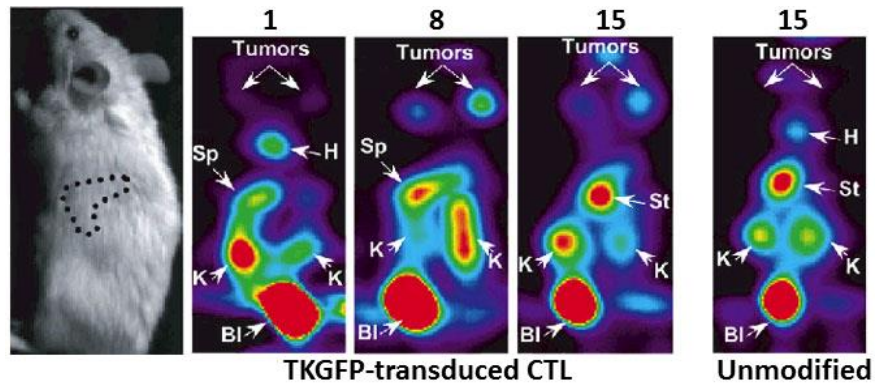


**Figure 9: Tracking CTLs with HSV-TK PET reporter imaging.** Sequential oblique projections of summed coronal images at a 45° angle to visualize the Sp-spleen, targeted tumors, K-kidneys, St-stomach, Bl-bladder, H-heart 4 h after [<sup>124</sup>I]FIAU injections on days 1, 8, and 15 after infusion of CTL-TKGFP. Tumors implanted are autologous and *HLA-A0201*<sup>+</sup> EBV<sup>+</sup> tumors. (Reprinted by permission from Macmillan Publishers Ltd: Nature Biotechnology (Koehne et al.), copyright (2003))



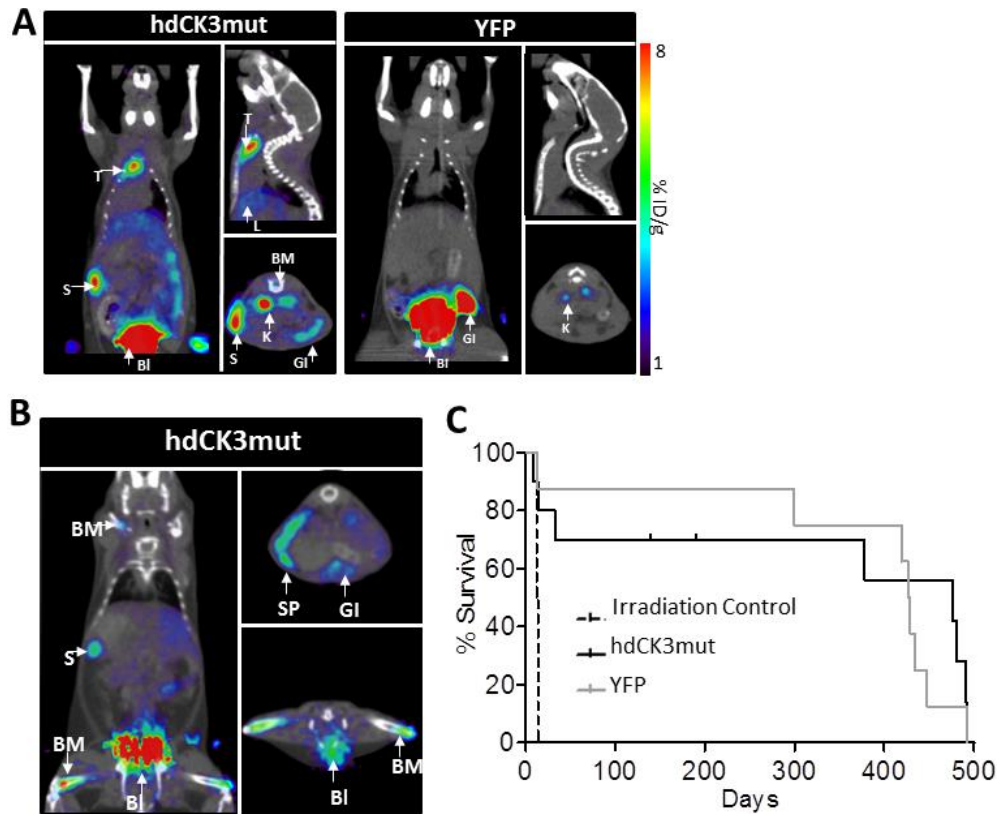


**Figure 10: hdCK3mut PET reporter gene imaging of hematopoietic reconstitution.** A) Recipient mice received a BMT with either hdCK3mut expressing cells or YFP, scan was obtained 4 weeks after transplant. Signal was observed in the T-thymus, S-Spleen, BM-bone marrow of hdCK3mut. Clearance of the probe was seen in both recipients in the GI-gastrointestinal tract, K-kidney, Bl-bladder. B) Persistent reporter signal was observed in the BM- bone marrow and Sp-spleen of reporter mice up to 32 weeks post BMT. C) No defect in longevity or life expectancy was observed between hdCK3mut and YFP recipients. (Adapted from McCracken et al. 2013)

## References:

1. Belardelli F, Ferrantini M (2002) Cytokines as a link between innate and adaptive antitumor immunity. *Trends Immunol* 23:201-208.
2. Cunningham-Rundles C, Ponda PP (2005) Molecular defects in T- and B-cell primary immunodeficiency diseases. *Nat Rev Immunol* 5:880-892.
3. Park TS, Rosenberg SA, Morgan RA (2011) Treating cancer with genetically engineered T cells. *Trends in biotechnology* 29:550-557.
4. Hildebrandt IJ, Gambhir SS (2004) Molecular imaging applications for immunology. *Clin Immunol* 111:210-224.
5. Cherry SR, Gambhir SS (2001) Use of positron emission tomography in animal research. *ILAR journal / National Research Council, Institute of Laboratory Animal Resources* 42:219-232.
6. Phelps ME (2000) Positron emission tomography provides molecular imaging of biological processes. *Proc Natl Acad Sci U S A* 97:9226-9233.
7. Massoud TF, Gambhir SS (2003) Molecular imaging in living subjects: seeing fundamental biological processes in a new light. *Genes & development* 17:545-580.
8. Gambhir SS (2002) Molecular imaging of cancer with positron emission tomography. *Nat Rev Cancer* 2:683-693.
9. Boswell CA, Brechbiel MW (2007) Development of radioimmunotherapeutic and diagnostic antibodies: an inside-out view. *Nucl Med Biol* 34:757-778.
10. van Dongen GA, Visser GW, Lub-de Hooge MN, de Vries EG, Perk LR (2007) Immuno-PET: a navigator in monoclonal antibody development and applications. *The oncologist* 12:1379-1389.

11. Dranoff G (2004) Cytokines in cancer pathogenesis and cancer therapy. *Nat Rev Cancer* 4:11-22.
12. Cramer T, Yamanishi Y, Clausen BE, et al. (2003) HIF-1alpha is essential for myeloid cell-mediated inflammation. *Cell* 112:645-657.
13. Serdons K, Verbruggen A, Bormans GM (2009) Developing new molecular imaging probes for PET. *Methods* 48:104-111.
14. Rapino F, Robles EF, Richter-Larrea JA, Kallin EM, Martinez-Climent JA, Graf T (2013) C/EBPalpha induces highly efficient macrophage transdifferentiation of B lymphoma and leukemia cell lines and impairs their tumorigenicity. *Cell reports* 3:1153-1163.
15. Miething C, Scuoppo C, Bosbach B, et al. (2014) PTEN action in leukaemia dictated by the tissue microenvironment. *Nature*.
16. Radu CG, Shu CJ, Shelly SM, Phelps ME, Witte ON (2007) Positron emission tomography with computed tomography imaging of neuroinflammation in experimental autoimmune encephalomyelitis. *Proc Natl Acad Sci U S A* 104:1937-1942.
17. Matsui T, Nakata N, Nagai S, et al. (2009) Inflammatory cytokines and hypoxia contribute to <sup>18</sup>F-FDG uptake by cells involved in pannus formation in rheumatoid arthritis. *J Nucl Med* 50:920-926.
18. Irmeler IM, Opfermann T, Gebhardt P, et al. (2010) In vivo molecular imaging of experimental joint inflammation by combined (18)F-FDG positron emission tomography and computed tomography. *Arthritis Res Ther* 12:R203.
19. Davies JR, Izquierdo-Garcia D, Rudd JH, et al. (2010) FDG-PET can distinguish inflamed from non-inflamed plaque in an animal model of atherosclerosis. *The international journal of cardiovascular imaging* 26:41-48.

20. Ishimori T, Saga T, Mamede M, et al. (2002) Increased (18)F-FDG uptake in a model of inflammation: concanavalin A-mediated lymphocyte activation. *J Nucl Med* 43:658-663.
21. Brewer S, McPherson M, Fujiwara D, et al. (2008) Molecular imaging of murine intestinal inflammation with 2-deoxy-2-[18F]fluoro-D-glucose and positron emission tomography. *Gastroenterology* 135:744-755.
22. Barthel H, Cleij MC, Collingridge DR, et al. (2003) 3'-deoxy-3'-[18F]fluorothymidine as a new marker for monitoring tumor response to antiproliferative therapy in vivo with positron emission tomography. *Cancer Res* 63:3791-3798.
23. Wagner M, Seitz U, Buck A, et al. (2003) 3'-[18F]fluoro-3'-deoxythymidine ([18F]-FLT) as positron emission tomography tracer for imaging proliferation in a murine B-Cell lymphoma model and in the human disease. *Cancer Res* 63:2681-2687.
24. Nair-Gill E, Wiltzius SM, Wei XX, et al. (2010) PET probes for distinct metabolic pathways have different cell specificities during immune responses in mice. *J Clin Invest* 120:2005-2015.
25. Zhang CC, Yan Z, Li W, et al. (2012) [(18)F]FLT-PET imaging does not always "light up" proliferating tumor cells. *Clin Cancer Res* 18:1303-1312.
26. Nottebrock H, Then R (1977) Thymidine concentrations in serum and urine of different animal species and man. *Biochemical pharmacology* 26:2175-2179.
27. Radu CG, Shu CJ, Nair-Gill E, et al. (2008) Molecular imaging of lymphoid organs and immune activation by positron emission tomography with a new [18F]-labeled 2'-deoxycytidine analog. *Nat Med* 14:783-788.

28. Austin WR, Armijo AL, Campbell DO, et al. (2012) Nucleoside salvage pathway kinases regulate hematopoiesis by linking nucleotide metabolism with replication stress. *J Exp Med* 209:2215-2228.
29. Toy G, Austin WR, Liao HI, et al. (2010) Requirement for deoxycytidine kinase in T and B lymphocyte development. *Proc Natl Acad Sci U S A* 107:5551-5556.
30. Namavari M, Chang YF, Kusler B, Yaghoubi S, Mitchell BS, Gambhir SS (2011) Synthesis of 2'-deoxy-2'-[18F]fluoro-9-beta-D-arabinofuranosylguanine: a novel agent for imaging T-cell activation with PET. *Mol Imaging Biol* 13:812-818.
31. Dhilly M, Guillouet S, Patin D, et al. (2014) 2-[18F]fludarabine, a novel positron emission tomography (PET) tracer for imaging lymphoma: a micro-PET study in murine models. *Mol Imaging Biol* 16:118-126.
32. Fox CJ, Hammerman PS, Thompson CB (2005) Fuel feeds function: energy metabolism and the T-cell response. *Nat Rev Immunol* 5:844-852.
33. Paik JY, Lee KH, Byun SS, Choe YS, Kim BT (2002) Use of insulin to improve [18 F]fluorodeoxyglucose labelling and retention for in vivo positron emission tomography imaging of monocyte trafficking. *Nuclear medicine communications* 23:551-557.
34. Griessinger CM, Kehlbach R, Bukala D, et al. (2014) In vivo tracking of Th1 cells by PET reveals quantitative and temporal distribution and specific homing in lymphatic tissue. *J Nucl Med* 55:301-307.
35. Melder RJ, Elmaleh D, Brownell AL, Brownell GL, Jain RK (1994) A method for labeling cells for positron emission tomography (PET) studies. *Journal of immunological methods* 175:79-87.

36. Nair-Gill ED, Shu CJ, Radu CG, Witte ON (2008) Non-invasive imaging of adaptive immunity using positron emission tomography. *Immunol Rev* 221:214-228.
37. Adonai N, Nguyen KN, Walsh J, et al. (2002) Ex vivo cell labeling with  $^{64}\text{Cu}$ -pyruvaldehyde-bis(N4-methylthiosemicarbazone) for imaging cell trafficking in mice with positron-emission tomography. *Proc Natl Acad Sci U S A* 99:3030-3035.
38. Knowles SM, Wu AM (2012) Advances in immuno-positron emission tomography: antibodies for molecular imaging in oncology. *J Clin Oncol* 30:3884-3892.
39. Weeks AJ, Paul RL, Marsden PK, Blower PJ, Lloyd DR (2010) Radiobiological effects of hypoxia-dependent uptake of  $^{64}\text{Cu}$ -ATSM: enhanced DNA damage and cytotoxicity in hypoxic cells. *Eur J Nucl Med Mol Imaging* 37:330-338.
40. Sundaresan G, Yazaki PJ, Shively JE, et al. (2003)  $^{124}\text{I}$ -labeled engineered anti-CEA minibodies and diabodies allow high-contrast, antigen-specific small-animal PET imaging of xenografts in athymic mice. *J Nucl Med* 44:1962-1969.
41. Tolmachev V, Stone-Elander S (2010) Radiolabelled proteins for positron emission tomography: Pros and cons of labelling methods. *Biochim Biophys Acta* 1800:487-510.
42. Wu AM (2009) Antibodies and antimatter: the resurgence of immuno-PET. *J Nucl Med* 50:2-5.
43. Lewis MR, Shively JE (1998) Maleimidocysteineamido-DOTA derivatives: new reagents for radiometal chelate conjugation to antibody sulfhydryl groups undergo pH-dependent cleavage reactions. *Bioconjugate chemistry* 9:72-86.
44. Tinianow JN, Gill HS, Ogasawara A, et al. (2010) Site-specifically  $^{89}\text{Zr}$ -labeled monoclonal antibodies for ImmunoPET. *Nucl Med Biol* 37:289-297.

45. Chen X, Hou Y, Tohme M, et al. (2004) Pegylated Arg-Gly-Asp peptide:  $^{64}\text{Cu}$  labeling and PET imaging of brain tumor  $\alpha\text{v}\beta_3$ -integrin expression. *J Nucl Med* 45:1776-1783.
46. Kimura RH, Cheng Z, Gambhir SS, Cochran JR (2009) Engineered knottin peptides: a new class of agents for imaging integrin expression in living subjects. *Cancer Res* 69:2435-2442.
47. Miao Z, Ren G, Liu H, Jiang L, Cheng Z (2010) Small-animal PET imaging of human epidermal growth factor receptor positive tumor with a  $^{64}\text{Cu}$  labeled affibody protein. *Bioconjugate chemistry* 21:947-954.
48. Vaneycken I, D'Huyvetter M, Hernot S, et al. (2011) Immuno-imaging using nanobodies. *Current opinion in biotechnology* 22:877-881.
49. Natarajan A, Hackel BJ, Gambhir SS (2013) A novel engineered anti-CD20 tracer enables early time PET imaging in a humanized transgenic mouse model of B-cell non-Hodgkins lymphoma. *Clin Cancer Res* 19:6820-6829.
50. Wadas TJ, Wong EH, Weisman GR, Anderson CJ (2010) Coordinating radiometals of copper, gallium, indium, yttrium, and zirconium for PET and SPECT imaging of disease. *Chemical reviews* 110:2858-2902.
51. Tavare R, McCracken MN, Zettlitz KA, et al. (2014) Engineered antibody fragments for immuno-PET imaging of endogenous CD8<sup>+</sup> T cells in vivo. *Proc Natl Acad Sci U S A* 111:1108-1113.
52. Natarajan A, Gowrishankar G, Nielsen CH, et al. (2012) Positron emission tomography of  $^{64}\text{Cu}$ -DOTA-Rituximab in a transgenic mouse model expressing human CD20 for clinical translation to image NHL. *Mol Imaging Biol* 14:608-616.
53. Holliger P, Hudson PJ (2005) Engineered antibody fragments and the rise of single domains. *Nat Biotechnol* 23:1126-1136.

54. Herschman HR (2004) PET reporter genes for noninvasive imaging of gene therapy, cell tracking and transgenic analysis. *Critical reviews in oncology/hematology* 51:191-204.
55. Tjuvajev JG, Finn R, Watanabe K, et al. (1996) Noninvasive imaging of herpes virus thymidine kinase gene transfer and expression: a potential method for monitoring clinical gene therapy. *Cancer Res* 56:4087-4095.
56. Kircher MF, Gambhir SS, Grimm J (2011) Noninvasive cell-tracking methods. *Nature reviews Clinical oncology* 8:677-688.
57. McCracken MN, Gschweng EH, Nair-Gill E, et al. (2013) Long-term in vivo monitoring of mouse and human hematopoietic stem cell engraftment with a human positron emission tomography reporter gene. *Proc Natl Acad Sci U S A* 110:1857-1862.
58. Likar Y, Zurita J, Dobrenkov K, et al. (2010) A new pyrimidine-specific reporter gene: a mutated human deoxycytidine kinase suitable for PET during treatment with acycloguanosine-based cytotoxic drugs. *J Nucl Med* 51:1395-1403.
59. Lam AP, Dean DA (2010) Progress and prospects: nuclear import of nonviral vectors. *Gene Ther* 17:439-447.
60. Fischer A, Hacein-Bey-Abina S, Cavazzana-Calvo M (2010) 20 years of gene therapy for SCID. *Nat Immunol* 11:457-460.
61. Blumenthal M, Skelton D, Pepper KA, Jahn T, Methangkool E, Kohn DB (2007) Effective suicide gene therapy for leukemia in a model of insertional oncogenesis in mice. *Mol Ther* 15:183-192.
62. Gambhir SS, Bauer E, Black ME, et al. (2000) A mutant herpes simplex virus type 1 thymidine kinase reporter gene shows improved sensitivity for imaging reporter gene expression with positron emission tomography. *Proc Natl Acad Sci U S A* 97:2785-2790.



63. Shu CJ, Campbell DO, Lee JT, et al. (2010) Novel PET probes specific for deoxycytidine kinase. *J Nucl Med* 51:1092-1098.
64. Acton PD, Zhou R (2005) Imaging reporter genes for cell tracking with PET and SPECT. *Q J Nucl Med Mol Imaging* 49:349-360.
65. Pastor-Anglada M, Casado FJ, Valdes R, Mata J, Garcia-Manteiga J, Molina M (2001) Complex regulation of nucleoside transporter expression in epithelial and immune system cells. *Molecular membrane biology* 18:81-85.
66. Tiberghien P, Reynolds CW, Keller J, et al. (1994) Ganciclovir treatment of herpes simplex thymidine kinase-transduced primary T lymphocytes: an approach for specific in vivo donor T-cell depletion after bone marrow transplantation? *Blood* 84:1333-1341.
67. Traversari C, Markt S, Magnani Z, et al. (2007) The potential immunogenicity of the TK suicide gene does not prevent full clinical benefit associated with the use of TK-transduced donor lymphocytes in HSCT for hematologic malignancies. *Blood* 109:4708-4715.
68. Berger C, Flowers ME, Warren EH, Riddell SR (2006) Analysis of transgene-specific immune responses that limit the in vivo persistence of adoptively transferred HSV-TK-modified donor T cells after allogeneic hematopoietic cell transplantation. *Blood* 107:2294-2302.
69. Le LQ, Kabarowski JH, Wong S, Nguyen K, Gambhir SS, Witte ON (2002) Positron emission tomography imaging analysis of G2A as a negative modifier of lymphoid leukemogenesis initiated by the BCR-ABL oncogene. *Cancer cell* 1:381-391.
70. Koehne G, Doubrovin M, Doubrovina E, et al. (2003) Serial in vivo imaging of the targeted migration of human HSV-TK-transduced antigen-specific lymphocytes. *Nat Biotechnol* 21:405-413.

71. Dobrenkov K, Olszewska M, Likar Y, et al. (2008) Monitoring the efficacy of adoptively transferred prostate cancer-targeted human T lymphocytes with PET and bioluminescence imaging. *J Nucl Med* 49:1162-1170.
72. Dubey P, Su H, Adonai N, et al. (2003) Quantitative imaging of the T cell antitumor response by positron-emission tomography. *Proc Natl Acad Sci U S A* 100:1232-1237.
73. Vatakis DN, Koya RC, Nixon CC, et al. (2011) Antitumor activity from antigen-specific CD8 T cells generated in vivo from genetically engineered human hematopoietic stem cells. *Proc Natl Acad Sci U S A* 108:E1408-1416.
74. Shu CJ, Guo S, Kim YJ, et al. (2005) Visualization of a primary anti-tumor immune response by positron emission tomography. *Proc Natl Acad Sci U S A* 102:17412-17417.
75. Doubrovin MM, Doubrovina ES, Zanzonico P, Sadelain M, Larson SM, O'Reilly RJ (2007) In vivo imaging and quantitation of adoptively transferred human antigen-specific T cells transduced to express a human norepinephrine transporter gene. *Cancer Res* 67:11959-11969.
76. Barat B, Kenanova VE, Olafsen T, Wu AM (2011) Evaluation of two internalizing carcinoembryonic antigen reporter genes for molecular imaging. *Mol Imaging Biol* 13:526-535.
77. Kenanova V, Barat B, Olafsen T, et al. (2009) Recombinant carcinoembryonic antigen as a reporter gene for molecular imaging. *Eur J Nucl Med Mol Imaging* 36:104-114.
78. Ponomarev V, Doubrovin M, Lyddane C, et al. (2001) Imaging TCR-dependent NFAT-mediated T-cell activation with positron emission tomography in vivo. *Neoplasia* 3:480-488.
79. Campbell DO, Yaghoubi SS, Su Y, et al. (2012) Structure-guided engineering of human thymidine kinase 2 as a positron emission tomography reporter gene for enhanced phosphorylation of non-natural thymidine analog reporter probe. *J Biol Chem* 287:446-454.

80. Herrmann K, Dahlbom M, Nathanson D, et al. (2013) Evaluation of the Genisys4, a bench-top preclinical PET scanner. *J Nucl Med* 54:1162-1167.
81. Chatziioannou AF, Cherry SR, Shao Y, et al. (1999) Performance evaluation of microPET: a high-resolution lutetium oxyorthosilicate PET scanner for animal imaging. *J Nucl Med* 40:1164-1175.
82. Hoffman EJ, Huang SC, Phelps ME (1979) Quantitation in positron emission computed tomography: 1. Effect of object size. *Journal of computer assisted tomography* 3:299-308.
83. Maeda H (2012) Vascular permeability in cancer and infection as related to macromolecular drug delivery, with emphasis on the EPR effect for tumor-selective drug targeting. *Proceedings of the Japan Academy Series B, Physical and biological sciences* 88:53-71.
84. Maeda H, Wu J, Sawa T, Matsumura Y, Hori K (2000) Tumor vascular permeability and the EPR effect in macromolecular therapeutics: a review. *Journal of controlled release : official journal of the Controlled Release Society* 65:271-284.

## **CHAPTER 2:**

Application of a Rapid, Simple, and Accurate  
Adenovirus-Based Method to Compare  
PET Reporter Gene/PET Reporter Probe Systems.

# Application of a Rapid, Simple, and Accurate Adenovirus-Based Method to Compare PET Reporter Gene/PET Reporter Probe Systems

Jose S. Gil,<sup>1,2</sup> Hidevaldo B. Machado,<sup>1,2</sup> Dean O. Campbell,<sup>2</sup> Melissa McCracken,<sup>2</sup> Caius Radu,<sup>2</sup> Owen N. Witte,<sup>2,3</sup> Harvey R. Herschman<sup>1,2</sup>

<sup>1</sup>Department of Biological Chemistry, David Geffen School of Medicine, UCLA, 341 Boyer Hall, 611 Charles E Young Drive, Los Angeles, CA, 90095-1570, USA

<sup>2</sup>Department of Molecular and Medical Pharmacology, David Geffen School of Medicine, UCLA, Los Angeles, CA, USA

<sup>3</sup>Department of Microbiology, Immunology and Molecular Genetics, David Geffen School of Medicine, UCLA, Los Angeles, CA, USA

## Abstract

**Purpose:** This study aims to use a simple, quantitative method to compare the HSV1sr39TK/<sup>18</sup>F-FHBG PET reporter gene/PET reporter probe (PRG/PRP) system with PRGs derived from human nucleoside kinases.

**Procedures:** The same adenovirus vector is used to express alternative PRGs. Equal numbers of vectors are injected intravenously into mice. After PRP imaging, quantitative hepatic PET signals are normalized for transduction by measuring hepatic viral genomes.

**Results:** The same adenovirus vector was used to express equivalent amounts of HSV1sr39TK, mutant human thymidine kinase 2 (TK2-DM), and mutant human deoxycytidine kinase (dCK-A100VTM) in mouse liver. HSV1sr39TK expression was measured with <sup>18</sup>F-FHBG, TK2-DM and dCK-A100VTM with <sup>18</sup>F-L-FMAU. TK2-DM/<sup>18</sup>F-L-FMAU and HSV1sr39TK/<sup>18</sup>F-FHBG had equivalent sensitivities; dCK-A100VTM/<sup>18</sup>F-L-FMAU was twice as sensitive as HSV1sr39TK/<sup>18</sup>F-FHBG.

**Conclusions:** The human PRG/PRP sensitivities are comparable and/or better than HSV1sr39TK/<sup>18</sup>F-FHBG. However, for clinical use, identification of the best PRP substrate for each enzyme, characterization of probe distribution, and consequences of overexpressing nucleoside kinases must be evaluated.

**Key words:** PET reporter gene, PET reporter probe, Gene therapy, Cell therapy, Reporter gene, Positron emission tomography, Adenovirus, Herpes Simplex Virus thymidine kinase, Deoxycytidine kinase, Thymidine kinase 2

Electronic supplementary material The online version of this article (doi:10.1007/s11307-012-0596-5) contains supplementary material, which is available to authorized users.

Owen N. Witte is an Investigator of the Howard Hughes Medical Institute.

Correspondence to: Harvey Herschman; e-mail: hherschman@mednet.ucla.edu

## Introduction

Both use of exogenous platforms (e.g., liposomes, nanoparticles, and viral vectors) to deliver therapeutic genes and development of targeted cell therapies (e.g., modified T

cells, embryonic stem cells, and induced pluripotent stem cells) have advanced from preclinical development to clinical trials and, in some cases, to standard of care for therapy. As these new therapies are developed, monitoring duration of their availability *in vivo* and their targeting selectivity, and correlating these parameters with treatment outcomes is critical in their evaluation and adoption for standard of care.

Incorporation of “reporter genes” which activities can be examined noninvasively by whole-body imaging provides a means to monitor both pharmacokinetics and targeting of these new vector- and cell-based therapeutic agents. In murine preclinical models, bioluminescence (e.g., alternative luciferases as reporter genes and their substrates as reporter probes) has provided convenient, inexpensive reporter gene–reporter probe systems to noninvasively monitor therapeutic gene delivery and cell-based therapies [1–4]. However, reporter gene immunogenicity, tissue attenuation of the signal, and lack of adequate resolution preclude bioluminescence imaging in most clinical contexts. For clinical applications, the most common approach has been the use of PET reporter genes (PRGs) which activities can be monitored noninvasively by positron emission tomography (PET) [5, 6].

Although PRGs that encode transporters, receptors, and enzymes have been developed [5, 6], the most widely used PRG is the Herpes Simplex Virus type 1 thymidine kinase (HSV1-TK) gene. HSV1-TK can phosphorylate a variety of nucleoside analogues, including anti-herpetic acycloguanosines. HSV1-TK mutants engineered to more effectively use anti-herpetic drugs and to be less effective at phosphorylating endogenous thymidine have been developed as “suicide genes” to kill cells that ectopically express these kinases. Concurrently, positron-emitting derivatives of several acycloguanosine HSV1-TK substrates have been developed as probes for detecting HSV1-TK-based PRG expression. The combination of the HSV1-sr39TK PRG and 9-[4-<sup>18</sup>F-3 (hydroxymethyl) butyl]guanine (<sup>18</sup>F-FHBG) as its PET reporter probe (PRP) is among the most widely used PRG/PRP systems [6–10].

Despite their current utility, immunogenicity of HSV1-TK and its derivatives limits *in vivo* persistence of cells expressing these PRGs, and thus their utility in clinical applications [7, 11]. Several laboratories are developing PRGs from human genes to circumvent PRG immunogenicity. Mutated versions of two human nucleoside kinases, thymidine kinase 2 (TK2) and deoxycytidine kinase (dCK), which utilize positron-emitting nucleoside analogues as PRPs have been developed in anticipation of clinical use [12–15].

As new PRG–PRP systems are described, it becomes imperative to have reliable procedures to monitor their relative specificities (the PRP should accumulate only in cells expressing the PRG) and sensitivities (the ability to generate quantifiable signals). The most common method of evaluating PRG/PRP systems has been to express PRGs in

tumor cell lines, develop mouse xenografts, and image transgene PRG activity. However, differences in expression vectors (e.g., differing promoters and differing 3′ and 5′ untranslated regions), differing integration sites and copy numbers, differing rates of tumor growth, and distinctions in tumor vascularization and other biological variables make it difficult to compare such reports on relative efficacies of alternative PRP/PRG technologies.

We previously described the use of a common adenovirus delivery vector and a common gene expression construct to compare *in vivo* efficacy of alternative luciferase reporter genes for noninvasive imaging [16]. Postimaging measurement of hepatic viral genomes and subsequent normalization of imaging data for the hepatic reporter gene copy number eliminates any differences imposed by variations in reporter gene delivery. This assay eliminates inconsistencies due to differences in vector construction, reporter gene copy number, integration site modulation of gene expression (adenovirus genomes do not integrate into chromosomal sites), and differential vascularity of the target. Only the reporter gene and reporter probe differ in this procedure.

Our goal in establishing this procedure was to provide a common platform to evaluate reporter gene efficacy across imaging modalities. In this report, we demonstrate the utility of this procedure for evaluating differences in PRG/PRP efficacies by comparing the sensitivities of a mutated human TK2 PRG (TK2-N93D/L109F) [13] and a mutated human dCK PRG (dCK-A100V/R104M/D133A) [15, 17, McCracken *et al.*, in preparation] to one another, using the same PRP, 2′-deoxy-2-<sup>18</sup>F-5-methyl-1-β-L-arabinofuranosyluracil (<sup>18</sup>F-L-FMAU) [13], and to the commonly used HSV1-sr39TK/<sup>18</sup>F-FHBG PRG/PRP reporter system.

---

## Materials and Methods

### *Adenovirus Vector Construction*

Plasmids and adenoviral vectors are listed in Table 1; all primers are listed in Table 2. Adenovirus vectors expressing alternative PRG were constructed as described previously [16] and in the Supplemental Material for this report. Although these reporter genes have been used, in some cases, to create adenovirus vectors previously (e.g., LUC2 and HSV1sr39TK), we have renamed the viruses created here as Ad.HL viruses to facilitate the use of these viruses as proper control and comparison viruses by other laboratories in future studies.

### *Adenovirus Vector Propagation and Titration*

Adenovirus vectors were propagated on HEK293A cells using standard procedures [16, 17] and titrated on HeLa cells for to determine infectious genomes [16, 17]. Procedures have been described in detail in our comparisons of luciferase reporter genes [16] and are also described in the Supplemental Material.

**Table 1.** Plasmids and adenoviral vectors used in this study

Plasmid or virus	Description or relevant characteristics	Source
<b>Plasmids</b>		
pMSCV-sr39TK-IRES-YFP	HSV sr39TK containing retroviral plasmid	Radu Lab
pMSCV-TK2	Truncated human TK2 containing retroviral plasmid	Radu Lab
pMSCV-TK2-N93D/L109F	Human TK2-N93D/L109F containing plasmid	[13]
pMSCV hudCK WT optimized IRES-YFP	Human wild type dCK containing retroviral plasmid	Witte Lab
pMSCV hudCK DM optimized IRES-YFP	Human dCK double mutant containing retroviral plasmid	Witte lab
pMSCV hudCK TM optimized IRES-YFP	Human dCK triple mutant containing retroviral plasmid	Witte lab
pENTR4D	Gateway™ shuttle vector	Invitrogen
pAd/CMV/V5-DEST	Gateway™ destination adenoviral vector	Invitrogen
pENTRHM	pENTR4D with <i>Cm<sup>R</sup></i> and <i>ccdB</i> genes replaced by a synthetic multiple cloning site	[16]
pENTRHM-LUC2	pENTRHM containing <i>Luc2</i> gene	[16]
pENTRHM-TK2	pENTRHM containing TK2 soluble mutant gene	This study
pENTRHM-TK2-N93D-L109F	pENTRHM containing TK2-N93D-L109F mutant gene	This study
pENTRJG-dCK-WT	pENTRHM containing <i>dCK</i> wild type gene	This study
pENTRJG-dCK-DM	pENTRHM containing dCK-R104M/D133A double mutant gene	This study
pENTRHM-dCK-TM	pENTRHM containing dCK-A100V/R104M/D133A triple mutant gene	This study
pAdHM-LUC2	pAd/CMV/V5/DEST vector after recombination with pENTRHM-FLUC	[16]
pAdHM-TK2	pAd/CMV/V5/DEST vector after recombination with pENTRHM-TK2	This study
pAdHM-TK2-N93D-L109F	pAd/CMV/V5/DEST vector after recombination with pENTRHM-TK2-N93D-L109F	This study
pAdjG-dCK-WT	pAd/CMV/V5/DEST vector after recombination with pENTRJG-dCK-WT	This study
pAdjG-dCK-DM	pAd/CMV/V5/DEST vector after recombination with pENTRJG-dCK-DM	This study
AdHM-dCK-TM	pAd/CMV/V5/DEST vector after recombination with pENTRHM-dCK-TRP	This study
<b>Adenovirus</b>		
AdHM.LUC2 (referred to here as Ad.HL.Luc2)	Human adenovirus type 5 (Ad5) from Gateway System™ expressing <i>Luc2</i> from a CMV promoter	[16]
Ad.HL.TK2	Ad5 expressing TK2 cytoplasmic mutant from a CMV promoter	This study
Ad.HL.TK2-DM	Ad5 expressing TK2-N93D/L109F mutant from a CMV promoter	This study
Ad.HL.dCK-WT	Ad5 expressing dCK wild type from a CMV promoter	This study
Ad.HL.dCK-DM	Ad5 expressing dCK-R104/D133A double mutant from a CMV promoter	This study
Ad.HL.dCK-A100VTM	Ad5 expressing dCK-A100V/R104M/D133A triple mutant from a CMV promoter	This study

### PET Reporter Probe Synthesis

<sup>18</sup>F-FHBG and <sup>18</sup>F-L-FMAU syntheses were performed as previously described [9, 13], at the cyclotron facilities in the UCLA Crump Institute for Molecular Imaging and the UCLA Ahmanson Translational Imaging Division.

### In Vivo Studies

Female hairless SKH1 mice (Charles River, San Diego, CA, USA) were housed in accordance with the UCLA Division of Laboratory Animal Medicine guidelines. Mice between 10 and 16 weeks were used for all experiments. An optimal imaging time of 3–5 days after

**Table 2.** Primers used in this study

Primer sequence	Description	Source
Fwd: TCGACCAAGCTTTCGGTACCAGCCCGG GAGAGCTCAAGGATCCAAG Rev: AATTCTTGGATCCTTGAGCTCTCCCGGGC TGGTACCGAAAGCTTGG	Multiple cloning sites for pENTR4D: <i>SaI</i> – <i>HindIII</i> – <i>KpnI</i> – <i>SmaI</i> – <i>SacI</i> – <i>BamHI</i> – <i>EcoRI</i>	[16]
Fwd: TCGACCAAGCTTGGCACCATGCCACGCTACTGCGGGT Rev: TCTAGATATCTCGAGTTATCAGTTAGCCTCCCCATCT Fwd: TCGACCAAGCTTGGCACCATGTCAGTGATCTGTGTCGA Rev: TCTAGATATCTCGAGTTACTATGGCAATGCTTCCGAT	sr39TK from pMSCV-sr39TK-IRES-YFP. <i>HindIII/XhoI</i> directional cloning TK2 and TK2-N93D/L109F from pMSCV-TK2 and pMSCV-TK2-N93D/L109F, respectively. <i>HindIII/XhoI</i> directional cloning	This study This study
Fwd: AGTCGACCAAGCTTGGCACCATGGCTACTCTCTAAACG Rev: TGGGTCTAGATATCTCGAGTTATCAAAGTGT TGACAGAAATTC	dCK-WT, dCK-DM, and dCK-TM from pMSCV-hudCK-triple mutant-IRES-YFP. <i>HindIII/XhoI</i> directional cloning	This study
Fwd: TAAAGCTTAGCGACGATGGCCTCCAAG Rev: TTCTCGAGTACTGTTCGTTCTTCCAGC	RLuc8.6-535 from pRV2011. <i>HindIII/XhoI</i> directional cloning	This study
Fwd: ACTTAAGCTTGGCACCATGGAAGATGCCAAAAACATT Rev: AACTCGAGAATTATTACAGCGCATCTTGC	<i>Luc2</i> from pGL4.13. <i>HindIII/XhoI</i> directional cloning	This study
Fwd: ACTTAAGCTTGGCACCATGGCTTCCAAGGTGACGAC Rev: AACTCGAGAATTATTACTGCTGCTTCTTCCAGCAC	hRLuc from pHL-TK. <i>HindIII/XhoI</i> directional cloning	This study
Fwd: CAAGGGTTGAGTACTTGTGTTAGGGTTA Rev: GGTGGGTAGAGAGAAGAAATATCTGACT Probe: TAMRA-AGGACAATGGCCTTGGCTGGACAA-BHQ2A	TaqMan qPCR primer against mouse Oct4 promoter region	[16]
Fwd: TTGTGGTTCTTGACAGATATGGC Rev: TCGGAATCCCGGCACC Probe: FAM-CTCACCTGCCGCCTCCGTTTCC-TAMRA	TaqMan qPCR primer against adenovirus type 5 pX gene	[17]

Ad.HL.Luc2 vector tail vein injection was determined (Supplemental Fig. 1).

Titration studies to optimize numbers of viral particles per mouse were performed by injecting  $1 \times 10^{10}$ ,  $3 \times 10^{10}$ , or  $1 \times 10^{11}$  infectious genome units (IGUs) of Ad.HL.HSV1sr39TK. Three days after vector injection, mice were injected via tail vein with  $^{18}\text{F}$ -FHBG (200  $\mu\text{Ci}$ ). Three hours after tracer injection, mice were anesthetized (2 % isoflurane) and subjected to microPET/CT scanning (Inveon, Siemens Medical Solutions USA Inc.; MicroCAT, Imtek Inc.) [13]. This time was chosen because it is optimal for imaging the TK2DM/ $^{18}\text{F}$ -L-FMAU PRG/PRP imaging combination in mice [13].

To compare the efficacy of the PRG, groups of three animals were each injected via the tail vein with  $5 \times 10^{10}$  IGUs of the various adenovirus vectors. Four days after injection, mice that received either no vector or mice that received Ad.HL.Luc2, Ad.HL.dCK-WT, Ad.HL.dCK-R104M/D133A (referred to as Ad.HL.dCK-DM), Ad.HL.dCK-A100V/R104M/D133A (referred to as Ad.HL.dCK-A100VTM), Ad.HL.TK2, or Ad.HL.TK2-N93D/L109F (referred to as Ad.HL.TK2-DM) were imaged with  $^{18}\text{F}$ -L-FMAU (200  $\mu\text{Ci}$ ). Mice receiving Ad.HL.Luc2, Ad.HL.HSV1sr39TK, or no adenovirus vector were imaged with  $^{18}\text{F}$ -FHBG. The dCK mutant PRG expressed in Ad.HL.dCK-A100VTM (cloned and codon-optimized by us; McCracken *et al.*; in preparation) is distinguished from another dCK triple mutant of the dCK gene, dCK-S74E/R104M/D133A (dCK-S74ETM), described by Likar *et al.* [12].

Mice injected with Ad.HL.Luc2 and imaged with  $^{18}\text{F}$ -FHBG were used to determine background values for mice injected with Ad.HL.sr39TK and imaged with  $^{18}\text{F}$ -FHBG; additional mice injected with Ad.HL.Luc2 and imaged with  $^{18}\text{F}$ -L-FMAU were used to determine background values for mice injected with all other PRG adenovirus vectors and imaged with  $^{18}\text{F}$ -L-FMAU.

To quantify PET data, four identical 2-mm Regions of Interest (ROIs) were drawn within the liver for each mouse. The average PET signal in percentage of injected dose per gram (%ID/g) was determined for each mouse from these ROIs. For each mouse, a corrected percentage of injected dose per gram for the experimental PRG/PRP imaging pair was obtained by subtracting the average percentage of injected dose per gram from mice injected with Ad.HL.Luc2 and subsequently imaged with the appropriate PRP, i.e.,  $^{18}\text{F}$ -FHBG or  $^{18}\text{F}$ -L-FMAU. We did not use an ROI that covers the entire liver region because the gall bladder gives variable, nonspecific signals, both for alternative PRPs for nucleoside kinases and from mouse-to-mouse under common conditions.

After imaging, the mice were euthanized, the livers were removed, and triplicate liver samples were used for adenovirus vector and mouse genomic DNA analyses. DNA was isolated from liver samples using the DNeasy protocol (Qiagen, Thousand Oaks, CA, USA), adenoviral DNA and murine genomes were determined as described previously [16, 18], and as summarized in the Supplemental Material.

### Statistical Analyses

Graph production and analysis were performed with GraphPad Prism software, version 5. Multiple group ( $N$  equal to or greater than three) comparisons were analyzed using a one-way ANOVA test. When samples were statistically significant ( $P < 0.05$ ) a further comparison between two sample sets were done independently using the Student's unpaired  $t$  test. Graphs displayed contain Student's  $t$  test  $P$  values.

## Results

### Creation and Production of Adenovirus PRG Vectors

Comparisons between reporter genes are often confounded by differences in vector structure, e.g., different promoters, alternative 5' and/or 3' untranslated regions, and/or distinct polyadenylation signals. We mitigated these issues by using a single vector design for all PRGs. Each reporter gene was cloned into the same shuttle or "entry" vector, utilizing the commercially available Gateway System [16] and employing PCR primers with *HindIII/XhoI* restriction sites. Each of these entry vectors was used to insert the reporter gene, via Gateway cloning, into the viral pAd/CMV/V5-DEST vector (Fig. 1). This highly efficient and simple cloning procedure ensures that each adenovirus PRG vector is identical, with the exception of the reporter gene. Other researchers can easily create identical vectors, with the exception of their new reporter genes, and can evaluate their new reporter genes by direct comparison with our vectors as controls.

After conversion of the recombinant plasmid into a viral vector, amplification through serial rounds of infection, purification, and sequencing, the adenovirus vector stocks were titrated in culture for IGUs (Fig. 2), as described in "Materials and Methods" and in the Supplemental Material. Vector concentrations, in infectious genome unit per milliliter  $\pm$  SEM (Fig. 2), were: Ad.HL.Luc2,  $1.27 \pm 0.15 \times 10^{11}$ ; Ad.HL.sr39TK,  $9.7 \pm 0.40 \times 10^{11}$ ; Ad.HL.TK2,  $5.61 \pm 0.49 \times 10^{11}$ ; Ad.HL.TK2-DM,  $3.69 \pm 0.51 \times 10^{11}$ ; Ad.HL.dCK-WT,  $2.25 \pm 0.50 \times 10^{11}$ ; and Ad.HL.dCK-A100VTM,  $1.21 \pm 0.24 \times 10^{11}$ .

### Optimal Time and Viral Titer for Imaging Hepatic PRG Expression after Intravenous Adenovirus Administration

To determine the optimal time between adenoviral reporter gene administration and injection of the reporter probe imaging agent, we performed a time course with the Ad.HL.Luc2/luciferin reporter gene/reporter probe system. Repeated daily luciferin imaging of SKH1 mice that received Ad.HL.Luc2 ( $5 \times 10^{10}$  IGUs/mouse) indicated an optimal imaging window 3–5 days after adenovirus vector injection (Supplemental Material, and Supplemental Fig. 1).

Because PRP retention is dependent on the dose of adenovirus PRG vector administration [19], we first used the Ad.HL.sr39TK/ $^{18}\text{F}$ -FHBG PRG/PRP system to identify an Ad.HL.PRG dose for this vector that would be appropriate for comparison with other PRG/PRP combinations. Female SKH1 mice were injected intravenously with  $1 \times 10^{11}$ ,  $3 \times 10^{10}$ , or  $1 \times 10^{10}$  IGUs of Ad.HL.sr39TK or an Ad.HL.Luc2 control vector ( $3 \times 10^{10}$  IGUs). Three days later, mice were imaged with  $^{18}\text{F}$ -FHBG (Fig. 3).

A common vector titer of  $5 \times 10^{10}$  IGUs, in the midrange of the dose–response relationship, was chosen for comparison



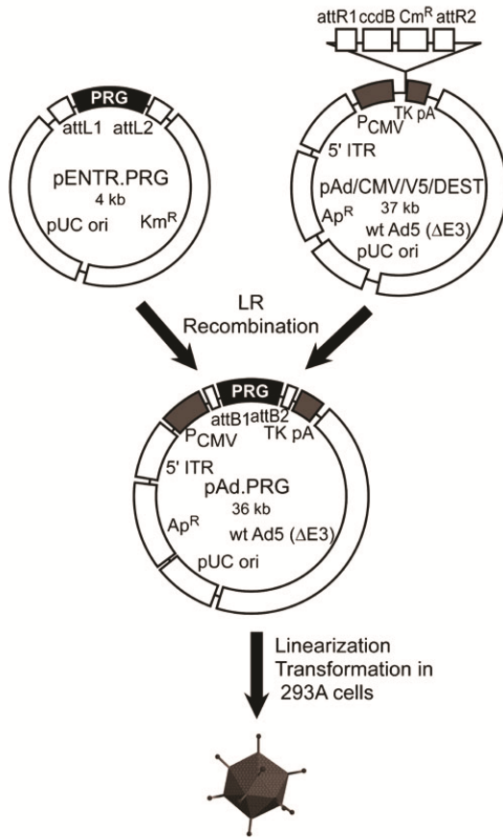


**Fig. 1.** Cloning and production of adenovirus vectors. Adenovirus vectors containing coding regions for TK2, TK2-DM, dCK-WT, dCK-DM, dCK-A100VTM, HSV1sr39TK (as a reference standard), and Luc2 as a negative control were constructed using Invitrogen's Gateway® Cloning System. The open reading frame of each reporter was inserted into an "entry" vector to create the pENTR-PRG plasmids and then transferred to the pAd/CMV/V5/DEST vector using the LR recombination reaction to create the seven pAd vectors. The adenoviral plasmids were linearized by *PacI* restriction enzyme digestion, purified, and transformed into HEK293A cells for vector rescue. After 100 % cytopathic effect was observed, lysates were serially passaged on increasing numbers of HEK293A cells with each round of infection until sufficient vector was produced, following cesium chloride buoyant density ultracentrifugation and purification for *in vivo* studies. Sites labeled *attR1/attR2/attL1/attL2* are the initial recombination regions; *attB1/attB2* are the recombination regions after the LR recombination reaction. *Cm<sup>R</sup>* chloramphenicol resistance gene, *Km<sup>R</sup>* kanamycin resistance gene, *Ap<sup>R</sup>* ampicillin resistance gene, *ccdB* the coding region for the cytotoxic protein CcdB used as a negative-selection marker in recombinant clones, *P<sub>CMV</sub>* CMV promoter, *TKpA* thymidine kinase polyadenylation signal, *5' ITR* the viral 5'-inverted terminal repeats, *wt Ad5 (ΔE3)* Ad5 sequences that include a 3' ITR and packaging signal.

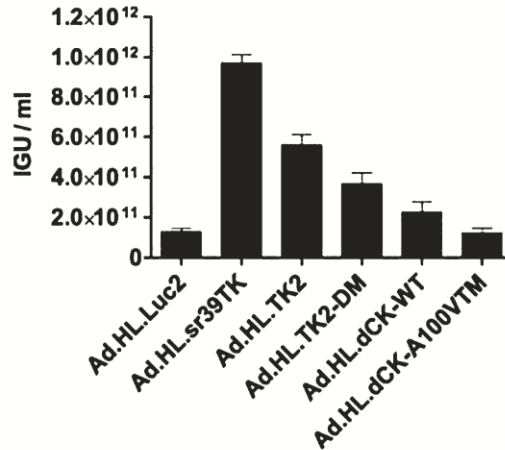


**Fig. 2.** Viral titers, measured as infectious genome units for the adenovirus vectors. IGU values for the seven adenovirus vector preparations were determined following HeLa cell transduction. Nuclei were harvested 3 h after vector addition. Vector genomes were measured by quantitative PCR as described in "Materials and Methods". Data are means ± SEM of duplicate qPCR assays for duplicate transductions.

of the various PRG/PRP systems. In this way, both greater and lesser efficacies relative to Ad.HL.sr39TK/<sup>18</sup>F-FHBG for the alternative human-derived PRG/PRP systems could be evaluated.

#### Hepatic Efficacy of the Alternative Adenoviral PRG/PRP Noninvasive Imaging Systems

Three mice in each alternative adenoviral PRG vector experimental group and two mice in each Ad.HL.Luc2 control group were injected intravenously with the appropriate adenovirus vector ( $5 \times 10^{10}$  IGU/mouse). Four days after adenovirus injection, the mice received either <sup>18</sup>F-L-FMAU (200 μCi) or <sup>18</sup>F-FHBG (200 μCi), as appropriate. Three hours later, the mice were anesthetized and subjected to PET/CT imaging (Fig. 4a). The following day, mice were euthanized and livers were removed. DNA was purified from liver samples, and DNA content was analyzed for viral and mouse genomes to normalize the imaging data for the number of viral genomes present in the livers. The numbers of vector genomes per liver cell, ±SEM, were Ad.HL.Luc2, 78 ± 2.5; Ad.HL.sr39TK, 104 ± 18; Ad.HL.TK2, 87 ± 14; Ad.HL.TK2-DM, 74 ± 9.5; Ad.HL.dCK-WT, 43 ± 1.5; and Ad.HL.dCK-A100VTM, 85 ± 7.8 (Fig. 4b).

PRG-dependent PRP hepatic retention was determined by choosing four identical 2-mm ROIs over the liver of each mouse and determining the percentage of injected dose per gram. To determine the PRG-dependent PRP retention, the

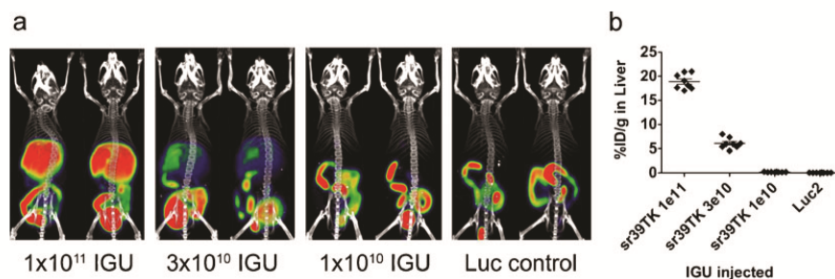


**Fig. 3.** Titration of Ad.HL.sr39TK for microPET/microCT quantification. **a** Two mice per group were injected intravenously with  $10^{11}$ ,  $3 \times 10^{10}$ , or  $10^{10}$ IGU of Ad.HL.sr39TK or with  $3 \times 10^{10}$ IGU of Ad.HL.Luc2. After 3 days, mice were injected with  $^{18}\text{F}$ -FHBG (200  $\mu\text{Ci}$ ) and subjected to microPET/microCT imaging. **b** 2-mm ROIs were drawn within the liver of each mouse and used to determine average %ID/g per liver. Data are means  $\pm$  SEM.

background hepatic signal (determined from mice injected with Ad.HL.Luc2 and the appropriate PRP) was subtracted. Percentage of injected dose per gram values, corrected for PRP background, but not corrected for differences in the numbers of PRGs delivered to the livers of each mouse, were Ad.HL.sr39TK,  $6.79 \pm 0.55$ ; Ad.HL.TK2,  $0.31 \pm 0.09$ ; Ad.HL.TK2-DM,  $5.02 \pm 1.13$ ; Ad.HL.dCK-WT,  $0.15 \pm 0.03$ ; and Ad.HL.dCK-A100VTM,  $11.43 \pm 0.89$  (Fig. 4c, values are means  $\pm$  SEMs).

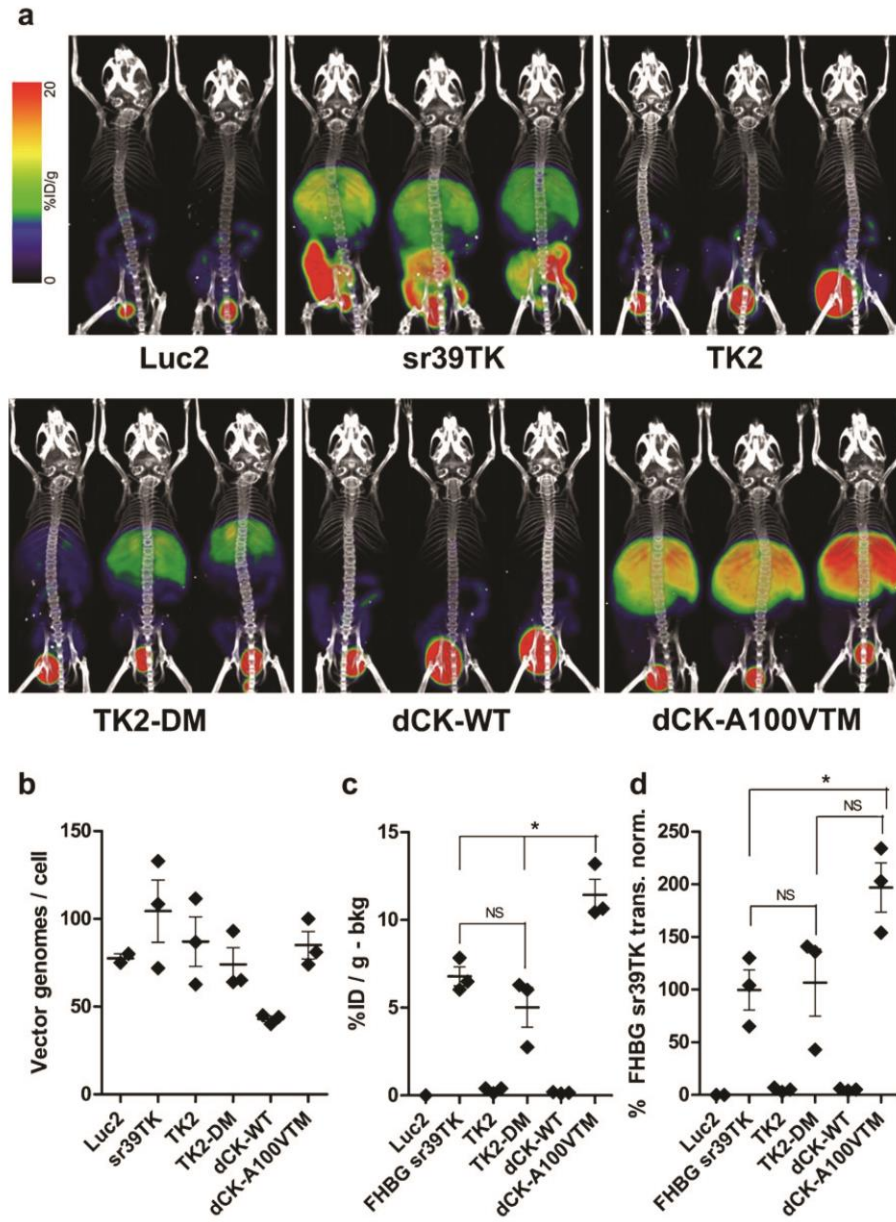
To eliminate the variability caused by differences in the number of PRGs present in the liver of each mouse, the [%ID/g-bkg] was normalized to vector transduction. Results for the alternative PRG vectors were then compared to the Ad.HL.sr39TK/ $^{18}\text{F}$ -FHBG standard. Normalized activities (Fig. 4d) were Ad.HL.sr39TK,  $100 \pm 19$  %; Ad.HL.TK2,  $5.0 \pm 1.2$  %; Ad.HL.TK2-DM,  $107 \pm 32$  %; Ad.HL.dCK-WT,  $5.0 \pm 0.6$  %; and Ad.HL.dCK-A100VTM,  $197 \pm 23$  %. Normalized PRG/PRP signal showed no significant difference between the commonly used HSV1sr39TK/ $^{18}\text{F}$ -FHBG PRG/PRP imaging system and the mutant human thymidine kinase 2 (TK2-DM)/ $^{18}\text{F}$ -L-FMAU imaging system by Student's *t* test ( $p=0.86$ ). In contrast, a significant ( $p=0.03$ ) difference between the HSV1sr39TK/ $^{18}\text{F}$ -FHBG and mutant human deoxycytidine kinase (dCK-A100VTM)/ $^{18}\text{F}$ -L-FMAU PRG/PRP combinations was observed. Although a difference in the TK2-DM/ $^{18}\text{F}$ -L-FMAU and dCK-A100VTM/ $^{18}\text{F}$ -L-FMAU imaging systems did not reach significance ( $p=0.08$ ), there appears to be a trend in that direction.

We also compared the efficacy of the dCK-DM reporter gene described by Likar *et al.* [13] with the dCK-A100VTM reporter gene, which has an additional amino acid substitution that was speculated to improve its utility as a PRG [20], using Ad.HL.dCK-DM and Ad.HL.dCKA100VTM adenovirus vectors. However, in this assay, we could not observe a statistically significant difference in the efficacy of dCK-DM and dCK-A100VTM using  $^{18}\text{F}$ -L-FMAU as a common PRP (described in the Supplemental Materials and Supplemental Fig. 2).

## Discussion

As the use of therapeutic gene delivery vectors and targeted cell therapies expands into clinical applications, the need to repeatedly, noninvasively, and quantitatively monitor the duration of their bioavailability, the specificity of their targeting, and their longevity at target sites becomes of

**Fig. 4.** TK2 and dCK PRG efficacies with L-FMAU as the PRP. **a** Three mice for each adenovirus vector were injected with  $5 \times 10^{10}$ IGU of Ad.HL.TK2, Ad.HL.TK2-DM, Ad.HL.dCK-WT, Ad.HL.dCK-A100VTM, Ad.HL.sr39TK (as reference standard), or Ad.HL.Luc2 (as negative control). Four days later mice were injected with 200  $\mu\text{Ci}$   $^{18}\text{F}$ -FHBG (Ad.HL.sr39TK) or 200  $\mu\text{Ci}$   $^{18}\text{F}$ -L-FMAU (Ad.HL.TK2, Ad.HL.TK2-DM, Ad.HL.dCK-WT, Ad.HL.dCK-A100VTM, Ad.HL.Luc2) and subjected to microPET/microCT imaging. **b** One day after imaging, mice were sacrificed. Viral and liver genomes were measured in liver extracts to determine numbers of viral vectors in the livers. Each point is the mean of three liver samples per mouse. **c** Four identical ROIs were drawn within the liver of each mouse and used to determine the %ID/g for liver. Values were then corrected by subtracting ROI values determined for the mice injected with Ad.HL.Luc2 virus and imaged with the appropriate PRP (negative control, bkg). An asterisk indicates statistically significant differences ( $p > 0.05$ ); individual *p* values follow: FHBG sr39TK vs. TK2-DM,  $p=0.23$ . FHBG sr39TK vs. dCK-A100VTM,  $p=0.01$ . TK2-DM vs. dCK-A100VTM,  $p=0.01$ . **d** The [%IDg-bkg] in liver for each adenovirus vector (from c) was normalized for the number of viral genomes per liver (from b). To compare the efficacies of the experimental TK2, TK2-DM, dCK-WT, and dCK-A100VTM/ $^{18}\text{F}$ -L-FMAU PRG/PRP noninvasive imaging systems with the efficacy of the HSV1sr39TK/ $^{18}\text{F}$ -FHBG PRG/PRP system, the values for the experimental systems using  $^{18}\text{F}$ -L-FMAU as the PRP are expressed as a percentage of the HSV1sr39TK/ $^{18}\text{F}$ -FHBG PRG/PRP system. An asterisk indicates statistically significant differences ( $p > 0.05$ ); individual *p* values follow: FHBG sr39TK vs. TK2-DM,  $p=0.86$ . TK2-DM vs. dCK-A100VTM,  $p=0.08$ . FHBG sr39TK vs. dCK-A100VTM,  $p=0.03$ . Data for **b**, **c**, and **d** are means  $\pm$  SEM.



increasingly greater importance in evaluating their relative therapeutic efficacies. As new reporter gene/reporter probe imaging systems are developed, a robust, quantifiable means for their evaluation becomes essential. The procedure we developed eliminates all variables except the reporter gene and the reporter probe, restricting comparisons to a single,

similarly vascularized organ and permitting postimaging normalization for the number of reporter genomes [16].

HSV1-TK and its mutated derivatives have become the *de facto* “gold standard” PRGs for PRG/PRP analysis in “translational” preclinical models and in clinical trials. However, because of the immunogenicity of HSV1-TK

and its derivatives, several groups have developed mutated human nucleoside kinases as PRGs. The “ideal” mutated nucleoside kinase PRG would (1) not be immunogenic in patients, (2) use as its PRP substrate a positron-emitting nucleoside analogue unable to be phosphorylated by the endogenous enzyme, and (3) be unable to phosphorylate the endogenous substrate.

To date, several mutant human nucleoside kinase PRG/PRP noninvasive imaging systems have been described. Two PRG studies have been published utilizing 2'-deoxy-2-<sup>18</sup>F-5-methyl-1-β-L-arabinofuranosyluracil (<sup>18</sup>F-FEAU) as the PRP; the first used a truncated human *TK2* gene as a PRG [21], while the second used a human dCK double mutant (dCK-R104M/D133A) [12]. More recently, two additional studies have used <sup>18</sup>F-FMAU as a PRP; one of these studies used a TK2 double mutant as the PRP [13] and the second used a dCK triple mutant (dCK-A100VTM) [McCracken *et al.*, in preparation].

To begin the comparison of alternative PRG/PRP imaging combinations, using the rigorous system developed previously [16], we compared the efficacies of the TK2-DM and dCK-A100VTM PRGs, using the common PRP <sup>18</sup>F-L-FMAU, to the efficacy of the HSV1sr39TK/<sup>18</sup>F-FHBG PRG/PRP imaging combination. Our data suggest that in the adenovirus/hepatic mouse model system we developed, the TK2-DM/<sup>18</sup>F-L-FMAU PRG/PRP combination is as effective as the HSV1sr39TK/<sup>18</sup>F-FHBG combination, while the dCK-A100VTM/<sup>18</sup>F-L-FMAU PRG/PRP combination has a significant advantage over the HSV1sr39TK/<sup>18</sup>F-FHBG combination (Fig. 4).

As we developed this comparative analytical system for PRG/PRP imaging combinations, it became apparent that there are a number of additional constraints, considerations, and pitfalls to take into account in comparing alternative PRG/PRP systems. We compared two reporter genes (*TK2-DM* and *dCK-A100VTM*) both to one another, using a common PRP (<sup>18</sup>F-L-FMAU), and to a distinct PRG/PRP imaging system (HSV1sr39TK/<sup>18</sup>F-FHBG). While all three PRGs are expressed from the same expression vector and the transgene PRG copy numbers can be determined after imaging, thus assuring that the imaging results can be normalized for levels of PRG expression, we do not know if the two <sup>18</sup>F-PRPs are present in adequate levels in the liver for comparable use as substrates. While the efficacy comparisons of TK2-DM/<sup>18</sup>F-L-FMAU and dCK-A100VTM/<sup>18</sup>F-L-FMAU in the liver are controlled for essentially all variables, it is quite possible that the relative availabilities of the <sup>18</sup>F-FHBG and <sup>18</sup>F-L-FMAU PRP substrates may be quite different in the liver for these alternative PRGs. Thus, substrate availability, and not PRG expression, may be limiting, perhaps in a tissue-specific fashion, for PRP/PRG reporter systems. In preclinical reporter gene/reporter probe systems, this is perhaps most graphically illustrated by the firefly luciferase/luciferin system; no matter what the level of luciferase expression, no image can be detected in the brain—luciferin cannot penetrate the blood-brain barrier.

A second pitfall for translation from preclinical to clinical applicability for PRG/PRP imaging systems in patients lies in differences between mice (and other species used in preclinical analyses) and humans for PRP biodistribution. <sup>18</sup>F-L-FMAU biodistribution in mice, using a xenograft tumor model, showed no significant probe retention in tissues other than tumor, with variable signal in intestine. Indeed, in mice, the nonspecific probe retention for <sup>18</sup>F-L-FMAU was less than that observed for <sup>18</sup>F-FHBG [13, 22]. However, in distribution studies in humans, extensive hepatic <sup>18</sup>F-L-FMAU retention was observed [13], suggesting that the clinical use of either the TK2-DM/<sup>18</sup>F-L-FMAU PRG/PRP reporter system or the dCK-A100VTM/<sup>18</sup>F-L-FMAU PRG/PRP monitoring system in patients will be restricted to extrahepatic applications.

In developing the dCK-DM PRG, Likar *et al.* [12] used <sup>18</sup>F-FEAU as the PRP and compared the efficacy of the dCK-DM/<sup>18</sup>F-FEAU imaging combination to the HSV1R176Qsr39TK/<sup>18</sup>F-FHBG combination. Their study used transduced xenograft tumors for comparison. The difficulties in trying to compare and evaluate alternative PRG/PRP reporter systems from various laboratories are illustrated by trying to evaluate prior studies by Likar *et al.* [12] of their dCK-based PRG with those of the TK2-based PRG by Campbell *et al.* [13]; these reports used different vectors, different transduced tumor cells, different xenograft conditions likely to lead to distinct target sizes and variable vascularization, and distinct PRPs. Using a rigorous protocol that equalizes many of these conditions in preclinical studies will help to make the pursuit of clinically useful systems more effective. For example, by comparing alternative substrates (e.g., <sup>18</sup>F-FEAU and <sup>18</sup>F-L-FMAU) in this adenovirus-based model and evaluating the biodistribution of the two PRPs, a definitive comparison of the two presumably nonimmunogenic PRGs (TK2-DM and dCK-A100VTM) and the two alternative PRPs (<sup>18</sup>F-FEAU and <sup>18</sup>F-L-FMAU) could be performed.

Differences in biodistribution for potential PRPs between mouse and human, or between human and any other species, presents an often unanticipated but significant barrier in PRP/PRG imaging system development. <sup>18</sup>F-L-FMAU is a case in point; its pristine lack of retention in mice is, unfortunately, not reflected in human studies [13]. As a result, we are adopting a new “reverse” approach to the development of PRG/PRP imaging systems. Alternative positron-emitting nucleoside analogues are synthesized, and biodistribution studies are carried out in volunteers to identify potential PRPs with optimal biodistribution characteristics [23]. After identification of potential PRPs with appropriate biodistribution properties, modifications of nucleoside kinases are made and *in vitro* analyses of their ability to phosphorylate both the modified and the endogenous substrates are evaluated to identify mutant PRGs that can phosphorylate the potential PRP and have reduced kinase activity on the endogenous substrate.

Reducing the ability of the mutated nucleotide kinase PRG to utilize the endogenous substrate may appear to be

simply a bonus because it will effectively increase the specific activity *in vivo* of the PRG for the PRP; the “cold” endogenously produced compound will no longer compete with the positron-emitting PRP for the mutated PRG nucleotide kinase. However, there is another important potential value in reducing/eliminating PRG kinase activity for the endogenous substrate. While the PRPs are present in tracer, non-physiological amounts and will have no biological effect, high PRG levels, if active on an endogenous substrate, might drastically modify nucleoside/nucleotide pools in target cells and, as a result, have profound biological consequences. In principle, the “ideal” PRG kinase would be orthogonal to the native enzyme, able to phosphorylate the positron-emitting PRP and unable to phosphorylate the endogenous substrate (or any other cellular component).

It is clear that reporter probe biodistribution, duration of availability, and clearance from tissues will present problems that must be overcome in optimizing noninvasive reporter gene/reporter probe combinations. Similarly, optimizing reporter gene delivery, bioavailability, and expression are among the many factors that must also be considered in developing optimal clinical reporter gene/reporter probe combinations for patient applications, whether the analysis be PET, SPECT, MRI, ultrasound, etc. We anticipate that using rigorously controlled experimental methodologies, like the one used here, will be required to bring the best methods for reporter gene/reporter probe imaging to the clinic as rapidly and cost-effectively as possible.

**Acknowledgments.** We thank Arthur Catapang for technical help; David Stout, Liu Wei, and Waldemar Ladno for advice and assistance with imaging experiments; and members of the Herschman, Radu, and Witte laboratories for helpful discussions. This study was funded by the National Cancer Institute In Vivo Cellular and Molecular Imaging Center (ICMIC) award P50 CA086306 (HRH), the National Cancer Institute grant 5U54 CA119347 (CGR), and the National Institute of Biomedical Imaging and Bioengineering grant IR01CA16077001 (CGR). JG was supported by a Scholars in Oncologic Medical Imaging (SOMI) fellowship from the National Cancer Institute (Award R25T CA098010).

**Conflict of interest.** DOC and CR have filed a patent application for the TK2-DM/<sup>18</sup>F-L-FMAU PRG/PRP system. The remaining authors declare they have no conflict of interest.

## References

- Bhaumik S, Gambhir SS (2004) Optical imaging of *Renilla* luciferase, synthetic *Renilla* luciferase, and firefly luciferase reporter gene expression in living mice. *J Biomed Opt* 9:578–586
- Gheysens O, Gambhir SS (2005) Studying molecular and cellular processes in the intact organism. *Prog Drug Res* 62:117–150
- Lewis JS, Achilefu S, Garbow JR, Laforest R, Welch MJ (2002) Small animal imaging. Current technology and perspectives for oncological imaging. *Eur J Cancer* 38:2173–2188
- Jenkins DE, Oei Y, Hornig YS, Yu S-F, Dusich J, Purchio T, Contag PR (2003) Bioluminescent imaging (BLI) to improve and refine traditional murine models of tumor growth and metastasis. *Clin Exp Metastasis* 20:733–744
- Iyer M, Sato M, Johnson M, Gambhir SS, Wu L (2005) Applications of molecular imaging in cancer gene therapy. *Curr Gene Ther* 5:607–618
- Pysz MA, Gambhir SS, Willmann JK (2010) Molecular imaging: current status and emerging strategies. *Clin Radiol* 65:500–516
- Berger C, Flowers ME, Warren EH, Riddell SR (2006) Analysis of transgene-specific immune responses that limit the *in vivo* persistence of adoptively transferred HSV-TK-modified donor T cells after allogeneic hematopoietic cell transplantation. *Blood* 107:2294–2302
- Gambhir SS, Bauer E, Black ME, Liang Q, Kokoris MS, Barrio JR, Iyer M, Namavari M, Phelps ME, Herschman HR (2000) A mutant herpes simplex virus type 1 thymidine kinase reporter gene shows improved sensitivity for imaging reporter gene expression with positron emission tomography. *Proc Natl Acad Sci* 97:2785–2790
- Yaghoubi S, Barrio JR, Dahlbom M, Iyer M, Namavari M, Satyamurthy N, Goldman R, Herschman HR, Phelps ME, Gambhir SS (2001) Human pharmacokinetic and dosimetry studies of [(18)F]FHBG: a reporter probe for imaging herpes simplex virus type-1 thymidine kinase reporter gene expression. *J Nucl Med* 42:1225–1234
- Yaghoubi SS, Jensen MC, Satyamurthy N, Budhiraja S, Paik D, Czernin J, Gambhir SS (2009) Noninvasive detection of therapeutic cytolytic T cells with 18 F-FHBG PET in a patient with glioma. *Nat Clin Pract Oncol* 6:53–58
- Traversari C, Markt S, Magnani Z, Mangia P, Russo V, Ciceri F, Bonini C, Borgdignon C (2007) The potential immunogenicity of the TK suicide gene does not prevent full clinical benefit associated with the use of TK-transduced donor lymphocytes in HSCT for hematologic malignancies. *Blood* 109:4708–4715
- Likar Y, Zurita J, Dobrenkov K, Shenker L, Cai S, Neschadim A, Medin JA, Sadelain M, Hricak H, Ponomarev V (2010) A new pyrimidine-specific reporter gene: a mutated human deoxycytidine kinase suitable for PET during treatment with acycloguanosine-based cytotoxic drugs. *J Nucl Med* 51:1395–1403
- Campbell DO, Yaghoubi SS, Su Y, Lee JT, Auerbach MS, Herschman H, Satyamurthy N, Czernin J, Lavi A, Radu CG (2012) Structure-guided engineering of human thymidine kinase 2 as a positron emission tomography reporter gene for enhanced phosphorylation of non-natural thymidine analog reporter probe. *J Biol Chem* 287:446–454
- Hazra S, Sabini E, Ort S, Konrad M, Lavie A (2009) Extending thymidine kinase activity to the catalytic repertoire of human deoxycytidine kinase. *Biochemistry* 48:1256–1263
- Iyidogan P, Lutz S (2008) Systematic exploration of active site mutations on human deoxycytidine kinase substrate specificity. *Biochemistry* 16:4711–4720
- Gil JS, Machado HB, Herschman HR (2012) A method to rapidly and accurately compare the relative efficacies of non-invasive imaging reporter genes in a mouse model and its application to luciferase reporters. *Mol Imaging Biol* 14:462–471
- Gallaher SD, Gil JS, Dorigo O, Berk AJ (2009) Robust *in vivo* transduction of a genetically stable EBV episome to hepatocytes in mouse by a hybrid viral vector. *J Virol* 83:3249–3257
- Gil JS, Gallaher SD, Berk AJ (2010) Delivery of an EBV episome by a self-circularizing helper-dependent adenovirus: long-term transgene expression in immunocompetent mice. *Gene Ther* 17:1288–1293
- Gambhir SS, Barrio JR, Phelps ME, Iyer M, Namavari M, Satyamurthy NWL, Green LA, Bauer E, MacLaren DC, Nguyen K, Berk AJ, Cherry SR, Herschman HR (1999) Imaging adenoviral-directed reporter gene expression in living animals with positron emission tomography. *Proc Natl Acad Sci* 96:2333–2338
- Sabini E, Ort S, Monnerjahn C, Konrad M, Lavie A (2003) Structure of human dCK suggests strategies to improve anticancer and antiviral therapy. *10:513–519*
- Ponomarev V, Doubrovina M, Shavrin A, Serganova I, Beresten T, Ageyeva L, Cai C, Balatoni J, Alauddin M, Gelovani J (2007) A human-derived reporter gene for noninvasive imaging in humans: mitochondrial thymidine kinase type 2. *J Nucl Med* 48:819–826
- Alauddin MM, Shahinian A, Gordon EM, Conti PS (2004) Direct comparison of radiolabeled probes FMAU, FHBG, and FHPG as PET imaging agents for HSV1-tk expression in a human breast cancer model. *Mol Imaging* 3:76–84
- Schwarzenberg J, Radu CG, Benz M, Fueger B, Tran AQ, Phelps ME, Witte ON, Satyamurthy N, Czernin J, Schiepers C (2011) Human biodistribution and radiation dosimetry of novel PET probes targeting the deoxyribonucleoside salvage pathway. *Eur J Nucl Med Mol Imaging* 38:711–721

## **SUPPLEMENTAL MATERIALS for**

**Title:** “Application of a rapid, simple and accurate Adenovirus-based method to compare PET reporter gene/PET reporter probe systems “

**Journal:** Molecular Imaging and Biology

**Authors:** Jose S. Gil, Hidevaldo B. Machado, Dean O. Campbell, Melissa McCracken, Caius Radu, Owen Witte and Harvey R. Herschman

**e-mail address, and affiliations of the corresponding author:**

**hherschman@mednet.ucla.edu**; Department of Biological Chemistry and Department of Molecular and Medical Pharmacology; David Geffen School of Medicine, UCLA.

### ***Supplemental Methods***

#### *Adenovirus vectors*

Adenovirus vectors were constructed using the Gateway System (Invitrogen, Carlsbad, CA), with the pENTR shuttle vectors [1] containing each of the reporter genes, recombined into the adenoviral plasmid vector, pAd/CMV/V5-DEST using LR recombination. Vector construction is diagramed in Fig. 1 of the main text. All reporter gene coding regions were amplified using Phusion DNA polymerase (Finnzymes/New England Biolabs), according to the manufacturer’s instructions. The luciferase 2 (*Luc2*) as a vector control was amplified from pGL4.13 (Promega, Madison, WI) as previously described [1]. These constructs were then recombined with pAd/CMV/V5-DEST, using LR Clonase II (Invitrogen), according to the manufacturer’s protocol, to generate the pAd plasmids.

To generate adenovirus vectors, plasmid DNA for each construct was digested for 2 hours at 37°C with *PacI*, then purified with PCR Cleanup (Invitrogen, Carlsbad,

CA). 1.6 µg DNA was used to transfect HEK293A cells seeded on 12-well cell culture plates, using Lipofectamine 2000 (Invitrogen). After 10 days, cells from wells showing 100% cytopathic effect (CPE) were collected by scraping, the entire well contents (1 mL) were transferred to screw cap tubes, and the cells and debris were subjected to three cycles of freeze/thaws for lysis. The suspension was centrifuged, and the supernatant was used to propagate the adenovirus vectors in fresh HEK293A cells.

*Propagation of Adenovirus vectors expressing the PET reporter genes*

90% confluent 10cm tissue culture dishes of HEK293A cells were infected with adenovirus vector containing supernatant, incubated for 2 to 3 days until complete CPE was evident. Cells were collected by scraping, lysed with 3 rounds of freeze/thaw and followed by centrifugation. One more round of infection with the supernatant was performed onto two 500 cm<sup>2</sup> tissue culture plates of 90% confluent HEK293A cells. After 2 to 3 days, with cells showing 100% CPE, plates were collected, and cells were pelleted in 5% original volume, followed by lysis using deoxycholate (0.5% final concentration). After a clarification centrifugation, supernatants were loaded onto a 50 mM Tris-HCl pH 8.0 cesium chloride buoyant density step gradients with 1.35 g/mL and 1.25 g/mL densities. Bands were consolidated, and density and volume were adjusted to 1.33 g/mL for linear gradient ultracentrifugation. Purified adenovirus vector was dialyzed against a 3% sucrose storage buffer and snap frozen in aliquots in liquid nitrogen for storage.

*Titration of Adenovirus vectors, using the Infectious Genome protocol [1, 2]*

Adherent HeLa cells (American Type Culture Collection, Manassas, VA) were cultured in Dulbecco's Modified Eagle Medium (DMEM) supplemented with 10% fetal bovine serum, penicillin (100 U/mL) and streptomycin (100 µg/mL). Cells were seeded

at 1:2 dilutions onto 6-well tissue culture plates one day prior to adenovirus vector infection. Wells were infected with the adenovirus vectors by aspirating media, and cells were infected with vector diluted in 0.25 mL DMEM.

HeLa cells were infected for three hours, then washed twice with PBS. Nuclei were isolated using an NP-40 lysis protocol (10 minutes at room temperature) in 0.65% NP-40, 150 mM NaCl, 10 mM Tris-HCl pH 8.0, 1.5 mM MgCl<sub>2</sub>, followed by pelleting nuclei and removing supernatant). DNA was purified using the DNeasy Blood & Tissue kit (Qiagen, Valencia, CA) and subjected to TaqMan quantitative real-time PCR (Applied Biosystems, Foster City, CA). Primers and probe specific for the adenoviral pX protein gene were used for absolute quantification, using a plasmid standard with known copy number. The numbers of Infectious Genome Units (IGUs) are determined by comparing the amount of PCR product from the nuclear extracts, normalized to one copy of the amplification region in the plasmid standard.

#### *Measurement of adenovirus DNA and murine genomic DNA in liver extracts*

TaqMan PCR based absolute quantification for vector genomes and liver cell genomes was performed on purified DNA, using the same adenovector primers and TaqMan probe used in the cell culture titrations, and primers and probe specific for the mouse *Oct4* gene. Standard curves to measure the number of liver genomes were prepared from pre-weighed liver samples subjected to DNeasy DNA purification, based on an estimation of  $1.35 \times 10^8$  hepatocytes per gram [3]. Standard curves to measure the number of adenovirus vectors were prepared from purified vector DNA quantified by optical density.

#### *Determination of optimal time for imaging of reporter gene efficacy after adenovirus reporter gene intravenous injection*



Three mice were injected via tail vein with Ad.HL.Luc2 ( $5 \times 10^{10}$  IGU/mouse). The mice were then imaged, following luciferin injection [1] with an IVIS instrument (Caliper Life Science, Inc.), at days 1, 2, 3, 4, 5, 6 and 10 after Ad.HL.LUC2 injection. We found a broad peak between days 3 and 5 (Supplemental Fig. 1).

#### *In vivo studies*

*In vivo* studies to compare efficacy of wild-type dCK and the two dCK mutants dCK-R104M/D133A (dCK-DM) and dCK-A100V/R104M/D133A (dCK-A100VTM) were performed as described in the main manuscript, with the modification that two mice per group imaged in one experiment and the experiment was repeated a second time, again with two mice per group. For the comparison of dCK and the two dCK mutants as PRGs, the data from the two experiments were pooled.

#### **Supplemental Results**

To determine the time for optimal imaging after adenovirus injection in our protocol, we injected 3 mice with  $5 \times 10^{10}$  Ad.HL.Luc2 [1], and imaged with luciferase [1] daily for 6 days, then at 10 days. For each optical imaging session mice were anesthetized with 2% isoflurane. For each image, luciferin (3 mg, in 100  $\mu$ L) was administered intraperitoneally. Mice were imaged in an IVIS<sup>®</sup> Lumina II imaging system (Caliper Life Sciences, Hopkinton, MA) [1]. Optimal imaging was observed between days 3-5 (Supplemental Figure 1).

*Hepatic efficacy of wild type dCK, the double mutant dCK-DM and the triple mutant dCK-A100VTM as PRGs, with <sup>18</sup>F-L-FMAU as a PRP*

Four mice per group were injected intravenously with adenovirus vectors ( $5 \times 10^{10}$  IGU/mouse); Ad.HL.Luc2, Ad.HL.dCK-WT, Ad.HL.dCK-DM and Ad.HL.dCK-A100VTM.

Imaging with  $^{18}\text{F}$ -L-FMAU was performed 4 days after vector injection (Supplemental Figure 2a), followed by liver DNA purification. The numbers of vector genomes/liver cell,  $\pm$  S.E.M, were Ad.HL.Luc2,  $86 \pm 10$ ; Ad.HL.dCK-WT,  $77 \pm 14$ ; Ad.HL.dCK-DM,  $80 \pm 18$  and Ad.HL.dCK-A100VTM,  $72 \pm 19$  (Supplemental Figure 2b). Differences in viral genome transductions between groups were not statistically significant ( $p=0.94$ ), demonstrating consistent transduction efficiency.

PRP-dependent PRG hepatic retention was determined as described in the main manuscript. %ID/g values, corrected for PRP background, but not corrected for differences in the numbers of PRGs present in the liver, were Ad.HL.dCK-WT,  $0.05 \pm 0.01$ ; Ad.HL.dCK-DM,  $5.0 \pm 0.56$ ; and Ad.HL.dCK-A100VTM,  $5.2 \pm 0.58$ . (Supplemental figure 2c). Values are means  $\pm$ S.E.M.s. Differences between dCK-WT and each mutant were significant (\*\*\*) indicates  $p=0.0001$  for both dCK-DM and dCK-A100VTM). However, no statistical difference between dCK-DM and dCK-A100VTM was detected ( $p=0.80$ ).

To eliminate the variability caused by differences in numbers of PRGs present in livers of each mouse, the [%ID/g-bkg] was normalized to vector transduction. Results for the dCK vectors were Ad.HL.dCK-WT,  $7.6 \pm 2.6 \times 10^{-4}$ ; Ad.HL.dCK-DM,  $7.6 \pm 2.5 \times 10^{-2}$ ; and Ad.HL.dCK-A100VTM,  $9.1 \pm 2.8 \times 10^{-2}$ . Both Ad.HL.dCK-DM/ $^{18}\text{F}$ -L-FMAU and Ad.HL.dCK-A100VTM/ $^{18}\text{F}$ -L-FMAU signals differed significantly from the Ad.HL.dCK-WT/ $^{18}\text{F}$ -L-FMAU signal (\*indicates  $p=0.02$ ). In contrast no significant difference could be demonstrated between the signals from the Ad.HL.dCK-DM/ $^{18}\text{F}$ -L-FMAU and Ad.HL.dCK-A100VTM/ $^{18}\text{F}$ -L-FMAU ( $p=0.70$ ).

### ***Supplemental Figure Legends***

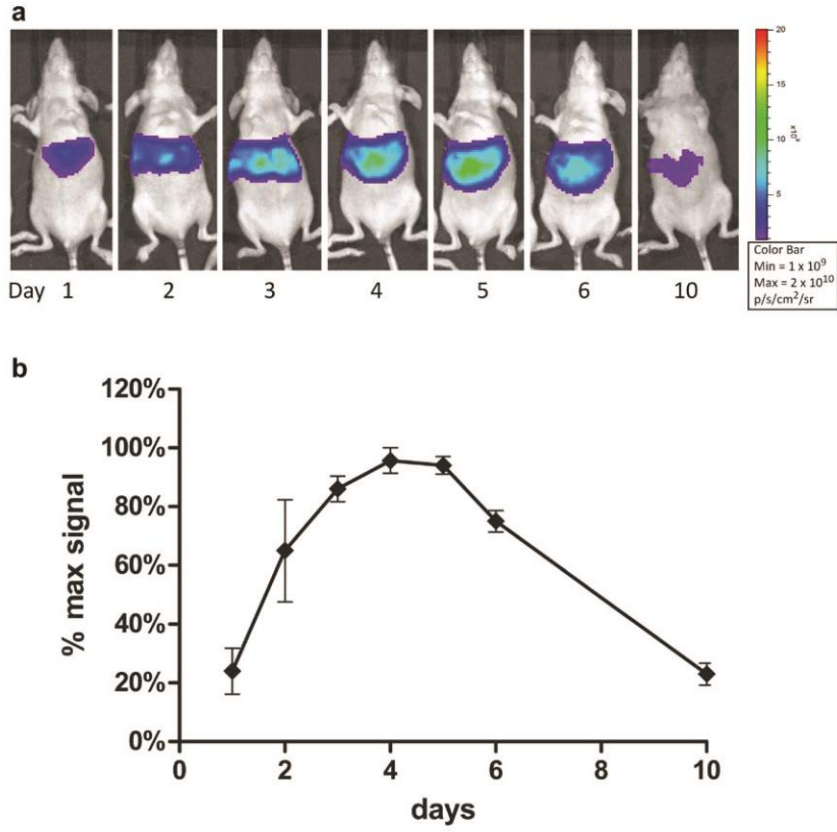
**Supplemental Fig. 1. Time course for hepatic adenovirus reporter gene expression.** Three mice were injected with Ad.HL.Luc2 ( $5 \times 10^{10}$  IGU) on day 0, then subjected to luciferin-dependent bioluminescent imaging on days 1, 2, 3, 4, 5, 6 and 10 after virus administration. (Panel a) Successive optical images for one mouse. (Panel b) Signal was normalized to 100% of the maximum for each mouse, and averaged. Data are means  $\pm$  S.E.M. of triplicate assays for three mice imaged at each time point.

**Supplemental Fig. 2. Comparative efficacy of dCK-DM and dCKA100VTM as PRGs, with 18F-L-FMAU as PRP.** (Panel a) Four mice per group were injected with either  $5 \times 10^{10}$  IGU of Ad.HL.Luc2, Ad.HL.dCK-WT, Ad.HL.dCK-DM, or Ad.HL.dCK-A100VTM, and imaged 4 days later (1 representative image for Ad.HL.dCK-WT, dCK-DM and dCKA100VTM is shown). (Panel b) One day after imaging the mice were sacrificed and liver samples were processed to determine transduction as measured by qPCR-detected vector genomes. Each point is the mean of three liver samples per mouse. The horizontal lines are the means of all mice in each group, error bars denote  $\pm$  S.E.M. (panel c) 4 ROIs were drawn within the liver of each animal, and quantified to determine average %ID/g. Each point is the mean of the four liver ROIs with background signal (Ad.HL.Luc2 negative control mouse) subtracted. Error bars indicate means  $\pm$  S.E.M. Differences between dCK-WT and each mutant were significant (\*\*\*) indicates  $p=0.0001$  for both dCK-DM and dCK-A100VTM). Differences between dCK-DM and dCK-A100VTM were not statistically significant ( $p=0.80$ ). (Panel d) Signal was normalized for number of hepatic viral genomes. Differences between dCK-WT and each mutant were significant (\* indicates  $p=0.02$ ). Differences between dCK-DM and dCK-A100VTM were not statistically significant ( $p=0.70$ ). Error bars denote  $\pm$  S.E.M.

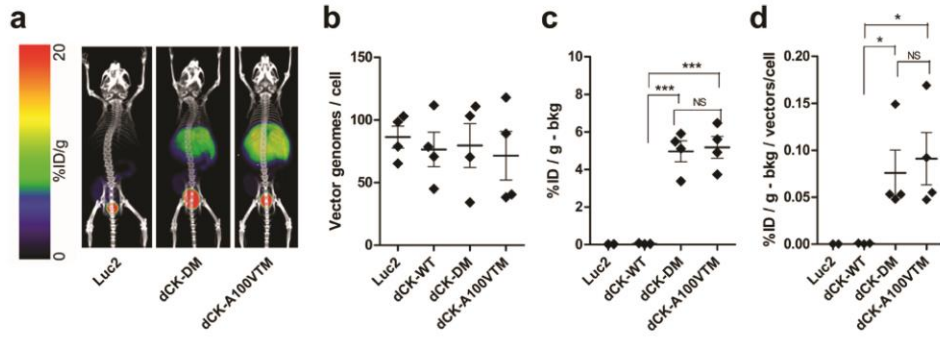
## REFERENCES

1. Gil, J.S., Machado, H.B., and Herschman, H.R. (2011). A Method to Rapidly and Accurately Compare the Relative Efficacies of Non-invasive Imaging Reporter Genes in a Mouse Model and its Application to Luciferase Reporters. *Molecular Imaging and Biology* **14**: 462-471.
2. Gil, J.S., Gallaher, S.D., Berk, A.J. (2010). Delivery of an EBV episome by a self-circularizing helper-dependent adenovirus: Long-term transgene expression in immunocompetent mice. *Gene Therapy* **17**, 1288-1293.
3. Sohlenius-Sternbeck, A.-K. (2006). Determination of the hepatocellularity number for human, dog, rabbit, rat and mouse livers from protein concentration measurements. *Toxicology in Vitro* **20**, 1582-1586.
4. Gallaher, S.D., Gil, Jose S., Dorigo, Oliver, Berk, Arnold J. (2009). Robust In Vivo Transduction of a Genetically Stable EBV Episome to Hepatocytes in Mouse by a Hybrid Viral Vector. *Journal of Virology* **83**: 3249-3257.

Gil et al, Supplemental Figure 1.



Gil et al, Supplemental Figure 2



### **CHAPTER 3:**

Long-term in vivo monitoring of mouse and human  
hematopoietic stem cell engraftment with a  
human positron emission tomography reporter gene.

# Long-term in vivo monitoring of mouse and human hematopoietic stem cell engraftment with a human positron emission tomography reporter gene

Melissa N. McCracken<sup>a</sup>, Eric H. Gschwend<sup>b</sup>, Evan Nair-Gill<sup>a</sup>, Jami McLaughlin<sup>b</sup>, Aaron R. Cooper<sup>c</sup>, Mireille Riedinger<sup>a</sup>, Donghui Cheng<sup>d</sup>, Christopher Nosala<sup>e</sup>, Donald B. Kohn<sup>b,e,f</sup>, and Owen N. Witte<sup>a,b,c,d,e,1</sup>

<sup>a</sup>Department of Molecular and Medical Pharmacology, David Geffen School of Medicine, University of California, Los Angeles, CA 90095; <sup>b</sup>Department of Microbiology, Immunology and Molecular Genetics, University of California, Los Angeles, CA 90095; <sup>c</sup>Molecular Biology Institute, University of California, Los Angeles, CA 90095; <sup>d</sup>Howard Hughes Medical Institute, University of California, Los Angeles, CA 90095; <sup>e</sup>Eli and Edythe Broad Center of Regenerative Medicine and Stem Cell Research, University of California, Los Angeles, CA 90095; and <sup>f</sup>Department of Pediatrics, University of California, Los Angeles, CA 90095

Contributed by Owen N. Witte, December 14, 2012 (sent for review October 29, 2012)

**Positron emission tomography (PET) reporter genes allow noninvasive whole-body imaging of transplanted cells by detection with radiolabeled probes. We used a human deoxycytidine kinase containing three amino acid substitutions within the active site (hdCK3mut) as a reporter gene in combination with the PET probe [<sup>18</sup>F]-L-FMAU (1-(2-deoxy-2-<sup>18</sup>F-fluoro-β-L-arabinofuranosyl)-5-methyluracil) to monitor models of mouse and human hematopoietic stem cell (HSC) transplantation. These mutations in hdCK3mut expanded the substrate capacity allowing for reporter-specific detection with a thymidine analog probe. Measurements of long-term engrafted cells (up to 32 wk) demonstrated that hdCK3mut expression is maintained in vivo with no counter selection against reporter-labeled cells. Reporter cells retained equivalent engraftment and differentiation capacity being detected in all major hematopoietic lineages and tissues. This reporter gene and probe should be applicable to noninvasively monitor therapeutic cell transplants in multiple tissues.**

gene therapy | molecular imaging

Genetically modifying cells can offer novel therapeutic strategies for currently untreatable diseases (1). Standard methods for monitoring the long-term viability of transplanted cells are inadequate. Improved methods to serially detect transplanted cells in several tissues throughout the body simultaneously and noninvasively are critical to measure therapeutic efficacy (2, 3).

Hematopoietic stem cell transplants (HSCT) from both autologous and allogeneic sources have been successfully used in regenerative medicine (4). Genetic engineering through viral vector integration repairs defects in HSCs expanding clinical applications (5). Effective transplantation requires the engraftment of HSCs followed by an expansion into mature hematopoietic lineages repopulating multiple organs and peripheral blood. Measurement of mature hematopoietic cells in the peripheral blood is the primary diagnostic method for evaluating transplant efficacy. The major limitation of this approach is the lack of information about the engraftment within hematopoietic tissues.

Cells engineered to express a positron emission tomography (PET) reporter gene can be serially imaged in vivo with a reporter-specific probe (2). Most studies have used variants of the herpes simplex virus type 1 thymidine kinase (HSV1-TK or HSV1-sr39TK) and a radiolabeled penciclovir analog (9-(4-[<sup>18</sup>F]-fluoro-3-hydroxymethylbutyl)guanine, [<sup>18</sup>F]-FHBG) to detect reporter-labeled cells (6, 7). However, HSV1-TK is immunogenic and cells expressing this enzyme are selectively cleared over time potentially causing therapeutic failure (8–10). This immunogenicity has prevented the routine use of PET reporter genes clinically (11, 12).

Alternative potentially nonimmunogenic PET reporter genes have been investigated (3). Human nucleoside kinases deoxycytidine kinase (dCK) and thymidine kinase 2 (TK2) have similar substrate specificity to HSV1-TK. Several studies demonstrated

the specific detection of reporter-labeled cells in mouse models with these human nucleoside kinases as PET reporters. Two studies developed xenografts expressing truncated TK2 or a mutant TK2 demonstrating reporter-specific imaging when probed with [<sup>18</sup>F]-thymidine analogs (13, 14). Infiltrating tumor-specific human T cells expressing a mutant dCK (dCKDM: R104M, D133A) reporter were detected within lung lesions of mice after transplantation by 2'-[<sup>18</sup>F]fluoro-5-ethyl-1-beta-D-arabinofuranosyluracil ([<sup>18</sup>F]-FEAU) PET (15). These reporter-labeled T cells were tested for cytolytic activity in vitro against target cells demonstrating that expression of dCKDM did not alter their short-term function (15).

Further investigation of human dCK as a PET reporter was selected based on multiple factors. mRNA encoding DCK is ~800 bp, smaller than HSV1-TK, causing a minimal size increase when inserted into therapeutic vectors. The biological function of dCK has been described in genetic knockout mice (16, 17). The enzyme structure and kinetics of dCK are well characterized (18) with known point mutations that shift substrate specificity (18–20). A previous study successfully demonstrated the use of an alternate mutant dCK reporter and probe (15). Endogenous dCK activity can be monitored with PET using an alternate radiolabeled nucleoside analog (21).

How human nucleoside kinase reporters affect long-term cell-based therapies remains uncertain. Specifically it is unknown if constitutive expression in reporter-labeled cells is maintained within the recipient with no perturbation on cell function. Knockout dCK mice have a significant reduction in the total quantity of T and B lymphocytes caused by cellular stress from imbalanced nucleotide pools (22). Ectopic expression of nucleoside kinases could cause similar imbalances. Potential complications may include growth defect, disadvantage, or counterselection resulting in the loss of engrafted cells over time.

Our study demonstrates that a hdCK PET reporter can successfully monitor transplanted cells long term with no toxicity or survival disadvantage in modified cells. Models of mouse and human hematopoietic reconstitution were used to compare our reporter tracking for monitoring engraftment to peripheral blood sampling. Reporter-labeled cells exhibited identical behavior to non-labeled cells with no differences detected regarding cell cycle, lineage, or tissue location. Our data provide evidence that hdCK3mut is an optimal reporter gene for hematopoietic cell tracking with future applications in a broad range of therapeutic cell transplants.

Author contributions: M.N.M., D.B.K., and O.N.W. designed research; M.N.M., E.H.G., E.N.-G., J.M., A.R.C., M.R., D.C., C.N., and O.N.W. performed research; M.R. contributed new reagents/analytic tools; M.N.M., E.H.G., E.N.-G., J.M., A.R.C., D.C., C.N., and O.N.W. analyzed data; and M.N.M. and O.N.W. wrote the paper.

The authors declare no conflict of interest.

Freely available online through the PNAS open access option.

<sup>1</sup>To whom correspondence should be addressed. E-mail: owenwitte@mednet.ucla.edu.

This article contains supporting information online at [www.pnas.org/lookup/suppl/doi:10.1073/pnas.1221840110/-DCSupplemental](http://www.pnas.org/lookup/suppl/doi:10.1073/pnas.1221840110/-DCSupplemental).



## Results

**Mutant Human dCK Functions as a PET Reporter When Probed with Thymidine Analogs.** hdCK3mut contained three point mutations (A100V, R104M, and D133A) that were chosen based on a previous study that demonstrated a 1,100-fold increase in thymidine activity compared with wild-type dCK in enzyme kinetic assays (20). L1210-10K, a mouse leukemic cell line with no endogenous dCK was selected as a model cell line for in vitro studies (23). Stable expression of wild-type (WT) hdCK or hdCK3mut coexpressed with yellow fluorescent protein (YFP) through an internal ribosome entry site (IRES) in L1210-10K cells were generated to test probes for specific retention in hdCK3mut cells (Fig. 1A and vector maps in Fig. S1). Two thymidine analogs, 2'-fluoro-2'-deoxyarabinofuranosyl-5-ethyluracil (FEAU) and 1-(2-deoxy-2-fluoro- $\beta$ -L-arabinofuranosyl)-5-methyluracil (L-FMAU), showed significant accumulation in reporter cell lines compared with wild type. Retention of the probe L-FMAU was 18-fold higher in hdCK3mut cells compared with WT hdCK (Fig. 1B and C).

Enzyme kinetic analysis further demonstrated high substrate affinity of hdCK3mut to L-FMAU with a measured  $K_m$  of  $\sim 13$   $\mu$ M. hdCK3mut had a fourfold lower  $K_m$  for L-FMAU compared with the previously published dCKDM reporter (13  $\mu$ M versus 56  $\mu$ M). A high affinity PET reporter and probe combination is optimal because probes are administered at high specific activities with low concentrations of substrate. The decreased  $K_m$  of hdCK3mut for L-FMAU demonstrates that it will achieve a higher velocity at a lower substrate concentration (Table S1).

Immune compromised NOD.Cg-Prkdc<sup>scid</sup> Il2rg<sup>tm1Wj</sup>/SzJ (NSG) mice were implanted with two s.c. grafts. The right side contained L1210-10K cells and the left side contained L1210-10k cell lines engineered to express WT hdCK or hdCK3mut. To determine tumor viability, animals were imaged by PET/CT with 2-deoxy-2-<sup>18</sup>F-fluoro-D-glucose (<sup>18</sup>F-FDG), a glucose analog used to measure glycolytic consumption. F-18 has a half-life of  $\sim 110$  min with probes decayed to undetectable levels within 24 h allowing for sequential scans with alternate probes. The following day [<sup>18</sup>F]-L-FMAU PET/CT scans detected hdCK3mut reporter

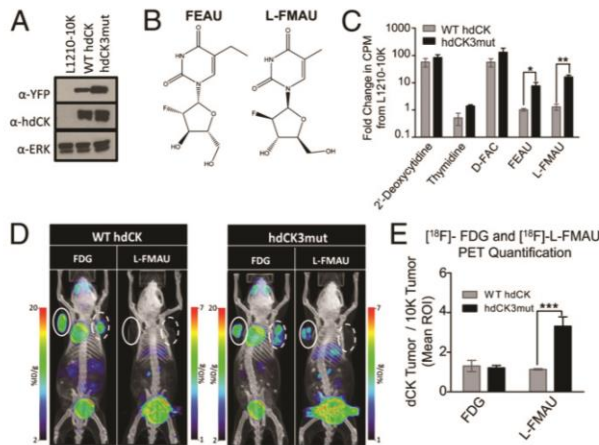


**Fig. 1.** Development of a human thymidine selective PET reporter gene hdCK3mut. (A) Western blot analysis for equal expression of dCK and the linked fluorescent marker YFP in stable cell lines. (B) Chemical structure of two thymidine analogs FEAU and L-FMAU. (C) In vitro [<sup>3</sup>H]-nucleoside uptake assay. Results are displayed on a log<sub>10</sub> scale as a fold change in counts per minute (cpm) from L1210-10K, a dCK-deficient cell line. (FEAU  $P = 0.027$ , L-FMAU  $P = 0.0052$ ) (D) [<sup>18</sup>F]-FDG and [<sup>18</sup>F]-L-FMAU MicroPET scans of NSG mice with s.c. grafts. Right side is control L1210-10K (dotted line). Left side is L1210-10K cells with stable expression of WT dCK or hdCK3mut (solid line). (E) Region-of-interest quantification for [<sup>18</sup>F]-FDG and [<sup>18</sup>F]-L-FMAU ( $P = 0.0006$ ).

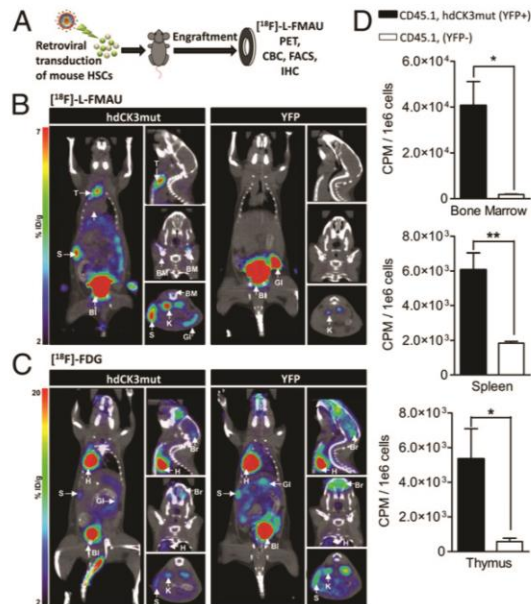


**Fig. 2.** hdCK3mut and [<sup>18</sup>F]-L-FMAU PET can track reporter-labeled mouse hematopoietic cells during early engraftment and expansion in bone marrow chimeric mice. (A) Lethally irradiated C57BL/6 (CD45.2) mice were transplanted with retrovirally transduced 5-FU-enriched HSCs (CD45.1). Animals were monitored for hematopoietic reconstitution over their total lifespan. MicroPET scans shown from Left, coronal; Right Upper, sagittal; Center, coronal; and Lower, transverse. (B) [<sup>18</sup>F]-L-FMAU at 4 wk posttransplant. Reporter signal observed in hdCK3mut animals in spleen (S), thymus (T), and bone marrow (BM). Probe metabolism in both cohorts seen in gastrointestinal (GI), bladder (Bl), and kidney (K). (C) [<sup>18</sup>F]-FDG MicroPET scan at 4 wk posttransplant. Nonreporter-specific signal observed in both cohorts in heart (H), spleen (S), gastrointestinal (GI), brain (Br), with metabolism in kidneys (K) and bladder (Bl). (D) In vivo accumulation of [<sup>18</sup>F]-L-FMAU in sorted hematopoietic cells from hdCK3mut animals. Reporter positive: CD45.1<sup>+</sup>, YFP<sup>+</sup> and reporter negative: CD45.1<sup>+</sup>, YFP<sup>-</sup>. ( $P < 0.05$ ).

expression with signal observed within hdCK3mut grafts (Fig. 1D). PET images were then quantified for total probe accumulation. Images were dose corrected to total radioactivity at the scan start time. Tumors were then selected in a region of interest (ROI) and the mean percent injected dose per gram (%ID/g) over the entire tumor was calculated. Tumor signal of the dCK transduced graft is compared as the fold change in probe retention to the nontransduced L1210-10K tumors of each animal. Tumors expressing hdCK3mut had a 3.3-fold increase in [<sup>18</sup>F]-L-FMAU retention ( $P = 0.0006$ ) compared with WT hdCK grafts (Fig. 1E and Fig. S2). These results determined that hdCK3mut and L-FMAU make a suitable PET reporter gene and probe combination for in vivo studies.

### Expression of hdCK3mut in Mouse HSCs Allow Noninvasive Detection of Reporter Cell Transplantation Before Normalization of Peripheral Blood Counts.

A competitive mouse bone marrow transplantation (BMT) study was chosen to test whether hdCK3mut can detect transplanted cells during early hematopoietic reconstitution (24–28).

Donor cells were generated by treating mice with 5-fluorouracil 5 d preharvest for HSC enrichment. Collected bone marrow was retrovirally infected with  $\sim 40$ – $60\%$  transduction efficiency to express hdCK3mut (coexpressed with YFP through an IRES) or the control of IRES-YFP only (Fig. S1). Recipient mice then received a lethal irradiation dose of 900 rads to eliminate host bone marrow. Mice were transplanted with the mixed population of reporter/nonreporter HSC-enriched donor bone marrow (Fig. 2A).

Under standard conditions mice will display normalized engraftment and complete blood counts (CBC) within ~8 wk after BMT (27). We hypothesized that early engraftment and expansion could be monitored by reporter imaging before normalization of peripheral blood measurements. At 4 wk post-BMT, animals received PET/CT scans with [<sup>18</sup>F]-FDG and the following day [<sup>18</sup>F]-L-FMAU (Fig. 2 B and C).

Whole-body glucose consumption was measured by [<sup>18</sup>F]-FDG MicroPET and was indistinguishable between the two cohorts of animals. Weak signal was detected within the spleen and bone marrow indicating a similar glycolytic rate across all animals (Fig. 2C). The following day PET/CT with [<sup>18</sup>F]-L-FMAU detected only hdCK3mut cells engrafted within the spleen, thymus, and focal areas within the bone marrow of reporter-labeled animals (Fig. 2B and Fig. S3). Animals in the control YFP cohort had no hematopoietic signal observed with [<sup>18</sup>F]-L-FMAU (Fig. 2B). Visualization of [<sup>18</sup>F]-L-FMAU in hematopoietic tissues of hdCK3mut recipients verified that reporter imaging can monitor early engraftment after BMT.

To confirm that [<sup>18</sup>F]-L-FMAU accumulation was specific for hdCK3mut cells, in vivo reporter and nonreporter accumulation was measured. Donor hematopoietic cells from hdCK3mut recipients were sorted for reporter positive or negative and then were counted for total radioactivity in counts per minute (cpm) normalized to cpm/1e6 cells. Cells expressing hdCK3mut had a significantly ( $P < 0.05$ ) higher accumulation of [<sup>18</sup>F]-L-FMAU compared with unlabeled cells in all hematopoietic tissues (Fig. 2D).

**Reporter Labeled Mouse HSCs Retain Expression of hdCK3mut with Equivalent Engraftment and Differentiation Capacity.** Overexpression of enzymes or reporter genes can potentially cause cellular stress, developmental defects during differentiation, growth disadvantage, or transformation (29, 30). The long-term effects from forced expression of hdCK3mut on mouse HSC's engraftment and differentiation capacity was investigated. Reconstituted chimeric mice were evaluated to confirm that hdCK3mut expression was preserved and that mouse HSCs expressing the reporter maintained normal function after transplantation.

Reconstituted chimeric mice 6–8 wk post-BMT were analyzed by flow cytometry and immunohistochemical (IHC) analysis (Fig. 3A and Figs. S4 and S5). Flow cytometry analysis evaluated the spleen, thymus, bone marrow, and peripheral blood for total donor engraftment by lineage, reporter expression (YFP expression), and cell cycle. A representative fluorescent-activated cell sorting (FACS) plot of hdCK3mut engraftment within the spleen is displayed (Fig. 3A). No significant difference in reporter engraftment based on tissue location, lineage distribution, or cell cycle profiles from nonreporter labeled cells or in comparison with the YFP cohort was observed (Fig. S4).

Tissue architecture of the spleen and thymus was examined by hematoxylin and eosin staining (H&E) with normal morphology in both hdCK3mut and YFP mice. hdCK3mut engraftment was then detected although IHC of anti-dCK with no staining seen in YFP recipients. Anti-YFP IHC detected the linked fluorescent marker in both tissues and cohorts of animals confirming the flow cytometry data. Both dCK and YFP IHC identified the same engrafted hematopoietic cells in hdCK3mut animals, demonstrating the specificity of reporter detection using a newly developed monoclonal antibody generated in our laboratory (Fig. S5).

Mice received HSC-enriched bone marrow that was retrovirally transduced to express hdCK3mut or YFP in ~50% of cells. This enrichment technique also contains residual committed short-term progenitor cells that can express the reporter. Transplantation of these progenitor cells is necessary for animal survival but these cells confound analysis of HSC differentiation at early time points. Measurements of mature hematopoietic cells from HSCs and progenitor cells are indistinguishable in peripheral blood analysis. A methylcellulose (MC) colony forming assay measured the expansion and differentiation capacity of reporter-labeled bone marrow 6 wk posttransplantation. Recipient animals' bone marrow was harvested, sorted, and placed in MC for 12 d (Fig. S6A) (25). Quantification of the MC assay determined that cells from hdCK3mut recipient mice were equivalent to YFP animals and nonchimeric bone marrow in colony forming capacity (CFC) as well as colony type distribution (Fig. S6 B–F). Sorted hdCK3mut or YFP positive cells were comparable in CFC and colony type, demonstrating that expression of

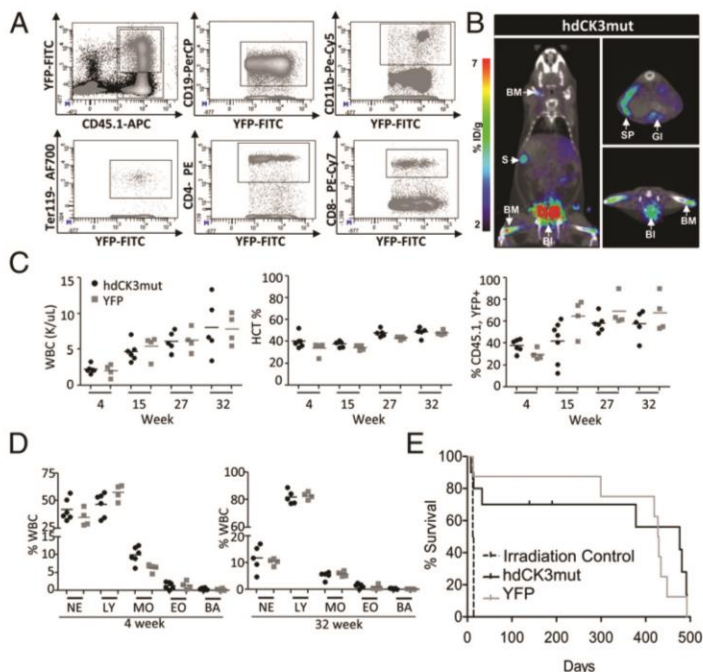


**Fig. 3.** hdCK3mut mouse HSCs persist in vivo allowing long-term monitoring of therapeutic cell transplantation. (A) Representative FACS plot for hdCK3mut engraftment within the spleen. Cells were monitored for CD45.1 (donor) and YFP (reporter) positive. Further gating demonstrates that reporter positive (YFP<sup>+</sup>) cells can be found in all major lineages. (B) [<sup>18</sup>F]-L-FMAU MicroPET at 32 wk post-BMT. (C) Serial monitoring of peripheral blood. Animals were monitored for total white blood cell (WBC), hematocrit (HCT), and reporter-labeled donor engraftment (CD45.1<sup>+</sup>, YFP<sup>+</sup>). (D) Distribution of white blood cells at early and late engraftment are indistinguishable between YFP and hdCK3mut animals. NE, neutrophils; LY, lymphocytes; MO, monocyte; EO, eosinophil; BA, basophil. (E) No survival disadvantage seen in hdCK3mut reporter animals.

hdCK3mut does not cause a disadvantage during *in vitro* differentiation (Fig. S6E). Sorted cells from both YFP and hdCK3mut recipients retained reporter expression during *in vitro* differentiation detected through flow cytometry, confirming the continued expression of hdCK3mut throughout cell development (Fig. S6F).

Together these experiments demonstrate that expression of the hdCK3mut reporter gene has no observable selective disadvantage on hematopoietic cell engraftment and expansion capacity in a mouse HSC transplantation model.

**hdCK3mut Mouse HSCs Persist *In Vivo* Allowing Long-Term Monitoring of Therapeutic Cell Transplantation.** Long-term effects from the expression of human nucleoside reporters are poorly defined. Potential concerns include selective vector silencing or counterselection of reporter-labeled cells over time.

We examined whether reporter cells in BMT-recipient mice retained the PET reporter function through serial imaging *in vivo*. Consecutive scans and peripheral blood analysis were obtained at 4, 15, 27, and 32 wk post-BMT allowing for detection of both short- and long-lived reporter HSCs (27, 28).

At 32 wk post-BMT hdCK3mut reporter-specific signal was detected within the spleen and bone marrow, demonstrating long-term engraftment capability of reporter-labeled hematopoietic cells (Fig. 3B). Previous scans of the same animals demonstrated similar signal at 15 and 27 wk (Fig. S7). Serial detection of hdCK3mut through PET/CT reveals that the reporter gene functions through hematopoiesis. It is hypothesized that each sequential scan is detecting different hematopoietic cells that have homed to the spleen.

Peripheral blood was collected at each time point and analyzed for CBC and reporter engraftment by flow cytometry. No significant difference was observed in the retention of circulating

reporter positive hematopoietic cells between hdCK3mut and YFP recipients. Comparison of the total white blood cell (WBC) count and hematocrit were normal and equivalent between both hdCK3mut and YFP after BMT (Fig. 3C). Peripheral WBC differential demonstrated that at both early and late engraftment the distribution of WBC subtypes were consistent between both groups (Fig. 3D).

Reporter-labeled bone marrow transduced with YFP or hdCK3mut was able to successfully rescue lethally irradiated recipient animals. Long-term monitoring determined there was no survival disadvantage for hdCK3mut recipients over YFP as indicated in a Kaplan–Meier survival curve (Fig. 3E). Collectively these experiments demonstrate that expression of hdCK3mut is an inert reporter gene capable of long-term noninvasive tracking method throughout the recipients' lifespan.

**hdCK3mut Allows for Noninvasive Detection of Human HSC Engraftment.** Probe retention in reporter-labeled cells is dependent upon transport of the radio-labeled probe intracellularly with sequential phosphorylation by hdCK3mut. Although mice and humans have similar nucleoside transporters, total expression or variation based on cell lineage may differ between species (31, 32). A humanized xenotransplantation model was used to validate that hdCK3mut would function as a reporter in human HSCs. Human hematopoiesis occurs within the spleen, bone marrow, and thymus of NSG mice when transplanted as neonates providing a tool to study *in vivo* human HSC differentiation (33). Isolated CD34<sup>+</sup> cord blood HSCs were transduced with hdCK3mut or control lentiviral vectors (Fig. S1B) and transplanted into sublethally irradiated neonate NSG recipient animals (Fig. 4A). When transplanted as neonates CD34<sup>+</sup> cells engraft and expand within multiple tissues

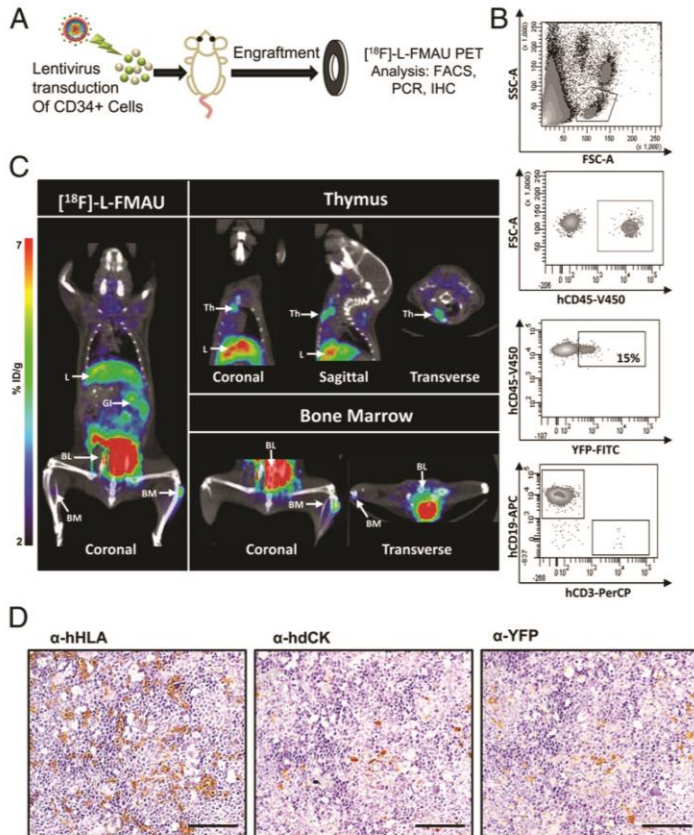


**Fig. 4.** hdCK3mut allows for noninvasive detection of human HSC engraftment. (A) Schematic of human HSC xenotransplantation. CD34<sup>+</sup> cells from cord blood donors are transduced with lentivirus. Sublethally irradiated neonate NSG recipients are intrahepatically transplanted. (B) FACS plots for total human engraftment at 8 wk posttransplantation. hCD45 denotes total human cells, reporter cells are detected by YFP<sup>+</sup>. (C) [<sup>18</sup>F]-L-FMAU MicroPET detects human hematopoietic cells expressing hdCK3mut within the bone marrow (BM) and thymus (Th). Background signal from probe metabolism is seen in liver (L), gastrointestinal (GI) with probe clearance through the bladder (BL). NSG mice displayed higher probe background compared with C57Bl6 animals seen by increased nonspecific liver signal. (D) IHC detects hdCK3mut-labeled human hematopoietic cells within the spleen. Total engraftment detected with α-hHLA, reporter cells detected by α-hdCK and α-YFP. (Scale bar, 100 μm.)

and can home to the empty NSG thymus. These mice develop partial human hematopoietic systems with mature human myeloid, T-, and B cells.

At 8 wk post human HSC transplantation peripheral blood analysis detected hdCK3mut reporter human engraftment by flow cytometry (Fig. 4B). Peripheral blood mononuclear cells (PBMCs) were stained for human CD45 to detect total human engraftment. Additional markers were used to detect human myeloid, B-cell, T-cell, and YFP for reporter-labeled cells. MicroPET scans with [<sup>18</sup>F]-L-FMAU detected hdCK3mut cells within the thymus and bone marrow of chimeric recipient mice (Fig. 4C). This demonstrates that human cells labeled with hdCK3mut retain expression of the reporter and are capable of engrafting after transplantation.

IHC analysis of human HSC engraftment in the spleen and thymus was performed at the experimental endpoint (Fig. 4D and Fig. S8). Total human engraftment was detected with human-specific HLA staining. Sequential sections verified reporter positive cells by anti-dCK and anti-YFP staining. Anti-dCK IHC in the spleen stained a fraction of the total engrafted human cells, consistent with the peripheral blood FACS (Fig. 4B), which revealed ~15% of human cells that were reporter positive based on YFP expression (Fig. 4D). This supports the hypothesis that human hematopoietic cell maturation and homing is retained in cells expressing hdCK3mut.

**Overlapping Integration Sites in hdCK3mut-Labeled Human Hematopoietic Cells Defines a Common Cell of Origin with Multilineage Differentiation Capacity in Vivo.** A concern of gene therapy trials for the correction of inherited diseases is the potential for insertional mutagenesis that has been observed in rare cases (34). Vector integration within tumor suppressors, near the transcriptional start site of oncogenes, or at sites that alter cell function are potential complications when using viral integration methods. Integration of lentiviral vectors is less likely to cause oncogenic transformation that was previously seen with other retroviral vectors (35). Recent studies have focused on identifying integration sites of modified hHSCs to detect potential problems such as dominant clonal expansion or lineage restriction (36,37). Integration site analysis on long-term engrafted human chimeric mice was used to determine if expression and integration of hdCK3mut resulted in an abnormal event.

Cells were sorted from the spleens of engrafted animals into three lineages based on human CD33, CD3, or CD19 expression. Total genomic DNA was isolated and sequences flanking the vector integration sites were amplified by using common primers within the LTRs. Short primers were then ligated to the 3' end of all amplified DNA allowing uniform ends of all fragments. A second PCR amplification was then performed to attach unique barcode sequences to the 3' end. This allows multiple samples to be sequenced together and each sample to be precisely identified. Pooled samples underwent paired-end 50-nt Illumina sequencing to identify the unique integration site. Results were then aligned against genomic DNA to identify the exact integration location. Comparison of myeloid, B- and T-cell integrations were analyzed for each animal identifying individual and overlapping integrations (Fig. 5A).

Lineage-specific integrations identified committed progenitor cells. Integration sites found in all three populations are derived from a common transduced cell of origin (HSC) which then differentiated into all lineages (Fig. 5B-D). Previous vector copy number per cell was determined by PCR to be ~0.5 (0.485, hdCK3mut; 0.494, YFP) after transduction. It is estimated that each HSC integration site represents a single engrafted clone.

A comparison of the total number of integrations from each sample in hdCK3mut and YFP animals confirms that the number of integrations detected is similar between vectors. This demonstrates that the expression of hdCK3mut does not prevent hHSCs from differentiating into all major hematopoietic lineages within the humanized mouse model. hdCK3mut also had no effect on long-term engraftment and was detected up to 5 mo post-HSC transplant with no lineage restriction due to gene toxicity or clonal expansion due to growth advantage.

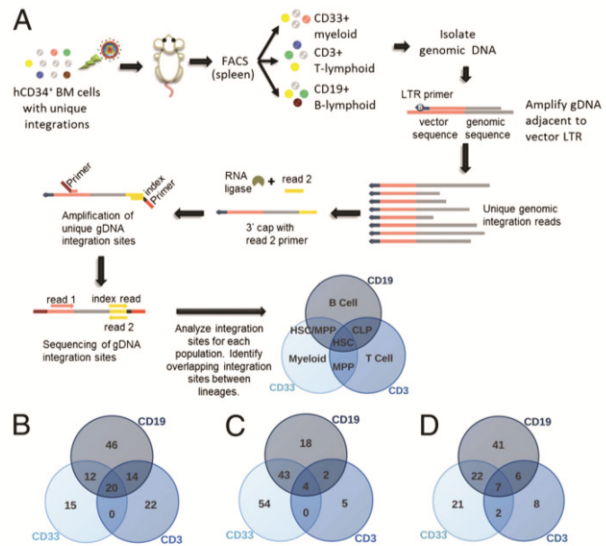


**Fig. 5.** Overlapping integration sites in hdCK3mut-labeled human hematopoietic cells defines a common cell of origin with multipotent lineage capacity in vivo. (A) Schematic of integration site analysis. Cells from the spleens of engrafted animals are sorted into three populations. DNA is amplified from the LTR and a 3' cap is attached. Unique index sequence is placed on all samples in a second amplification. Samples are sequenced, and genomic integration sites are determined. Overlapping integration sites from multiple lineages determines a common cell of origin differentiated into multiple hematopoietic lineages. (B) YFP-engrafted animal. (C and D) hdCK3mut-engrafted animals.

## Discussion

We have demonstrated that an alternate dCK mutant (hdCK3mut) is well-tolerated, highly sensitive, and capable of monitoring long-term HSC engraftment.

**Expression of HSV1-TK After Gene Transfer Provides a Safety Mechanism in Aberrant Reporter Cell Populations Through Reporter-Specific Cytotoxicity (38, 39).** hdCK3mut provides an alternative PET reporter gene to sr39TK. One concern for alternate reporters is the loss of suicide gene function, which is gained when HSV1-TK and mutants are used (40). Gene transfer of HSV1-TK into select cell populations allowed for targeted cytotoxicity when treated with FDA-approved acycloguanosine-based antiviral drugs such as ganciclovir (41). This eliminates all cells expressing the reporter with limited off-target cytotoxicity (38). A limitation in HSV1-TK expression is that prophylaxis treatment with acycloguanosine antivirals to minimize cytomegalovirus infection in immunocompromised individuals cannot be administered without potentially eliminating the donor cells (42).

In previous studies, hdCK3mut also exhibited higher substrate specificity for several chemotherapeutic and antiviral nucleoside analogs in comparison with wild-type dCK (18–20). hdCK3mut had a higher activity with gemcitabine (2',2'-difluorodeoxycytidine, dFdC) with little activity toward acycloguanosine drugs. dFdC is an FDA-approved chemotherapeutic that works through self-potential in the diphosphate and triphosphate forms (43). The triphosphate form is then incorporated into DNA, causing chain termination. Treatment with drugs that have a higher affinity for hdCK3mut may allow a targeted suicide gene therapy. Proper in vivo models will need to be tested to validate hdCK3mut enhanced sensitivity and to evaluate the off-target effects from treatment.

**Evaluating the Potential Immunogenicity of hdCK3mut in Short-Term Therapeutic Cell Transplants.** Before transitioning hdCK3mut into a clinical PET reporter for stem cell or long-term therapeutic

transplants experimental short-lived transplanted cells need to be investigated. The immunogenicity of HSV1-TK was found when reporter-labeled lymphocytes caused a CD8 immune response selectively killing reporter cells (8–10). A similar study could determine if expression of hdCK3mut will cause an immune response.

hdCK3mut contains only three point mutations and is expected to not cause an immunogenic epitope for MHC class I presentation. Using a predictive software for MHC class I presentation (44), hdCK3mut has only one additional peptide fragment, which is predicted to be different from WT hdCK. This peptide, which incorporates the mutated amino acid methionine at position 104, could use the methionine as an anchoring residue within the MHC (45). All other amino acids that are displayed in the MHC are natural, and therefore the peptide fragments displayed from hdCK3mut are predicted to be recognized as “self” avoiding immune cell detection.

**Summary.** We demonstrate how long-term follow-up of transplanted cells can be managed noninvasively by using reporter PET imaging. This study provides a comprehensive analysis on the inert

biological effect of hdCK3mut on hematopoietic cells. Therefore, it is anticipated that hdCK3mut monitoring will provide a safe and effective mechanism for longitudinal monitoring of a broad range of transplanted cells.

## Materials and Methods

Detailed information on animals, constructs and cloning, cell lines, uptake assays, enzyme kinetic assay, grafts, mouse HSC transplant, human HSC transplant, MicroPET imaging, peripheral blood analysis, FACS, methylcellulose assay, antibodies, Western blot, IHC, integration site analysis, and statistics can be found in *SI Materials and Methods*.

**ACKNOWLEDGMENTS.** We thank Dr. Nagichettiar Satyamurthy and Jeffery Collins for the radiosynthesis of [<sup>18</sup>F]-FDG and [<sup>18</sup>F]-L-FMAU and Dr. Waldemar Lando, Dr. David Stout, and Darrin Williams in the Crump Institute for Molecular Imaging facility for their technical help with PET/CT scans. M.N.M. is supported by California Institute for Regenerative Medicine Training Grant TG2-01169. E.H.G. is supported by Eli and Edythe Broad Center of Regenerative Medicine and Stem Cell Research at UCLA. A.R.C. is supported by a Philip Whitcome training grant. C.N. is supported by the California Institute for Regenerative Medicine Bridges Training Program. O.N.W. is supported by a California Institute for Regenerative Medicine Tools/Technology Award RT1-01126. O.N.W. is an Investigator of the Howard Hughes Medical Institute.

- Sng J, Lufkin T (2012) Emerging stem cell therapies: Treatment, safety, and biology. *Stem Cells Int* 2(12):521343.
- Herschman HR (2004) PET reporter genes for noninvasive imaging of gene therapy, cell tracking and transgenic analysis. *Crit Rev Oncol Hematol* 51(3):191–204.
- Serganova I, Ponomarev V, Blasberg R (2007) Human reporter genes: Potential use in clinical studies. *Nucl Med Biol* 34(7):791–807.
- Gyurkocza B, Rezvani A, Storb RF (2010) Allogeneic hematopoietic cell transplantation: The state of the art. *Expert Rev Hematol* 3(3):285–299.
- Kohn DB (2010) Update on gene therapy for immunodeficiencies. *Clin Immunol* 135(2):247–254.
- Gambhir SS, et al. (2000) A mutant herpes simplex virus type 1 thymidine kinase reporter gene shows improved sensitivity for imaging reporter gene expression with positron emission tomography. *Proc Natl Acad Sci USA* 97(6):2785–2790.
- Tjuvajev JG, et al. (1998) Imaging herpes virus thymidine kinase gene transfer and expression by positron emission tomography. *Cancer Res* 58(19):4333–4341.
- Berger C, Flowers ME, Warren EH, Riddell SR (2006) Analysis of transgene-specific immune responses that limit the in vivo persistence of adoptively transferred HSV-TK-modified donor T cells after allogeneic hematopoietic cell transplantation. *Blood* 107(6):2294–2302.
- Riddell SR, et al. (1996) T-cell mediated rejection of gene-modified HIV-specific cytotoxic T lymphocytes in HIV-infected patients. *Nat Med* 2(2):216–223.
- Traversari C, et al. (2007) The potential immunogenicity of the TK suicide gene does not prevent full clinical benefit associated with the use of TK-transduced donor lymphocytes in HSCT for hematologic malignancies. *Blood* 109(11):4708–4715.
- Mercier-Letondal P, et al. (2008) Early immune response against retrovirally transduced herpes simplex virus thymidine kinase-expressing gene-modified T cells co-infused with a T cell-depleted marrow graft: An altered immune response? *Hum Gene Ther* 19(9):937–950.
- Oliveira G, Greco R, Lupo-Stanghellini MT, Vago L, Bonini C (2012) Use of TK-cells in haploidentical hematopoietic stem cell transplantation. *Curr Opin Hematol* 19(6):427–433.
- Campbell DO, et al. (2012) Structure-guided engineering of human thymidine kinase 2 as a positron emission tomography reporter gene for enhanced phosphorylation of a non-natural thymidine analog reporter probe. *J Biol Chem* 287(1):446–454.
- Ponomarev V, et al. (2007) A human-derived reporter gene for noninvasive imaging in humans: Mitochondrial thymidine kinase type 2. *J Nucl Med* 48(5):819–826.
- Likar Y, et al. (2010) A new pyrimidine-specific reporter gene: A mutated human deoxycytidine kinase suitable for PET during treatment with acycloguanosine-based cytotoxic drugs. *J Nucl Med* 51(9):1395–1403.
- Choi O, et al. (2012) A deficiency in nucleoside salvage impairs murine lymphocyte development, homeostasis, and survival. *J Immunol* 188(8):3920–3927.
- Toy G, et al. (2010) Requirement for deoxycytidine kinase in T and B lymphocyte development. *Proc Natl Acad Sci USA* 107(12):5551–5556.
- Sabini E, Ort S, Monnerjahn C, Konrad M, Lavie A (2003) Structure of human dCK suggests strategies to improve anticancer and antiviral therapy. *Nat Struct Biol* 10(7):513–519.
- Hazra S, Sabini E, Ort S, Konrad M, Lavie A (2009) Extending thymidine kinase activity to the catalytic repertoire of human deoxycytidine kinase. *Biochemistry* 48(6):1256–1263.
- Iydogan P, Lutz S (2008) Systematic exploration of active site mutations on human deoxycytidine kinase substrate specificity. *Biochemistry* 47(16):4711–4720.
- Radu CG, et al. (2008) Molecular imaging of lymphoid organs and immune activation by positron emission tomography with a new [<sup>18</sup>F]-labeled 2'-deoxycytidine analog. *Nat Med* 14(7):783–788.
- Austin WR, et al. (2012) Nucleoside salvage pathway kinases regulate hematopoiesis by linking nucleotide metabolism with replication stress. *J Exp Med* 209(12):2215–2228.
- Jordheim LP, et al. (2004) Characterization of a gemcitabine-resistant murine leukemic cell line: Reversion of in vitro resistance by a mononucleotide prodrug. *Clin Cancer Res* 10(16):5614–5621.
- Baum C, et al. (2003) Side effects of retroviral gene transfer into hematopoietic stem cells. *Blood* 101(6):2099–2114.
- Drize N, Chertkov J, Sadovnikova E, Tiessen S, Zander A (1997) Long-term maintenance of hematopoiesis in irradiated mice by retrovirally transduced peripheral blood stem cells. *Blood* 89(5):1811–1817.
- Stewart FM, Crittenden RB, Lowry PA, Pearson-White S, Quesenberry PJ (1993) Long-term engraftment of normal and post-5-fluorouracil murine marrow into normal nonmyeloablated mice. *Blood* 81(10):2566–2571.
- Kang E, et al. (2001) In vivo persistence of retrovirally transduced murine long-term repopulating cells is not limited by expression of foreign gene products in the fully or minimally myeloablated setting. *Hum Gene Ther* 12(13):1663–1672.
- Zavidij O, et al. (2012) Stable long-term blood formation by stem cells in murine steady-state hematopoiesis. *Stem Cells* 30(9):1961–1970.
- Gambhir SS, et al. (2000) Imaging transgene expression with radionuclide imaging technologies. *Neoplasia* 2(1–2):118–138.
- Hallek M, Wanders L, Strohmeyer S, Emmerich B (1992) Thymidine kinase: a Tumor marker with prognostic value for non-Hodgkin's lymphoma and a broad range of potential clinical applications. *Ann Hematol* 65(1):1–5.
- Baldwin SA, et al. (2004) The equilibrative nucleoside transporter family, SLC29. *Pflugers Arch* 447(5):735–743.
- Gray JH, Owen RP, Giacomini KM (2004) The concentrative nucleoside transporter family, SLC28. *Pflugers Arch* 447(5):728–734.
- Park CY, Majeti R, Weissman IL (2008) In vivo evaluation of human hematopoiesis through xenotransplantation of purified hematopoietic stem cells from umbilical cord blood. *Nat Protoc* 3(12):1932–1940.
- Corrigan-Curay J, et al. (2012) Challenges in vector and trial design using retroviral vectors for long-term gene correction in hematopoietic stem cell gene therapy. *Mol Ther* 20(6):1084–1094.
- Biffi A, et al. (2011) Lentiviral vector common integration sites in preclinical models and a clinical trial reflect a benign integration bias and not oncogenic selection. *Blood* 117(20):5332–5339.
- Gonzalez-Murillo A, Lozano ML, Montini E, Bueren JA, Guenechea G (2008) Unaltered repopulation properties of mouse hematopoietic stem cells transduced with lentiviral vectors. *Blood* 112(8):3138–3147.
- Ronen K, et al. (2011) Distribution of lentiviral vector integration sites in mice following therapeutic gene transfer to treat  $\beta$ -thalassemia. *Mol Ther* 19(7):1273–1286.
- Bonini C, et al. (1997) HSV-TK gene transfer into donor lymphocytes for control of allogeneic graft-versus-leukemia. *Science* 276(5319):1719–1724.
- Ciceri F, et al. (2007) Antitumor effects of HSV-TK-engineered donor lymphocytes after allogeneic stem-cell transplantation. *Blood* 109(11):4698–4707.
- Lupo-Stanghellini MT, et al. (2010) Clinical impact of suicide gene therapy in allogeneic hematopoietic stem cell transplantation. *Hum Gene Ther* 21(3):241–250.
- Tiberghien P, et al. (1994) Ganciclovir treatment of herpes simplex thymidine kinase-transduced primary T lymphocytes: An approach for specific in vivo donor T-cell depletion after bone marrow transplantation? *Blood* 84(4):1333–1341.
- Hébrard C, Dumontet C, Jordheim LP (2009) Development of gene therapy in association with clinically used cytotoxic deoxynucleoside analogues. *Cancer Gene Ther* 16(7):541–550.
- Burris HA, 3rd, et al. (1997) Improvements in survival and clinical benefit with gemcitabine as first-line therapy for patients with advanced pancreas cancer: A randomized trial. *J Clin Oncol* 15(6):2403–2413.
- Hakenberg J, et al. (2003) MAPP: MHC class I antigenic peptide processing prediction. *Appl Bioinformatics* 2(3):155–158.
- Reche PA, Glutting JP, Reinherz EL (2002) Prediction of MHC class I binding peptides using profile motifs. *Hum Immunol* 63(9):701–709.

# Supporting Information

McCracken et al. 10.1073/pnas.1221840110

## SI Materials and Methods

**Animals.** Immunocompetent C57BL/6 and C57BL/6 SJL female mice and immunodeficient NOD.Cg-Prkdc<sup>scid</sup> Il2rg<sup>tm1Wjl</sup>/SzJ (NSG) mice were bred and maintained according to the guidelines of the Department of Laboratory Animal Medicine (DLAM) at the University of California, Los Angeles. All animal studies were carried out by using protocols that had been approved by DLAM.

**Constructs and Cloning.** Codon optimized human deoxycytidine kinase (hdCK) sequence was purchased from DNA 2.0. PCR amplification added EcoRI and XhoI restriction sites. hdCK was then placed in murine stem cell virus (pMSCV) vector ahead of an internal ribosomal entry site (IRES) and yellow fluorescent protein (YFP). Amino acid mutations were made by multisite-directed mutagenesis (Stratagene) at the following locations: A100V, R104M, and D133A. A lentiviral vector (2F-X, pCCL based) was constructed for infection of human HSCs. hdCK3mut-IRES-YFP was cut from MSCV, and BamHI sites were added by phosphate linkers. 2F-X was digested with BamHI and hdCK3mut-IRES-YFP was ligated into the vector. Helper plasmids for making ectropic retrovirus was PCL-II. Third-generation nonreplicating lentiviral helper plasmids were used (VSVg, PREV, and PMDL).

**Cell Lines.** L1210 and L1210-10K mouse leukemia cell lines were a gift from Charles Dumontet (Université Claude Bernard Lyon I, Lyon, France). All stable cell lines were made with retroviral transduction with ectropic packaging of pMSCV constructs. Cell lines were sorted to equal expression of YFP by FACS and grown in cell-specific media conditions.

**In Vitro Uptake Assay.** Suspension cell lines: 100,000 cells in 100  $\mu$ L media were plated in triplicate in a 0.22 micron filter bottom plates. 3H-probe was diluted to 5  $\mu$ Ci/mL in media. A total of 100  $\mu$ L (0.5  $\mu$ Ci) was added per well. Cells were incubated at 37 °C for 1 h, washed five times, and dried. Scintillation fluid was added and counted for counts per minute (cpm) for 1 min on a BetaMax plate reader (PerkinElmer).

**Recombinant Protein Production.** For bacterial expression of His-tagged human dCK, 5' and 3' primers (5'-CATGGATCCATGGCCACCCCGCCCAAGAG-3' and 5'-GTAGGTACCTCACAAAGTACTCAAAAACCTCTTTGACCTTTTC-3') were designed introducing BamHI and KpnI sites for cloning into pQE-80L vector (Qiagen). TOP10 bacteria were transformed with pQE-80L-hdCK3mut, dCKDM, or hdCK. A single colony was used for an overnight starter culture. A large-scale 1-L culture was inoculated and induced at OD<sub>600</sub>: 0.6 with isopropylthio- $\beta$ -galactoside (IPTG) to 1 mM. Cells were harvested 4 h later and cleared lysate was prepared according to Qiagen instructions. Lysate was combined with 1 mL bed volume Ni-NTA agarose and transferred to a 20-mL column. Beads were washed extensively and eluted in PBS 150 mM NaCl, 250 mM imidazole, 5% (wt/vol) glucose.

**Enzyme Kinetic Assay.** A coupled spectrophotometric kinase assay was adapted to determine kinetics for L-FMAU (1). Reads were performed in ~30-s intervals at 37 °C for 30 min. An NADH standard curve was constructed. Nonlinear regression analysis and Michaelis-Menten plots determined the  $K_m$  values.

**Grafts.** Cells were counted, washed, and resuspended in a 1:1 mixture of sterile RPMI and Matrigel. Each graft contained  $2 \times 10^5$  cells in 100  $\mu$ L total volume. Grafts were implanted s.c. in 6- to 8-wk-old female NSG mice. [<sup>18</sup>F]-FDG (2-deoxy-2-<sup>18</sup>fluoro-

D-glucose) was performed on day 7 or 8, with sequential [<sup>18</sup>F]-L-FMAU (1-(2-deoxy-2-<sup>18</sup>fluoro- $\beta$ -L-arabinofuranosyl)-5-methyluracil) scans on day 8 or 9 depending on tumor growth rate. Grafts were removed after [<sup>18</sup>F]-L-FMAU imaging, weighed, and total cpm/g was determined by the amount of radioactivity in each graft measured using a Wallac Wizard 3" 1480 Automatic Gamma Counter (PerkinElmer).

**Mouse HSC Transplant.** Six- to 10-wk-old C57BL/6 SJL mice were injected i.v. with 150 mg/kg 5-fluorouracil (APP Pharmaceuticals). BM was harvested 5 d after treatment and cultured with IL-3 (6 ng/mL), IL-6 (10 ng/mL), stem cell factor (SCF) (100 ng/mL), and 5% (vol/vol) conditioned media from WeHI-3 cells (WeHI) as growth factors. After 24 h, the cells were infected with Murine Stem Cell Viruses (MSCV), MSCV-hdCK3mut-IRES-YFP or MSCV-IRES-YFP and 1.6  $\mu$ g/mL of polybrene under spin conditions (2,500 rpm, 90 min, 30 °C, Beckman CS-6R centrifuge) and then incubated overnight at 37 °C. Cells were superinfected the next day, washed, and counted for total cell number. Six- to 8-wk-old C57BL/6 mice were lethally irradiated (900 rad) before i.v. injection of  $5 \times 10^5$  transduced BM cells on the same day. Each population was ~40–60% transduced, with each animal transplanted with a mixed population of reporter and nonreporter cells.

**Human HSC Transplant.** Hematopoietic stem and progenitor cells were enriched from Ficoll fractionated cord blood or bone marrow with CD34+MACS beads (Miltenyi). Cells were thawed and prestimulated for 24 h in RetroNectin (TaKaRa)-coated nontissue culture treated 24-well plates (Falcon) in X-VIVO 15 medium (Lonza) containing SCF (50 ng/mL), fms-like tyrosine kinase-3 (Flt-3) ligand (50 ng/mL), Thrombopoietin (TPO) (50 ng/mL), and IL-3 (20 ng/mL). The next day, cells were transduced at a lentiviral vector concentration of  $2 \times 10^8$  transduction units/mL. Cells were injected 24 h after transduction. Neonatal (1-3 days old) NOD.Cg-Prkdc<sup>scid</sup> Il2rg<sup>tm1Wjl</sup>/SzJ mice were conditioned with 150 cGy total body irradiation. Twenty-four hours postconditioning, mice were injected intrahepatically with CD34<sup>+</sup>-enriched cord blood or bone marrow cells at a dose of  $3 \times 10^5$  cells in 50  $\mu$ L of medium.

**Anti-hdCK Antibody Generation.** Six His-tagged human dCK was produced in bacteria, purified by Ni-NTA (nickel-nitrilotriacetic acid) resin chromatography and used as immunogen. Four mice (BALB/c females 6–8 wk) were immunized by i.p. injection of 200  $\mu$ g 6 His-hdCK in RIBI adjuvant (Sigma) followed by four monthly boosts of 100  $\mu$ g immunogen i.p. in RIBI. Antibody titer was determined in the serum by ELISA. Spleen of the highest titer mouse was excised and dissociated. Isolated splenocytes were fused to the myeloma cell line sp2/0 at a ratio of 5:1 splenocytes/myeloma using PEG1500 (Roche). Twenty percent of fusion was plated in hypoxanthine-aminopterin-thymidine medium (HAT medium) onto 10 $\times$  flat bottom 96-well plates at 200  $\mu$ L/well, the remaining fusion was frozen down. Fusion was cultured until clones appeared in the wells and covered 25–50% of well. Supernatant was collected and ELISA performed: 96-well flat bottom assay plates (Nunc Maxisorp) were coated with 10  $\mu$ g/ $\mu$ L immunogen, blocked with PBS 1% (wt/vol) BSA. Supernatants were applied to wells, goat antimouse HRP was used to detect binding, and reaction was developed with 2,2'-Azinobis [3-ethylbenzothiazoline-6-sulfonic acid]-diammonium salt (ABTS). Positive wells were replated in 24-well plates in hypoxanthine-thymidine

(HT) medium. ELISA was repeated on previously positive wells when cultures got 50% confluent. Positive supernatants were tested for ability to detect immunogen by Western blot at 1:10 dilution in PBST-5% (wt/vol) milk. Positive wells were subcloned by limiting dilution to obtain single clones per well in 96-well flat bottom plates. Subclones were tested by ELISA and highest positives were tested on Western blot. Clones were tested for IHC staining ability and clone 9D4 (plate 9 well D4) was determined to be the best in overall performance. Preparative amounts of antibody were produced in CELLline-1000 flasks (Integra Bioscience) and purified by affinity chromatography (protein G sepharose, Prosep-G; Millipore). Anti-dCK clone 9D4 is now commercially available with Millipore.

**Antibodies and Western Blot.** A total of 20 µg of total cell lysate in RIPA buffer was run on SDS/PAGE using Precise Tris-Hepes protein gels, 4–20%. Gels were transferred onto 0.22 micron nitrocellulose and blocked for 1 h at room temperature in 5% (wt/vol) milk in PBS with 0.05% Tween. Antibodies were diluted in 5% (wt/vol) milk in PBS with 0.05% Tween as follows: dCK (Witte Laboratory-9D4, see *SI Materials and Methods*; Millipore) 1:1,000, YFP (Witte Lab, polyclonal rAb) 1:5,000, ERK2 (Santa Cruz; SC-154) 1:5,000, goat antimouse IgG HRP (Bio-Rad; 172–1011) 1:10,000, goat antirabbit IgG HRP (Bio-Rad; 170–6515) 1:15,000. ECL substrate (Millipore) was used for detection and development on GE/Amersham film.

**Immunohistochemistry.** Tissue was fixed in 10% phosphate-buffered formalin overnight. Sections were fixed in paraffin and cut at 0.4 µm, with staining for hematoxylin and eosin for representative histology every five slides. Tissue sections were heated at 65 °C for 1 h to melt the paraffin followed by rehydration. Antigen retrieval was performed using citric acid buffer and visualization was performed using a liquid DAB<sup>+</sup> kit (Dako). Slides were blocked for endogenous peroxidase activity with 3% (vol/vol) H<sub>2</sub>O<sub>2</sub> in PBS for 5 min, then blocked for mouse IgG by using Vector Labs Mouse-on-Mouse (M.O.M.) kit (BMK-2202). Primary antibodies were diluted with M.O.M. diluent as follows: dCK (Witte Lab-94D, 1:2,000), YFP (Witte Lab-Mouse Monoclonal, 1:200), HLA (Santa Cruz; 1:100), mouse IgG (Santa Cruz; 0.4 µg/µL), and incubated at 4 °C overnight. Secondary antibody was added (ImmPRESS antimouse Ig (peroxidase) Polymer Detection kit).

**Flow Cytometry and Fluorescent-Activated Cell Sorting.** Single-cell suspensions from spleen, thymus, bone marrow, and peripheral blood were stained with the following fluorochrome-conjugated antibodies: anti-CD45.1, anti-CD4, anti-CD8, anti-Ter119, anti-CD71, anti-CD11b, anti-GR1, anti-B220, anti-CD19, anti-IgM, anti-CD43, and Hoechst for cell cycle analysis. Human engraftment was monitored with the following fluorochrome-conjugated antibodies: anti-hCD45, anti-hCD3, anti-hCD19, and anti-hCD33. In all reporter BM chimera animals, reporter-labeled cells were defined as YFP (FITC channel) positive. Cell sorting was performed on the FACSAria automated cell sorter (BD Biosciences), and flow cytometry was performed on the BD FACScanto II.

**MicroPET and Image Analysis.** Mice were warmed under gas anesthesia (2% (vol/vol) isoflurane) and injected i.v. with 200 µCi of either [<sup>18</sup>F]-FDG or [<sup>18</sup>F]-L-FMAU (radiochemical synthesis described in ref. 2), followed by 1-h unconscious or 3-h conscious uptake. Mice were then positioned in an imaging chamber for sequential imaging with the Siemens Preclinical Solutions MicroPET Focus 220 and MicroCAT II CT systems (Siemens). MicroPET data were acquired for 10 min and reconstructed with a filtered background projection probability algorithm. MicroPET and CT images were coregistered. Quantification of PET signal was performed by drawing 3D region of interests (ROIs) around the area of interest using AMIDE software ([\[sourceforge.net/\]\(http://sourceforge.net/\)\). The mean intensity of the ROI, based on the percent injected dose per gram, was normalized to control grafts of L1210-10K ROI drawn around untransduced grafts in the same animal. Data are presented as fold change over L1210-10K grafts. Images are presented here using a false-color scale that is proportional to tissue concentration \(% injected dose/gram, %ID/g\) of positron-labeled probe. Red represents the highest with yellow, green, and blue corresponding to lower concentrations.](http://amide.</a></p></div><div data-bbox=)

**In Vivo Uptake Assay.** BM chimera animals were placed under anesthesia with 2% (vol/vol) isoflurane in heated chambers. One microcurie of [<sup>18</sup>F]-L-FMAU was injected i.v. with 1-h unconscious probe uptake. Animals were euthanized and spleen, femur, tibia, and thymus were removed. Cells were then dissociated into single cell suspension and stained for CD45.1. In each tissue 200,000 cells of CD45.1, YFP<sup>+</sup> (donor and reporter labeled), or CD45.1 (donor) were sorted. The amount of radioactivity in each cell type was measured using a Wallac Wizard 3-Inch 1480 Automatic Gamma Counter (PerkinElmer).

**Peripheral Blood Analysis.** Peripheral blood was collected through serial retroorbital bleeds into Capiject EDTA collection tubes (T-MQK). Complete blood counts were performed by Department of Laboratory Animal Medicine, University of California, Los Angeles core laboratory with Hemavet. Engraftment was determined by flow cytometry.

**Methylcellulose Assay.** One hdCK3mut and one YFP BM chimera animal 6 wk posttransplant were compared with a wild-type SJL (B6.SJL-Ptprc) mouse for each experiment in three independent experiments. Bone marrow from both femurs and tibia was extracted. Total bone marrow was plated in duplicate. FACS was used to isolate donor cells through sorting CD45.1 positive and YFP (reporter) positive or YFP negative; cells were plated in duplicate. Commercial methylcellulose for CFC was used (R&D Systems). Colonies were analyzed on day 11, and fluorescent analysis was analyzed by flow cytometry.

**Integration Site Analysis.** DNA was isolated from FACS-sorted cells using the PureLink Genomic DNA Mini kit (Invitrogen). Dependent on availability, 1–100 ng of DNA was used to perform nonrestrictive linear amplification-mediated PCR (3). Briefly, 100 cycles of linear amplification were performed with primer HIV3linear (biotin-AGTAGTGTGTGCCCGTCTGT). Linear reactions were purified using 1.5 volumes of AMPure XP beads (Beckman Genomics) and captured onto M-280 streptavidin Dynabeads (Invitrogen Dynal). Captured single strand DNA was ligated to read 2 linker (Phos-AGATCGGAAGAGCACACGTCTGAACCTCCAGTCAC-3C spacer) using CircLigase II (Epicentre) in a 10-µL reaction at 65° for 2 h. PCR was performed on these beads using primer HIV3-right (AATGATACGGCGACCACCGAGATCTACACTGATCCCTCAGACCCCTTTAGTC) and an appropriate indexed reverse primer (CAAGCAGAAGACGGCATACGAGAT-index-GTGACTGGAGTTCAGACGTGT). PCR products were mixed and quantified by probe-based qPCR and appropriate amounts were used to load Illumina v3 flow cells. Paired-end 50-bp sequencing was performed on an Illumina HiSeq 2000 instrument using a custom read 1 primer (CCCTCAGACCCCTTTAGTC-AGTGTGGAAAATCTCTAGCA). Reads were aligned to the hg19 build of the human genome with Bowtie (4) and alignments were condensed and annotated using custom Perl and Python scripts to locate vector integrations. A custom Python script was written to assess for overlapping integration sites between different samples, and a conservative estimate of 5% FACS sorting impurity was used to set a cutoff to eliminate overlaps with technical causes.

**Graphs, Statistics, and Survival Analysis.** Graphs are plotted as mean with SE of mean (SEM) for error bars. Statistics were analyzed

using a Student's nonpaired *t* test. Survival analysis was plotted in Graphpad and determined based on overall length of animal

survival. (Two animals were excluded from survival analysis due to premature death caused from malocclusion.)

- lyidogan P, Lutz S (2008) Systematic exploration of active site mutations on human deoxycytidine kinase substrate specificity. *Biochemistry* 47(16):4711–4720.
- Campbell DO, et al. (2012) Structure-guided engineering of human thymidine kinase 2 as a positron emission tomography reporter gene for enhanced phosphorylation of a non-natural thymidine analog reporter probe. *J Biol Chem* 287(1):446–454.
- Paruzynski A, et al. (2010) Genome-wide high-throughput integrome analyses by nrLAM-PCR and next-generation sequencing. *Nat Protoc* 5(8):1379–1395.
- Langmead B, Schatz MC, Lin J, Pop M, Salzberg SL (2009) Searching for SNPs with cloud computing. *Genome Biol* 10(11):R134.

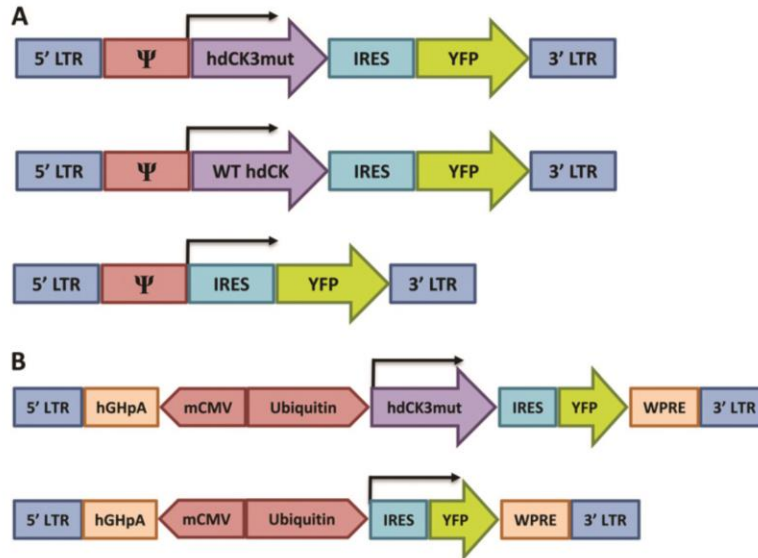


**Fig. S1.** (A) Vector maps of pMSCV retroviruses used in generating stable ectopic expressing L1210-10K cell lines, and mouse HSC experiments. (B) 2F-X lentivirus vector maps used in human HSC experiments.

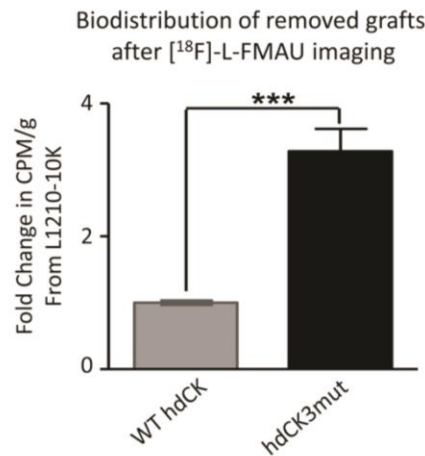


**Fig. S2.** Grafts were excised after [<sup>18</sup>F]-L-FMAU MicroPET and were weighed and placed in a gamma counter. Counts were normalized to counts per minute per gram (cpm/g) and compared with nontransduced tumors for background cpm (*P* < 0.0001).



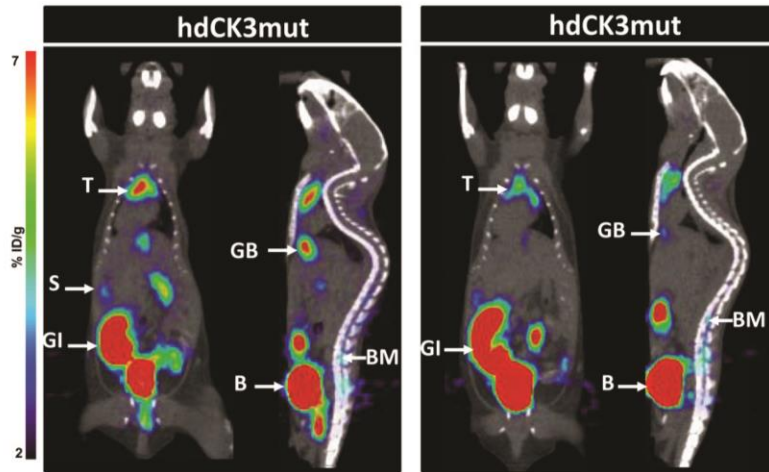


Fig. 53. Additional [ $^{18}\text{F}$ ]-L-FMAU MicroPET scans at 4 wk postmouse BMT in reporter chimeric mice.

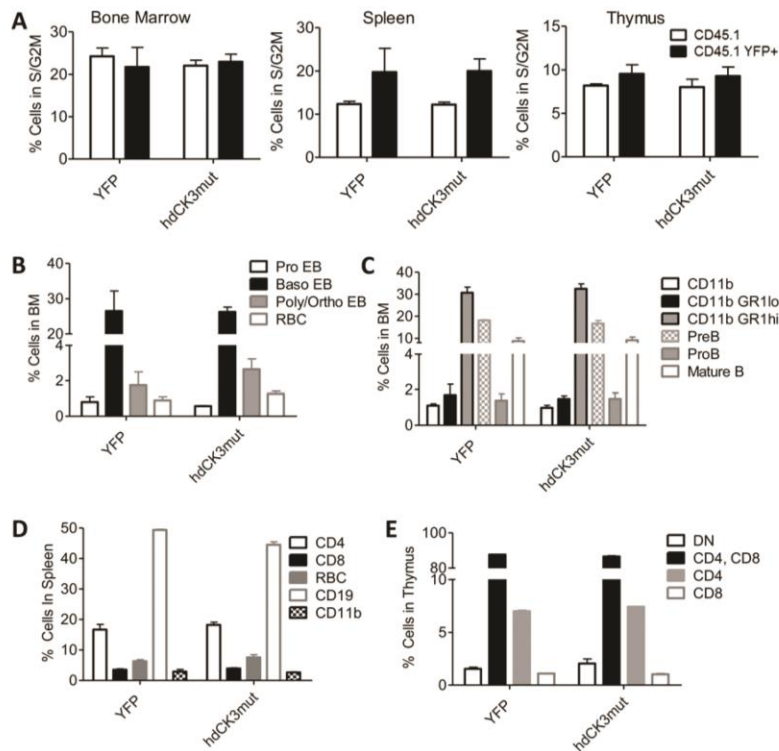
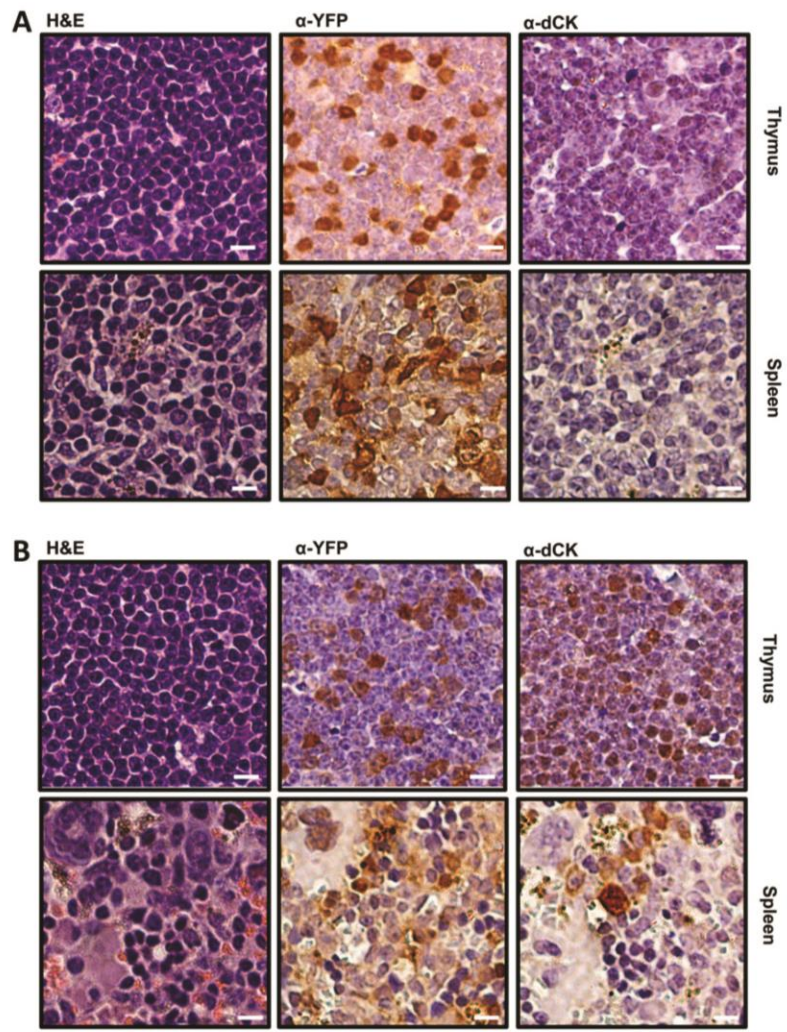
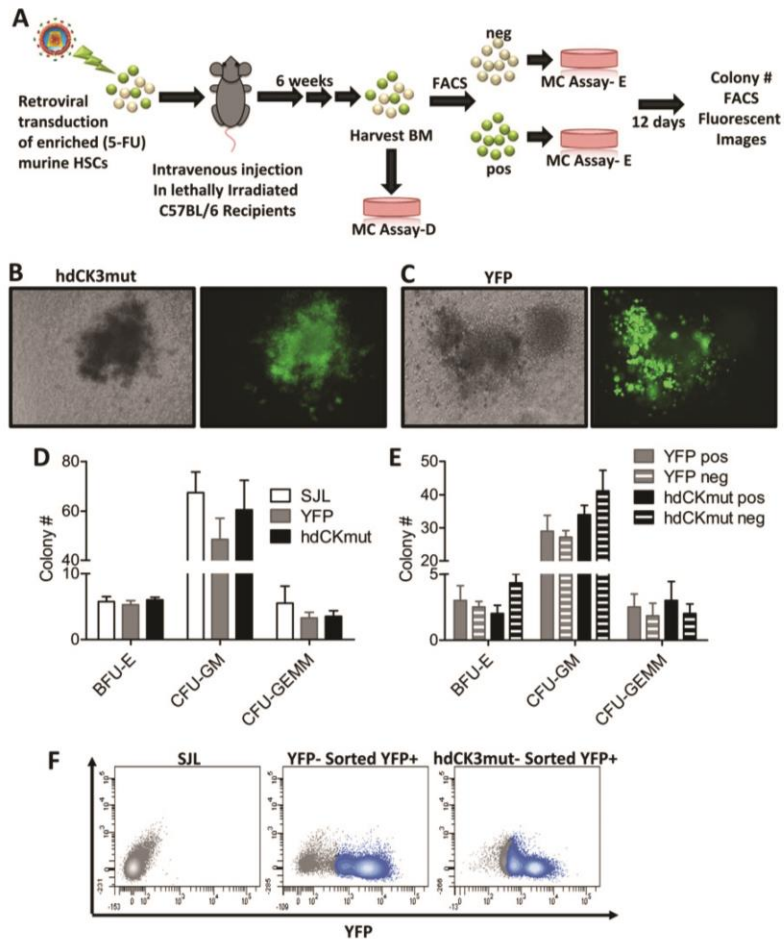


Fig. 54. Quantification of flow cytometry from hdCK3mut and YFP mHSC recipient mice. (A) Cell cycle analysis by Hoechst staining. (B and C) Analysis of bone marrow (BM) lineage distribution. (B) Red blood cell development with CD71 and Ter119 staining. Pro EB-CD71<sup>+</sup>, Ter119<sup>+</sup>; Baso EB-CD71<sup>+</sup>, Ter119<sup>+</sup>; Poly/Ortho EB-CD71 low, Ter119<sup>+</sup>; RBC-CD71<sup>-</sup>, Ter119<sup>+</sup>. (C) Myeloid and B-cell development Pre B-B220<sup>+</sup>, CD43<sup>-</sup>; Pro B-B220<sup>+</sup>, CD43<sup>+</sup>; mature B-B220<sup>+</sup>, IgM<sup>+</sup>. (D) Total engraftment within the spleen. (E) Thymus engraftment.



**Fig. 55.** IHC of mHSC recipient animals of (A) YFP and (B) hdCK3mut at 8 wk post-BMT. Spleen and thymus were analyzed for normal tissue architecture through H&E. IHC of  $\alpha$ -YFP detected vector positive cells in YFP and hdCK3mut.  $\alpha$ -dCK detected reporter cells only within hdCK3mut recipient mice. (Scale bar, 10  $\mu$ m.)



**Fig. S6.** (A) Schematic of MC assay. *hdCK3mut* or YFP recipients at 6 wk post-BMT were harvested for total bone marrow. (B and C) Representative white and fluorescent images demonstrate the normal morphology of methylcellulose colonies for *hdCK3mut* and YFP. (D) Cells were placed in a MC assay, with an aged matched normal BL6 (CD45.1). (E) Remaining bone marrow was sorted based on CD45.1 YFP<sup>+</sup> or CD45.1 YFP<sup>-</sup> and placed in MC assay. Total colonies were counted at 12 d postplating. (F) Cells from C were analyzed for retained YFP expression through flow cytometry.

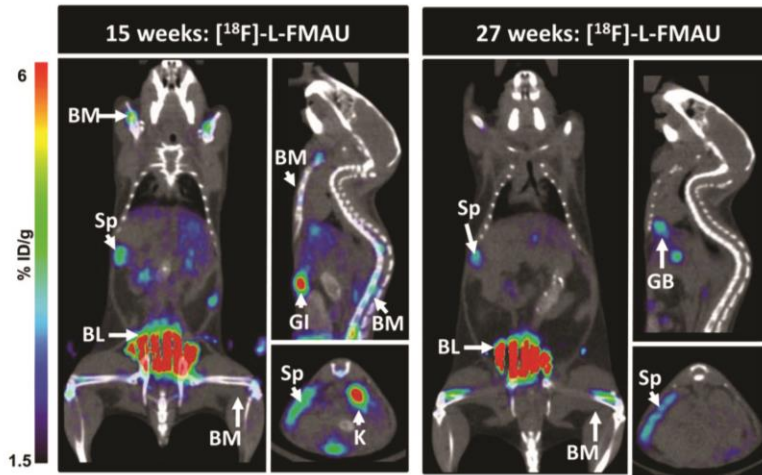


Fig. S7. Sequential scans of hdCK3mut recipient mice at 15 and 27 wk post-BMT. Reporter signal is observed within the spleen (Sp) and bone marrow (BM). Probe metabolism is seen within the kidneys (K), gallbladder (GB), and bladder (Bl).

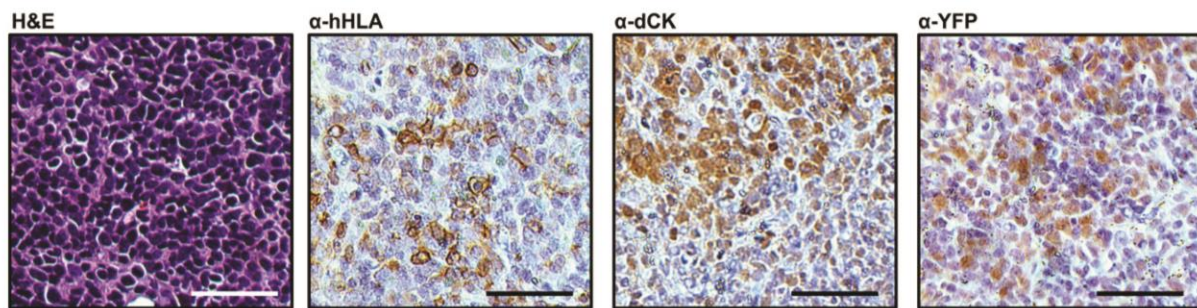


Fig. S8. IHC of hdCK3mut recipient hHSC recipient animal. Thymus was analyzed for normal tissue architecture through H&E. IHC of  $\alpha$ -hHLA detected total human engraftment.  $\alpha$ -YFP detected vector positive cells with  $\alpha$ -dCK detecting hdCK3mut reporter cells. (Scale bar, 50  $\mu$ m.)

Table S1. Enzyme kinetics for hdCK3mut and hdCKDM with L-FMAU

Enzyme	L-FMAU		
	$K_m$ ( $\mu$ M)	$V_{max}$ , nmol/min/ $\mu$ g	$R^2$
hdCK3mut	$12.681 \pm 3.893$	$0.724 \pm 0.217$	0.899
hdCKDM	$55.970 \pm 6.880$	$1.671 \pm 0.312$	0.975

Enzymatic studies were performed using His-tagged recombinant dCK in a coupled enzyme assay with LDH/PK. Values are an average of three independent experiments.

## **CHAPTER 4:**

Non-invasive detection of tumor infiltrating engineered  
T cells by human PET reporter imaging.

**TITLE: Non-invasive detection of tumor infiltrating engineered T cells by human PET reporter imaging**

**AUTHORS:** Melissa N. McCracken<sup>1</sup>, Dimitrios N. Vatakis<sup>2,3,4</sup>, Dhaval Dixit<sup>2,3,4</sup>, Jami McLaughlin<sup>5</sup>, Jerome A. Zack<sup>2,3,4,5,6</sup>, Owen N. Witte<sup>1,4,5,6,7,8</sup>

**AFFILIATIONS:**

<sup>1</sup>Department of Molecular and Medical Pharmacology, David Geffen School of Medicine, University of California, Los Angeles, CA 90095

<sup>2</sup>Departments of Medicine, Division of Hematology-Oncology, David Geffen School of Medicine, University of California, Los Angeles, CA 90095

<sup>3</sup>University of California, Los Angeles AIDS Institute

<sup>4</sup>Eli and Edythe Broad Center of Regenerative Medicine and Stem Cell Research, University of California, Los Angeles, CA 90095

<sup>5</sup>Department of Microbiology, Immunology and Molecular Genetics, University of California, Los Angeles, CA 90095

<sup>6</sup>Jonsson Comprehensive Cancer Center, David Geffen School of Medicine at the University of California, Los Angeles CA 90095

<sup>7</sup>Molecular Biology Institute, University of California, Los Angeles, CA 90095

<sup>8</sup>Howard Hughes Medical Institute, University of California, Los Angeles, CA 90095

**CORRESPONDING AUTHORS: Owen N. Witte**

University of California, Los Angeles  
675 Charles E. Young Dr. South, 5-748 MRL  
Los Angeles, CA 90095-1662  
Phone: 310-206-0386  
Fax: 310-206-8822  
E-mail: [OwenWitte@mednet.ucla.edu](mailto:OwenWitte@mednet.ucla.edu)

## **ABSTRACT:**

Adoptive transfer of tumor reactive T cells have reduced tumor burden, but in rare cases, on-target/off-tumor effects have been lethal. As novel T cell therapies are developed, there is an essential need for a non-invasive method to track engineered cells with high sensitivity and resolution to observe correct cell homing or dangerous off-target locations in pre-clinical and clinical applications. Human deoxycytidine kinase triple mutant (hdCK3mut), a non-immunogenic PET reporter, was previously demonstrated as an effective tool for whole-body monitoring of hematopoiesis. Here, we engineered hdCK3mut to be co-expressed with the anti-melanoma T cell receptor F5 in human CD34 cells in a model of immunotherapy. Expression of hdCK3mut allowed for visualization of engrafted cells within the bone marrow. T cell homing was detected by the accumulation of [<sup>18</sup>F]-L-FMAU in hdCK3mut expressing T cells located intra-tumorally. Animals coexpressing hdCK3mut with the anti-melanoma TCR had demonstrably higher signals in HLA matched tumors when compared to animals solely expressing hdCK3mut. Stimulation of engineered T cells caused IFN- $\gamma$  production and activation. hdCK3mut can simultaneously monitor engraftment and tumor infiltration without affecting T cell function. Our findings suggest that hdCK3mut reporter imaging can be applied in clinical immunotherapies for whole-body detection of engineered cell locations.

## **INTRODUCTION:**

Adoptive cellular immunotherapy provides an alternative cancer treatment to traditional chemotherapies and antibody based therapies (1, 2). Patient specific lymphocytes are isolated via blood or tumor resections, expanded by cytokine stimulation and in some cases engineered to express transgenic T cell receptors (TCRs) or chimeric antigen receptors (CARs) that specifically recognize the tumor (3-5). Infused lymphocytes are required to successfully home to the target tumors and mediate cytotoxicity (1, 5).

The large expansion *ex vivo* prior to infusion can cause defects in T cell function (6, 7). Expansion can alter the tumor homing function reducing the efficacy of infused cells (8). Non-specific expansion or TCR mismatching when cells are engineered to express a specific TCR can increase the number of alloreactive T cells possibly causing issues of autoimmunity and graft versus host disease (9-11). In the case of engineered TCRs or CARs these cells have the potential to recognize on-target/off-tumor sites of proper epitope display, or of epitopes similar to the target (4, 9). Off-target toxicity can be lethal and reinforces the need for improved preclinical and clinical methods of determining non-tumor localization (12).

Peripheral blood analysis is a fast, simple, and routine method for monitoring transplanted lymphocytes. Cells isolated from blood can define quantity, phenotype and cytokine levels. The limitation to peripheral blood sampling is the lack of information regarding lymphocyte location in sites outside the circulation. Non-invasive, whole-body measurements are needed to determine additional sites of transplanted cells *in vivo* (13). Reporter imaging by positron emission tomography (PET) provides a 3D, highly sensitive method to detect transplanted cell locations



for both pre-clinical and clinical therapies (13, 14). Expression of a PET reporter gene in specific cell populations allows investigators to serially monitor the initial transplant and subsequent tumor infiltration or off-target locations of engineered cells (15, 16).

Herpes Simplex Virus Thymidine Kinase (HSV-TK) was the first PET reporter gene translated into clinical use (17, 18). The specificity of HSV-TK for its radiolabeled probe 9-[4-<sup>18</sup>F]fluoro-3-(hydroxymethyl)butyl]guanine (<sup>18</sup>F]FHBG) allows for precise detection of cells expressing this PET reporter gene. HSV-TK has had limited clinical utility due to the immunogenicity and clearance of lymphocytes expressing the PET reporter gene (19, 20). Most patients will be seropositive for HSV prior to transfusion of labeled cells, indicating an adaptive immune memory response of B cells from prior exposure to HSV (21). Previous clinical applications found that labeled cells expressing HSV-TK were cleared quickly due to a memory CD8 T cell response (19, 20). This suggests that HSV-TK will have limited utility for monitoring transplanted cell populations long-term.

The non-immunogenic human based PET reporter gene hdCK3mut was developed as an alternative to other human PET reporters and HSV-TK (16). hdCK3mut is smaller in size which is beneficial in constructing therapeutic vectors that have size limitations. hdCK3mut is more sensitive than alternative PET reporters allowing for increased signal at sites expressing hdCK3mut (22). The engineered substrate affinity of hdCK3mut is towards thymidine analogs (23, 24) while HSV-TK is engineered towards acycloguanosine substrates (25). In some chemotherapy and bone marrow transplant regimens a continuous administration of acycloguanosine compounds are given as prophylactic antivirals limiting the use of HSV-TK in

these settings (14, 21). The use of hdCK3mut as a PET reporter would allow for the continuous treatment with such antivirals.

We previously showed that hdCK3mut can visualize hematopoietic engraftment after HSC transplantation and found expression of hdCK3mut to be non-deleterious to cell engraftment, expansion, and development (16).

hdCK3mut is a mutant deoxycytidine kinase and could potentially cause toxicity during immune cell activation by changing cellular nucleotide pools. In ADA SCID a buildup of deoxyadenosine triphosphate (dATP) causes T cell toxicity (26). Mice with a genetic loss of dCK also have a dramatic reduction in both T and B cells identified as a replication stress defect due to the imbalanced nucleotide pools (27).

To test whether hdCK3mut PET reporter affects T cell function we utilized a previously described humanized mouse model of adoptive immunotherapy (28). Human hematopoietic stem cells (HSCs) are engineered for TCR expression *ex vivo* and developed into cytotoxic T cells *in vivo*. hdCK3mut alone or hdCK3mut co-expressed with the F5 TCR reactive against melanoma antigen recognized by T-cells 1 (MART-1) was utilized as a model to demonstrate the utility, safety and the biologically inert effect of hdCK3mut on T cell function.

We demonstrate that hdCK3mut can be used to monitor adoptive cell therapy utilizing engineered TCRs in human HSCs. Functional splenocytes were isolated and stimulated *ex vivo* at experimental end point. These isolated cytotoxic T lymphocytes (CTLs) were capable of IFN-

$\gamma$  production after stimulation. F5 T cells were activated and detected by surface activation markers in flow cytometry after antigen presentation by co-culturing MART-1 expressing artificial antigen presenting cells (aAPCs). In vivo the antigen positive HLA-matched tumors in animals receiving F5 TCR with hdCK3mut (F5/hdCK3mut) transduced HSCs have increased accumulation of [ $^{18}\text{F}$ ]-L-FMAU in comparison to HLA mismatched tumors. HLA matched tumors from the F5/hdCK3mut had an increase in [ $^{18}\text{F}$ ]-L-FMAU accumulation due to the infiltrated antigen specific cytotoxic T cells in comparison to the hdCK3mut recipients. F5/hdCK3mut animals had increased cell death within the tumor. In this study we demonstrate that hdCK3mut provides a safe, non-immunogenic method for measuring engineered adoptive cell transplant (ACT) therapy engraftment and tumor infiltration in vivo.

## **RESULTS:**

**Development of the humanized mice transplanted with engineered HSCs.** A modified human bone marrow, liver, thymus (BLT) mouse model was utilized (28). Animals are made through two independent steps. Initially a human thymic graft is implanted in a NOD.Cg-Prkdcscid Il2rgtm1Wjl/SzJ (NSG) animal. After 8 weeks the animals are then transplanted with gene modified CD34 cells intravenously. This allows for the development of human T, B and myeloid cells in NSG mice.

Non-transduced HLA-A2.1 donor cells were used to establish the thymic graft that is implanted sub-renally (Figure 1a). The human thymic implant provides the environment for positive and negative selection for lymphocyte progenitors during T cell development. Notably, cells within the thymus are not tolerized to the PET reporter hdCK3mut or the engineered TCR due to the initial graft being made with naïve non-transduced cells.

We gene modified the CD34<sup>+</sup> cells by lentiviral transduction, and viably froze them for 8 weeks allowing the thymic graft to implant and establish *in vivo*. CD34 cells were transduced to express one lentiviral vector and separated into one of three cohorts: CD34 control with no vector transduction, hdCK3mut alone, and the engineered MART-1 TCR F5 with hdCK3mut (F5/hdCK3mut) (Figure 1b). These three animal cohorts allow for the investigation of the effect of hdCK3mut on T cell development and function *in vivo*.

Transplanted CD34 cells engraft within the bone marrow and develop into lymphocyte progenitors which home to the thymic graft (29). Only a fraction of the CD34 cells are gene

modified, and a diverse T cell repertoire will develop in vivo (11, 28, 29). It is possible that the F5 expressing cells may be eliminated by negative selection due to TCR mismatching from endogenous TCR and the F5 TCR. Additional human B cells, NK cells and myeloid cells are developed in the “BLT” mouse and can express the hdCK3mut PET reporter gene if vector marked. Animals are then tumor challenged with two MART1 positive melanoma tumors. M202 express HLA A2.1 and M207 is an HLA mismatched tumor. Engineered T cells can only recognize the MART1 peptide in an HLA A2.1 MHC class 1 presentation.

Total engraftment was evaluated at experimental endpoint by flow cytometry analysis of cells from the spleen. Flow cytometry provides information on total engraftment of human cells in hdCK3mut (Figure 2a), and F5/hdCK3mut (Figure 2b). MART-1 tetramer staining measures the percentage of T cells that are engineered to express the F5 TCR and is seen only in F5/hdCK3mut recipient animals (Figure 2b). Expression of the F5/hdCK3mut or hdCK3mut alone did not affect the human cell engraftment or lineage development. In all cohorts total human cell engraftment was approximately 50% of the gated lymphocyte compartment from forward scatter (FSC) and side scatter (SSC) (Figure 2c). Composition of the human cell engraftment was roughly equivalent for the percentage of CD19, CD33, CD4, and CD8 cells in all treatment cohorts (Figure 2d). The comparable human cell engraftment and development between groups demonstrates that hdCK3mut expression is not deleterious during immune cell development.

**hdCK3mut expressing T cells developed in humanized mice are capable of activation and cytokine secretion.** T cells from splenocytes of BLT mice were cultured in low IL-2 and

stimulated by phorbol 12-myristate 13-acetate (PMA) and ionomycin. Intracellular interferon gamma (IFN- $\gamma$ ) was measured by intracellular flow (Figure 3a). Cytotoxic T cells (CD3, CD8) produced IFN- $\gamma$  after overnight stimulation indicative of immune cell activation (Figure 3b). No difference in the quantity of IFN- $\gamma$  levels or the total percentage of activated cells in reporter labeled versus untransduced cells was detected (Figs. 3b,c). Production of IFN- $\gamma$  in CD8 cells demonstrates an activated phenotype with proper cytotoxic T cell function. Although PMA/ionomycin causes general cell stimulation in T cells, exhausted or developmentally impaired CD8 cells should lack the capability to produce cytokines upon stimulation. T cells expressing hdCK3mut had no impairment in IFN- $\gamma$  production and were equivalent to the control animals.

**F5 TCR T cells expressing hdCK3mut can be activated by artificial antigen presenting cells (aAPCs) with MART1 peptide.** K562s were used as an aAPC and engineered to express MART-1 or hdCK3mut. Isolated splenocytes were co-cultured with aAPCs and low IL-2 for 3 days (Figure 4a). Since MART-1 is a self-peptide, we monitored the activation of alloreactive T cells. The upregulation of the surface markers CD25 and CD71 are indicative of alloreactive T cells (30). CD25, the IL-2 receptor, is an early activation marker for CD8 T cells. CD71, the transferrin receptor, is used as a later marker in T cell activation. We measured the quantity of activated T cells that were CD3+, CD8+, CD25+, CD71+ after stimulation by aAPCs (Figure 4b).

F5 T cells from the F5/hdCK3mut recipients were activated by the antigen matched MART1 aAPCs (Figure 4b). F5 T cells were not activated against the hdCK3mut expressing aAPCs (Figure 4c).

We compared the total activated CD8 cells from F5/hdCK3mut and hdCK3mut animals when cultured with aAPCs expressing hdCK3mut or MART-1 (Figure 4d). A slight increase in the CD25+ CD71+ was seen with F5/hdCK3mut co-cultured with MART-1, with no change seen in the hdCK3mut T cells (Figure 4d). A non-significant number of CD8 cells were activated against the aAPCs expressing the hdCK3mut. This indicates that there is not a recurrent population of mature CD8 or memory CD8 cells specific to hdCK3mut.

The activation of engineered F5 T cells when cultured with MART-1 aAPCs was 8 fold higher in comparison to the hdCK3mut aAPCs (Figure 4e). This demonstrates that engineered F5 T cells are capable of antigen specific activation.

**hdCK3mut expressing T cells home and cause selective cytotoxicity to the HLA matched tumor in vivo.** All animals were challenged with two MART-1 positive tumors. M202 was HLA matched, M207 was a control HLA mismatched tumor (Figure 5a). At experimental endpoint, approximately 6 weeks after tumor challenge, tumors were removed and fixed for sectioning. The F5 TCR has previously been demonstrated to cause cytotoxicity to M202 cells in this model(28). Addition of the hdCK3mut PET reporter did not alter this function and the F5/hdCK3mut recipients had increased areas of tumor lysis seen by non-contact, apoptotic tumor cells in hematoxylin and eosin (H&E) histology in the M202 tumors compared to M207 (Figure

5b). In the hdCK3mut recipients alone, minimal tumor lysis was observed due to the lack of engineered T cells against the MART-1 cancer antigen (Supplemental Figure S1).

PET is highly sensitive and capable of monitoring small numbers of cells *in vivo*. Previous studies demonstrated that approximately 0.5% of cells within the tumors are hCD45, with 5-10% of hCD45 being the engineered T cells (28). The diameter of a T cell is approximately 5 microns with the average tumor cell close to 20 microns, making the volume of a T cell 60 times smaller than a tumor cell. It is challenging to accurately quantify the total immune cell infiltrate because of the absolute quantity and size difference between cells. Instead we validated by IHC analysis that both hCD3 and hCD8 cells were present in the M202 and M207 tumors (Figure 5c-d). This presence of immune cells suggests that the tumor lysis seen in M202 tumors of F5/hdCK3mut recipients is most likely due to T cell cytotoxicity *in vivo* (Figure 5b-d, Supplemental Figure S2). hCD8 and hCD3 cells were detected in tumors of the hdCK3mut recipients as well (Supplemental Figure S1). Although the total immune infiltrate is low, a small number of tumor reactive T cells are proficient in causing tumor cell lysis *in vivo*. The increase in T cells and tumor cytotoxicity specific to the M202 tumor in F5/hdCK3mut demonstrates the T cells capacity to home, and selectively lyse the HLA matched tumor *in vivo*.

**Non-invasive [<sup>18</sup>F]-L-FMAU PET reporter imaging visualizes the enhanced tumor infiltration of engineered cytotoxic T cells.** PET was used to measure two distinct cellular processes. One scan measured tumor location and viability while the second scan measured the location of hdCK3mut reporter cells. The first scan was a glucose analog, 2-deoxy-2-(<sup>18</sup>F)fluoro-D-glucose ([<sup>18</sup>F]-FDG), to measure the glycolytic activity of the tumors (Figure 6a,



Supplemental Figure S3). Signal observed in both M202 and M207 tumors was quantified as a ratio of the maximum signals (percent injected dose/gram (%ID/g)) in the tumor to muscle in all animals (Figure 6b). All tumors from each cohort had similar glycolytic activity as measured by [<sup>18</sup>F]-FDG accumulation (Non-significant by one-way ANOVA, P=0.42) indicating that all tumors were engrafted with viable tissue. The regions of interest (ROIs) drawn from the [<sup>18</sup>F]-FDG scans were used to identify tumor size and location in the follow-up PET reporter imaging scan.

To determine the relative engraftment and location of the engineered cells, [<sup>18</sup>F]-L-FMAU PET reporter imaging was performed. [<sup>18</sup>F]-L-FMAU specifically accumulates in cells expressing hdCK3mut. In both cohorts engineered to express hdCK3mut a constitutive promoter was used allowing for detection of all cells that are vector marked. The advantage is that the vector marked stem, progenitor, and differentiated cells can all be detected with one non-invasive scan. Engraftment of progenitors within the bone marrow of F5/hdCK3mut and hdCK3mut animals can be visualized (Figure 7a-b). Additional sites of engraftment can include the lymph nodes and spleen. No strong spleen signal was observed, signal may be present and weak but is difficult to distinguish based on the high clearance of probe through the kidneys adjacent to the spleen.

Engineered cells can mature into myeloid, B or T cells in vivo. Only cells that are CD3 positive will express the engineered F5 TCR. It is possible that signal may be observed in additional sites including M207 tumors due to the infiltration of non-specific immune cells. To validate that the signal seen within M202 tumors is specific to engineered T cells expressing hdCK3mut, we

compared the signal from animals receiving only the hdCK3mut PET reporter to the F5/hdCK3mut recipients (Figure 6c, Supplemental Figure S4).

Applying hdCK3mut PET reporter imaging allowed for the detection of engineered tumor infiltrating lymphocytes in M202 tumors. The control non-transduced cohort had equivalent signal (tumor/muscle with max %ID/g) in both M202 and M207 tumors verifying that the tumor cell lines have equivalently low non-specific accumulation of [<sup>18</sup>F]-L-FMAU. Quantification of the [<sup>18</sup>F]-L-FMAU PET scan determined that the M202 signal was highest in F5/hdCK3mut animals in comparison to M202 signal in hdCK3mut alone (P<0.005) (Figure 6d). Both F5/hdCK3mut and hdCK3mut groups had increased [<sup>18</sup>F]-L-FMAU signal in HLA matched tumors (M202) compared to HLA mismatch (M207). The increase in signal from M202 tumors of hdCK3mut suggests that immune cells will traffic to HLA matched tumors even when cells are not engineered towards a specific cancer antigen.

F5/hdCK3mut recipients had 2 fold higher accumulation of [<sup>18</sup>F]-L-FMAU in the M202 tumors than the matched M207 tumors. This allowed for visualization by PET reporter imaging of engineered T cells homing to the HLA matched tumor (Figure 6d).

## **DISCUSSION:**

Our work demonstrates that hdCK3mut and [<sup>18</sup>F]-L-FMAU are an appropriate PET reporter gene and probe combination for monitoring the presence of engineered lymphocytes in HLA matched tumors. The expression of hdCK3mut in this model did not alter T cell function, development, or cause a non-specific activation of T cells when evaluated by both in vitro and in vivo assays. hdCK3mut PET reporter imaging is a safe and effective method for monitoring adoptive cell therapies.

**PET reporter imaging can be applied to current cell based therapies.** The improved sensitivity of hdCK3mut in detecting small infiltrating populations can be a valuable tool for preclinical and clinical studies investigating the locations of all engineered cells. This can provide information on cell locations prior to the detection of complications. As novel TCRs and CARs are developed the capacity to serially monitor the location, and potentially circumvent complications of off-target locations is essential (12, 31). hdCK3mut utilizes a high specific activity, short half-life, small molecule probe that allows for serial scans as needed. The major safety limitation of PET scans is the risk for radiochemical toxicity within the bladder and kidneys if multiple scans are necessary. Pre-clinical and clinical toxicity work has been done with [<sup>18</sup>F]-L-FMAU to determine a safe dose per patient (32).

In our model system, we detected quantifiable signal with cells at an estimated density of less than 0.5% within tumors. In clinical settings the density of hdCK3mut cells in vivo may be substantially higher after bulk infusion of engineered T cells (33). The increased quantity of cells will increase the reporter signal allowing for a better resolution of signal to noise in the [<sup>18</sup>F]-L-

FMAU PET scan (34, 35). This is important in detecting the correct homing capacity as well as the potential off-target locations of hdCK3mut expressing cells.

Current adoptive cell therapies have relied on the infusion of expanded lymphocytes (1), with limited methods for follow-up measurements outside of peripheral blood. The addition of a PET reporter can help evaluate whether the loss of engineered cells in the peripheral blood correlates with decreased T cells within the tumor, or if the quantity of cells is exclusive and cytotoxic T cells remain within sites beyond the circulation (36). Serial scans can monitor the decline in total infiltrated cell numbers over time, providing a non-invasive method for kinetic measurements of the engineered immunotherapy.

#### **Methods to further enhance the sensitivity of hdCK3mut PET reporter detection.**

hdCK3mut was demonstrated to be approximately two fold more sensitive in a comparison study between alternate PET reporter genes(22). It has been noted that the gene transfer mechanism (retro, or lentivirus) as well as the promoter can alter the efficacy of the PET reporter genes (22). Alternatively, future PET reporter applications could utilize lineage specific promoters to track a subset of cells. The metabolic state of the reporter labeled cells may also change the total accumulation of the PET reporter probe due to differences in active versus quiescent cell populations (34). Future studies will investigate whether changes in cell cycle or metabolism alters the PET reporter function *in vivo*.

**Model limitations of BLT mice in T cell development.** The T cells developed within this model do not contain a full T cell repertoire and can have variable T cell development including

low total number of cells and therefore may not fully depict what will be seen in human patients (29). The establishment of a non-transduced thymic graft helps to recapitulate the clinical settings where patients are not tolerized prior to infusion of the PET reporter gene. In vitro and in vivo T cell activation experiments demonstrate the functionality of cells expressing hdCK3mut. Further optimization in the model system may increase the total T cell quantity, but importantly the expression of hdCK3mut was not deleterious and did not hinder or alter total output.

**Future applications combining in vivo detection of T cell locations with single cell analysis methods to monitor function.** Novel methods are able to evaluate the behavior of T cells on a single cell basis and provide insight into how ex vivo manipulation can affect function. A multiplex, bar-code ELISA was recently developed to measure the production of up to 19 cytokines from a single cell (36, 37). This allows for rapid analysis of individual cells at a high frequency. Improvements in single-cell RNA sequencing can also provide information on the T cell transcriptional state (38, 39).

The combination of PET reporter imaging to detect cell locations, followed by isolation and interrogation of T cell function may help address whether the T cells that home to intra-tumor sites versus off-target locations have different transcription or cytokine profiles. If subsets of T cells function incorrectly in vivo, it may be possible to exclude or eliminate these cells prior to infusion providing an enhanced safety mechanism.

**Concluding remarks.** Previous studies evaluated the expression of a human PET reporter for short-term (6 hours after infusion) T cell trafficking (40). To date this is the first study that

validates that a human PET reporter gene can simultaneously monitor engraftment and tumor infiltration without altering T cell development and function. hdCK3mut can be broadly applicable to monitoring all cell based therapies and provides the necessary tool for the tracking of cellular immunotherapies.

## **METHODS:**

**Statistics:** Graphs are plotted as mean with standard error of mean (SEM) for error bars. Statistics were analyzed using a one-way ANOVA followed by Dunnett's or Tukey's secondary multiple comparison test, or a Student's T-test.

**Study Approval:** All animal protocols were performed under the approval of the University of California, Los Angeles (UCLA) Animal Research Committee.

**Mice:** Immunodeficient NOD.Cg-Prkdcscid Il2rgtm1Wjl/SzJ (NSG) mice were bred and maintained according to the guidelines of the Department of Laboratory Animal Medicine (DLAM) at the University of California, Los Angeles. All animal studies were carried out by using protocols that had been approved by DLAM.

**Human BLT establishment:** Mice were generated as previously described (28). Three weeks after the generation of humanized BLT mice, the mice were then irradiated at 300 rad using a cobalt-60 source to remove endogenous cells. Then the frozen transduced CD34 cells were thawed and injected. Mice were bled approximately 8 weeks after injection to assess reconstitution.

**Construction of hdCK3mut expressing Lentiviral Vectors .** The lentiviral vector pF5-sr39tk expressing the F5 TCR chains and the sr39tk reporter was constructed as previously described (28). The TCR and sr39tk were removed and the hdCK3mut-IRES-YFP (16) was inserted. The lentiviral vector containing the MSCV promoter and F5 TCR and sr39tk (From Richard Koya)

was used to establish the F5/hdCK3mut vector. sr39tk was replaced with hdCK3mut. The TCR chains and the reporter gene are separated by picornaviral-derived 2A sequences that allow the expression of a polycistronic mRNA and the generation of the three protein products. Lentiviral vector stocks were produced by transfection of 293T cells with the lentiviral construct and the helper plasmids VSVG, PMDL and pREV.

**Transduction of human HSCs:** Isolation and Transduction of CD34 hHSC. Fresh human fetal liver was obtained from Advanced Bioscience Resources Inc. (Alameda, CA). The tissue was processed, and CD34 cells were purified as previously described and were transduced (multiplicity of infection = 5) using retronectin (Takara Bio, Inc. Otsu, Japan)(28). Cells were then washed and frozen for CD34 cell injections.

**Immunohistochemistry:** Tissue was fixed in 10% phosphate buffered formalin overnight. Sections were cut at 0.4 micron, with staining for hematoxylin and eosin for representative histology every 5 slides. Tissue sections were heated at 65 °C for 1 h to melt the paraffin followed by rehydration. Antigen retrieval was performed using citric acid buffer (pH 6) or Tris/EDTA (pH 9) and visualization was performed using liquid DAB+ kit (DAKO, Carpinteria, CA). Slides were blocked for endogenous peroxidase activity with 3% H<sub>2</sub>O<sub>2</sub> in PBS for 5 min, then blocked with 2.5% normal horse serum. Primary antibodies were diluted with 2.5% normal horse serum as follows:  $\alpha$ -CD3 (AbCam AB828, use 1:50) (Cambridge, MA),  $\alpha$ -CD8 (eBiosciences C8/144B, 5 $\mu$ g/mL) (San Diego, CA) and incubated at 4C overnight. Secondary antibody was added (ImmPRESS Anti-Mouse or Anti-Rabbit Ig (peroxidase) Polymer Detection Kit) (Burlingame, CA).



**Flow cytometry and fluorescent activated cell sorting:** Single-cell suspensions from spleen and peripheral blood were stained with the following fluorochrome-conjugated antibodies: MART1 tetramer (Beckman Coulter, Brea, CA), with eBiosciences (San Diego, CA) antibodies for anti-hCD45, anti-hCD4, anti-hCD8, anti-hCD3, anti-hCD33, anti-hCD56, anti-hCD123, anti-hCD19, anti-hIgG, and anti-IFN- $\gamma$ . Flow cytometry was performed on the BD FACScanto II.

**MicroPET and image analysis:** Mice were warmed under gas anesthesia (2% isoflurane) and injected intravenously with 200  $\mu$ Ci of either [ $^{18}$ F]-FDG or [ $^{18}$ F]-L-FMAU (radiochemical synthesis described(32)), followed by 1 hour unconscious or 3 hour conscious uptake. Mice were then positioned in an imaging chamber for sequential imaging with the Siemens Preclinical Solutions MicroPET Focus 220 and MicroCAT II CT systems (Siemens). MicroPET data were acquired for 10 minutes and reconstructed with a filtered back projection probability algorithm. MicroPET and CT images were coregistered. Quantification of PET signal was performed by drawing 3D ROIs around the area of interest using AMIDE software (<http://amide.sourceforge.net/>). The max intensity of the ROI, based on the percent injected dose per gram, was normalized to control muscle of the left hamstring. Data are presented as fold change over muscle. Images are presented here using a false-color scale that is proportional to tissue concentration (%ID/g) of positron-labeled probe. Red represents the highest with yellow, green, and blue corresponding to lower concentrations.

**Cell Line:** The human melanoma cell lines M202 and M207 were used(41). M202 is HLA-A\*0201<sup>+</sup> MART<sup>+</sup>, M207 is HLA-A\*0201<sup>-</sup> MART<sup>+</sup>. Both cell lines express the MART1 antigen. Cell lines were cultured in complete serum media containing RPMI 160 with L-glutamine with 10% (all percentages represent v/v) fetal bovine serum, 1% penicillin and streptomycin at 37°C with 5% CO<sub>2</sub>. Artificial antigen presenting cells K562 were transduced with HLA-A\*0201 and CD80 under neomycin selection. K562-HLA-A\*0201 cells were then transduced with MART-IRES-YFP, hdCK3mut-IRES-YFP, or YFP alone. K562 aAPCs were maintained in RPMI, 10% FBS, P/S, L-glutamine, G418.

**Xenografts:** Confluent plates of M202 and M207 cells were trypsinized and counted. 5e6 cells per xenograft were implanted subcutaneously on the flank of “BLT” humanized mice in 100uL total volume with a 50% matrigel, 50% DMEM mixture. M202 were placed on the left side and M207 were implanted on the right side of all animals (28).

**In Vitro Stimulation and Activation with aAPC:** Spleens were harvested and homogenized into single cells through a 40 micron filter in RPMI, 5% FBS media followed by RBC lysis for 5 min at room temperature. Cells were then resuspended in RPMI, 5% heat inactivated FBS, HEPES, BME, 600 IU/mL IL-2. Cultures were monitored for 3 days, with media supplementation as needed. On day 4 cells were counted and cocultured with aAPCs, or alone. Cocultures with aAPCs were incubated for 48 hours after plating. Lymphocytes plated alone were incubated with 1x cell stimulation cocktail (eBiosciences, San Diego, CA) (PMA/ionomycin) overnight with Golgiplug (BD Biosciences, San Jose, CA) added 6hr prior to

analysis. Cells were then harvested, fixed and permeabilized and flow cytometry was used to determine intracellular IFN-gamma levels.

## **ACKNOWLEDGEMENTS:**

We would like to thank the UCLA Crump Institute for Molecular Imaging and technical staff. Mark Lazari for radiochemistry. The UCLA AIDS institute and Center for AIDS research (5P30 AI028697) cores for the supply of fetal tissue, human PBMC, and the generation of humanized mice. Melissa N. McCracken was supported by the CIRM training grant (TG2-01169). This work was supported by the California Institute for Regenerative Medicine Tools/Technology Award RT1-01126, *NanoSystems Biology Cancer Center* U54 CA151819 (Heath), and NIH/NCI/CalTech Prime P01 CA132681 (Baltimore). Owen N. Witte is an investigator of the Howard Hughes Medical Institute and partially support by the Eli and Edythe Broad Center of Regenerative Medicine and Stem Cell Research.

## **FIGURE LEGENDS: (7 figures)**

**Figure 1: Establishment of humanized mice harboring F5 TCR against MART-1.** (a) HLA-A\*0201 donor tissue was combined to create an artificial human thymus, transplanted sub-renally as a “thymic” graft in NSG mice. After 8 weeks animals received low dose, full body irradiation and were transplanted with gene modified (expressing F5/hdCK3mut or hdCK3mut) hCD34 cells. Two subcutaneous tumors were implanted, M202-left side (HLA match) and M207-right side (HLA mismatch). After 6 weeks animals were subjected to microPET scans, and ex vivo analysis of the engineered cells. (b) Vector diagrams of the F5/hdCK3mut and hdCK3mut lentivirus used.

**Figure 2: Engraftment and hematopoiesis of human cells in BLT mice.** Cells were viably isolated from the spleens of BLT animals at experimental endpoint. Total engraftment and phenotype was analyzed by flow cytometry. Representative engraftment of hdCK3mut animals (a) and F5/hdCK3mut (b) are shown. Average human engraftment shown as mean with +/- SD (c) and distribution of cell phenotypes from all animals was determined shown as mean with + SD (d).

**Figure 3: hdCK3mut expressing T cells developed in vivo are capable of cytokine production.** (a) Representative FACs plots of cultures incubated with PMA/Ionomycin. Subgate on CD8 cells shows intracellular IFN- $\gamma$  by intracellular flow cytometry. IgG Isotype used as a control for background staining. (b) Percentage of CD8 cells that produce IFN- $\gamma$  shown as mean with +/- SD. (c) Relative IFN- $\gamma$  production was equivalent based on MFI from CD8 cells shown as mean with +/- SD.

**Figure 4: In vitro function of MART-1 specific T cells developed in vivo.** (a) Schematic of aAPC (K562) and T cell co-culture experiment. Representative flow cytometry plots from T cells of F5/hdCK3mut animals co-cultured with MART-1 expressing aAPCs (b) or hdCK3mut aAPCs (c). Top panel gated showing F5 T cells only, bottom panel shows all CD8 T cells. (d) Total activated T cells after 48hr coculture with aAPCs (CD25+, CD71+) for F5/hdCK3mut or hdCK3mut recipients. White bars are cells cultured with hdCK3mut aAPCs, black bars are cells cultured with MART-1 aAPCs (NS by one way ANOVA) shown as mean +SEM (n=3). (e) Engineered F5 T cells activation with aAPCs (P<0.005) shown as mean +SEM (n=3).

**Figure 5: Immunohistochemistry of immune infiltrates from xenografts removed from F5/hdCK3mut animals.** (a) Schematic of xenograft location on F5/hdCK3mut animals. (b) H&E from M202 (HLA-A\*0201<sup>+</sup>) and M207 (HLA-A\*0201<sup>-</sup>) a white border is drawn to distinguish viable tumor from tumor necrosis. (c)  $\alpha$ -CD3 and (d)  $\alpha$ -CD8 from representative sections of M202 or M207 xenografts. (Scale bar is 50 $\mu$ M)

**Figure 6: Detection of hdCK3mut engineered TILs by [<sup>18</sup>F]-L-FMAU PET reporter imaging.** (a) [<sup>18</sup>F]-FDG images from F5/hdCK3mut and hdCK3mut recipient animals. M202 xenografts are circled in red with M207 xenografts circled in aqua. (b) Quantification of the tumor/muscle ratio from [<sup>18</sup>F]-FDG images (NS by one way ANOVA) shown as mean +/- SEM (n=3 up to n=7). (c) [<sup>18</sup>F]-L-FMAU images from F5/hdCK3mut and hdCK3mut recipient animals. (d) Quantification of the tumor/muscle ratio from [<sup>18</sup>F]-L-FMAU images (P=0.0001) shown as mean +/- SEM (n=3 up to n=11).

**Figure 7: Visualization of engrafted stem and progenitor cells expressing the hdCK3mut PET reporter gene.** Engraftment of hdCK3mut expressing cells could be detected within the

bone marrow of (a) F5/hdCK3mut and (b) hdCK3mut recipients. Areas of engraftment are circled in red.

**SUPPLEMENTARY FIGURE LEGENDS: (4 figures)**

**Supplemental Figure S1: IHC of M202 and M207 Tumors from hdCK3mut recipient animals.** H&E,  $\alpha$ -CD3 and  $\alpha$ -CD8 from representative sections of M202 (HLA-A\*0201<sup>+</sup>) and M207 (HLA-A\*0201<sup>-</sup>) xenografts from hdCK3mut recipients. (Scale bar is 50 $\mu$ M)

**Supplemental Figure S2: Additional IHC of M202 and M207 Tumors from F5/hdCK3mut recipient animals.** H&E from M202 (HLA-A\*0201<sup>+</sup>) and M207 (HLA-A\*0201<sup>-</sup>) a white border is drawn to distinguish viable tumor from tumor necrosis.  $\alpha$ -CD3 and  $\alpha$ -CD8 from representative sections of M202 or M207 xenografts. (Scale bar is 50 $\mu$ M)

**Supplemental Figure S3: Additional [<sup>18</sup>F]-FDG scans of BLT animals.** Scans from F5/hdCK3mut and hdCK3mut recipient animals. M202 tumors are circled in red, M207 tumors are circled in aqua.

**Supplemental Figure S4: Additional [<sup>18</sup>F]-L-FMAU scans of BLT animals.** Scans from F5/hdCK3mut and hdCK3mut recipient animals. M202 tumors are circled in red, M207 tumors are circled in aqua.



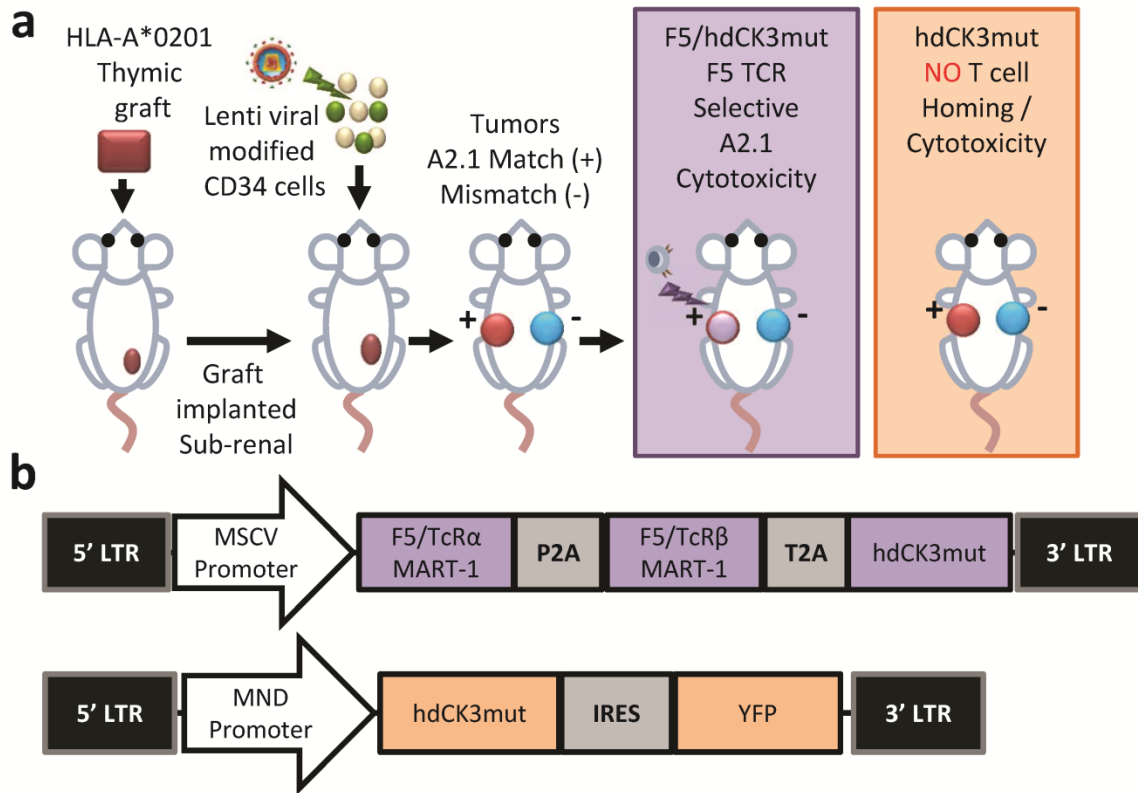


**Figure 1: Establishment of humanized mice harboring F5 TCR against MART-1.** (a) HLA-A\*0201 donor tissue was combined to create an artificial human thymus, transplanted sub-renal as a “thymic” graft in NSG mice. After 8 weeks animals received low dose, full body irradiation and were transplanted with gene modified (expressing F5/hdCK3mut or hdCK3mut) hCD34 cells. Two subcutaneous tumors were implanted, M202-left side (HLA match) and M207-right side (HLA mismatch). After 6 weeks animals were subjected to microPET scans, and ex vivo analysis of the engineered cells. (b) Vector diagrams of the F5/hdCK3mut and hdCK3mut lentivirus used.

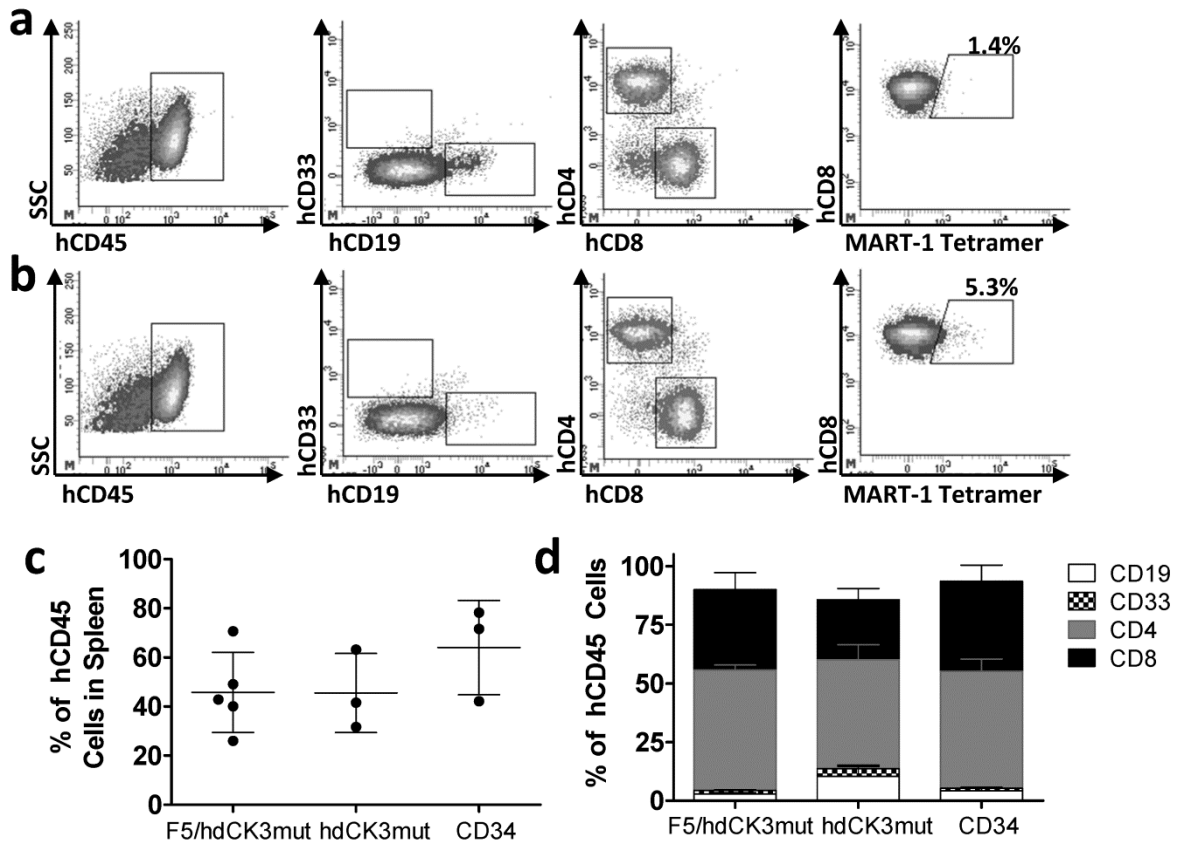


**Figure 2: Engraftment and hematopoiesis of human cells in BLT mice.** Cells were viably isolated from the spleens of BLT animals at experimental endpoint. Total engraftment and phenotype was analyzed by flow cytometry. Representative engraftment of hdCK3mut animals (a) and F5/hdCK3mut (b) are shown. Average human engraftment shown as mean with +/- SD (c) and distribution of cell phenotypes from all animals was determined shown as mean with + SD (d).

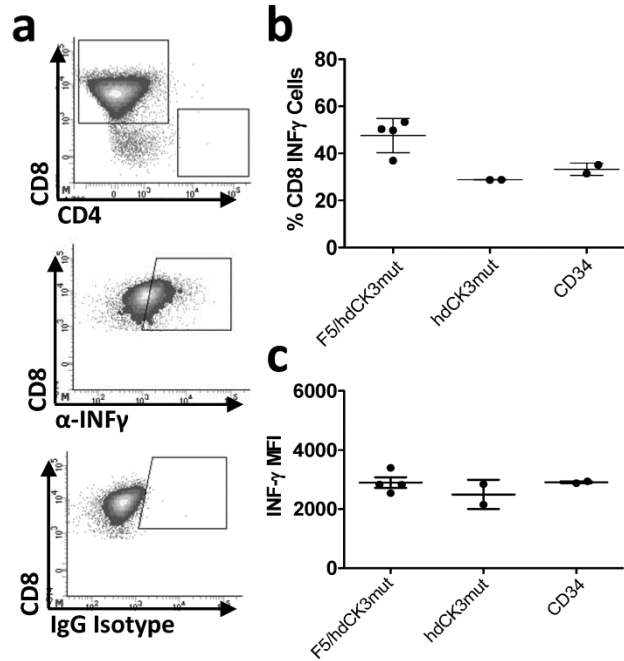


**Figure 3: hdCK3mut expressing T cells developed in vivo are capable of cytokine production.** (a) Representative FACS plots of cultures incubated with PMA/Ionomycin. Subgate on CD8 cells shows intracellular IFN- $\gamma$  by intracellular flow cytometry. IgG Isotype used as a control for background staining. (b) Percentage of CD8 cells that produce IFN- $\gamma$  shown as mean with +/- SD. (c) Relative IFN- $\gamma$  production was equivalent based on MFI from CD8 cells shown as mean with +/- SD.

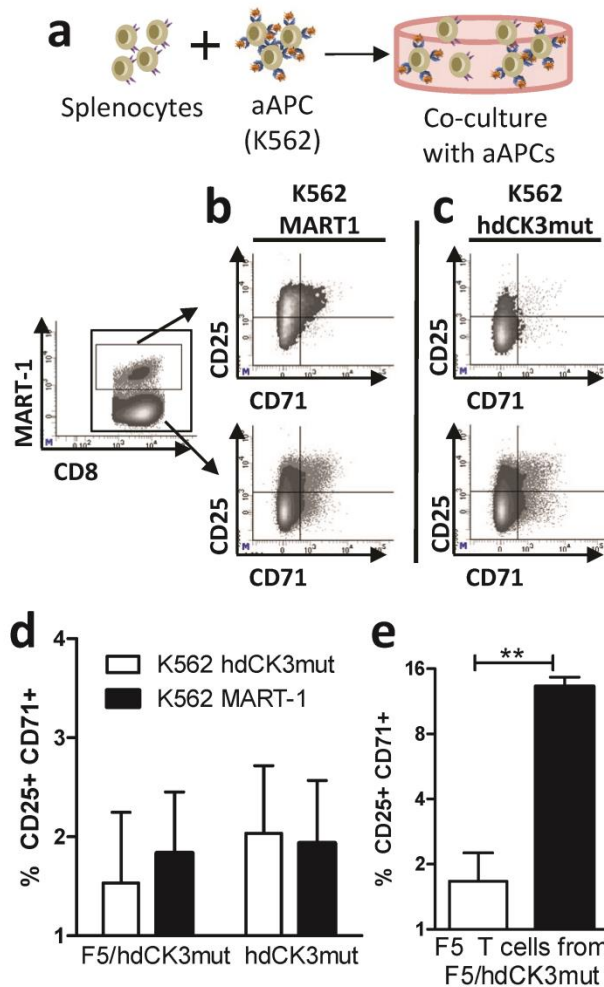


**Figure 4: In vitro function of MART-1 specific T cells developed in vivo.** (a) Schematic of aAPC (K562) and T cell co-culture experiment. Representative flow cytometry plots from T cells of F5/hdCK3mut animals co-cultured with MART-1 expressing aAPCs (b) or hdCK3mut aAPCs (c). Top panel gated showing F5 T cells only, bottom panel shows all CD8 T cells. (d) Total activated T cells after 48hr coculture with aAPCs (CD25+, CD71+) for F5/hdCK3mut or hdCK3mut recipients. White bars are cells cultured with hdCK3mut aAPCs, black bars are cells cultured with MART-1 aAPCs (NS by one way ANOVA) shown as mean +SEM (n=3). (e) Engineered F5 T cells activation with aAPCs (P<0.005) shown as mean +SEM (n=3).

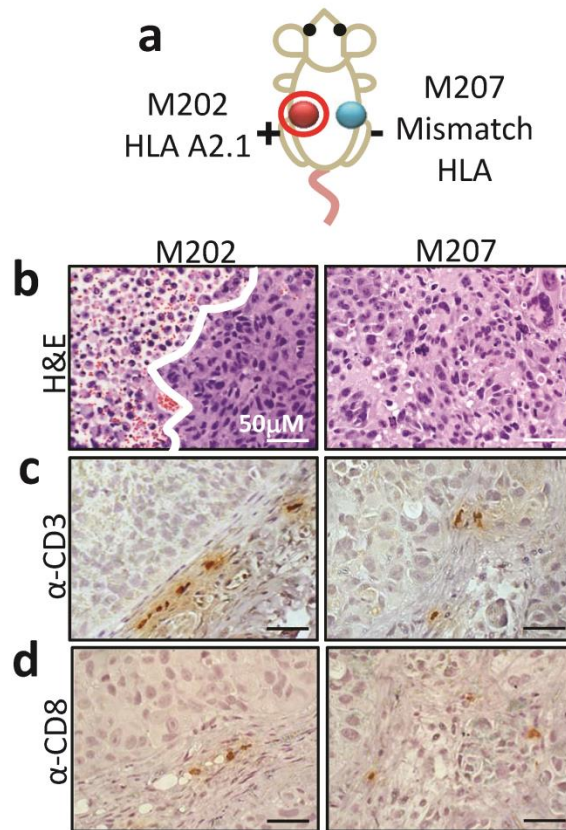


**Figure 5: Immunohistochemistry of immune infiltrates from xenografts removed from F5/hdCK3mut animals.** (a) Schematic of xenograft location on F5/hdCK3mut animals. (b) H&E from M202 (HLA-A\*0201<sup>+</sup>) and M207 (HLA-A\*0201<sup>-</sup>) a white border is drawn to distinguish viable tumor from tumor necrosis. (c) α-CD3 and (d) α-CD8 from representative sections of M202 or M207 xenografts. (Scale bar is 50μM)

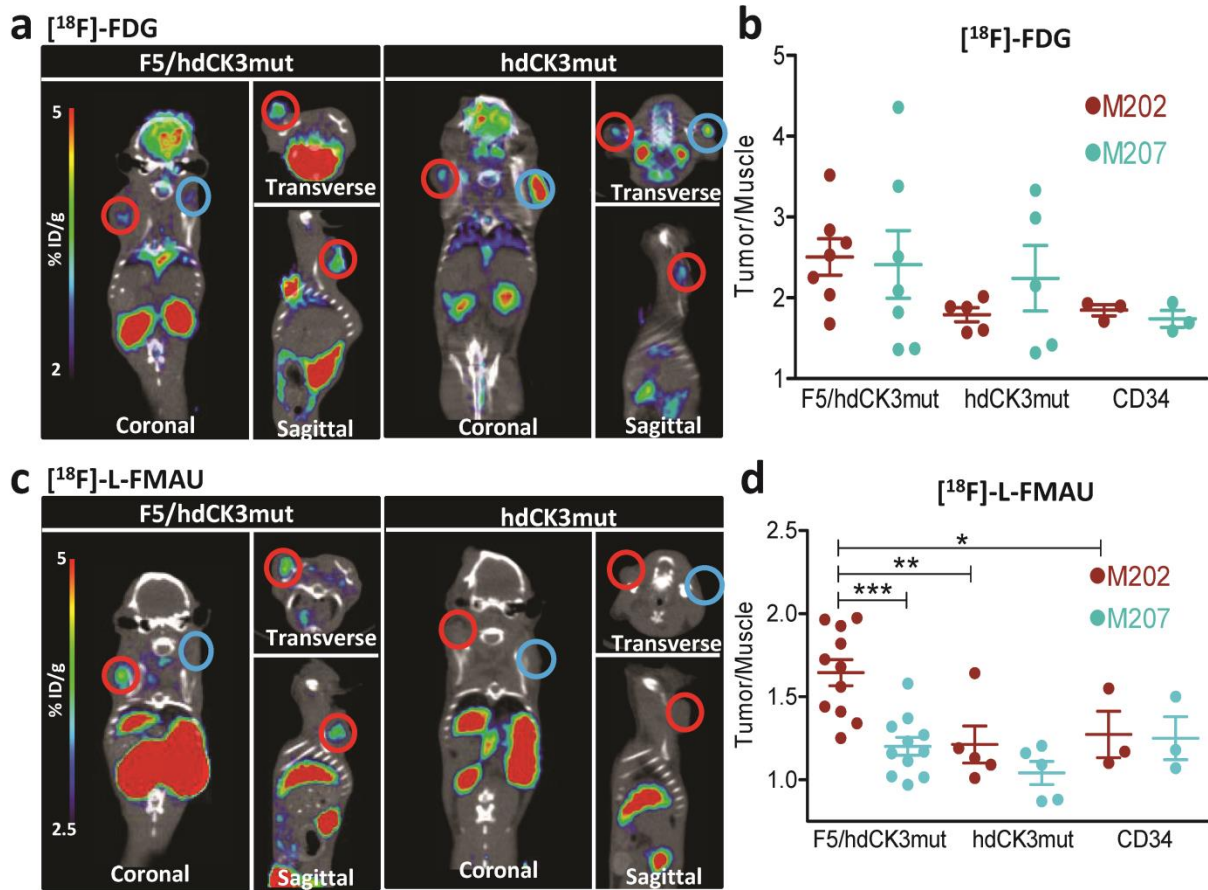


**Figure 6: Detection of hdCK3mut engineered TILs by  $[^{18}\text{F}]\text{-L-FMAU}$  PET reporter imaging.** (a)  $[^{18}\text{F}]\text{-FDG}$  images from F5/hdCK3mut and hdCK3mut recipient animals. M202 xenografts are circled in red with M207 xenografts circled in aqua. (b) Quantification of the tumor/muscle ratio from  $[^{18}\text{F}]\text{-FDG}$  images (NS by one way ANOVA) shown as mean  $\pm$  SEM (n=3 up to n=7). (c)  $[^{18}\text{F}]\text{-L-FMAU}$  images from F5/hdCK3mut and hdCK3mut recipient animals. (d) Quantification of the tumor/muscle ratio from  $[^{18}\text{F}]\text{-L-FMAU}$  images (P=0.0001) shown as mean  $\pm$  SEM (n=3 up to n=11).

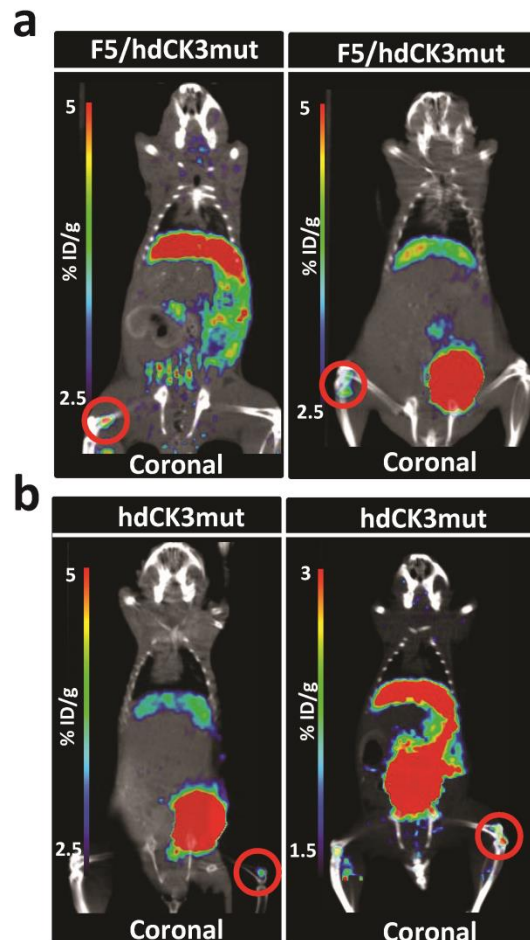
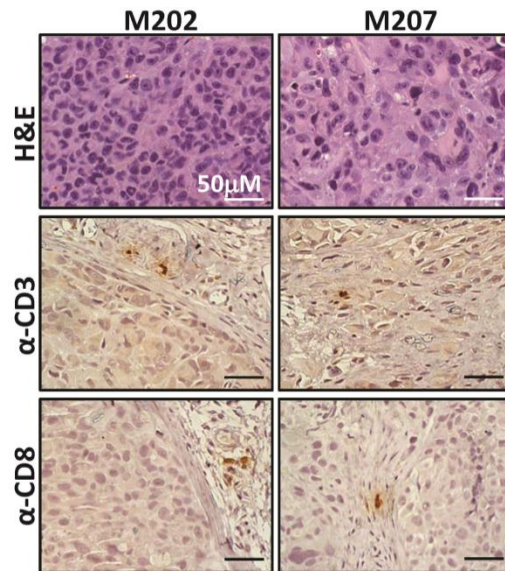
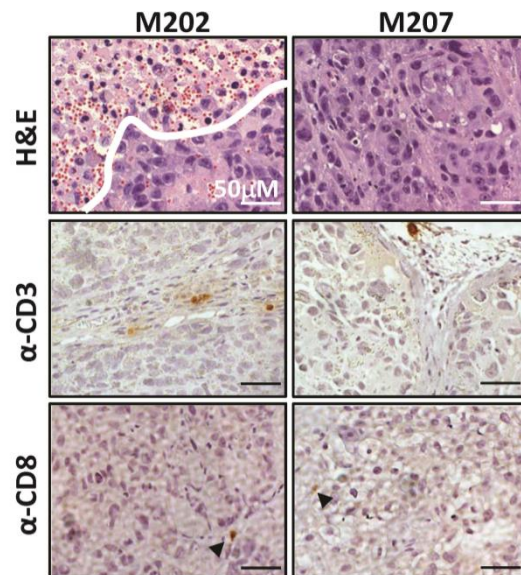


**Figure 7: Visualization of engrafted stem and progenitor cells expressing the hdCK3mut PET reporter gene.** Engraftment of hdCK3mut expressing cells could be detected within the bone marrow of (a) F5/hdCK3mut and (b) hdCK3mut recipients. Areas of engraftment are circled in red.

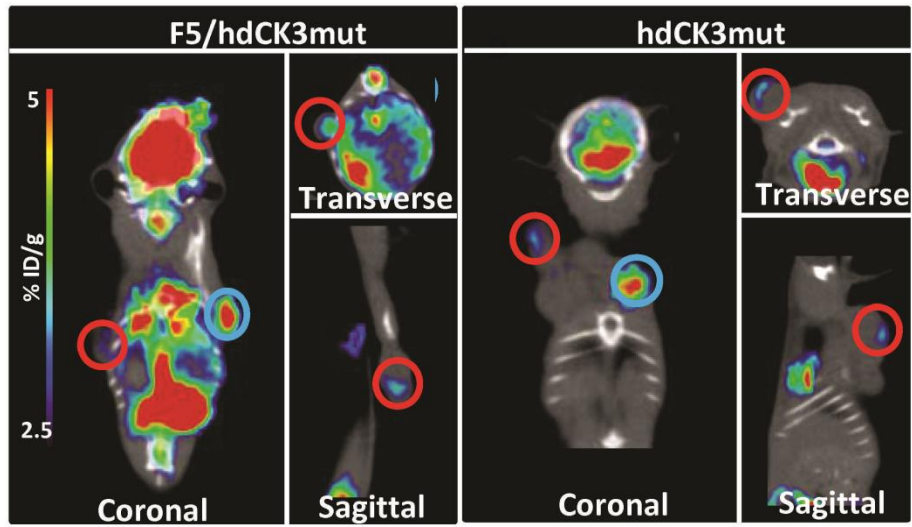


**Supplemental Figure S1: IHC of M202 and M207 Tumors from hdCK3mut recipient animals.** H&E,  $\alpha$ -CD3 and  $\alpha$ -CD8 from representative sections of M202 (HLA-A\*0201<sup>+</sup>) and M207 (HLA-A\*0201<sup>-</sup>) xenografts from hdCK3mut recipients. (Scale bar is 50 $\mu$ M)

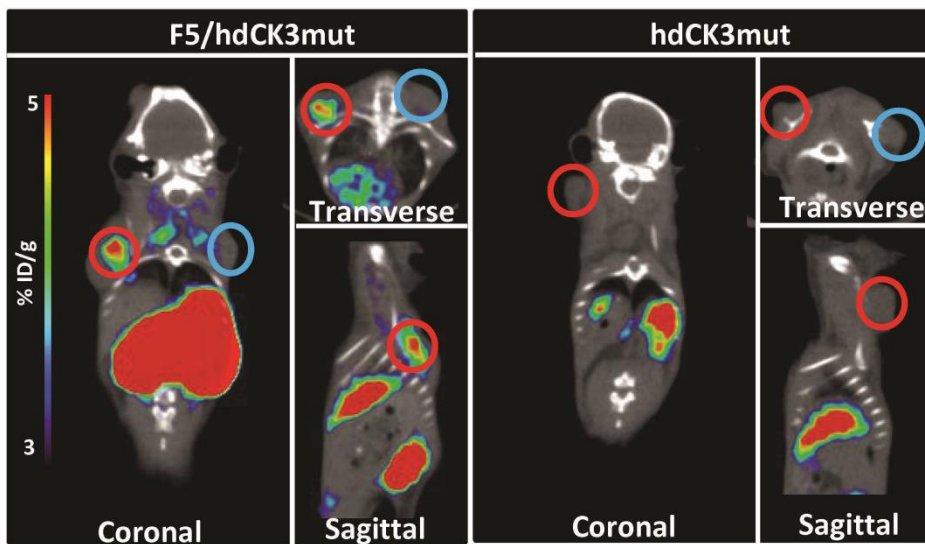


**Supplemental Figure S2: Additional IHC of M202 and M207 Tumors from F5/hdCK3mut recipient animals.** H&E from M202 (HLA-A\*0201<sup>+</sup>) and M207 (HLA-A\*0201<sup>-</sup>) a white border is drawn to distinguish viable tumor from tumor necrosis.  $\alpha$ -CD3 and  $\alpha$ -CD8 from representative sections of M202 or M207 xenografts. (Scale bar is 50 $\mu$ M)





**Supplemental Figure S3: Additional [ $^{18}\text{F}$ ]-FDG scans of BLT animals.** Scans from F5/hdCK3mut and hdCK3mut recipient animals. M202 tumors are circled in red, M207 tumors are circled in aqua.



**Supplemental Figure S4: Additional [ $^{18}\text{F}$ ]-L-FMAU scans of BLT animals.** Scans from F5/hdCK3mut and hdCK3mut recipient animals. M202 tumors are circled in red, M207 tumors are circled in aqua.

## **REFERENCES:**

1. Rosenberg, S.A., Restifo, N.P., Yang, J.C., Morgan, R.A., and Dudley, M.E. 2008. Adoptive cell transfer: a clinical path to effective cancer immunotherapy. *Nat Rev Cancer* 8:299-308.
2. Dudley, M.E., and Rosenberg, S.A. 2003. Adoptive-cell-transfer therapy for the treatment of patients with cancer. *Nat Rev Cancer* 3:666-675.
3. Dudley, M.E., Wunderlich, J.R., Shelton, T.E., Even, J., and Rosenberg, S.A. 2003. Generation of tumor-infiltrating lymphocyte cultures for use in adoptive transfer therapy for melanoma patients. *J Immunother* 26:332-342.
4. Park, T.S., Rosenberg, S.A., and Morgan, R.A. 2011. Treating cancer with genetically engineered T cells. *Trends Biotechnol* 29:550-557.
5. Morgan, R.A., Dudley, M.E., Wunderlich, J.R., Hughes, M.S., Yang, J.C., Sherry, R.M., Royal, R.E., Topalian, S.L., Kammula, U.S., Restifo, N.P., et al. 2006. Cancer regression in patients after transfer of genetically engineered lymphocytes. *Science* 314:126-129.
6. Chambers, C.A., Kuhns, M.S., Egen, J.G., and Allison, J.P. 2001. CTLA-4-mediated inhibition in regulation of T cell responses: mechanisms and manipulation in tumor immunotherapy. *Annu Rev Immunol* 19:565-594.
7. Klebanoff, C.A., Gattinoni, L., and Restifo, N.P. 2006. CD8<sup>+</sup> T-cell memory in tumor immunology and immunotherapy. *Immunol Rev* 211:214-224.
8. Russo, V., Bondanza, A., Ciceri, F., Bregni, M., Bordignon, C., Traversari, C., and Bonini, C. 2012. A dual role for genetically modified lymphocytes in cancer immunotherapy. *Trends Mol Med* 18:193-200.

9. Bendle, G.M., Linnemann, C., Hooijkaas, A.I., Bies, L., de Witte, M.A., Jorritsma, A., Kaiser, A.D., Pouw, N., Debets, R., Kieback, E., et al. 2010. Lethal graft-versus-host disease in mouse models of T cell receptor gene therapy. *Nat Med* 16:565-570, 561p following 570.
10. Dudley, M.E., Wunderlich, J.R., Robbins, P.F., Yang, J.C., Hwu, P., Schwartzentruber, D.J., Topalian, S.L., Sherry, R., Restifo, N.P., Hubicki, A.M., et al. 2002. Cancer regression and autoimmunity in patients after clonal repopulation with antitumor lymphocytes. *Science* 298:850-854.
11. Giannoni, F., Hardee, C.L., Wherley, J., Gschwend, E., Senadheera, S., Kaufman, M.L., Chan, R., Bahner, I., Gersuk, V., Wang, X., et al. 2013. Allelic exclusion and peripheral reconstitution by TCR transgenic T cells arising from transduced human hematopoietic stem/progenitor cells. *Mol Ther* 21:1044-1054.
12. Morgan, R.A., Yang, J.C., Kitano, M., Dudley, M.E., Laurencot, C.M., and Rosenberg, S.A. 2010. Case report of a serious adverse event following the administration of T cells transduced with a chimeric antigen receptor recognizing ERBB2. *Mol Ther* 18:843-851.
13. Nair-Gill, E.D., Shu, C.J., Radu, C.G., and Witte, O.N. 2008. Non-invasive imaging of adaptive immunity using positron emission tomography. *Immunol Rev* 221:214-228.
14. Yaghoubi, S.S., Campbell, D.O., Radu, C.G., and Czernin, J. 2012. Positron emission tomography reporter genes and reporter probes: gene and cell therapy applications. *Theranostics* 2:374-391.
15. Koehne, G., Doubrovin, M., Doubrovina, E., Zanzonico, P., Gallardo, H.F., Ivanova, A., Balatoni, J., Teruya-Feldstein, J., Heller, G., May, C., et al. 2003. Serial in vivo imaging

- of the targeted migration of human HSV-TK-transduced antigen-specific lymphocytes. *Nat Biotechnol* 21:405-413.
16. McCracken, M.N., Gschwend, E.H., Nair-Gill, E., McLaughlin, J., Cooper, A.R., Riedinger, M., Cheng, D., Nosala, C., Kohn, D.B., and Witte, O.N. 2013. Long-term in vivo monitoring of mouse and human hematopoietic stem cell engraftment with a human positron emission tomography reporter gene. *Proc Natl Acad Sci U S A* 110:1857-1862.
  17. Penuelas, I., Mazzolini, G., Boan, J.F., Sangro, B., Marti-Climent, J., Ruiz, M., Ruiz, J., Satyamurthy, N., Qian, C., Barrio, J.R., et al. 2005. Positron emission tomography imaging of adenoviral-mediated transgene expression in liver cancer patients. *Gastroenterology* 128:1787-1795.
  18. Yaghoubi, S.S., Jensen, M.C., Satyamurthy, N., Budhiraja, S., Paik, D., Czernin, J., and Gambhir, S.S. 2009. Noninvasive detection of therapeutic cytolytic T cells with 18F-FHBG PET in a patient with glioma. *Nat Clin Pract Oncol* 6:53-58.
  19. Berger, C., Flowers, M.E., Warren, E.H., and Riddell, S.R. 2006. Analysis of transgene-specific immune responses that limit the in vivo persistence of adoptively transferred HSV-TK-modified donor T cells after allogeneic hematopoietic cell transplantation. *Blood* 107:2294-2302.
  20. Traversari, C., Markt, S., Magnani, Z., Mangia, P., Russo, V., Ciceri, F., Bonini, C., and Bordignon, C. 2007. The potential immunogenicity of the TK suicide gene does not prevent full clinical benefit associated with the use of TK-transduced donor lymphocytes in HSCT for hematologic malignancies. *Blood* 109:4708-4715.
  21. Saral, R., Burns, W.H., Laskin, O.L., Santos, G.W., and Lietman, P.S. 1981. Acyclovir prophylaxis of herpes-simplex-virus infections. *N Engl J Med* 305:63-67.

22. Gil, J.S., Machado, H.B., and Herschman, H.R. 2012. A method to rapidly and accurately compare the relative efficacies of non-invasive imaging reporter genes in a mouse model and its application to luciferase reporters. *Mol Imaging Biol* 14:462-471.
23. Iyidogan, P., and Lutz, S. 2008. Systematic exploration of active site mutations on human deoxycytidine kinase substrate specificity. *Biochemistry* 47:4711-4720.
24. Sabini, E., Ort, S., Monnerjahn, C., Konrad, M., and Lavie, A. 2003. Structure of human dCK suggests strategies to improve anticancer and antiviral therapy. *Nat Struct Biol* 10:513-519.
25. Gambhir, S.S., Bauer, E., Black, M.E., Liang, Q., Kokoris, M.S., Barrio, J.R., Iyer, M., Namavari, M., Phelps, M.E., and Herschman, H.R. 2000. A mutant herpes simplex virus type 1 thymidine kinase reporter gene shows improved sensitivity for imaging reporter gene expression with positron emission tomography. *Proc Natl Acad Sci U S A* 97:2785-2790.
26. Aiuti, A., Slavin, S., Aker, M., Ficara, F., Deola, S., Mortellaro, A., Morecki, S., Andolfi, G., Tabucchi, A., Carlucci, F., et al. 2002. Correction of ADA-SCID by stem cell gene therapy combined with nonmyeloablative conditioning. *Science* 296:2410-2413.
27. Austin, W.R., Armijo, A.L., Campbell, D.O., Singh, A.S., Hsieh, T., Nathanson, D., Herschman, H.R., Phelps, M.E., Witte, O.N., Czernin, J., et al. 2012. Nucleoside salvage pathway kinases regulate hematopoiesis by linking nucleotide metabolism with replication stress. *J Exp Med* 209:2215-2228.
28. Vatakis, D.N., Koya, R.C., Nixon, C.C., Wei, L., Kim, S.G., Avancena, P., Bristol, G., Baltimore, D., Kohn, D.B., Ribas, A., et al. 2011. Antitumor activity from antigen-

- specific CD8 T cells generated in vivo from genetically engineered human hematopoietic stem cells. *Proc Natl Acad Sci U S A* 108:E1408-1416.
29. Wege, A.K., Melkus, M.W., Denton, P.W., Estes, J.D., and Garcia, J.V. 2008. Functional and phenotypic characterization of the humanized BLT mouse model. *Curr Top Microbiol Immunol* 324:149-165.
  30. Samarasinghe, S., Mancao, C., Pule, M., Nawroly, N., Karlsson, H., Brewin, J., Openshaw, P., Gaspar, H.B., Veys, P., and Amrolia, P.J. 2010. Functional characterization of alloreactive T cells identifies CD25 and CD71 as optimal targets for a clinically applicable allodepletion strategy. *Blood* 115:396-407.
  31. Scholler, J., Brady, T.L., Binder-Scholl, G., Hwang, W.T., Plesa, G., Hege, K.M., Vogel, A.N., Kalos, M., Riley, J.L., Deeks, S.G., et al. 2012. Decade-long safety and function of retroviral-modified chimeric antigen receptor T cells. *Sci Transl Med* 4:132ra153.
  32. Campbell, D.O., Yaghoubi, S.S., Su, Y., Lee, J.T., Auerbach, M.S., Herschman, H., Satyamurthy, N., Czernin, J., Lavie, A., and Radu, C.G. 2012. Structure-guided engineering of human thymidine kinase 2 as a positron emission tomography reporter gene for enhanced phosphorylation of non-natural thymidine analog reporter probe. *J Biol Chem* 287:446-454.
  33. Johnson, L.A., Morgan, R.A., Dudley, M.E., Cassard, L., Yang, J.C., Hughes, M.S., Kammula, U.S., Royal, R.E., Sherry, R.M., Wunderlich, J.R., et al. 2009. Gene therapy with human and mouse T-cell receptors mediates cancer regression and targets normal tissues expressing cognate antigen. *Blood* 114:535-546.

34. Shu, C.J., Guo, S., Kim, Y.J., Shelly, S.M., Nijagal, A., Ray, P., Gambhir, S.S., Radu, C.G., and Witte, O.N. 2005. Visualization of a primary anti-tumor immune response by positron emission tomography. *Proc Natl Acad Sci U S A* 102:17412-17417.
35. Su, H., Forbes, A., Gambhir, S.S., and Braun, J. 2004. Quantitation of cell number by a positron emission tomography reporter gene strategy. *Mol Imaging Biol* 6:139-148.
36. Ma, C., Cheung, A.F., Chodon, T., Koya, R.C., Wu, Z., Ng, C., Avramis, E., Cochran, A.J., Witte, O.N., Baltimore, D., et al. 2013. Multifunctional T-cell analyses to study response and progression in adoptive cell transfer immunotherapy. *Cancer Discov* 3:418-429.
37. Ma, C., Fan, R., Ahmad, H., Shi, Q., Comin-Anduix, B., Chodon, T., Koya, R.C., Liu, C.C., Kwong, G.A., Radu, C.G., et al. 2011. A clinical microchip for evaluation of single immune cells reveals high functional heterogeneity in phenotypically similar T cells. *Nat Med* 17:738-743.
38. Ramskold, D., Luo, S., Wang, Y.C., Li, R., Deng, Q., Faridani, O.R., Daniels, G.A., Khrebtukova, I., Loring, J.F., Laurent, L.C., et al. 2012. Full-length mRNA-Seq from single-cell levels of RNA and individual circulating tumor cells. *Nat Biotechnol* 30:777-782.
39. Tang, F., Barbacioru, C., Wang, Y., Nordman, E., Lee, C., Xu, N., Wang, X., Bodeau, J., Tuch, B.B., Siddiqui, A., et al. 2009. mRNA-Seq whole-transcriptome analysis of a single cell. *Nat Methods* 6:377-382.
40. Likar, Y., Zurita, J., Dobrenkov, K., Shenker, L., Cai, S., Neschadim, A., Medin, J.A., Sadelain, M., Hricak, H., and Ponomarev, V. 2010. A new pyrimidine-specific reporter

gene: a mutated human deoxycytidine kinase suitable for PET during treatment with acycloguanosine-based cytotoxic drugs. *J Nucl Med* 51:1395-1403.

41. Sondergaard, J.N., Nazarian, R., Wang, Q., Guo, D., Hsueh, T., Mok, S., Sazegar, H., MacConaill, L.E., Barretina, J.G., Kehoe, S.M., et al. 2010. Differential sensitivity of melanoma cell lines with BRAFV600E mutation to the specific Raf inhibitor PLX4032. *J Transl Med* 8:39.



## **CHAPTER 5:**

In vivo HSV-sr39TK positron emission tomography

and suicide gene elimination of human

hematopoietic stem cells and their progeny in humanized mice.

***In vivo* HSV-sr39TK positron emission tomography and suicide gene elimination of human hematopoietic stem cells and their progeny in humanized mice**

Running title: sr39TK PET and suicide gene elimination of human HSCs

Keywords: imaging, suicide gene, hematopoietic stem cell, gene therapy, immunotherapy

Eric H. Gschwend,<sup>1</sup> Melissa N. McCracken,<sup>2</sup> Michael L. Kaufman,<sup>1</sup> Michelle Ho,<sup>1</sup> Roger P. Hollis,<sup>1</sup> Xiaoyan Wang,<sup>3</sup> Navdeep Saini,<sup>1</sup> Richard C. Koya,<sup>4</sup> Thinle Chodon,<sup>4</sup> Antoni Ribas,<sup>2,5,7,8</sup> Owen N. Witte,<sup>1,2,7,8</sup> and Donald B. Kohn<sup>1,6,7,8\*</sup>

<sup>1</sup>Department of Microbiology, Immunology and Molecular Genetics, University of California, Los Angeles, CA; <sup>2</sup>Department of Medical and Molecular Pharmacology, University of California, Los Angeles, CA; <sup>3</sup>Department of Medicine Statistics Core; <sup>4</sup>Center for Immunotherapy, Roswell Park Cancer Institute, Buffalo, NY; <sup>5</sup>Department of Medicine, Division of Hematology/Oncology, University of California, Los Angeles, CA; <sup>6</sup>Department of Pediatrics, Division of Hematology/Oncology, Mattel Children's Hospital, University of California, Los Angeles, CA; <sup>7</sup>Jonsson Comprehensive Cancer Center, Los Angeles, CA, and <sup>8</sup>The Eli and Edythe Broad Center for Regenerative Medicine and Stem Cell Research, Los Angeles, CA

**Corresponding author:**

**Donald B. Kohn, M.D.**

**3163 Terasaki Life Science Bldg.**

**610 Charles E. Young Drive South**

**Los Angeles, CA 90095**

**P-310-794-1964**

**F-310-206-0356**

**e-mail: [dkohn@mednet.ucla.edu](mailto:dkohn@mednet.ucla.edu)**

The authors declare no conflicts of interest.

Word count: Abstract = 198. Main text = 3,887

Main text = 6 figures. Supplemental material = 3 figures, 1 table.

## Abstract

Engineering immunity by lentiviral introduction of antigen-specific T-cell-receptors (TCR) into hematopoietic stem cells (HSC) for adoptive immunity can potentially generate a long-term supply of effector T-cells to eradicate malignant disease. The ability to monitor gene-modified cells *in vivo* and ablate them in the case of an adverse event provides crucial safety to this therapeutic modality. The dual purpose positron emission tomography (PET) reporter imaging/suicide gene modified from herpes-simplex-virus-thymidine-kinase (sr39TK) allows non-invasive assessment of engrafted gene-modified cells, as well as the ability to eliminate such modified cells in the event of on-target/off-organ reactivity or insertional oncogenesis. Here we demonstrate the *in vivo* imaging of human hematopoietic cells derived from G-CSF mobilized CD34 enriched peripheral-blood stem cells (PBSC) modified with a lentivirus containing the NY-ESO-1-TCR co-expressed with sr39TK in a humanized mouse model. Human cells were detected with PET reporter imaging in hematopoietic niches such as femurs, humeri, vertebrae, and thymus. Ablation of PET signal, NY-ESO-1-TCR bearing cells, and lentiviral vector elements were observed in niches upon treatment with ganciclovir (GCV), but not with vehicle control. We demonstrate that sr39TK is an efficient PET reporter and effective suicide gene for immunotherapy of TCR transduced PBSCs and their progeny *in vivo*.

## Introduction

The genetic modification of hematopoietic stem cells (HSC) is an attractive approach for the treatment of disease, first demonstrated in primary immune deficiencies (1-3). Transplantation of gene-modified HSCs into patients resulted in long term correction of disease in the majority of subjects, and paved the way for future applications using viral vectors to modify hematopoietic cells (4). Gene therapy has also proven a promising modality for engineered immunity. Preclinical studies and clinical trials that engineered peripheral T-cells with cancer-antigen reactive T-cell-receptors (TCR) and chimeric antigen receptors (CAR) have achieved tumor regression in patients (5-8). Unfortunately, not all patients developed a lasting and complete response with most demonstrating transient anti-tumor reactivity. The observation that many patients initially responded with a reduction in tumor burden yet ultimately relapsed is hypothesized to be due to the nature of the *ex vivo* T-cell expansion protocol, which pushes T-cells to a differentiation state characterized by robust cytotoxic effector function at the cost of regenerative capacity (9-11). The ability to generate an antigen specific T-cell infusion product with long-lasting *in vivo* persistence, such as central memory T cells, is an area of active pre-clinical and clinical investigation (12-16).

HSCs represent the most primitive hematopoietic cells with the greatest regenerative potential, and recent preclinical studies have examined the modification of HSCs for cancer immunotherapy. The introduction of a pre-arranged TCR to HSCs was first demonstrated in mice (17), and later in humanized mouse models (18-20). These studies demonstrated that engineered HSCs give rise to progeny T-cells expressing the introduced transgenic TCR, and are reactive against cells expressing the target antigen. CARs have also been shown useful in the modification of HSCs for therapeutic immunotherapy, specifically against CD19 for B-cell

malignancies (21). The duration of *de novo* T-cell production in this chimeric setting is currently unknown, though clinical evidence supports the notion that HSCs support long-lasting thymopoiesis (22, 23).

The use of strong enhancer/promoter sequences within the vector necessary to achieve therapeutic levels of the introduced transgene can result in activation of proto-oncogenes in proximity of the integration site, and clonal expansion culminating in leukemic transformation of modified hematopoietic cells (24). These events, while rare, mandate the incorporation of safety elements in vector design including insulators (25) or internal promoters with self-inactivating long terminal repeats (LTR) lacking strong enhancers (26-28). An additional concern particular to T-cell immunotherapy is that the introduction of a self-antigen-specific TCR or CAR has the potential to induce an auto-immune reaction. There have been several reports of cytokine storm syndrome after the transplant of CAR-transduced T cells (29, 30) which may benefit from an approach to decrease the number of transgenic cells through the use of a suicide gene. Immunotherapy is designed to focus primarily on tumor-specific antigens, though low level of these antigens may be expressed by normal tissue leading to unintended off-target reactivity. In clinical trials targeting melanoma by transfer of T-cells engineered to express a human TCR against the <sup>27-35</sup>MART-1 peptide, acute skin rash and auto-immune vitiligo are often observed due to reaction against normal melanocytes that also express the MART-1 antigen (31). More concerning is the recent report of the death of two patients in a clinical trial using autologous T-cells modified with an affinity-enhanced TCR against the MAGE3 antigen due to unpredicted reactivity to cardiac Titin (32). The possibility of occult cytotoxicity of the TCR or CAR further supports the inclusion of a method to eliminate gene-modified cells *in vivo*.

Suicide genes can be incorporated as a safety switch to selectively ablate gene-modified cells during an adverse event. These have been demonstrated in the setting of clonal outgrowth from activation of a proto-oncogene (33) and graft versus host disease (GvHD) and on-target/off-organ cytotoxicity (34). Selective uptake of DNA replication chain terminator drugs by engineered nucleoside kinases such as native or modified herpes-simplex-virus-thymidine-kinase (sr39TK) (35), initiation of apoptosis mediated by inducible caspase systems by chemical dimerizers (36, 37), or surface proteins designed as antibody targets (38) have all been used to eliminate gene-modified cells. sr39TK (39) is advantageous over other modalities in that it additionally serves as a positron emission tomography (PET) reporter gene, allowing *in vivo* imaging to non-invasively track gene modified cells using radio-labeled substrates such as 9-(4-[<sup>18</sup>F]-fluoro-3-[hydroxymethyl]butyl)guanine ([<sup>18</sup>F]-FHBG) (40). Despite clear potential benefit, the characterization of the utility of sr39TK as both a PET reporter and suicide gene in human HSCs and their progeny has yet to be demonstrated.

Here we report the use of a lentiviral vector encoding sr39TK to gene-modify human HSCs, demonstrate a lack of developmental skewing due to the transgene; visualization of gene-modified HSCs and their progeny at high resolution serial scans *in vivo*; and the ablation of gene-modified cells in hematopoietic tissues after a single course of the pro-drug GCV as evaluated by biochemical, cell-biological, and molecular biological techniques. These results lend support for the inclusion of sr39TK in clinical trials for the modification of HSCs with a cancer-antigen reactive TCR or CAR to both monitor successful transplant and provide a safety-feature allowing the ablation of cells during a serious adverse event.

## **Materials and Methods**

### ***HSC Transduction***

Cells were thawed in a 37°C water bath and transferred to 50ml tubes. X-VIVO-15 was added drop-wise with agitation to dilute thawed cell product 1:10. Cells were spun at 500g for 5min and supernatant was aspirated. Cells were resuspended in 50ml X-VIVO-15 and counted using a ViCELL Cell Viability Analyzer (Beckman Coulter, Brea, CA). Cells were spun down at 500g for 5min, and supernatant was aspirated. Cells were resuspended in X-VIVO-15 + [50ng/ml] SCF, [50ng/ml] Flt3-L, [50ng/ml] TPO, and [20ng/ml] IL-3 (Peprotech, Rocky Hill, NJ) at a density of  $4 \times 10^6$  cells/ml. Twenty-four-well non-tissue-culture treated plates coated with RetroNectin (TaKaRa, Shiga, Japan) were seeded with 0.25ml ( $1.0 \times 10^6$  cells) of cell suspension and incubated overnight. The following day, concentrated NY-ESO-1-TCR/sr39TK lentiviral prep was added for a final vector concentration of  $1.0 \times 10^8$  TU/ml in a final volume of 500ul X-VIVO-15 + cytokines as described above. Cells were incubated overnight. The following day, cells were collected from wells and rinsed thrice in X-VIVO-15 without cytokines. Cells were counted, and resuspended at a density of  $2.0 \times 10^7$  cells/ml in X-VIVO-15 + cytokines as described above.

### ***Generation of Humanized Mice***

Humanized mice were generated by the intrahepatic transfer of  $1.0 \times 10^6$  NY-ESO-1-TCR/sr39TK- or mock-transduced CD34+ PBSCs to neonatal NSG-HLA-A2.1 mice on day 3-5 post-birth using a 28G tuberculin syringe(18). Neonates were preconditioned immediately before injection with 100cGy irradiation from a  $^{137}\text{Cs}$  source (JL Shepherd, San Fernando, CA). For tissue harvest, animals were euthanized by 5% CO<sub>2</sub> asphyxiation immediately before dissection.

Single cell suspensions of thymus and spleen were prepared by dissociating organs with a 3ml syringe plunger over 70um mesh in FACS buffer (DPBS, 2% FBS, 2mM EDTA) . Individual bones (femurs, humeri, and sternum) were kept separate to investigate potential differences in marrow spaces by flow cytometry and ddPCR. Marrow spaces were flushed with a 23G needle through 70uM mesh. Cells were enumerated and  $1 \times 10^6$  splenocytes,  $1 \times 10^6$  cells from the marrow, and  $1 \times 10^5$  thymocytes were stained with antibodies as described below. Immunological cytotoxicity assays were performed as previously described(41).

### ***Flow Cytometry***

Blood was drawn from the retro-orbital sinus using heparin coated capillary tubes (Thermo Fisher, Waltham, MA). The following antibodies (Becton Dickinson (BD), Laguna Hills, CA) were used to assess human engraftment: murine CD45-V500 clone 30-F11, human CD45-V450 clone HI30, human CD19-PE-Cy7 clone SJ25C1, human CD3-PerCP clone SK7, human CD4-APC clone RPA-T4, and human CD8-FITC clone HIT8a. Expression of the NY-ESO-1-TCR was determined by binding to a PE-labeled HLA-A2.1 MHC-tetramer loaded with the <sup>157-165</sup>NY-ESO-1 SLLMWITQC (Beckman Coulter, Brea, CA). Antibodies were added to 80ul whole blood, incubated in the dark for 30min, RBC lysed with 1ml FACS Lyse (BD), washed with 3ml FACS buffer, spun at 500g for 5min, and resuspended in 250ul FACS buffer. Data were acquired on a FACS Fortessa (BD). Analysis was performed on an average of 2,000 to 10,000 hCD45+ cells per 80ul peripheral blood drawn per mouse.



### ***PET Scan***

[<sup>18</sup>F]-FHBG was synthesized as described(42). Mice were injected IV with 250 $\mu$ Ci [<sup>18</sup>F]-FHBG in 50-100 $\mu$ l, and allowed a 3h conscious uptake. Mice were anesthetized with 2% isoflurane for sequential imaging in the Siemens Preclinical Solutions MicroPET Focus 220 and MicroCAT IICT (Siemens Malvern, PA). PET data were acquired for 10 min and reconstructed with a filtered background projection probability algorithm. PET/CT images were co-registered. Quantification of PET signal was performed by drawing 3D regions of interest (ROIs) using AMIDE software (<http://amide.sourceforge.net/>). MAP projections were generated for display in figures. The max intensity of the muscle ROI, based on the percent injected dose per gram, was subtracted from each hematopoietic niche ROI to normalize for background. Images are presented in false-color volumetric renderings generated in AMIDE.

### ***Statistical Analysis***

Descriptive statistics for quantitative variables such as the mean and standard error by experimental groups were summarized and presented. Differences between experimental groups were assessed by unpaired t-test (Figures 2a-2g) or pairwise comparison (Figures 6a-6d) within the framework of one-way analysis of variance (ANOVA). To account for variation from individual animals, linear mixed effect models with random intercept (43) were used to evaluate the between-experimental group difference (Figures 5a-5c, Figures 6e-6f) as well as pre- and post-treatment difference (Figures 5a-5c). For all statistical investigations, tests for significance were 2-tailed unless otherwise specified. A p-value less than the 0.05 significance level was considered to be statistically significant. All statistical analyses were performed using SAS version 9.3 (SAS, Cary, NC).

## Results

### **NY-ESO-1-TCR/sr39TK modified human HSCs engraft in NSG-A2.1 mice and generate functional NY-ESO-1 reactive T-cells *in vivo***

To test the function of sr39TK, we generated a lentiviral vector composed of a codon optimized NY-ESO-1-TCR linked by a 2A cleavage-peptide to sr39TK (ESO/TK) driven by the strong retroviral long-terminal-repeat promoter MSCV (**Figure 1A**). Humanized mice were generated by transplanting neonatal NSG-A2.1 mice with ESO/TK transduced CD34 enriched peripheral blood stem cells (PBSC) via intrahepatic injection (**Figure 1B**). At two months post-transplant, mice were screened by peripheral blood immunophenotyping. Human cell chimerism in the mice was determined by evaluating lymphocytes for human CD45% divided by total (human+murine) CD45%. Human cells were gated into hCD19+ B-cells and hCD3+ T-cells, and the CD3+ population was sub-fractionated to CD4 helper and CD8 cytotoxic subsets with the NY-ESO-1 tetramer binding activity of each assayed (**Figure 1C**). The transplant of PBSCs to neonatal NSG-A2.1 mice resulted in human chimerism in peripheral blood beginning at 2 months post-transplant. The transduction of PBSCs with an ESO/TK lentiviral vector did not result in a significant change in total human cell chimerism nor alter the composition of human lymphoid cells (**Figure 2A-E** and **Supplemental Table 1**). NY-ESO-1-TCR+ cells, identified by co-staining with the <sup>157-165</sup>NY-ESO-1 HLA-A2.1 tetramer, were only observed in the animals transplanted with gene-modified cells. CD4+ T-cells bearing NY-ESO-1-TCR were not observed (**Figure 2F**). CD8+ NY-ESO-1-TCR bearing cells developed solely in the ESO/TK-transduced group, and 8 out of 15 mice had readily detectable TCR-positive CD8 T-cells in the periphery as early as 2 months post-transplant (**Figure 2G**).

To validate the effector function of NY-ESO-1-TCR bearing T cells developed *in vivo* from transduced HSCs, experimental mice were harvested, splenocytes dissociated, and expanded by co-culture with artificial antigen presenting cells loaded with the <sup>157-165</sup>NY-ESO-1 peptide. Controls were generated from healthy adult donor peripheral blood T-cells activated by CD3/CD28 beads and transduced with the ESO/TK vector or mock transduced. *Ex vivo* expanded splenocytes from humanized mice or control human T-cells were co-cultured with non-HLA-A2.1 (M257) or HLA-A2.1 (M257/A2.1 and M407) patient derived melanoma cell lines expressing the NY-ESO-1 antigen. <sup>51</sup>Chromium release assays to assess cytotoxicity revealed humanized mouse derived T-cells killed target cells in an HLA-restricted fashion (**Figure 3A, 3B**), comparable to control normal donor T-cells transduced with the NY-ESO-1-TCR (**Figure 3C**). Minimal background cytotoxicity in non-transduced donor T-cells was observed (**Figure 3D**). ELISA assays revealed similar results, with both humanized mouse derived- and healthy donor transduced NY-ESO-1 antigen-specific T-cells secreting the effector cytokine interferon-gamma when cultured in the presence of target cells (**Figure 3E**).

A subset of mice were selected for PET imaging studies (non-transduced humanized N=3, ESO/TK-transduced humanized N=10) based on equivalent human chimerism and lymphocyte composition, with an additional (N=3) non-transplanted age-matched NSG-A2.1 control animals to examine background biodistribution.

### **sr39TK shows selective uptake of [<sup>18</sup>F]-FHBG *in vivo***

The PET reporter/suicide gene sr39TK is an engineered herpes-simplex-virus-thymidine-kinase with approximately 300x greater affinity for GCV than wild type HSV-TK (44). The ESO/TK vector was first tested in Jurkat cells *in vitro*. Cells transduced at an MOI of 10 and 100

expressed the NY-ESO-1-TCR (**Supplemental Figure 1A**), showed selective uptake of [<sup>18</sup>F]-FHBG (**Supplemental Figure 1B**), and were selectively killed by GCV (**Supplemental Figure 1C**) confirming the functional activity of the ESO/TK vector.

To test the function of sr39TK as a PET reporter/suicide gene *in vivo*, we designed an experiment to serially scan humanized mice with the PET reporter [<sup>18</sup>F]-FHBG before and after treatment with the prodrug Ganciclovir (GCV) followed by investigation of cell composition by cell- and molecular-biological methods (**Figure 3A**). Non-transplanted NSG-A2.1 mice and transplant recipients of mock transduced or ESO/TK gene-modified human PBSC were injected with 250 $\mu$ Ci [<sup>18</sup>F]-FHBG and imaged on a Siemens MicroPET scanner followed by CT scan for overlay. Non-transplanted NSG-A2.1 mice were imaged to determine background biodistribution of [<sup>18</sup>F]-FHBG, which is known to have a high background in the abdominal area due to the probe elimination through the biliary tree and the GI tract in mice (45). As expected, non-humanized NSG-A2.1 mice exhibited predominantly gastrointestinal tract (GI), gall bladder, and bladder signal, with no signal in presumptive hematopoietic niches, or areas of high metabolic activity such as the brain or heart (**Figure 3B**). Evaluation of uptake in the spleen was occluded by GI signal. Non-transduced humanized mice showed similar background biodistribution of [<sup>18</sup>F]-FHBG probe, and lack of hematopoietic niche signal (**Figure 3C**). In contrast, mice humanized with ESO/TK transduced PBSCs exhibited strong signal in hematopoietic compartments (i.e. long bones, skull, vertebrae, and thymus) in addition to background GI biodistribution (**Figure 3D**). Signal quantitation was performed in Amide software by drawing 3-dimensional regions of interest (ROI) on individual femurs, humeri, the thymus, and arm muscle (**Supplemental Figure 2A**). The maximum percent injected dose/g (%ID/g) was determined for each ROI, and muscle was subtracted from hematopoietic niche ROIs to normalize background

tissue uptake. Significant accumulation of probe in ROIs was observed in hematopoietic compartments in the ESO/TK-transduced cohort vs. the non-transduced humanized group (**Supplemental Figure 2B**).

### **Gene-modified cells are selectively ablated by GCV**

To test the suicide gene function of sr39TK in transduced human cells *in vivo*, previously scanned non-transduced humanized mice and ESO/TK-transduced humanized mouse cohorts were treated intraperitoneally for 5 days with vehicle or [50mg/kg] of the nucleoside prodrug GCV which is converted to a cytotoxic nucleotide when phosphorylated by sr39TK. PET/CT imaging was performed one week after the final drug injection to allow ablation of gene-modified cells and clearance of residual GCV. Vehicle treated ESO/TK mice demonstrated specific uptake in hematopoietic niches in pre- and post-treatment scans (**Figure 4A**); however, GCV completely ablated PET signal in post-treatment scans in all hematopoietic niches previously observed to harbor probe accumulation in ESO/TK-transduced humanized mice (**Figure 4B**). No difference in signal accumulation was detected in pre- and post-treatment scans in the non-transduced humanized cohort (**Supplemental Figure 2C**). Vehicle treated ESO/TK-transduced recipient mice showed no significant difference in signal accumulation in hematopoietic compartments as determined by pre- and post-treatment scans (**Figure 4C**). GCV treated ESO/TK-transduced recipient mice showed significant ablation of [<sup>18</sup>F]-FHBG PET signal in hematopoietic compartments in post-treatment scans (**Figure 4D**). The post-treatment signal of GCV treated ESO/TK mice were not significantly different than background uptake in non-transduced humanized mice.

Animals were euthanized one day after the final scan, and tissues were collected and dissociated. Cell suspensions were enumerated, and allocated for subsequent analyses. Flow cytometry of splenocytes to measure chimerism revealed human cells present in all cohorts; non-transduced humanized, vehicle treated- and GCV-treated ESO/TK-transduced humanized mice. There was not a significant reduction of human chimerism in GCV treated ESO/TK mice (**Figure 5A**). CD19 B-cells and CD3 T-cells were detected in all cohorts at endpoint analysis with no significant difference between vehicle and GCV treated ESO/TK mice (**Figures 5B,C**). In contrast, NY-ESO-1-TCR bearing CD3+CD8+ T-cells were reduced to background levels in the GCV treated ESO/TK-transduced humanized mice (**Figure 5D**).

Quantitation of PET signal and flow cytometric analyses demonstrated ablation of gene-modified cells while sparing non-modified cells. However, cells with low metabolic activity may not be sensitive to drug selection nor show specific uptake of [<sup>18</sup>F]-FHBG. In addition, as surface TCR expression requires co-expression of CD3, flow cytometry is unable to measure the presence of this transgene in non-T-cells. In order to investigate persistence of other gene-modified cells, quantitative PCR was performed to measure the amount of lentiviral vector psi element per human genome in each organ compartment. No vector genomes were detected in non-transduced humanized mice (**Figure 5E**). The amount of vector present in the ESO/TK-transduced mice treated with vehicle varied among different animals (mean=0.918±0.131, range=0.552–1.72), but was relatively consistent among the different tissues tested for each recipient (**Figure 5F**). In the cohort treated with a course of GCV, there was a significant reduction of integrated vector (mean=0.123±0.131) compared with the vehicle treated cohort (**Figure 5G**) (P<0.001).

## Discussion

Gene therapy using HSCs has proven to be an efficacious treatment for monogenetic diseases, and is currently of interest for immunotherapy applications. Pre-clinical studies have provided evidence that HSCs transduced to express a transgenic TCR are capable of producing antigen specific effector T-cells *in vivo* paving the way for a first-in-man study nearing Phase I clinical trial (CIRM Disease Team Grant DR2A-05309). However, several questions remain. Enthusiasm for engineered immunity is tempered by the possibility of on-target/off-organ reactivity of the modified cells, and the cautionary tales of clonal outgrowth in HSC gene therapy patients merit the inclusion of safety measures in vector design. The inclusion of a suicide gene could provide a safety switch capable of ablating gene-modified cells in the event of undesirable off-target reactivity or clonal transformation. The ability to non-invasively track gene-modified cells *in vivo* would allow early detection of successful engraftment, active thymopoiesis, and homing to tumor tissue.

The humanized mouse allows the study of HSCs and development of their progeny *in vivo*. We used this model system to investigate the potential application of the PET reporter/suicide gene sr39TK in the setting of HSC based engineered immunotherapy to non-invasively locate and ablate gene modified cells. We observed no detrimental effect of lentiviral transduction with the ESO/TK vector on the engraftment of PBSCs as evidenced by equivalent human chimerism and lymphoid composition between transduced and mock transduced cohorts. Detection of gene-modified cells by PET was ubiquitous in ESO/TK transduced humanized mice (N=15), though only 8/15 (53.33%) had detectable NY-ESO-1-TCR+ cells in peripheral blood at 2-months post-transplant. Therefore, PET imaging allowed early assessment of engraftment of

gene-modified cells before NY-ESO-1-TCR+ cells have developed and migrated to the periphery in sufficient numbers for flow cytometric analysis.

A previous report used bioluminescent imaging and the luciferase reporter to visualize gene-modified human HSCs and their progeny residing in hematopoietic niches in a humanized mouse model (46). Our work expands on this pioneering study by using PET imaging, a higher-resolution, directly clinically translatable approach to locate human HSCs *in vivo*. HSCs modified to express sr39TK were observed in hematopoietic niches, such as the long bones of the arms and legs and the thymus after dosing with [<sup>18</sup>F]-FHBG. Strong sternal signal in mice led us to include this hematopoietic niche in our harvests, a practice not routinely performed in humanized mouse studies yet an abundant source of hematopoietic cells. Punctate murine vertebral marking with engraftment of vector-bearing cells (**Supplemental Figure 3**) directly demonstrates the high-resolution possible with this imaging technology. The limit of detection using [<sup>18</sup>F]-FHBG as a probe with the HSV-sr39TK PET reporter gene was previously determined to be  $1 \times 10^6$  cells/mm<sup>3</sup>(47). The thymus of a well-engrafted humanized mouse is populated by approximately  $2.5 \times 10^6$  human thymocytes, the majority of which are TCR positive in transduced cohorts, and is approximately 1mm<sup>3</sup> in volume (EHG unpublished observation). In the clinical setting, the number of transduced cells along with the richer soil of a human host for transduced/transplanted human HSCs is likely to result in robust PET imaging in excess of seen in our humanized mouse study.

While the immunogenicity of sr39TK has been reported in human studies of gene modified T-cells (48, 49), in the setting of gene modified HSCs, *de novo* generated DCs may home to the thymus and induce tolerance to the introduced gene product (50). Currently, only *in silico* predictive models of human immunogenicity exist, and the only true test is to evaluate the



development of an immune reaction to a transgene in clinical trials. Still, there are alternative approaches that do not rely on viral-derived or otherwise xenogeneic reporter genes (37, 51).

Although PET signal was completely ablated after GCV treatment, we detected a small amount of vector-containing cells in harvested hematopoietic compartments by qPCR. This may indicate that some transduced HSCs were GCV resistant and generated new cells post-GCV treatment. Longitudinal studies to examine these possibilities in small animals are technically difficult owing to the paucity of human cells generated, though a recent study examining sr39TK mediated ablation of rhesus macaque HSCs provides evidence that a single round of GCV is sufficient to ablate stem cells (52). The elimination of the majority of modified cells should be sufficient to control major toxicities.

sr39TK allows evaluation of successful engraftment of gene-modified HSCs *in vivo* with high resolution, and the detection of thymic engraftment indicative of developing anti-cancer TCR expressing T-cells. It may further be used to examine the homing of gene-modified T-cells to intended tumor targets and eradication of disease. In the event of off-target cytotoxicity by engineered T-cells, GvHD, or insertional oncogenesis, the suicide gene function of sr39TK could be harnessed to eliminate modified cells while importantly sparing the remaining unmodified graft. Our study supports the hypothesis that a clinical approach to engineered HSC immunotherapy would benefit from the inclusion of an imaging/suicide gene.

## **Acknowledgments**

These studies were supported by awards from the National Cancer Institute, NIH (PO1 CA132681). EHG and MNM are supported by the Broad Stem Cell Research Center (BSCRC) – California Institute of Regenerative Medicine (CIRM) TG2-01169. AR is supported by the CIRM New Faculty Award RN2-00902-1. ONW is an investigator of the Howard Hughes Medical Institute. We acknowledge the BSCRC for administrative and infrastructure support, Jessica Scholes and Felicia Codrea of the BSCRC Flow Cytometry Core for technical assistance, Dr. Sam Sadeghi and Jeffery Collins for radiosynthesis of [<sup>18</sup>F]-FHBG, and Dr. Waldemer Lando, Dr. David Stout, and Darrin Williams in the Crump Institute for Molecular Imaging facility for their technical help with PET/CT scans. We thank the Cell Processing and Manipulation Core in the Translational Cores, Physicians and Nurses at Cincinnati Children's Hospital Medical Center (CCHMC), and the CCHMC Translational Research Trials Office. This paper is dedicated to the memory of CW.

## **Authorship Contributions**

EHG, MNM, RPH, AR, ONW, and DBK designed research. EHG, MNM, MLK, NS, RCK, and TC performed research. MLK, MH, RPH, RCK, TC, and AR contributed vital reagents. EHG, MNM, and XW analyzed data. EHG and DBK wrote the paper, and MNM, XW, AR, and ONW contributed significantly to manuscript preparation.

## **Disclosure of Conflicts of Interest**

The authors declare no competing financial interests.

## Figure Legends

**Figure 1. Experimental system to test ESO/TK PET reporter and suicide gene function *in vivo*.** (A) Schematic of lentiviral vector used to engineer HSCs to express the ESO/TK transgene. (B) CD34 enriched G-CSF mobilized peripheral blood stem cells from healthy donors were stimulated overnight then transduced with a lentivirus encoding the ESO/TK vector. The next day, cells were transplanted to irradiated NSG-A2.1 neonates by intrahepatic injection. Two months post-transplant, peripheral blood was screened for human chimerism and lymphoid development by flow cytometry. (C) Cells were first gated on the characteristic lymphocyte SSC x FSC profile, followed by examination of murine and human CD45 to exclude non-nucleated cells. Human CD45+ cells were examined for hCD19 to identify B- and hCD3 to identify T-lineage cells. T-cells were gated into separate hCD4 helper and hCD8 effector subsets, and evaluated for their ability to bind the NY-ESO-1 tetramer as indicative of TCR expression.

**Figure 2. Human cells develop in NSG-A2.1 mice transplanted with PBSCs.** Non-transduced and ESO/TK transduced PBSC transplanted humanized mouse peripheral blood was assayed by flow cytometry at 2 months post-transplant. No significant difference was observed in proportions of (A) human chimerism, (B) B-cells, (C) T-cells, (D) the CD4 subset, (E) or the CD8 subset of T-cells. (F) NY-ESO-1-TCR bearing CD4 cells were not observed. (G) NY-ESO-1-TCR bearing CD8 T-cells developed only in the ESO/TK cohort.

**Figure 3. Effector function of *in vivo* derived NY-ESO-1-TCR bearing cells from HSCs.** *Ex vivo* expanded splenocytes from ESO/TK humanized mice were evaluated alongside ESO/TK

transduced or mock transduced normal donor PBMCs.  $^{51}\text{Cr}$  release assays were performed on (A,B) splenocytes from ESO/TK humanized mice (ms1 and ms2), (C) healthy donor ESO/TK transduced T-cells, and (D) mock transduced T-cells cocultured with HLA mismatched (M257) or HLA matched (M257/A2.1 and M407) melanoma cell lines. (E) IFN $\gamma$  ELISA was performed to validate results from cytotoxicity assays.

**Figure 4. High-resolution sr39TK PET reporter imaging of gene-modified cells *in vivo*.** (A)

Experimental procedure for PET imaging. Mice were injected with 250uCi [ $^{18}\text{F}$ ]-FHBG and PET/CT imaged. Scans of (B) non-transplanted NSG-A2.1, (C) non-transduced humanized, and (D) ESO/TK-transduced humanized mice. Probe was detected in the gastrointestinal tract and gall bladder in all mice. In ESO/TK-transduced humanized mice, signal was detectable in the long bones of the arms and legs, the sternum, the thymus, and vertebrae.

**Figure 5. GCV ablates gene modified cells hematopoietic niches.** Mice were PET/CT scanned

with [ $^{18}\text{F}$ ]-FHBG before and 7d after treatment with (A) vehicle or (B) GCV. Three of five representative vehicle treated mice and five of five GCV treated mice are shown. Neutral density masks were drawn to visually mute background GB and GI signal. ROIs were drawn on femurs, humeri, and the thymus of each mouse in pre- and post-treatment scans. (C) ESO/TK mice treated with vehicle showed no significant difference between pre- and post-treatment scans (P=0.402). (D) There was a significant decrease in [ $^{18}\text{F}$ ]-FHBG PET signal in hematopoietic ROIs in ESO/TK mice treated with GCV (P<0.001).

**Figure 6. Immunophenotyping and VCN analysis after drug treatment.** Harvested splenocytes from non-transduced humanized, vehicle treated ESO/TK-transduced humanized, and GCV treated ESO/TK-transduced humanized mice were evaluated by flow cytometry. No significant difference was observed for (A) human chimerism, (B) human B-cell or (C) T-cell composition. (D) A significant decrease of CD8+NY-ESO-1-TCR+ cells was observed after GCV treatment in the ESO/TK group (P=0.006). (E-G) VCN analysis of gDNA harvested from the sternum, thymus, femurs, humeri, and spleen were measured for each treatment group.

## Supplemental Material

**Supplemental Table 1.** Total human chimerism and lymphoid composition in NSG recipients of ESO/TK-transduced or non-transduced PBSC.

	<b>Non-Transduced</b>	<b>ESO/TK-Transduced</b>
<b>Total PB Chimerism</b> <b>(% of lymphocytes)</b>	35.44±10.60%	32.00±2.97%
<b>CD19+ B Cells</b>	70.94±15.09%	69.47±6.24%
<b>CD3+ T Cells</b>	7.70±5.55%	8.49±4.03%
<b>% CD4+/CD3+ T Cells</b>	22.36±8.09%	35.67±10.23%
<b>% CD8+/CD3+ T Cells</b>	19.74±6.63%	31.59±4.93%

**Supplemental Figure 1. Validation of sr39TK function in Jurkat cells.** (A) Mock or ESO/TK transduced Jurkats were evaluated by flow cytometry for NY-ESO-1 tetramer binding. (B) Cells were cultured with 0.5 $\mu$ Ci [ $^{18}$ F]-FHBG for 1 hour, washed, and evaluated for uptake. (C) Cells were cultured in half-log increasing concentrations of GCV for 48h and evaluated for viability.

**Supplemental Figure 2. ROI Analysis.** (A) Schematic of ROIs drawn on PET imaged mice. 3d cylindrical or spherical ROIs were drawn using Amide software on hematopoietic niches to determine probe uptake and arm muscle for background subtraction. (B) There was significant [ $^{18}$ F]-FHBG uptake in the hematopoietic niches of ESO/TK mice compared with mock

transduced controls. (C) [<sup>18</sup>F]-FHBG uptake in non-transduced humanized mice before and after GCV treatment.

### **Supplemental Figure 3. Chimerism, vector marking, and PET probe signal in vertebrae.**

(A) Cells harvested from individual vertebrae were evaluated for human chimerism by flow cytometry and vector marking by qPCR. (B) Data were matched with [<sup>18</sup>F]-FHBG PET scan.

### **Supplemental Methods**

#### ***NY-ESO-1-TCR/sr39TK vector cloning and virus production***

The TCR recognizing the NY-ESO-1 cancer/testes antigen has been previously described (1). Modifications to this self-inactivating (SIN) lentiviral vector include codon optimization of the 2A-linked TCR alpha and beta cDNA and 2A linkage to a codon-optimized sr39TK sequence, internal Murine Stem Cell Virus (MSCV) LTR promoter, and the WPRE (ESO/TK). Large-scale manufacture of concentrated lentivirus using a 2<sup>nd</sup> generation self-inactivating HIV-1 vector system was performed as described previously (2). Briefly, 239T cells were transfected with (150ug) ESO/TK transfer plasmid, (150ug) p8.9 HIV-1 gag-pol expression plasmid, and (30ug) pMD-G VSV-G expression plasmid. One day following transfection, sodium butyrate induction was performed for 8h. Viral supernatant was harvested on d4 and d5 of production, followed by 2000-fold concentration by tangential flow filtration (SpectrumLabs, CA) with diafiltration to 10% X-VIVO-15 medium (Lonza, Walkersville, MD). qPCR titers on HT29 cells of concentrated preps ranged from 7.6x10<sup>8</sup> TU/ml-4.0x10<sup>9</sup> TU/ml.

#### ***NSG-A2.1 Mice***

NSG mice harboring a transgene encoding the human HLA-A2.1 protein covalently linked to human beta 2 microglobulin (NOD.Cg-Prkdcscid Il2rgtm1Wjl Tg(HLA-A/H2-D/B2M)1Dvs/SzJ, Stock number 014570) were obtained from The Jackson Laboratory (Bar Harbor, ME) (3). Mice were bred, housed, and monitored according to UCLA Department of Laboratory Animal Medicine standards.

### ***Transduction of Jurkat cells and uptake assay***

Jurkat cells (ATCC TIB-152) were transduced with the ESO/TK lentiviral vector at an MOI of 10 and 100, cultured for 2 weeks, and assayed for surface TCR expression by tetramer staining to validate transduction. Mock transduced, MOI-10 and MOI-100 transduced Jurkats were cultured in 0.5 $\mu$ Ci [ $^{18}$ F]-FHBG for 1hr, cells were washed 3X, and resuspended in 1ml culture medium. Uptake was measured on a Wallac WIZARD scintillation counter (Perkin Elmer, Waltham, MA) using RiaCalc WIZ software (Perkin Elmer).

### ***HSC Isolation and Purification***

G-CSF mobilized peripheral blood units were purchased from Cincinnati Children's Hospital Medical Center and processed with the CliniMACS CD34 Reagent System, CD34 Kit, and Tubing System (Miltenti, Auburn, CA) per manufacturer's instructions. Approximately  $3.44 \times 10^9$  CD34+ cells were obtained from approximately 150ml apheresis product at a purity of >98% as assessed by flow cytometry. Aliquots of  $5.0 \times 10^6$  cells were frozen in Pentastarch + 10% DMSO at -80C overnight then transferred to liquid nitrogen for long-term storage.

### ***VCN Analysis***

Vector copy number was determined by digital droplet quantitative PCR (ddPCR) for the lentiviral psi element (FWD: AAG TAG TGT GTG CCC GTC TG, REV: CCT CTG GTT TCC CTT TCG CT, PRO: 5'-FAM / CCC TCA GAC / ZEN / CCT TTT AGT) and normalized to the



endogenous human SDC4 reference gene (FWD: CAG GGT CTG GGA GCC AAG T, REV: GCA CAG TGC TGG ACA TTG ACA, PRO: 5'-HEX / CCC ACC GAA CCC AAG AAA CTA). Genomic DNA was extracted using the NucleoSpin Tissue kit (Macherey Nagel, Bethlehem, PA). PCR using 200ng genomic DNA template, [400nM] primers and [100nM] probe, and 1000U *DraI* per reaction was digested for 1hr at 37C. Digested pre-PCR reactions were run through the QX100 Droplet Generator (BioRad, Hercules, CA) followed by the following reaction conditions: 95C for 10min, [94C for 30sec, 60C for 1min] for 55 cycles, 98C for 10min, and 12C hold on a T100 thermal cycler (BioRad). Droplets were read on a QX100 Droplet Reader (BioRad).

### Supplemental References

1. Robbins, P.F., Li, Y.F., El-Gamil, M., Zhao, Y., Wargo, J.A., Zheng, Z., Xu, H., Morgan, R.A., Feldman, S.A., Johnson, L.A., et al. 2008. Single and dual amino acid substitutions in TCR CDRs can enhance antigen-specific T cell functions. *J Immunol* 180:6116-6131.
2. Cooper, A.R., Patel, S., Senadheera, S., Plath, K., Kohn, D.B., and Hollis, R.P. 2011. Highly efficient large-scale lentiviral vector concentration by tandem tangential flow filtration. *J Virol Methods* 177:1-9.
3. Shultz, L.D., Saito, Y., Najima, Y., Tanaka, S., Ochi, T., Tomizawa, M., Doi, T., Sone, A., Suzuki, N., Fujiwara, H., et al. 2010. Generation of functional human T-cell subsets with HLA-restricted immune responses in HLA class I expressing NOD/SCID/IL2r gamma(null) humanized mice. *Proc Natl Acad Sci U S A* 107:13022-13027.

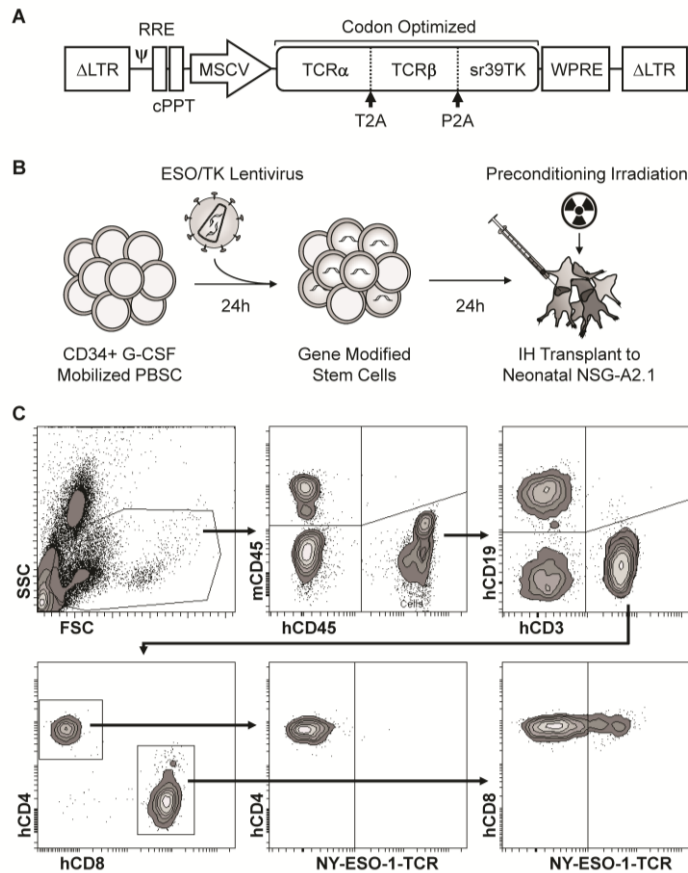


**Figure 1. Experimental system to test ESO/TK PET reporter and suicide gene function *in vivo*.** (A) Schematic of lentiviral vector used to engineer HSCs to express the ESO/TK transgene. (B) CD34 enriched G-CSF mobilized peripheral blood stem cells from healthy donors were stimulated overnight then transduced with a lentivirus encoding the ESO/TK vector. The next day, cells were transplanted to irradiated NSG-A2.1 neonates by intrahepatic injection. Two months post-transplant, peripheral blood was screened for human chimerism and lymphoid development by flow cytometry. (C) Cells were first gated on the characteristic lymphocyte SSC x FSC profile, followed by examination of murine and human CD45 to exclude non-nucleated cells. Human CD45<sup>+</sup> cells were examined for hCD19 to identify B- and hCD3 to identify T-lineage cells. T-cells were gated into separate hCD4 helper and hCD8 effector subsets, and evaluated for their ability to bind the NY-ESO-1 tetramer as indicative of TCR expression.

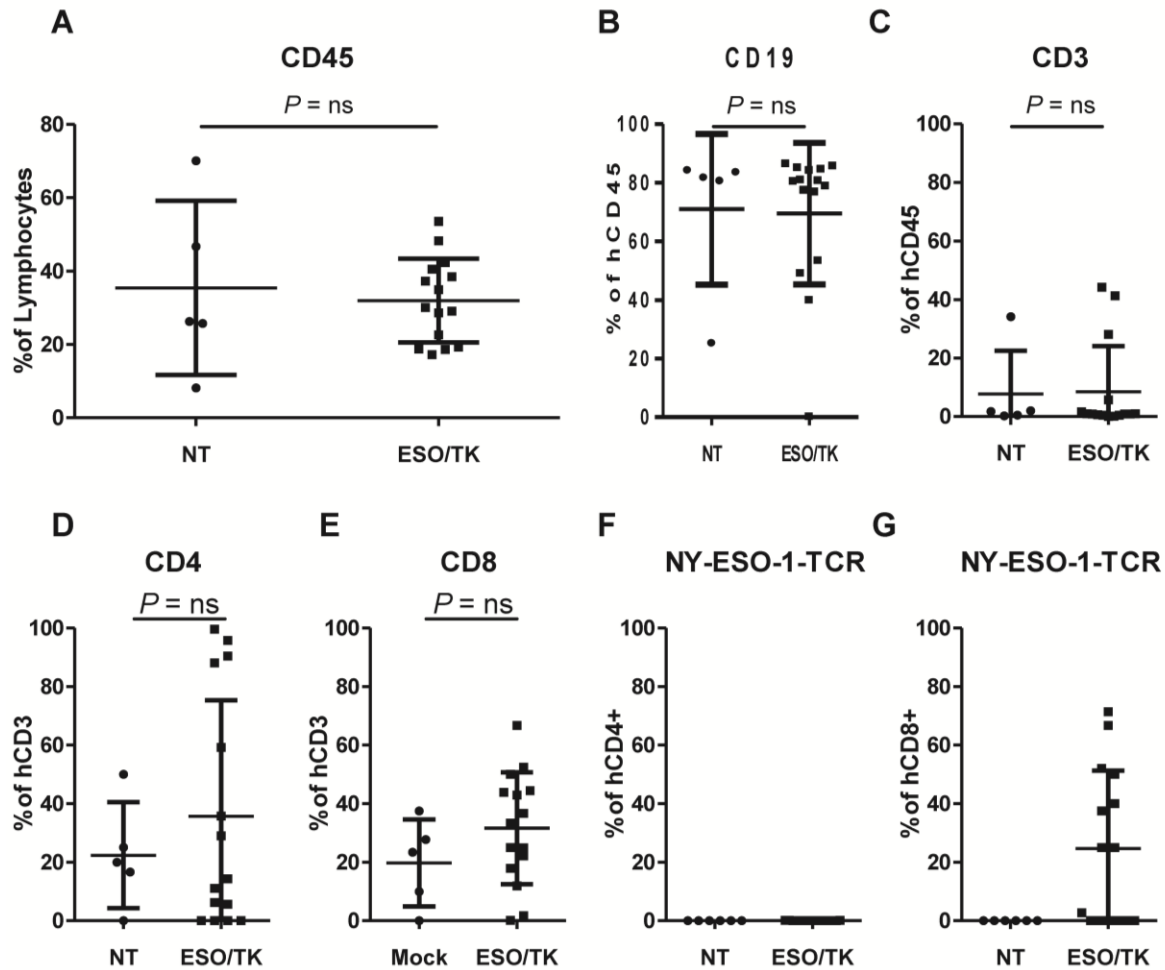


**Figure 2. Human cells develop in NSG-A2.1 mice transplanted with PBSCs.** Non-transduced and ESO/TK transduced PBSC transplanted humanized mouse peripheral blood was assayed by flow cytometry at 2 months post-transplant. No significant difference was observed in proportions of (A) human chimerism, (B) B-cells, (C) T-cells, (D) the CD4 subset, (E) or the CD8 subset of T-cells. (F) NY-ESO-1-TCR bearing CD4 cells were not observed. (G) NY-ESO-1-TCR bearing CD8 T-cells developed only in the ESO/TK cohort.

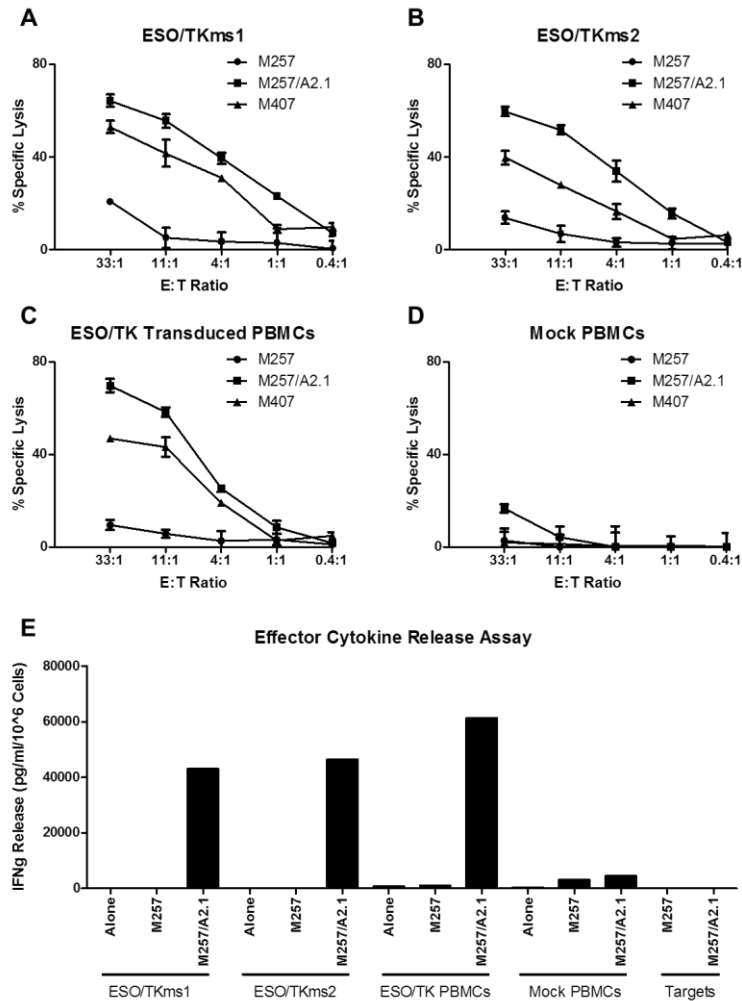


**Figure 3. Effector function of *in vivo* derived NY-ESO-1-TCR bearing cells from HSCs.** *Ex vivo* expanded splenocytes from ESO/TK humanized mice were evaluated alongside ESO/TK transduced or mock transduced normal donor PBMCs. <sup>51</sup>Cr release assays were performed on (A,B) splenocytes from ESO/TK humanized mice (ms1 and ms2), (C) healthy donor ESO/TK transduced T-cells, and (D) mock transduced T-cells cocultured with HLA mismatched (M257) or HLA matched (M257/A2.1 and M407) melanoma cell lines. (E) IFN $\gamma$  ELISA was performed to validate results from cytotoxicity assays.

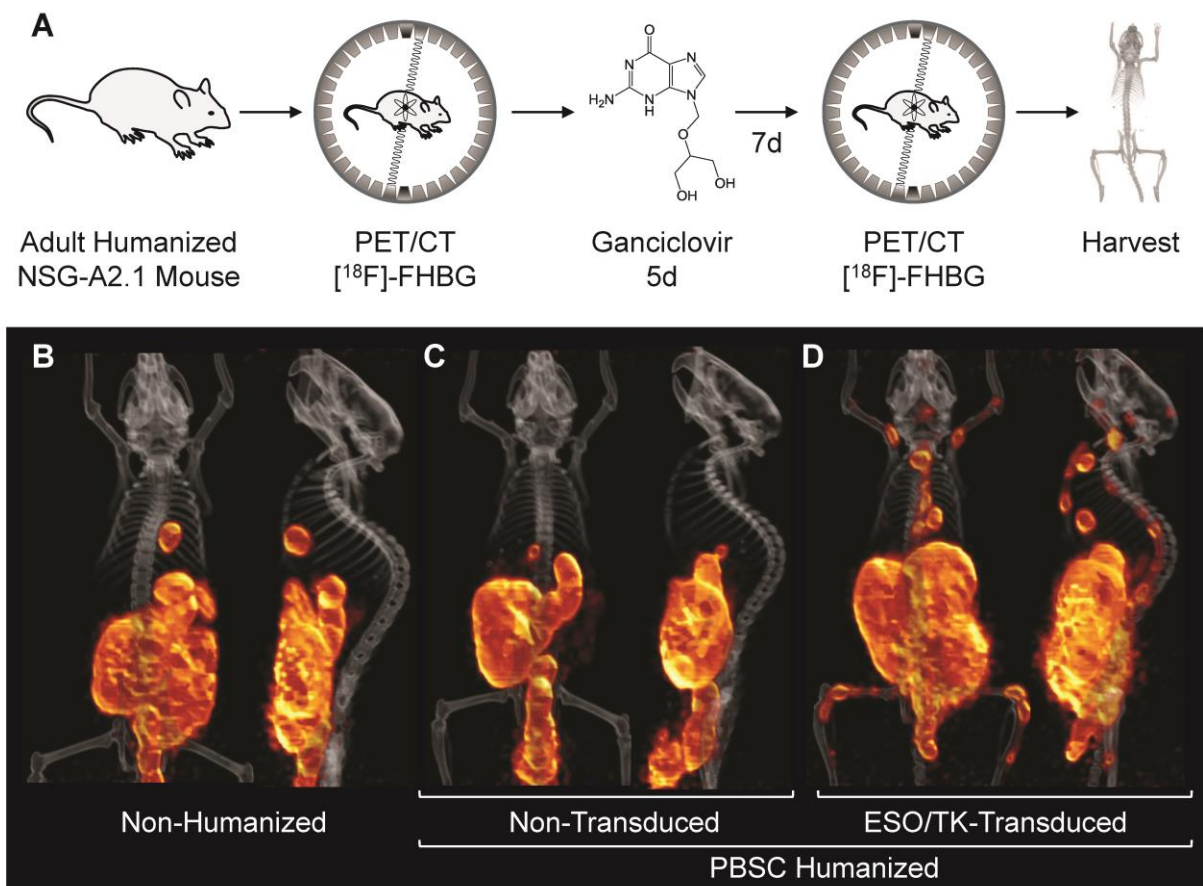


**Figure 4. High-resolution sr39TK PET reporter imaging of gene-modified cells *in vivo*.** (A) Experimental procedure for PET imaging. Mice were injected with 250uCi [<sup>18</sup>F]-FHBG and PET/CT imaged. Scans of (B) non-transplanted NSG-A2.1, (C) non-transduced humanized, and (D) ESO/TK-transduced humanized mice. Probe was detected in the gastrointestinal tract and gall bladder in all mice. In ESO/TK-transduced humanized mice, signal was detectable in the long bones of the arms and legs, the sternum, the thymus, and vertebrae.

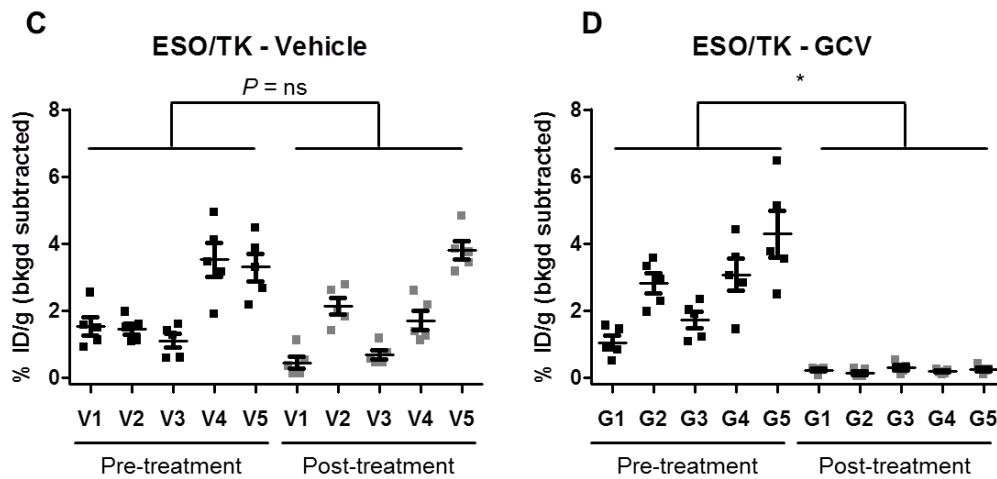
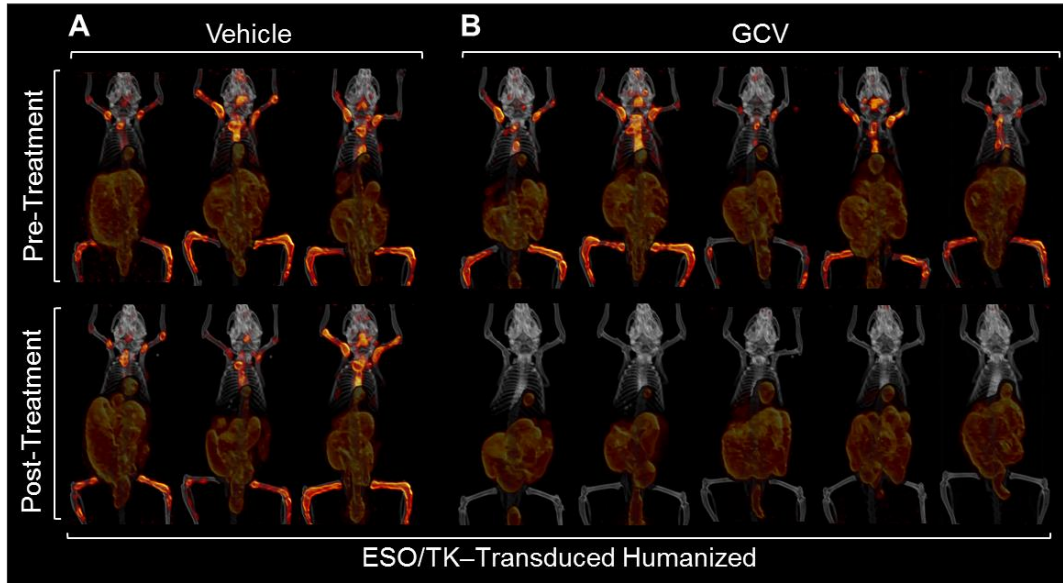


**Figure 5. GCV ablates gene modified cells hematopoietic niches.** Mice were PET/CT scanned with [<sup>18</sup>F]-FHBG before and 7d after treatment with (A) vehicle or (B) GCV. Three of five representative vehicle treated mice and five of five GCV treated mice are shown. Neutral density masks were drawn to visually mute background GB and GI signal. ROIs were drawn on femurs, humeri, and the thymus of each mouse in pre- and post-treatment scans. (C) ESO/TK mice treated with vehicle showed no significant difference between pre- and post-treatment scans (P=0.402). (D) There was a significant decrease in [<sup>18</sup>F]-FHBG PET signal in hematopoietic ROIs in ESO/TK mice treated with GCV (P<0.001).

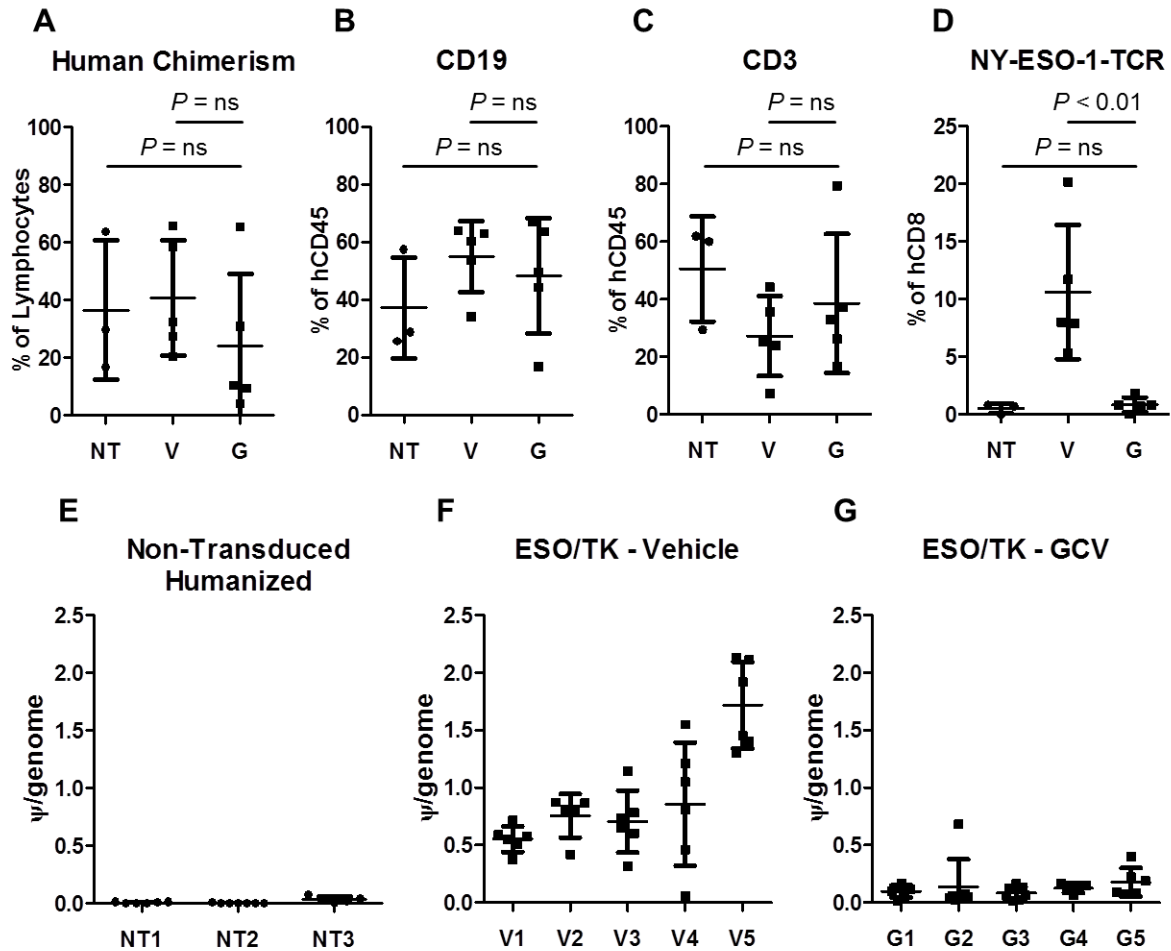
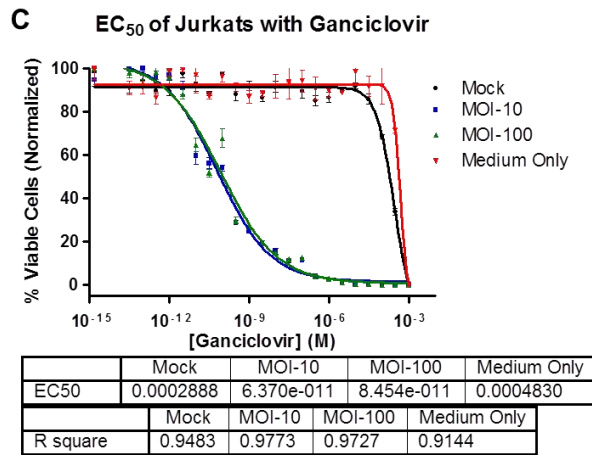
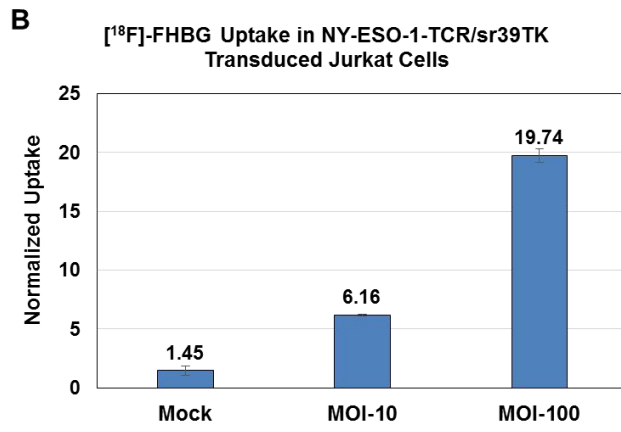
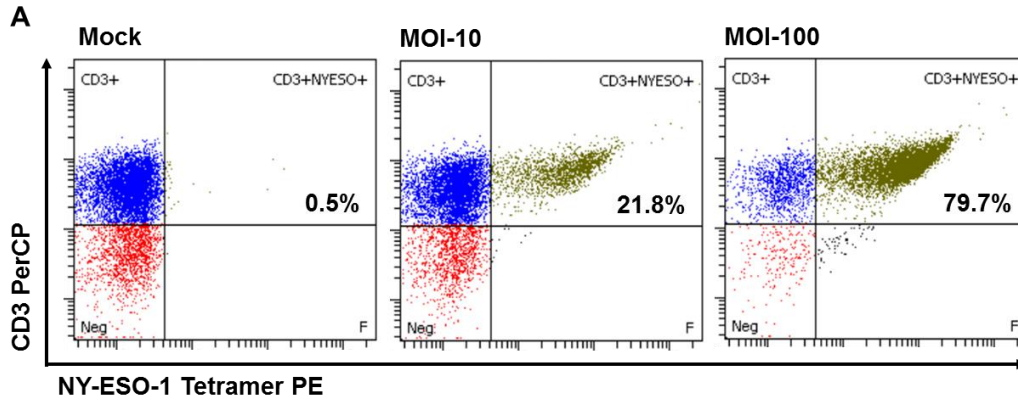
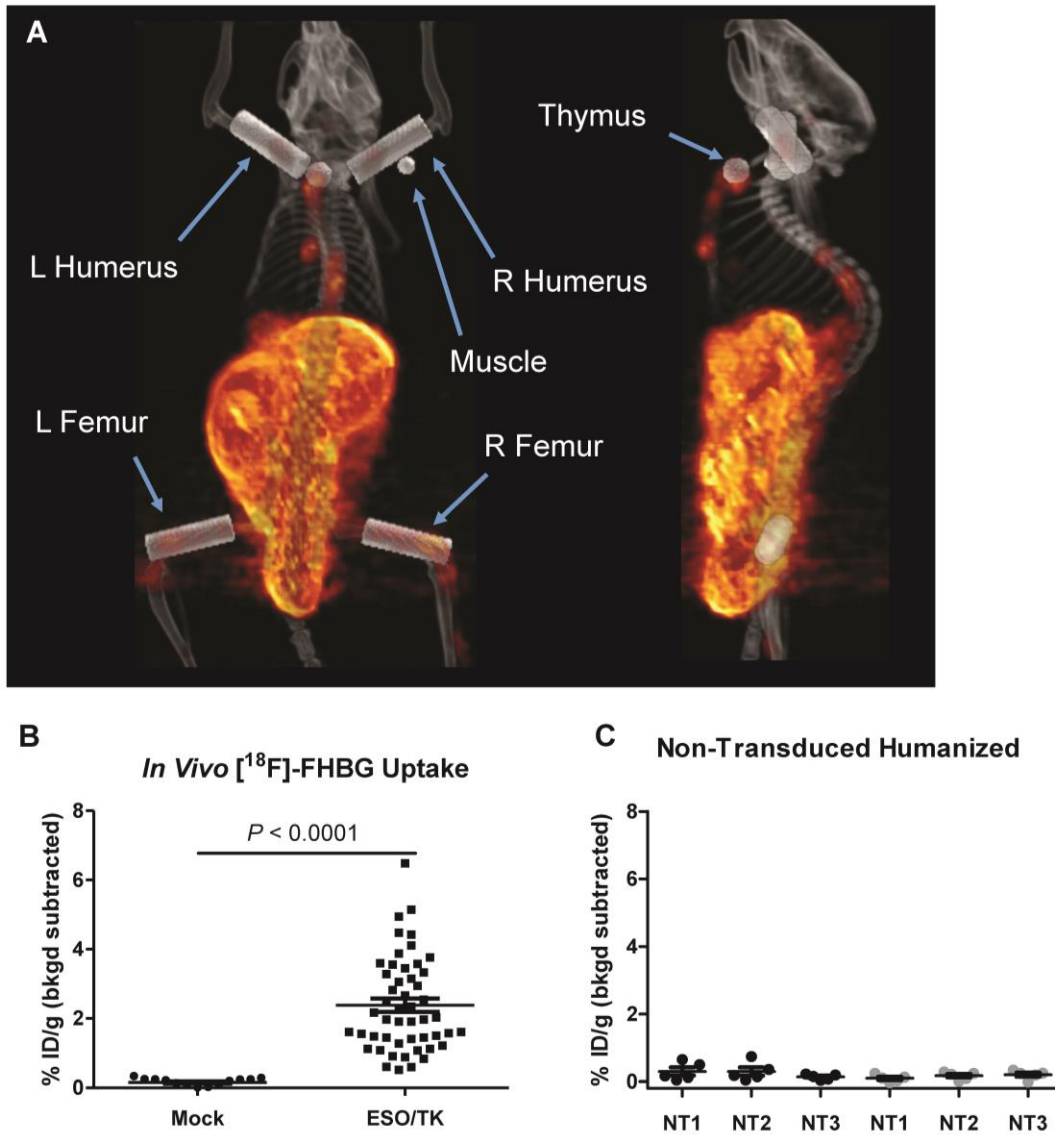


**Figure 6. Immunophenotyping and VCN analysis after drug treatment.** Harvested splenocytes from non-transduced humanized, vehicle treated ESO/TK-transduced humanized, and GCV treated ESO/TK-transduced humanized mice were evaluated by flow cytometry. No significant difference was observed for (A) human chimerism, (B) human B-cell or (C) T-cell composition. (D) A significant decrease of CD8+NY-ESO-1-TCR+ cells was observed after GCV treatment in the ESO/TK group ( $P=0.006$ ). (E-G) VCN analysis of gDNA harvested from the sternum, thymus, femurs, humeri, and spleen were measured for each treatment group.

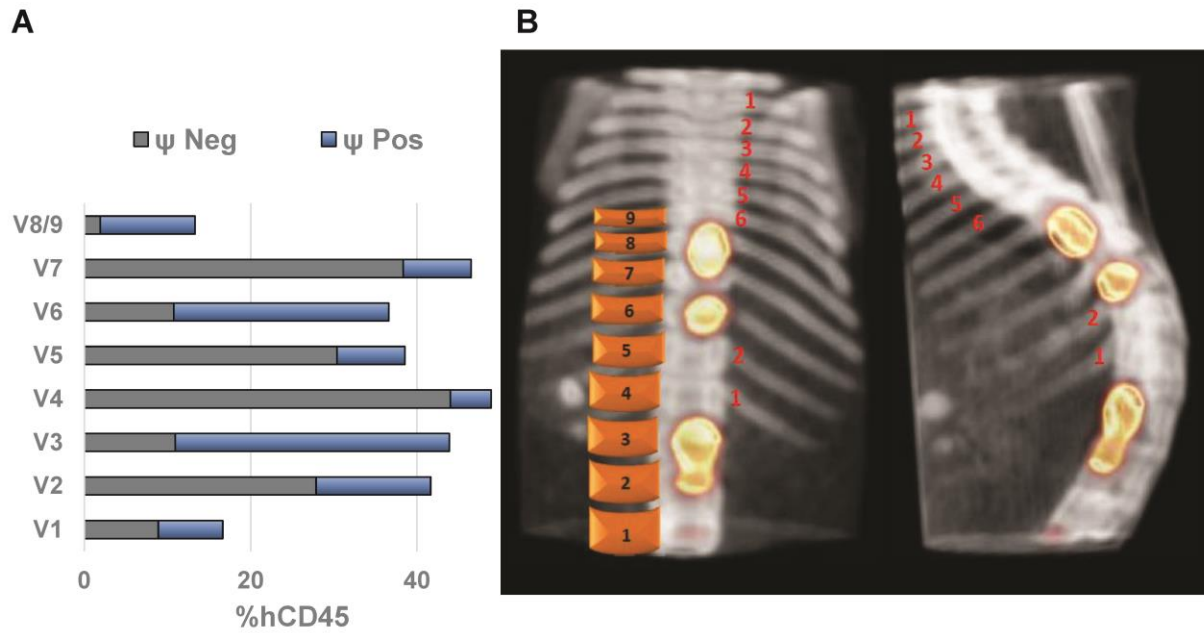


**Supplemental Figure 1. Validation of sr39TK function in Jurkat cells.** (A) Mock or ESO/TK transduced Jurkats were evaluated by flow cytometry for NY-ESO-1 tetramer binding. (B) Cells were cultured with 0.5 $\mu$ Ci [<sup>18</sup>F]-FHBG for 1 hour, washed, and evaluated for uptake. (C) Cells were cultured in half-log increasing concentrations of GCV for 48h and evaluated for viability.





**Supplemental Figure 2. ROI Analysis.** (A) Schematic of ROIs drawn on PET imaged mice. 3d cylindrical or spherical ROIs were drawn using Amide software on hematopoietic niches to determine probe uptake and arm muscle for background subtraction. (B) There was significant [<sup>18</sup>F]-FHBG uptake in the hematopoietic niches of ESO/TK mice compared with mock transduced controls. (C) [<sup>18</sup>F]-FHBG uptake in non-transduced humanized mice before and after GCV treatment.



**Supplemental Figure 3. Chimerism, vector marking, and PET probe signal in vertebrae.**

(A) Cells harvested from individual vertebrae were evaluated for human chimerism by flow cytometry and vector marking by qPCR. (B) Data were matched with [ $^{18}\text{F}$ ]-FHBG PET scan.

## References

- 1 Bordignon C, Notarangelo LD, Nobili N, et al. Gene therapy in peripheral blood lymphocytes and bone marrow for ADA- immunodeficient patients. *Science (New York, NY)*. 1995 Oct 20;**270**(5235):470-5.
- 2 Kohn DB, Weinberg KI, Nolta JA, et al. Engraftment of gene-modified umbilical cord blood cells in neonates with adenosine deaminase deficiency. *Nature medicine*. 1995 Oct;**1**(10):1017-23.
- 3 Aiuti A, Slavin S, Aker M, et al. Correction of ADA-SCID by stem cell gene therapy combined with nonmyeloablative conditioning. *Science (New York, NY)*. 2002 Jun 28;**296**(5577):2410-3.
- 4 Wirth T, Parker N, Yla-Herttuala S. History of gene therapy. *Gene*. 2013 Aug 10;**525**(2):162-9.
- 5 Morgan RA, Dudley ME, Wunderlich JR, et al. Cancer regression in patients after transfer of genetically engineered lymphocytes. *Science (New York, NY)*. 2006 Oct 6;**314**(5796):126-9.
- 6 Grupp SA, Kalos M, Barrett D, et al. Chimeric antigen receptor-modified T cells for acute lymphoid leukemia. *The New England journal of medicine*. 2013 Apr 18;**368**(16):1509-18.
- 7 Brentjens RJ, Davila ML, Riviere I, et al. CD19-targeted T cells rapidly induce molecular remissions in adults with chemotherapy-refractory acute lymphoblastic leukemia. *Science translational medicine*. 2013 Mar 20;**5**(177):177ra38.
- 8 Robbins PF, Morgan RA, Feldman SA, et al. Tumor regression in patients with metastatic synovial cell sarcoma and melanoma using genetically engineered lymphocytes reactive with NY-ESO-1. *Journal of clinical oncology : official journal of the American Society of Clinical Oncology*. 2011 Mar 1;**29**(7):917-24.

- 9 Gattinoni L, Klebanoff CA, Palmer DC, et al. Acquisition of full effector function in vitro paradoxically impairs the in vivo antitumor efficacy of adoptively transferred CD8<sup>+</sup> T cells. *The Journal of clinical investigation*. 2005 Jun;**115**(6):1616-26.
- 10 Zhou J, Shen X, Huang J, Hodes RJ, Rosenberg SA, Robbins PF. Telomere length of transferred lymphocytes correlates with in vivo persistence and tumor regression in melanoma patients receiving cell transfer therapy. *Journal of immunology (Baltimore, Md : 1950)*. 2005 Nov 15;**175**(10):7046-52.
- 11 Ma C, Cheung AF, Chodon T, et al. Multifunctional T-cell analyses to study response and progression in adoptive cell transfer immunotherapy. *Cancer discovery*. 2013 Apr;**3**(4):418-29.
- 12 Gattinoni L, Klebanoff CA, Restifo NP. Paths to stemness: building the ultimate antitumour T cell. *Nature reviews Cancer*. 2012 Oct;**12**(10):671-84.
- 13 Gattinoni L, Restifo NP. Moving T memory stem cells to the clinic. *Blood*. 2013 Jan 24;**121**(4):567-8.
- 14 Cieri N, Camisa B, Cocchiarella F, et al. IL-7 and IL-15 instruct the generation of human memory stem T cells from naive precursors. *Blood*. 2013 Jan 24;**121**(4):573-84.
- 15 Terakura S, Yamamoto TN, Gardner RA, Turtle CJ, Jensen MC, Riddell SR. Generation of CD19-chimeric antigen receptor modified CD8<sup>+</sup> T cells derived from virus-specific central memory T cells. *Blood*. 2012 Jan 5;**119**(1):72-82.
- 16 Wang X, Berger C, Wong CW, Forman SJ, Riddell SR, Jensen MC. Engraftment of human central memory-derived effector CD8<sup>+</sup> T cells in immunodeficient mice. *Blood*. 2011 Feb 10;**117**(6):1888-98.

- 17 Yang L, Baltimore D. Long-term in vivo provision of antigen-specific T cell immunity by programming hematopoietic stem cells. *Proceedings of the National Academy of Sciences of the United States of America*. 2005 Mar 22;**102**(12):4518-23.
- 18 Giannoni F, Hardee CL, Wherley J, et al. Allelic exclusion and peripheral reconstitution by TCR transgenic T cells arising from transduced human hematopoietic stem/progenitor cells. *Molecular therapy : the journal of the American Society of Gene Therapy*. 2013 May;**21**(5):1044-54.
- 19 Vatakis DN, Koya RC, Nixon CC, et al. Antitumor activity from antigen-specific CD8 T cells generated in vivo from genetically engineered human hematopoietic stem cells. *Proceedings of the National Academy of Sciences of the United States of America*. 2011 Dec 20;**108**(51):E1408-16.
- 20 Vatakis DN, Arumugam B, Kim SG, Bristol G, Yang O, Zack JA. Introduction of exogenous T-cell receptors into human hematopoietic progenitors results in exclusion of endogenous T-cell receptor expression. *Molecular therapy : the journal of the American Society of Gene Therapy*. 2013 May;**21**(5):1055-63.
- 21 De Oliveira SN, Ryan C, Giannoni F, et al. Modification of Hematopoietic Stem/Progenitor Cells with CD19-Specific Chimeric Antigen Receptors as a Novel Approach for Cancer Immunotherapy. *Human gene therapy*. 2013 Oct;**24**(10):824-39.
- 22 Gaspar HB, Cooray S, Gilmour KC, et al. Long-term persistence of a polyclonal T cell repertoire after gene therapy for X-linked severe combined immunodeficiency. *Science translational medicine*. 2011 Aug 24;**3**(97):97ra79.

- 23 Candotti F, Shaw KL, Muul L, et al. Gene therapy for adenosine deaminase-deficient severe combined immune deficiency: clinical comparison of retroviral vectors and treatment plans. *Blood*. 2012 Nov 1;**120**(18):3635-46.
- 24 Hacein-Bey-Abina S, von Kalle C, Schmidt M, et al. A serious adverse event after successful gene therapy for X-linked severe combined immunodeficiency. *The New England journal of medicine*. 2003 Jan 16;**348**(3):255-6.
- 25 Emery DW. The use of chromatin insulators to improve the expression and safety of integrating gene transfer vectors. *Human gene therapy*. 2011 Jun;**22**(6):761-74.
- 26 Yu SF, von Ruden T, Kantoff PW, et al. Self-inactivating retroviral vectors designed for transfer of whole genes into mammalian cells. *Proceedings of the National Academy of Sciences of the United States of America*. 1986 May;**83**(10):3194-8.
- 27 Zufferey R, Dull T, Mandel RJ, et al. Self-inactivating lentivirus vector for safe and efficient in vivo gene delivery. *Journal of virology*. 1998 Dec;**72**(12):9873-80.
- 28 Miyoshi H, Blomer U, Takahashi M, Gage FH, Verma IM. Development of a self-inactivating lentivirus vector. *Journal of virology*. 1998 Oct;**72**(10):8150-7.
- 29 Morgan RA, Yang JC, Kitano M, Dudley ME, Laurencot CM, Rosenberg SA. Case report of a serious adverse event following the administration of T cells transduced with a chimeric antigen receptor recognizing ERBB2. *Molecular therapy : the journal of the American Society of Gene Therapy*. 2010 Apr;**18**(4):843-51.
- 30 Porter DL, Levine BL, Kalos M, Bagg A, June CH. Chimeric antigen receptor-modified T cells in chronic lymphoid leukemia. *The New England journal of medicine*. 2011 Aug 25;**365**(8):725-33.

- 31 Johnson LA, Morgan RA, Dudley ME, et al. Gene therapy with human and mouse T-cell receptors mediates cancer regression and targets normal tissues expressing cognate antigen. *Blood*. 2009 Jul 16;**114**(3):535-46.
- 32 Linette GP, Stadtmauer EA, Maus MV, et al. Cardiovascular toxicity and titin cross-reactivity of affinity-enhanced T cells in myeloma and melanoma. *Blood*. 2013 Aug 8;**122**(6):863-71.
- 33 Blumenthal M, Skelton D, Pepper KA, Jahn T, Methangkool E, Kohn DB. Effective suicide gene therapy for leukemia in a model of insertional oncogenesis in mice. *Molecular therapy : the journal of the American Society of Gene Therapy*. 2007 Jan;**15**(1):183-92.
- 34 Bonini C, Ferrari G, Verzeletti S, et al. HSV-TK gene transfer into donor lymphocytes for control of allogeneic graft-versus-leukemia. *Science (New York, NY)*. 1997 Jun 13;**276**(5319):1719-24.
- 35 Black ME, Newcomb TG, Wilson HM, Loeb LA. Creation of drug-specific herpes simplex virus type 1 thymidine kinase mutants for gene therapy. *Proceedings of the National Academy of Sciences of the United States of America*. 1996 Apr 16;**93**(8):3525-9.
- 36 Straathof KC, Pule MA, Yotnda P, et al. An inducible caspase 9 safety switch for T-cell therapy. *Blood*. 2005 Jun 1;**105**(11):4247-54.
- 37 Di Stasi A, Tey SK, Dotti G, et al. Inducible apoptosis as a safety switch for adoptive cell therapy. *The New England journal of medicine*. 2011 Nov 3;**365**(18):1673-83.
- 38 Wang X, Chang WC, Wong CW, et al. A transgene-encoded cell surface polypeptide for selection, in vivo tracking, and ablation of engineered cells. *Blood*. 2011 Aug 4;**118**(5):1255-63.
- 39 Qasim W, Thrasher AJ, Buddle J, Kinnon C, Black ME, Gaspar HB. T cell transduction and suicide with an enhanced mutant thymidine kinase. *Gene therapy*. 2002 Jun;**9**(12):824-7.

- 40 Gambhir SS, Bauer E, Black ME, et al. A mutant herpes simplex virus type 1 thymidine kinase reporter gene shows improved sensitivity for imaging reporter gene expression with positron emission tomography. *Proceedings of the National Academy of Sciences of the United States of America*. 2000 Mar 14;**97**(6):2785-90.
- 41 Ribas A, Butterfield LH, Hu B, et al. Generation of T-cell immunity to a murine melanoma using MART-1-engineered dendritic cells. *Journal of immunotherapy (Hagerstown, Md : 1997)*. 2000 Jan;**23**(1):59-66.
- 42 Alauddin MM, Conti PS. Synthesis and preliminary evaluation of 9-(4-[<sup>18</sup>F]-fluoro-3-hydroxymethylbutyl)guanine ([<sup>18</sup>F]FHBG): a new potential imaging agent for viral infection and gene therapy using PET. *Nuclear medicine and biology*. 1998 Apr;**25**(3):175-80.
- 43 Laird NM, Ware JH. Random-effects models for longitudinal data. *Biometrics*. 1982 Dec;**38**(4):963-74.
- 44 Black ME, Kokoris MS, Sabo P. Herpes simplex virus-1 thymidine kinase mutants created by semi-random sequence mutagenesis improve prodrug-mediated tumor cell killing. *Cancer research*. 2001 Apr 1;**61**(7):3022-6.
- 45 Yaghoubi S, Barrio JR, Dahlbom M, et al. Human pharmacokinetic and dosimetry studies of [<sup>18</sup>F]FHBG: a reporter probe for imaging herpes simplex virus type-1 thymidine kinase reporter gene expression. *Journal of nuclear medicine : official publication, Society of Nuclear Medicine*. 2001 Aug;**42**(8):1225-34.
- 46 Wang X, Rosol M, Ge S, et al. Dynamic tracking of human hematopoietic stem cell engraftment using in vivo bioluminescence imaging. *Blood*. 2003 Nov 15;**102**(10):3478-82.



- 47 Su H, Forbes A, Gambhir SS, Braun J. Quantitation of cell number by a positron emission tomography reporter gene strategy. *Molecular imaging and biology : MIB : the official publication of the Academy of Molecular Imaging*. 2004 May-Jun;**6**(3):139-48.
- 48 Riddell SR, Elliott M, Lewinsohn DA, et al. T-cell mediated rejection of gene-modified HIV-specific cytotoxic T lymphocytes in HIV-infected patients. *Nature medicine*. 1996 Feb;**2**(2):216-23.
- 49 Berger C, Flowers ME, Warren EH, Riddell SR. Analysis of transgene-specific immune responses that limit the in vivo persistence of adoptively transferred HSV-TK-modified donor T cells after allogeneic hematopoietic cell transplantation. *Blood*. 2006 Mar 15;**107**(6):2294-302.
- 50 Fehr T, Sykes M. Tolerance induction in clinical transplantation. *Transplant immunology*. 2004 Sep-Oct;**13**(2):117-30.
- 51 McCracken MN, Gschwend EH, Nair-Gill E, et al. Long-term in vivo monitoring of mouse and human hematopoietic stem cell engraftment with a human positron emission tomography reporter gene. *Proceedings of the National Academy of Sciences of the United States of America*. 2013 Jan 29;**110**(5):1857-62.
- 52 Barese CN, Krouse AE, Metzger ME, et al. Thymidine kinase suicide gene-mediated ganciclovir ablation of autologous gene-modified rhesus hematopoiesis. *Molecular therapy : the journal of the American Society of Gene Therapy*. 2012 Oct;**20**(10):1932-43.

## **CHAPTER 6:**

Engineered antibody fragments for immunoPET  
imaging of endogenous CD8<sup>+</sup> T cells *in vivo*.

# Engineered antibody fragments for immuno-PET imaging of endogenous CD8<sup>+</sup> T cells in vivo

Richard Tavaré<sup>a</sup>, Melissa N. McCracken<sup>b</sup>, Kirstin A. Zettlitz<sup>a</sup>, Scott M. Knowles<sup>a</sup>, Felix B. Salazar<sup>a</sup>, Tove Olafsen<sup>a</sup>, Owen N. Witte<sup>b,c,d,e</sup>, and Anna M. Wu<sup>a,1</sup>

<sup>a</sup>Crump Institute for Molecular Imaging and <sup>b</sup>Department of Molecular and Medical Pharmacology, David Geffen School of Medicine, <sup>c</sup>Howard Hughes Medical Institute, <sup>d</sup>Department of Microbiology, Immunology, and Molecular Genetics, and <sup>e</sup>Eli and Edythe Broad Center of Regenerative Medicine and Stem Cell Research, University of California, Los Angeles, CA 90095

Edited\* by Michael E. Phelps, University of California, Los Angeles, CA, and approved November 27, 2013 (received for review September 25, 2013)

The noninvasive detection and quantification of CD8<sup>+</sup> T cells in vivo are important for both the detection and staging of CD8<sup>+</sup> lymphomas and for the monitoring of successful cancer immunotherapies, such as adoptive cell transfer and antibody-based immunotherapeutics. Here, antibody fragments are constructed to target murine CD8 to obtain rapid, high-contrast immuno-positron emission tomography (immuno-PET) images for the detection of CD8 expression in vivo. The variable regions of two anti-murine CD8-depleting antibodies (clones 2.43 and YTS169.4.2.1) were sequenced and reformatted into minibody (Mb) fragments (scFv-C<sub>H</sub>3). After production and purification, the Mbs retained their antigen specificity and bound primary CD8<sup>+</sup> T cells from the thymus, spleen, lymph nodes, and peripheral blood. Importantly, engineering of the parental antibodies into Mbs abolished the ability to deplete CD8<sup>+</sup> T cells in vivo. The Mbs were subsequently conjugated to S-2-(4-isothiocyanatobenzyl)-1,4,7-triazacyclononane-1,4,7-triacetic acid for <sup>64</sup>Cu radiolabeling. The radiotracers were injected i.v. into antigen-positive, antigen-negative, immunodeficient, antigen-blocked, and antigen-depleted mice to evaluate specificity of uptake in lymphoid tissues by immuno-PET imaging and ex vivo biodistribution. Both <sup>64</sup>Cu-radiolabeled Mbs produced high-contrast immuno-PET images 4 h postinjection and showed specific uptake in the spleen and lymph nodes of antigen-positive mice.

The rapid increase of therapeutic antibodies approved by the US Food and Drug Administration (FDA) and those currently in phase I–III clinical trials for oncological, autoimmune, and inflammatory diseases, among other conditions, has benefited from advances in antibody engineering, protein conjugation chemistry, and biomarker identification (1–3). Concurrently, immuno-PET imaging agents based on intact antibodies have shown promise both preclinically and clinically for the detection of cancer in vivo (4). Noninvasive detection of specific biomarkers of disease can provide crucial information for diagnosis, prognosis, response to therapy, dosage for radioimmunotherapy, and targeted therapy selection.

Although much progress has been made in the immuno-PET detection of oncological markers (4), the noninvasive monitoring of immune cells in the fields of oncology, autoimmunity, and infection remains challenging. Practiced methods for lymphocyte detection include isolation of cells from the peripheral blood or, less commonly, the tissue of interest. However, the invasive tissue sampling methods are prone to error and do not provide dynamic information that reflects the number, location, and movement of lymphoid cells. Therefore, problems still exist for the evaluation of immunotherapy protocols due to the lack of effective methods to monitor the extent and duration of the therapy.

Current methods to monitor immune cells noninvasively using emission tomography include direct cell labeling, reporter genes, small-molecule PET tracers, and radiolabeled intact antibodies. The ex vivo direct labeling of immune cells with PET or single-photon emission computed tomography probes before subsequent reinjection and imaging has enabled in vivo trafficking of lymphocytes (5, 6). However, this method has inherent limitations,

such as radioisotope  $t_{1/2}$  and cell division in vivo that lead to probe dilution. Reporter gene imaging, whereby cells are transfected with a PET reporter gene that encodes a protein specifically targeted via a radiolabeled reporter probe (7, 8), has been used to image adoptive cell transfer of transduced T-cell receptor-engineered lymphocytes (9). Reporter gene imaging allows for longitudinal tracking of cells but relies on the ex vivo transfection of cells and, for clinical translation, the development of nonimmunogenic PET reporter proteins (8).

In another approach, small-molecule PET probes targeting metabolic pathways, including [<sup>18</sup>F]-fluorodeoxyglucose ([<sup>18</sup>F]FDG), [<sup>18</sup>F]-fluorothymidine ([<sup>18</sup>F]FLT), and [<sup>18</sup>F]-1-(2-deoxy-2-fluoro-arabinofuranosyl)-cytosine ([<sup>18</sup>F]FAC), all have the potential to monitor diverse cell types of both innate and adaptive immunity noninvasively (reviewed in ref. 10). Clinically, [<sup>18</sup>F]FDG-PET has been used to evaluate inflammation in a range of diseases. However, in the context of immune cell detection in oncology, false-positive signals can arise from the utilization of glycolysis in both cancerous and immune cells, both innate and adaptive, in the tumor itself or in the draining lymph nodes (11, 12). [<sup>18</sup>F]FLT-PET accumulates in highly proliferative tissues, and most research has been focused on cancer detection. [<sup>18</sup>F]FLT-PET suffers from high uptake in proliferating bone marrow, therefore limiting detection of lesions in bone. However, [<sup>18</sup>F]FLT-PET was used clinically to detect cytotoxic T-lymphocyte antigen-4 blockade-induced cell replication in the spleens of patients with melanoma (13) and, more recently, to detect antigen-specific immune responses in patients with melanoma who have lymph node metastases using dendritic cell therapy (14). [<sup>18</sup>F]FAC-PET can distinguish between innate and adaptive immune cells due to the up-regulation of deoxycytidine kinase in proliferating T cells, but the uptake in a Moloney murine sarcoma virus/murine leukemia virus complex-proliferative sarcoma model was limited to proliferating T cells in the draining lymph nodes and spleen (15). Therefore, like the other metabolic tracers FDG and FLT, FAC uptake due to activation-induced T-cell

## Significance

Anti-CD8 immuno-PET imaging agents provide the potential to monitor the localization, migration, and expansion of CD8-expressing cells noninvasively in vivo. Shown here is the successful generation of functional anti-CD8 imaging agents based on engineered antibodies for use in a variety of preclinical disease and immunotherapeutic models.

Author contributions: R.T., T.O., O.N.W., and A.M.W. designed research; R.T., M.N.M., K.A.Z., S.M.K., F.B.S., and T.O. performed research; R.T., M.N.M., K.A.Z., O.N.W., and A.M.W. analyzed data; and R.T. and A.M.W. wrote the paper.

Conflict of interest statement: A.M.W. and T.O. have a financial interest in ImaginAb, Inc. T.O. is an employee of ImaginAb, Inc.

\*This Direct Submission article had a prearranged editor.

<sup>1</sup>To whom correspondence should be addressed. E-mail: awu@mednet.ucla.edu.

This article contains supporting information online at [www.pnas.org/lookup/suppl/doi:10.1073/pnas.1316922111/-/DCSupplemental](http://www.pnas.org/lookup/suppl/doi:10.1073/pnas.1316922111/-/DCSupplemental).

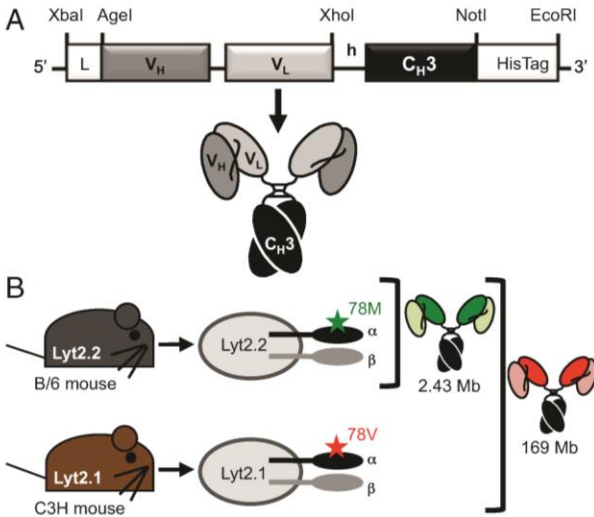


**Fig. 1.** Mb construction and epitope specificity are shown. (A) Anti-CD8 2.43 and YTS169 Mbs contain the rat  $V_H$ - $V_L$  separated by an 18-aa linker, followed by the murine IgG2a hinge (h), murine  $C_H3$ , and a C-terminal hexahistidine (HisTag). (B) Murine CD8 $\alpha$  (Lyt2) is expressed as two isoforms, Lyt2.1 and Lyt2.2, that differ in a single amino acid, and it is restricted to specific mouse strains. The 2.43 Mb binds CD8 $\alpha$  only in Lyt2.2<sup>+</sup> mouse strains, whereas the YTS169 Mb binds CD8 $\alpha$  in all mouse strains.

proliferation is restricted to the draining lymph nodes and was unable to image tumor T-cell infiltration (15). This makes immuno-PET imaging using antibody fragments targeting specific immune cell antigens (i.e., CD8 expressed on cytotoxic T cells and CD4 expressed on helper T cells) potentially critical for immunotherapeutic diagnosis, because the expression of CD8 is present on all cytotoxic T cells and binding is not proliferation-dependent.

Intact antibodies have relatively long serum  $t_{1/2s}$  (1–3 wk) compared with their engineered counterparts, such as the diabody and minibody (Mb), which have terminal  $t_{1/2s}$  that range from 2 to 5 h and from 5 to 12 h, respectively (16). Although decreasing the total uptake in tumors, the rapid clearance of engineered antibody fragments allows for higher tumor-to-background images at earlier times postinjection (p.i.). This not only allows for the potential of same-day imaging but reduces the overall radiation dose. Furthermore, engineered diabody and Mb fragments are biologically inert because they lack Fc effector functions. Intact antibodies have been used previously to image T cells in patients with a range of disorders (reviewed in ref. 17). The majority of these studies use planar gamma imaging using therapeutic intact mouse anti-human antibodies. The expanding knowledge of the importance of immune cell subtypes in diseases and the improvements in antibody-based immuno-PET imaging indicate that antibody-based imaging of immune cells in vivo should be revisited.

In this report, we develop two anti-murine CD8 Mbs (Fig. 1A) for the detection of CD8 expression. Murine CD8 is a cell surface glycoprotein expressed mainly on a subset of T cells known as cytotoxic T cells and a subset of dendritic cells. Functional CD8 is expressed as either the homodimer CD8 $\alpha\alpha$  or the heterodimer CD8 $\alpha\beta$  of the two isoforms of CD8,  $\alpha$  and  $\beta$ . Mice have two alleles for CD8 $\alpha$ , Lyt2.1 and Lyt2.2, which are restricted to certain mouse strains. Lyt2.1, for example, is expressed in the mouse strains CBA, AKR, C3H, and DBA, whereas Lyt2.2 is expressed in the mouse strains BALB/c and C57BL/6 (B/6). The difference between Lyt2.1 and Lyt2.2 is a methionine (Lyt2.2)-to-valine (Lyt2.1) substitution at residue 78 of the mature CD8 $\alpha$  (Fig. 1B).

In this study, the parental antibodies from the hybridomas YTS 169.4.2.1 (YTS169) and 2.43 were engineered into Mb fragments (Fig. 1A). Both the YTS169 and 2.43 antibodies bind mCD8 $\alpha$  (Lyt2). However, they differ in that the YTS169 antibody binds both Lyt2.1 and Lyt2.2, whereas the 2.43 antibody binds an epitope that is Lyt2.2-specific (Fig. 1B). These newly engineered Mbs retained their antigen specificity, as shown by flow cytometry and <sup>64</sup>Cu immuno-PET imaging. Most importantly, both the 2.43 and YTS169 Mbs produce high-contrast immuno-PET images of CD8<sup>+</sup> lymphoid organs at only 4 h p.i. This report details successful antibody fragment-based immuno-PET detection of CD8 expression in vivo.

## Results

**Sequencing Variable Regions of Parental Rat Anti-murine CD8 Antibodies.** RT-PCR was repeated until at least two individual experiments produced three replicates of the same sequence for the  $V_H$  and  $V_L$  domains for each hybridoma for sequence assurance. For further sequence validation of hybridoma 2.43, the  $V_H$  and  $V_L$  from RT-PCR sequences were confirmed with tryptic digest mass spectrometry (MS) of the parental antibody.  $V_H$  amino acid coverage was 35% (41 of 117), including the complete complementarity-determining region 1 (CDR1) and half of CDR2, and  $V_L$  amino acid coverage was 62% (66 of 107), including both CDR2 and CDR3. For YTS169, no MS sequence verification was performed.

**Production and Characterization of Mb Fragments.** Mb purification from NS0 supernatant was performed using nickel-nitrilotriacetic acid (Ni-NTA) columns and imidazole elution (Fig. S1A). SDS/PAGE showed that the Mb eluted between 25 and 45 min (Fig. S1B). The yields of the 2.43 and YTS169 Mbs were 6.6 and 8.9 mg/L, respectively. Purified protein was then analyzed on Superdex 200 size exclusion chromatography (SEC) and compared with reference standards to confirm assembly, purity, and dimerization (Fig. S1C). The 2.43 and YTS169 Mbs are purified as 81% or 23% 80-kDa dimers, respectively, as calculated by peak areas, with the remaining 19% and 77% eluting as higher molecular-weight multimers.

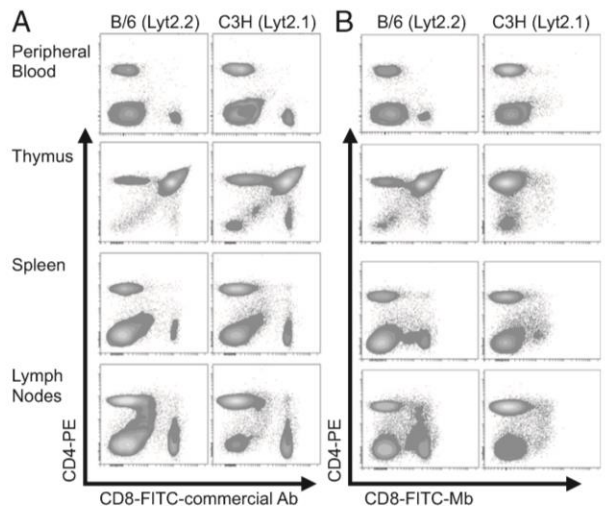


**Fig. 2.** The 2.43 Mb retains Lyt2.2 antigen specificity. Primary cells isolated from the peripheral blood, thymus, spleen, and lymph nodes of B/6 and C3H mice were stained with phycoerythrin (PE)-anti-CD4 and either a commercial FITC-anti-CD8 antibody (A) or the Lyt2.2-specific FITC-2.43 Mb (B). The lack of CD8-FITC staining in Lyt2.1<sup>+</sup> C3H mice shows the 2.43-Mb specificity for Lyt2.2<sup>+</sup> B/6 mice.

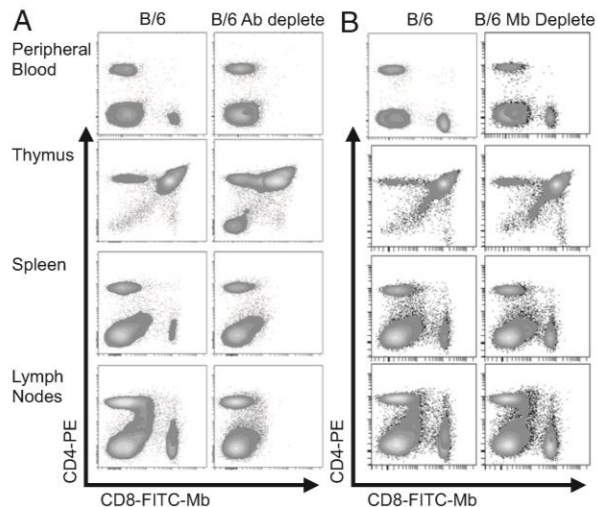


**Fig. 3.** Anti-CD8 Mb does not deplete CD8-expressing cells in vivo. B/6 mice were treated for three consecutive days with either 330  $\mu$ g of anti-CD8 depleting antibody (clone 53-6.7) injected i.p. (A) or 250  $\mu$ g of 2.43 Mb injected i.v. (B). Cells were then isolated from the peripheral blood, thymus, spleen, and lymph nodes for staining with anti-CD4-PE and FITC-conjugated 2.43 Mb.

Flow cytometry confirmed epitope specificity of the Mb fragments. The murine CD8<sup>+</sup> T-cell lymphoma lines BW58 (Lyt2.2<sup>+</sup>) and TK-1 (Lyt2.1<sup>+</sup>) were stained with either 2.43 or YTS169 Mb, followed by anti-mouse IgG2a-phycoerythrin (Fig. S1D). To demonstrate further the epitope specificity of the 2.43-Mb construct, the 2.43 Mb was conjugated to FITC at a 1.4:1 ratio of fluorescein/Mb. Single-cell suspensions from the peripheral blood, thymus, spleen, and lymph nodes of B/6 (Lyt2.2<sup>+</sup>) or C3H (Lyt2.1<sup>+</sup>) mice were stained with either the FITC-2.43 Mb or a commercial FITC-anti-CD8 antibody and anti-CD4 (Fig. 2). The 2.43 Mb shows comparable binding to cells isolated from antigen-positive Lyt2.2 B/6 mice and does not bind CD8 in primary cells from various organs of the antigen-negative Lyt2.1 C3H mice.

To determine the affinity of both the 2.43 and YTS169 Mb, a recombinant soluble CD8 $\alpha\beta$  (sCD8 $\alpha\beta$ ) heterodimer fusion protein was constructed by removing the transmembrane domains of both CD8 $\alpha$  and CD8 $\beta$  and fusing them with a 29-aa  $\alpha$ -helical linker. The soluble antigen was purified using Ni-NTA affinity chromatography, followed by SEC (Fig. S2). Solution-phase binding of the 2.43 and YTS169 Mbs to the purified sCD8 $\alpha\beta$

antigen was first confirmed by SEC. Briefly, equimolar amounts of soluble antigen and the Mb in question were incubated for 5 min in PBS before SEC analysis. All Mb peaks eluted 2.8–3 min earlier in the presence of sCD8 $\alpha\beta$ , confirming Mb and antigen-bound complexes of a larger size. Additionally, the Mb multimer detected by size exclusion eluted 2.5–2.8 min earlier (Fig. S3).

Surface plasmon resonance kinetic analysis was performed using Biacore 3000 (Precision Antibody, Inc.) with immobilized Mb and soluble monomeric sCD8 $\alpha\beta$ . The equilibrium constants ( $K_{ds}$ ) for 2.43 and YTS169 were 34 and 33 nM, respectively. A full analysis is provided in Fig. S4.

**In Vivo Depletion.** Single-cell suspensions from the spleen, peripheral blood, thymus, and lymph nodes of WT B/6 mice, B/6 mice treated with a CD8-depleting antibody, or B/6 mice treated with the 2.43 Mb were analyzed by flow cytometry for effective CD8 depletion (Fig. 3). Mice treated with the depleting antibody showed >95% loss of CD8<sup>+</sup> leukocytes, whereas mice treated with the 2.43 Mb did not show a reduction in CD8<sup>+</sup> leukocytes.

**NOTA Conjugation and Radiolabeling.** Following conjugation of both 2.43 and YTS169 Mb to S-2-(4-Isothiocyanatobenzyl)-1,4,7-triazacyclononane-1,4,7-triacetic acid (p-SCN-Bn-NOTA) and <sup>64</sup>Cu radiolabeling, <sup>64</sup>Cu incorporation was consistently >80% and the radiochemical purity was >98% after spin column purification ( $n = 10$  radiolabelings). The immunoreactive fraction of the <sup>64</sup>Cu-NOTA Mbs ranged from 65 to 75%. The specific activity was between 295 and 370 MBq/mg (8–10 mCi/mg), and mice were injected with 2.6–2.9 MBq (70–80  $\mu$ Ci) i.v.

**Immuno-PET and ex Vivo Biodistribution.** Due to the specificity for Lyt2.2, WT B/6 (Lyt2.2<sup>+</sup>) mice were initially imaged with <sup>64</sup>Cu-NOTA-2.43 Mb (Fig. 4). High-contrast immuno-PET images showed a high percent-injected dose per gram of tissue (%ID/g) uptake in the spleen, lymph nodes, and liver of the antigen-positive B/6 mice, and ex vivo biodistribution confirmed uptake of  $75 \pm 8.5\%$  ID/g,  $27 \pm 7.9\%$  ID/g, and  $57 \pm 11\%$  ID/g, respectively (Table 1). When injected into antigen-negative Lyt2.1 C3H mice, the <sup>64</sup>Cu-NOTA-2.43 Mb showed similar %ID/g uptake in the liver and five-to ninefold reduced uptake in the spleen ( $15 \pm 2.3\%$  ID/g) and lymph nodes ( $2.7 \pm 0.71\%$  ID/g) compared with the B/6 mice (Fig. S4 and Table 1). The average %ID/g blood after only 4 h in B/6 and C3H mice was  $0.90 \pm 0.14\%$  ID/g and  $1.3 \pm 0.10\%$  ID/g, respectively.

To confirm the radiotracer uptake of <sup>64</sup>Cu-NOTA-2.43 Mb in antigen-negative C3H mice, the <sup>64</sup>Cu-NOTA-2.43 Mb was injected into immunodeficient NOD.Cg-Prkdc<sup>scid</sup> Il2rg<sup>tm1Wjl</sup>/SzJ (NSG) mice that lack mature T cells, B cells, and natural killer cells. Immuno-PET images and ex vivo biodistribution in NSG mice were very similar to those of the <sup>64</sup>Cu-NOTA-2.43 Mb in

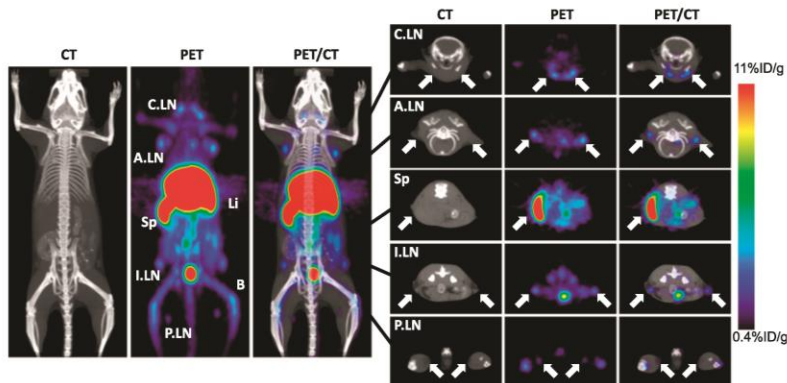


**Fig. 4.** Immuno-PET imaging of <sup>64</sup>Cu-NOTA-2.43 Mb 4 h p.i. is shown. Immuno-PET/CT images were acquired 4 h after i.v. injection in B/6 mice. The white arrows (2-mm transverse MIPs) are used to highlight uptake in various lymph nodes (Right) and the spleen seen in the whole-body 20-mm coronal MIPs (Left). A.LN, axillary lymph nodes; B, bone; C. LN, cervical lymph nodes; I.LN, inguinal lymph nodes; Li, liver; MIPs, maximum intensity projections; P.LN, popliteal lymph nodes; Sp, Spleen.

**Table 1. Ex vivo biodistribution analysis of <sup>64</sup>Cu-NOTA-2.43 Mb 4 h p.i. in Lyt2.2<sup>+</sup> B/6 mice, Lyt2.1<sup>+</sup> C3H mice, NSG SCID mice, antigen-blocked B/6 mice, and antigen-depleted B/6 mice**

Organ	%ID/g				
	WT B/6 (n = 6)	WT C3H (n = 3)	NSG (n = 3)	B/6 + block (n = 3)	B/6 + depletion (n = 3)
Blood	0.90 ± 0.14	1.3 ± 0.10**	0.89 ± 0.13	2.1 ± 0.31***	1.9 ± 0.10***
Axillary lymph nodes	27 ± 7.9	2.7 ± 0.71**	N/A	5.0 ± 1.3**	4.5 ± 2.7**
Spleen	75 ± 8.5	15 ± 2.3***	13 ± 3.9***	18 ± 1.9***	15 ± 1.0***
Stomach	1.1 ± 0.42	1.1 ± 0.11	0.43 ± 0.11*	1.0 ± 0.09	1.6 ± 0.92
Intestines	3.8 ± 0.58	3.2 ± 0.17	1.1 ± 0.04***	4.3 ± 0.47	3.4 ± 0.73
Liver	57 ± 11	47 ± 1.6	38 ± 1.0*	71 ± 1.2	59 ± 6.5
Kidneys	5.6 ± 0.72	5.8 ± 0.72	3.8 ± 0.26**	7.0 ± 0.31*	6.4 ± 0.50
Thymus	0.89 ± 0.63	0.46 ± 0.05	2.2 ± 0.89*	1.8 ± 0.42	1.1 ± 0.46
Heart	1.6 ± 0.22	2.3 ± 0.09**	1.3 ± 0.15	3.1 ± 0.36***	2.7 ± 0.19***
Lungs	3.3 ± 1.3	2.3 ± 0.61	1.2 ± 0.11	3.1 ± 0.05	2.4 ± 0.48
Muscle	0.16 ± 0.03	0.15 ± 0.01**	0.15 ± 0.03	0.42 ± 0.06***	0.3 ± 0.06**
Bone	8.2 ± 2.5	4.0 ± 0.34*	3.6 ± 0.49*	9.2 ± 0.7	9.0 ± 1.5
Carcass	0.91 ± 0.15	0.83 ± 0.04	0.53 ± 0.03**	1.4 ± 0.12**	1.3 ± 0.13**

Values are represented as mean ± SD. \*P < 0.05; \*\*P < 0.005; \*\*\*P < 0.0005. N/A, not applicable.

antigen-negative C3H mice, confirming the high liver uptake as unspecific hepatic clearance of the radiolabeled Mb (Fig. 5A and Table 1).

For the YTS169 Mb, the radiolabeling, specific activity, and immunoreactive fraction were similar to those of the <sup>64</sup>Cu-NOTA-2.43 Mb. The immuno-PET imaging and ex vivo biodistributions in WT B/6 mice using the <sup>64</sup>Cu-NOTA-YTS169 Mb were similar to those of <sup>64</sup>Cu-NOTA-2.43 Mb in B/6 mice (Fig. 5B and Table 2). Interestingly, the %ID/g in the liver and spleen of the <sup>64</sup>Cu-NOTA-YTS169 Mb in C3H mice is reduced by 29% and 48%, respectively, compared with B/6 mice (Fig. 5B and Table 2).

Finally, the <sup>64</sup>Cu-NOTA-2.43 Mb was injected into B/6 mice that were blocked with coinjection of 80 µg (4 mg/kg) cold 2.43 Mb or had received anti-CD8 antibody depletion therapy (16 mg/kg for three consecutive days). Immuno-PET images and ex vivo biodistribution acquired 4 h p.i. of antigen-blocked and antigen-depleted mice (Fig. 6B and C and Table 2) showed similar uptake in the spleen (18 ± 1.9%ID/g and 15 ± 1.0%ID/g, respectively) and lymph nodes (5.0 ± 1.3%ID/g and 4.5 ± 2.7%ID/g, respectively) relative to the antigen-negative C3H and NSG mice. CD8 depletion was confirmed using flow cytometry as described above.

## Discussion

The two anti-CD8 Mbs developed here for <sup>64</sup>Cu immuno-PET imaging of CD8 expression retain their respective antigen specificities following engineering to the Mb format. Both produced

at high yields in mammalian cell culture and could be purified using one-step immobilized metal affinity purification. In vivo studies demonstrated that both Mbs target the spleen and lymph nodes of antigen-positive mice. The lymph node uptake determined from the PET images is lower than the ex vivo biodistribution values due to the partial volume effect encountered when imaging small objects near or below the spatial resolution of the PET scanner (1.5 mm for the Inveon scanner). It has been calculated that a naive lymph node contains ~10<sup>6</sup> cells (18) and that 7–12% of the leukocytes in the lymph node are CD8<sup>+</sup>. This would suggest that we are able to detect an estimated 70,000–120,000 CD8<sup>+</sup> cells in a mouse lymph node. We have also demonstrated that our engineered antibody fragments lacking the full Fc domain do not deplete CD8<sup>+</sup> T cells in vivo, a critical feature in the development of a biologically inert imaging agent targeting immune cells. Mbs lacking the C<sub>H2</sub> domain do not have effector functions because they cannot bind Fcγ receptors. However, further studies need to be performed to see if CD8 cross-linking due to the bivalent nature of the Mb activates CD8<sup>+</sup> T cells in vivo.

Due to the low blood activity at only 4 h p.i., immuno-PET images were acquired at relatively early times p.i. compared with other Mb fragments. The 2.43 and YTS169 Mbs have 0.3–0.9% ID/g in the blood of antigen-positive mice when other reports indicate 6–7.5%ID/g at 6 h p.i. (19). The rapid clearance of the anti-CD8 Mbs could be due not only to the reduced size of the Mb compared with the intact antibody, but to the abundance of

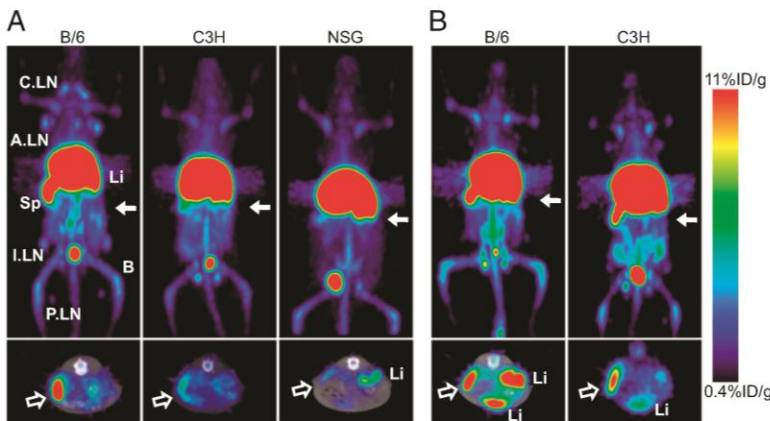


**Fig. 5. Immuno-PET imaging of <sup>64</sup>Cu-NOTA-2.43 Mb and <sup>64</sup>Cu-NOTA-YTS169 Mb shows in vivo specificity of the 2.43 Mb to Lyt2.2<sup>+</sup> mice. (A) <sup>64</sup>Cu-NOTA-2.43 Mb was injected into B/6, C3H, and NOD SCID gamma mice for immuno-PET imaging 4 h p.i. (B) <sup>64</sup>Cu-NOTA-YTS169 Mb was injected into B/6 and C3H mice for immuno-PET imaging 4 h p.i. Solid white arrows (Upper; 20-mm coronal MIPs) indicate where the transverse images (Lower; 2-mm MIPs) are acquired. Hollow white arrows indicate the location of the spleen.**

**Table 2. Ex vivo biodistribution analysis of  $^{64}\text{Cu}$ -NOTA-YTS169 Mb 4 h p.i. in  $\text{Lyt2.2}^+$  B/6 mice and  $\text{Lyt2.1}^+$  C3H mice**

Organ	%ID/g		%ID	
	WT B/6 (n = 3)	WT C3H (n = 3)	WT B/6 (n = 3)	WT C3H (n = 3)
Blood	0.33 ± 0.07	0.25 ± 0.01	N/A	N/A
Axillary lymph nodes	5.1 ± 1.1	5.8 ± 0.66	0.04 ± 0.01	0.09 ± 0.01*
Spleen	49 ± 3.5	26 ± 1.7**	2.7 ± 0.10	2.4 ± 0.06
Stomach	0.76 ± 0.20	0.40 ± 0.15	0.26 ± 0.04	0.17 ± 0.02
Intestines	2.8 ± 0.21	2.3 ± 0.34	3.3 ± 0.44	3.0 ± 0.39
Liver	60.4 ± 1.5	43 ± 2.2**	39 ± 1.0	38 ± 5.0
Kidneys	3.8 ± 0.76	2.6 ± 0.20	0.77 ± 0.21	0.69 ± 0.02
Thymus	0.31 ± 0.03	0.33 ± 0.09	0.01 ± 0.001	0.01 ± 0.002
Heart	0.81 ± 0.02	0.90 ± 0.07	0.07 ± 0.002	0.08 ± 0.01
Lungs	2.1 ± 0.20	1.9 ± 0.11	0.22 ± 0.03	0.26 ± 0.02
Muscle	0.09 ± 0.01	0.06 ± 0.01**	0.01 ± 0.001	0.01 ± 0.001
Bone	7.2 ± 0.81	3.06 ± 0.28*	0.38 ± 0.03	0.23 ± 0.004*
Carcass	0.69 ± 0.05	0.53 ± 0.01*	8.5 ± 0.59	8.8 ± 0.05

Values are represented as mean ± SD. \* $P < 0.05$ ; \*\* $P < 0.005$ . N/A, not applicable.

naturally expressed CD8 antigen throughout the body, termed the antigen sink. This results in rapid accumulation of the radiotracer in organs outside of the blood but makes imaging nonantigen sink organs (i.e., a tumor) difficult. The rapid biological  $t_{1/2}$  of these novel Mbs, however, is well matched to the intermediate physical  $t_{1/2}$  of  $^{64}\text{Cu}$  (12.7 h) immuno-PET radionuclide compared with other positron emitters, including  $^{18}\text{F}$  (1.8 h),  $^{124}\text{I}$  (100.2 h), and  $^{89}\text{Zr}$  (78.4 h).

Recent studies imaging CD20 in a human CD20-expressing transgenic mouse model using  $^{64}\text{Cu}$ - or  $^{89}\text{Zr}$ -radiolabeled rituximab mimic the targeting ability of the CD8 Mbs in vivo because the abundance and location of CD8 and CD20 antigen expression are similar in vivo (20, 21). Unlike the work presented here, the radiolabeled rituximab is still biologically active and not ideal for imaging studies. Engineering rituximab to other antibody formats could decrease the Fc-dependent biological activity of the imaging radiopharmaceutical (22, 23). In the context of

tumor targeting, this antigen sink has been overcome by blocking endogenous target with cold antibody either during (bolus injection) or before (predosing/blocking injection) administration of the radiotracer. Blocking studies were performed in the human CD20 transgenic model that resulted in an increased radiotracer blood  $t_{1/2}$  that could greatly influence the ability to target CD20<sup>+</sup> B-cell lymphomas in vivo. In fact, the FDA-approved radioimmunotherapeutic Zevalin, a  $^{90}\text{Y}$ -radiolabeled anti-CD20 antibody, requires a predose of cold rituximab to block accumulation of the  $^{90}\text{Y}$  radioimmunotherapeutic in the spleen and to increase targeting of lymphoma cells (24).

The technique of bolus or predosing injections has proven important for targets other than immunological cell surface molecules where antigen sinks exist. Bolus injections were used recently, for example, in an  $^{89}\text{Zr}$ -radiolabeled trastuzumab immuno-PET study that required high doses for reliable targeting in patients due to shed extracellular domain of HER2 in the plasma (25). Also, both  $^{111}\text{In}$ -radiolabeled anti-EGF receptor and anti-VEGF receptor antibodies demonstrated high lung and/or liver uptake that could be reduced and tumor uptake enhanced when higher protein doses were injected (26, 27). Furthermore, the concept of blocking the antigen sink has repercussions in the field of therapeutic antibody–drug conjugates. For example, predosing injections were used to block the antigen sink of tomoregulin, or TENB2, a transmembrane protein overexpressed in prostate tumors, to increase the therapeutic index of the monomethyl auristatin E-conjugated anti-TENB2 antibody (28). This study also highlights the fine balance between efficient blocking of the antigen sink vs. displacing the tumor uptake. The ability of these anti-CD8 Mb fragments to image either CD8<sup>+</sup> lymphomas or tumor-infiltrating CD8<sup>+</sup> T cells, for example, might rely on efficiently blocking the antigen sink for consistent targeting.

The rapid clearance of the anti-CD8 Mbs could also be due to the presence of multimers, causing increased liver uptake at early time points. At 4 h p.i., the CD8 Mbs have ~60–70%ID/g in the liver, compared with other  $^{64}\text{Cu}$ -radiolabeled Mbs that range from 15 to 32.4%ID/g at 4–5 h p.i. (19, 29). Nonspecific liver uptake and retention occur when using  $^{64}\text{Cu}$  due to the transchelation of copper to enzymes in the liver (30). However, an Mb dimer (~160 kDa) is similar in size to an intact antibody but lacks the full Fc domain that allows for neonatal Fc receptor recycling. When injected with  $^{64}\text{Cu}$ -NOTA-YTS169 Mb, both B/6 and C3H mice showed decreased uptake in lymph nodes, spleen, and blood compared with the  $^{64}\text{Cu}$ -NOTA-2.43 Mb. This could be attributed to the higher amount of multimer in the YTS169 Mb than in the 2.43 Mb, as shown by SEC, accelerating hepatic clearance and resulting in a decreased blood  $t_{1/2}$  and lower ability to target lymph nodes. It

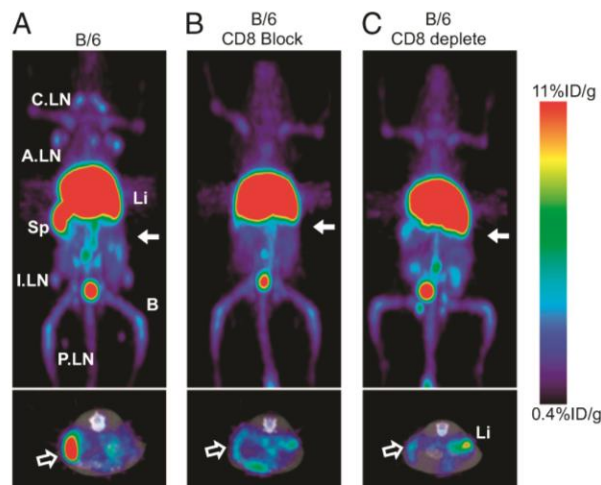


**Fig. 6.** Immuno-PET imaging of  $^{64}\text{Cu}$ -NOTA-2.43 Mb in antigen-blocked and antigen-depleted B/6 mice is shown. Immuno-PET images were acquired 4 h p.i. of  $^{64}\text{Cu}$ -NOTA-2.43 Mb into: WT B/6 (A), B/6 mice blocked with 4 mg/kg of cold Mb (B), and B/6 mice treated with an anti-CD8-depleting antibody (C). Solid white arrows (Upper, 20-mm coronal MIPs) indicate where the transverse images (Lower, 2-mm MIPs) are acquired. (Lower) Hollow white arrows indicate the location of the spleen.

should be noted that the Mb multimers of both YTS169 and 2.43 importantly retain their ability to bind sCD8 $\alpha\beta$ , as shown by SEC. Potential aggregation/dimerization due to inter-V<sub>H</sub>-V<sub>L</sub> binding can be reduced, for example, by engineering two cysteines that stabilize the interaction between V<sub>H</sub> and V<sub>L</sub>, among other methods (31, 32).

The <sup>64</sup>Cu-NOTA-YTS169 Mb that binds both Lyt2.1 and Lyt2.2 expressed in different mouse strains showed varying uptake in the spleens and livers of B/6 and C3H mice. In this study, however, the C3H mice were 20 wk old and the B/6 mice were 8 wk old, with average spleen and liver weights of either 96 ± 9 mg and 883 ± 43 mg or 54 ± 3 mg and 653 ± 10 mg, respectively. Therefore, the weights of the organs greatly affect the %ID/g, and the actual %ID per organ 4 h p.i. is similar in the spleen and liver (Table 2). This highlights an important fact that %ID/g values are not consistent for every experiment but are very reproducible within groups of mice of the same age and weight.

The development of these anti-CD8 immuno-PET radiotracers will be beneficial for studying a host of preclinical disease models, including, but not limited to, lymphoma detection and tumor T-cell infiltration. Preclinical immunotherapy models enhancing the dynamic function and proliferation of cytotoxic T cells could potentially be monitored noninvasively in vivo using immuno-PET. Furthermore, the lessons learned in a preclinical setting will prove beneficial for the development and translation of anti-human CD8 antibody fragments for immuno-PET imaging in the clinic.

## Conclusion

Described here is the successful development of functional CD8 imaging agents based on engineered antibodies for immuno-PET

imaging in a variety of preclinical disease and immunotherapeutic models. Two allele-specific Mb fragments were produced, characterized, radiolabeled with <sup>64</sup>Cu, and used in micro-PET imaging to quantify uptake in lymphoid organs in WT mice in vivo. Examining antibody-based immuno-PET imaging of mouse CD8 expression is useful not only for immuno-PET imaging of preclinical models of CD8-based immunotherapy, but it has further implications for the development of an anti-human CD8 antibody or fragment-based immuno-PET imaging agent that is translatable to the clinic.

## Materials and Methods

Animal studies were approved by the University of California, Los Angeles (UCLA) Chancellor's Animal Research Committee. Mice were purchased from Jackson Laboratory. Detailed information on animals, cloning, Mb and recombinant antigen design, protein expression and purification, protein conjugation, flow cytometry, depletion assays, radiolabeling, immuno-PET imaging, biodistribution, and data analysis can be found in *SI Materials and Methods*.

**ACKNOWLEDGMENTS.** We are grateful to Waldemar Ladno, Darin Williams, and Dr. David Stout at the Crump Institute for Molecular Imaging at UCLA for their help with the small-animal PET scans. We thank Drs. Antoni Ribas and Caius Radu for their inspiring discussions. We thank Washington University School of Medicine for the <sup>64</sup>Cu production. Furthermore, we thank the Jonsson Comprehensive Cancer Center (NIH Grant CA016042), the Genoseq Core Facility, and the Flow Cytometry Core Facility at UCLA. This work was supported by the UCLA Scholars in Oncologic Molecular Imaging training program [National Institutes of Health (NIH) Grant R25T CA098010] and by the California Institute for Regenerative Medicine (Grant RT1-01126-1). M.N.M. is supported by California Institute for Regenerative Medicine Training Grant TG2-01169. O.N.W. is an investigator of the Howard Hughes Medical Institute.

- Pillay V, Gan HK, Scott AM (2011) Antibodies in oncology. *New Biotechnol* 28(5):518–529.
- Rothe A, Rubbert A (2011) Recombinant proteins in rheumatology—Recent advances. *New Biotechnol* 28(5):502–510.
- Wu AM, Senter PD (2005) Arming antibodies: Prospects and challenges for immunoconjugates. *Nat Biotechnol* 23(9):1137–1146.
- Knowles SM, Wu AM (2012) Advances in immuno-positron emission tomography: Antibodies for molecular imaging in oncology. *J Clin Oncol* 30(31):3884–3892.
- Matsui K, Wang Z, McCarthy TJ, Allen PM, Reichert DE (2004) Quantitation and visualization of tumor-specific T cells in the secondary lymphoid organs during and after tumor elimination by PET. *Nucl Med Biol* 31(8):1021–1031.
- Pittet MJ, et al. (2007) In vivo imaging of T cell delivery to tumors after adoptive transfer therapy. *Proc Natl Acad Sci USA* 104(30):12457–12461.
- Nair-Gill ED, Shu CJ, Radu CG, Witte ON (2008) Non-invasive imaging of adaptive immunity using positron emission tomography. *Immunol Rev* 221:214–228.
- Yaghoubi SS, Campbell DO, Radu CG, Czernin J (2012) Positron emission tomography reporter genes and reporter probes: Gene and cell therapy applications. *Theranostics* 2(4):374–391.
- Koya RC, et al. (2010) Kinetic phases of distribution and tumor targeting by T cell receptor engineered lymphocytes inducing robust antitumor responses. *Proc Natl Acad Sci USA* 107(32):14286–14291.
- Laing RE, Nair-Gill E, Witte ON, Radu CG (2010) Visualizing cancer and immune cell function with metabolic positron emission tomography. *Curr Opin Genet Dev* 20(1):100–105.
- Juweid ME, Cheson BD (2006) Positron-emission tomography and assessment of cancer therapy. *N Engl J Med* 354(5):496–507.
- Mamede M, et al. (2003) Differential uptake of (18)F-fluorodeoxyglucose by experimental tumors xenografted into immunocompetent and immunodeficient mice and the effect of immunomodification. *Neoplasia* 5(2):179–183.
- Ribas A, et al. (2010) Imaging of CTLA4 blockade-induced cell replication with (18)F-FLT PET in patients with advanced melanoma treated with tremelimumab. *J Nucl Med* 51(3):340–346.
- Aarntzen EH, et al. (2011) Early identification of antigen-specific immune responses in vivo by [<sup>18</sup>F]-labeled 3'-fluoro-3'-deoxy-thymidine ([<sup>18</sup>F]FLT) PET imaging. *Proc Natl Acad Sci USA* 108(45):18396–18399.
- Nair-Gill E, et al. (2010) PET probes for distinct metabolic pathways have different cell specificities during immune responses in mice. *J Clin Invest* 120(6):2005–2015.
- Olafsen T, Wu AM (2010) Antibody vectors for imaging. *Semin Nucl Med* 40(3):167–181.
- Malviya G, Galli F, Sonni I, Pacilio M, Signore A (2010) Targeting T and B lymphocytes with radiolabelled antibodies for diagnostic and therapeutic applications. *Q J Nucl Med Mol Imaging* 54(6):654–676.
- Martin-Fontecha A, et al. (2003) Regulation of dendritic cell migration to the draining lymph node: Impact on T lymphocyte traffic and priming. *J Exp Med* 198(4):615–621.
- Olafsen T, et al. (2005) Optimizing radiolabeled engineered anti-p185HER2 antibody fragments for in vivo imaging. *Cancer Res* 65(13):5907–5916.
- Natarajan A, et al. (2012) Positron emission tomography of <sup>64</sup>Cu-DOTA-Rituximab in a transgenic mouse model expressing human CD20 for clinical translation to image NHL. *Mol Imaging Biol* 14(5):608–616.
- Natarajan A, Habte F, Gambhir SS (2012) Development of a Novel Long-Lived ImmunoPET Tracer for Monitoring Lymphoma Therapy in a Humanized Transgenic Mouse Model. *Bioconjug Chem* 23(6):1221–1229.
- Olafsen T, et al. (2010) ImmunoPET imaging of B-cell lymphoma using <sup>124</sup>I-anti-CD20 scFv dimers (diabodies). *Protein Eng Des Sel* 23(4):243–249.
- Olafsen T, et al. (2009) Recombinant anti-CD20 antibody fragments for small-animal PET imaging of B-cell lymphomas. *J Nucl Med* 50(9):1500–1508.
- Witzig TE, et al. (1999) Phase I/II trial of IDEC-Y2B8 radioimmunotherapy for treatment of relapsed or refractory CD20(+) B-cell non-Hodgkin's lymphoma. *J Clin Oncol* 17(12):3793–3803.
- Dijkers EC, et al. (2010) Biodistribution of <sup>89</sup>Zr-trastuzumab and PET imaging of HER2-positive lesions in patients with metastatic breast cancer. *Clin Pharmacol Ther* 87(5):586–592.
- Bumbaca D, et al. (2012) Maximizing tumour exposure to anti-neuropilin-1 antibody requires saturation of non-tumour tissue antigenic sinks in mice. *Br J Pharmacol* 166(1):368–377.
- Divgi CR, et al. (1991) Phase I and imaging trial of indium 111-labeled anti-epidermal growth factor receptor monoclonal antibody 225 in patients with squamous cell lung carcinoma. *J Natl Cancer Inst* 83(2):97–104.
- Boswell CA, et al. (2012) Differential effects of pre dosing on tumor and tissue uptake of an <sup>111</sup>In-labeled anti-TENB2 antibody-drug conjugate. *J Nucl Med* 53(9):1454–1461.
- Wu AM, et al. (2000) High-resolution microPET imaging of carcinoembryonic antigen-positive xenografts by using a copper-64-labeled engineered antibody fragment. *Proc Natl Acad Sci USA* 97(15):8495–8500.
- Rogers BE, et al. (1996) Comparison of four bifunctional chelates for radiolabeling monoclonal antibodies with copper radioisotopes: Biodistribution and metabolism. *Bioconjug Chem* 7(4):511–522.
- Glockshuber R, Malia M, Pfützinger I, Plückthun A (1990) A comparison of strategies to stabilize immunoglobulin Fv-fragments. *Biochemistry* 29(6):1362–1367.
- Wörn A, Plückthun A (2001) Stability engineering of antibody single-chain Fv fragments. *J Mol Biol* 305(5):989–1010.



# Supporting Information

Tavaré et al. 10.1073/pnas.1316922111

## SI Materials and Methods

C57BL/6, C3H, and NOD.Cg-Prkdc<sup>scid</sup> Il2rg<sup>tm1Wjl</sup>/SzJ (NSG) mice were ordered from the Jackson Laboratory and housed and maintained by the Department of Laboratory Animal Medicine at the University of California, Los Angeles (UCLA). Protocols for all animal studies were reviewed and approved by the UCLA Chancellor's Animal Research Committee.

### Determination of V<sub>H</sub> and V<sub>L</sub> Sequences from Parental Hybridomas.

The YTS 169.4.2.1 (YTS169) hybridoma was obtained from the Therapeutic Immunology Group at Oxford University and cultured in Iscove's modified Dulbecco's medium (American Type Culture Collection) plus 10% FBS and penicillin/streptomycin (Pen/Strep) (1). The 2.43 hybridoma was obtained from the American Type Culture Collection (TIB-210) and cultured in DMEM (Mediatech, Inc.) plus 10% FBS and Pen/Strep. V<sub>H</sub> and V<sub>L</sub> sequences were obtained by RT-PCR using primers published by Dübel et al. (2). RNA was isolated from hybridomas grown in culture using the Quick-RNA MicroPrep kit (Zymo Research) according to the manufacturer's instructions. Freshly isolated RNA was immediately used for RT-PCR using a combination of primers as reported by Dübel et al. (2) for the heavy-chain FR1 region (Bi3, Bi3b, and Bi3c) and the kappa-chain FR1 region (Bi6, Bi7, and Bi8). The heavy-chain C<sub>H</sub>1 primer used was 5'-CGG AAT TCA GGG GCC ATG GGA TAG AC. The kappa-chain constant domain primer used was 5'-CGG AAT TCG GAT GGT GGG AAG ATG GA. RT-PCR was performed using the OneStep RT-PCR kit (Qiagen) according to the manufacturer's instructions before Tris-acetate-EDTA-agarose gel extraction, ligation using a TOPO TA Cloning kit (Invitrogen), and DH5 $\alpha$  (Invitrogen) transformation. Colonies were selected for isolation of plasmid DNA using a Miniprep Kit (Invitrogen) for subsequent sequencing at the UCLA sequencing core facility. Sequences were analyzed with BLAST for V<sub>H</sub> or V<sub>L</sub> homology. Sequences were verified by three identical recovered sequences from at least two different experiments. For the hybridoma 2.43, the obtained V<sub>H</sub> and V<sub>L</sub> sequences were confirmed with trypsin digest-MS of the purified parental antibody, which was performed at the UCLA core facility. The YTS169 hybridoma was engineered to antibody fragments without further V<sub>H</sub> and V<sub>L</sub> validation.

**Design and Construction of Anti-mCD8 Minibodies.** The 2.43 and YTS169 minibody (Mb) constructs were synthesized by GeneArt (Invitrogen) to contain a Kozak sequence, followed by the mouse Ig kappa secretion signal, V<sub>H</sub>, an 18 GlySer-rich amino acid linker (GSTSGGGSGGGSGGGSS), V<sub>L</sub>, murine IgG2a hinge, the murine IgG2a C<sub>H</sub>3 domain, and a C-terminal hexahistidine sequence (Fig. 1A). The Mb cassette contains the N-terminal XbaI and C-terminal EcoRI restriction sites for subcloning into the mammalian expression vector pEE12 (Lonza).

**Expression and Purification of Engineered Mb Antibody Fragments.** A total of  $2 \times 10^6$  NS0 mouse myeloma cells were transfected with 10  $\mu$ g of FspI (New England Biolabs) linearized vector DNA by electroporation (Multiporator; Eppendorf) and selected in glutamine-deficient DMEM as previously described (3). The supernatants of individual clones were screened for expression by nickel-nitrotriacetic acid (Ni-NTA) HisSorb Plates (Qiagen) using the goat anti-mouse IgG2a-alkaline phosphatase conjugate for detection (1:2,500; Santa Cruz Biotechnologies). Expression was also confirmed for clones positive for expression by

ELISA by SDS/PAGE, followed by Western blot analysis using the same goat anti-mouse IgG2a-alkaline phosphatase conjugate (1:2,500) and developed with the NBT/BCIP Color Development substrate kit (Promega). The highest producing clones were expanded and brought to terminal culture for expression of secreted proteins.

Soluble Mbs were purified from cell culture supernatants using Ni-NTA affinity chromatography (GE Healthcare) using an ÄKTA purifier FPLC (GE Healthcare). Supernatants were loaded onto the column in the presence of 10 mM imidazole and eluted with a gradient of 10–500 mM imidazole. The purified proteins were then dialyzed against PBS using Slide-A-Lyzer dialysis cassettes [molecular weight cutoff (MWCO) = 10,000; Thermo Scientific] and concentrated with a Vivaspinn 20 (MWCO = 10,000; Sartorius). Final protein concentrations were determined by measuring UV absorbance at 280 nm. Purified proteins were analyzed by SDS/PAGE under nonreducing conditions. Native structural size was determined by Superdex 200 (GE Healthcare) size exclusion chromatography (SEC) using PBS as the running buffer.

**Production of Soluble CD8 $\alpha\beta$  Fusion Protein.** PCR was used to amplify the soluble domains of both CD8 $\alpha$  (residues Lys1–Ser124 of mature CD8 $\alpha$ , Lys2.2<sup>+</sup>) and CD8 $\beta$  (residues Leu1–Val117 of mature CD8 $\beta$ ) and to fuse them via a 29-aa  $\alpha$ -helical linker (AG-SADDARKDAGSKDDARKDDARKDGSSA). This linker is similar to the linker previously described for soluble CD8 $\alpha\beta$  (sCD8 $\alpha\beta$ ) fusion (4), except for the GS amino acids at linker positions 12 and 13 (underlined) due to the insertion of a BamHI site for cloning purposes. CD8 $\alpha$  was amplified to contain an N-terminal AgeI site and a C-terminal sequence corresponding to AGSADDARKDAGS. CD8 $\beta$  was amplified to contain the N-terminal amino acid sequence GSKDDARKDDARKDGSSA and a C-terminal NotI site. The following primers were used:

sCD8 $\alpha$ -Forward (F): 5'-CACACAGAGCTCACCGGTAAG-  
CCACAGGCACCCGAAC  
sCD8 $\alpha$ -Reverse (R): 5'-TGTGTGGGATCCCGCATCCTTT-  
CTTGATCGTCGGCAGATCCTGCAGAGTTCACCTTC-  
TGAAG  
sCD8 $\beta$ -F: 5'-CACACAGGATCCAAAGATGACGCAAGGA-  
AGGACGATGCTAGGAAGGATGGATCTTCCGCACTCA-  
TTCAGACCCCTTCG  
sCD8 $\beta$ -R: 5'-TGTGTGTCTAGACGCGGCCGCAACCACA-  
GTCAGCTTCGTC

Briefly, PCR products of sCD8 $\alpha$  and sCD8 $\beta$  were gel-purified, digested with BamHI, and ligated using T4 DNA ligase. Ligations were used as the template for PCR using the sCD8 $\alpha$ -F and sCD8 $\beta$ -R primers. The PCR product was restriction enzyme-digested with AgeI and NotI and ligated into the predigested pEE12-2.43 Mb cassette constructed above for the addition of a C-terminal His-Tag. Sequence verification, NS0 electroporation, clonal selection, protein production, and Ni-NTA purification were performed as described above. SEC using a Superdex 75 column (GE Healthcare) was required for final purification.

**Affinity Measurements.** Before surface plasmon resonance (SPR) analysis, solution-phase binding of the Mbs to the recombinant sCD8 $\alpha\beta$  was confirmed using SEC. Equimolar amounts of sCD8 $\alpha\beta$  and Mb were incubated together in PBS for 5 min before Superdex 200 SEC analysis. Binding was confirmed by both earlier elution times in SEC and SDS/PAGE analysis of the elution fractions from SEC. SPR analysis was performed on a Biacore 3000

(Precision Antibody, Inc.). Briefly, Mbs were captured using goat anti-mouse IgG Fc, and sCD8 $\alpha\beta$  antigen was flowed over the chip at 100, 50, 25, 12.5, 6.25, and 0 nM. The equilibrium dissociation constant ( $K_D$ ) was calculated from the observed association ( $k_a$ ) and dissociation ( $k_d$ ) rate constants.

**FITC Conjugation.** The 2.43 Mb was incubated with a 40-fold molar excess of FITC (Molecular Probes) at pH 8.5 for 4 h at 4 °C. Excess FITC was removed using a PD-10 column in PBS (GE Healthcare). Protein was concentrated using a 0.5-mL spin filter (MWCO = 3 kDa; Amicon), and the conjugation efficiency was evaluated using a NanoDrop (Thermo Scientific) to calculate the ratio of moles of fluorescein to moles of protein.

**Flow Cytometry.** A total of  $2 \times 10^5$  BW58, TK-1, or EL-4 cells (American Type Culture Collection) in 200  $\mu$ L of PBS plus 1% FBS was incubated with 2  $\mu$ g of the anti-CD8 Mb constructs for 45 min on ice. After two washes in PBS plus 1% FBS, they were subsequently stained with mouse goat anti-mouse IgG2a-phycoerythrin (PE; Santa Cruz Biotechnologies) for 45 min on ice in PBS plus 1% FBS. Following two additional washes in PBS plus 1% FBS, flow cytometry analysis was performed using a BD Biosciences LSR II at the UCLA flow cytometry core facility.

Flow cytometry on primary cells from Lyt2.2<sup>+</sup> C57BL/6 (B/6) and Lyt2.1<sup>+</sup> C3H mice was performed on single-cell suspensions from the spleen, bone marrow, peripheral blood, thymus, and lymph nodes. Organs were mashed over 75- $\mu$ m filters and then 40- $\mu$ m filters in RPMI plus 5% FBS to produce single-cell suspensions. Following RBC lysis using ammonium-chloride-potassium lysis buffer, the cells were stained for 1 h on ice with either Lyt2.2-specific fluorescein-conjugated 2.43 Mb or anti-CD8-fluorescein (clone 53-6.7; eBioscience) and anti-CD4-PE (clone GK1.5; eBioscience) or anti-CD45-allophycocyanin (clone 30-F11; eBioscience). Cells were then washed with PBS and analyzed using a BD FACSCanto (Becton Dickinson).

**CD8 Depletion.** Mice were treated for three consecutive days with 330  $\mu$ g of anti-CD8 depleting antibody (clone 53-6.7 purchased from University of California, San Francisco Monoclonal Antibody Core) injected i.p. (165  $\mu$ L in saline) or 250  $\mu$ g of 2.43 Mb injected i.v. (125  $\mu$ L in saline). Two to three days posttreatment, single-cell suspensions from the spleen, peripheral blood, thymus, and lymph nodes were isolated and stained as described above for CD8 depletion analysis.

**SCN-NOTA Conjugation.** All solutions were made metal-free (MF) using Chelex 100 (1.2 g/L; BioRad). The 2.43 and YTS169 Mbs were dialyzed against MF-PBS overnight using Slide-A-Lyzer MINI dialysis units (Thermo Scientific). Proteins at 1–2 mg/mL were then incubated with an 80-fold molar excess of S-2-(4-isothiocyanatobenzyl)-1,4,7-triazacyclononane-1,4,7-triacetic acid (p-SCN-Bn-NOTA; Macrocylics) for 4 h at 4 °C. The pH was

adjusted to 8.5 using 1 M MF-NaOH. Excess p-SCN-Bn-NOTA was removed by PD-10 desalting columns that were preequilibrated MF-PBS. Eluted protein was concentrated with Amicon Ultra centrifugal filters (MWCO = 0.5 mL and 10 kDa; Millipore) that had been washed twice with MF-PBS.

**<sup>64</sup>Cu Radiolabeling.** [<sup>64</sup>Cu]CuCl<sub>2</sub> was obtained from the Division of Radiological Sciences, Washington University School of Medicine. Five microliters of 250 mM ammonium acetate (pH 7.0) was added to ~37 MBq (~1 mCi) <sup>64</sup>CuCl<sub>2</sub> before the addition of 60–80  $\mu$ g of NOTA-conjugated Mb at 1.4 mg/mL in saline. Protein was incubated for 30–45 min at 42 °C, followed by a challenge of 5 mM EDTA for 5 min at room temperature. Radiolabeling efficiency was measured using instant thin-layer chromatography (ITLC) strips (Biodex Medical Systems) with saline as the mobile phase. The ITLC strip was cut in half, and sections were counted using a Wizard 3'' 1480 Automatic Gamma Counter (PerkinElmer). Radiochemical purity was assessed by ITLC using saline as the mobile phase. Protein was purified using BioRad6 Spin columns equilibrated with PBS if the radiochemical purity was <95%.

The percentage of functional <sup>64</sup>Cu-NOTA Mb postradiolabeling was measured by incubating 30–50 ng of radiolabeled Mb with >40  $\times 10^6$  antigen-positive (BW58) or antigen-negative (EL-4) murine lymphoma cells in PBS plus 1% FBS for 1 h. Cells were centrifuged, the amount of activity in supernatant vs. the pellet was counted in a gamma counter, and the immunoreactive fraction was calculated as (% cell bound activity/total activity) \* 100.

**Micro-PET Imaging.** Two hundred-microliter doses containing 2.6–2.9 MBq (70–80  $\mu$ Ci, 8–10  $\mu$ Ci/ $\mu$ g) of <sup>64</sup>Cu-radiolabeled Mb were prepared in saline and injected i.v. into B/6, C3H, or NSG mice. At 4 h postinjection, mice were anesthetized using 2% isoflurane and micro-PET scans were acquired using an Inveon microPET scanner (Siemens), followed by micro-CT scans (ImTek). Micro-PET images were reconstructed using nonattenuation or scatter-corrected filtered back-projection, and AMIDE was used for image analysis and display.

**Biodistribution.** After micro-PET/CT imaging, mice were euthanized, the organs and blood were collected and weighed, and the activity was determined in a gamma counter. The percent-injected dose per gram of tissue was calculated using a standard containing 2% of the injected dose. Left and right axillary lymph nodes were pooled and counted for biodistribution studies.

**Data Analysis.** Data values are reported as mean  $\pm$  SD. Statistical analysis was performed using a two-tailed Student *t* test. Ex vivo biodistributions of <sup>64</sup>Cu-NOTA-2.43 Mb in C3H, NSG, B/6 blocked, and B/6 depleted mice were compared with the WT B/6 mice individually. Micro-PET/CT images are displayed as 20- or 2-mm maximum intensity projections for coronal or transverse images, respectively.

1. Cobbold SP, Jayasuriya A, Nash A, Prospero TD, Waldmann H (1984) Therapy with monoclonal antibodies by elimination of T-cell subsets in vivo. *Nature* 312(5994): 548–551.
2. Dübel S, et al. (1994) Isolation of IgG antibody Fv-DNA from various mouse and rat hybridoma cell lines using the polymerase chain reaction with a simple set of primers. *J Immunol Methods* 175(1):89–95.

3. Yazaki PJ, et al. (2001) Mammalian expression and hollow fiber bioreactor production of recombinant anti-CEA diabody and minibody for clinical applications. *J Immunol Methods* 253(1-2):195–208.
4. Chang HC, et al. (2005) Structural and mutational analyses of a CD8 $\alpha$ beta heterodimer and comparison with the CD8 $\alpha$ alpha homodimer. *Immunity* 23(6): 661–671.

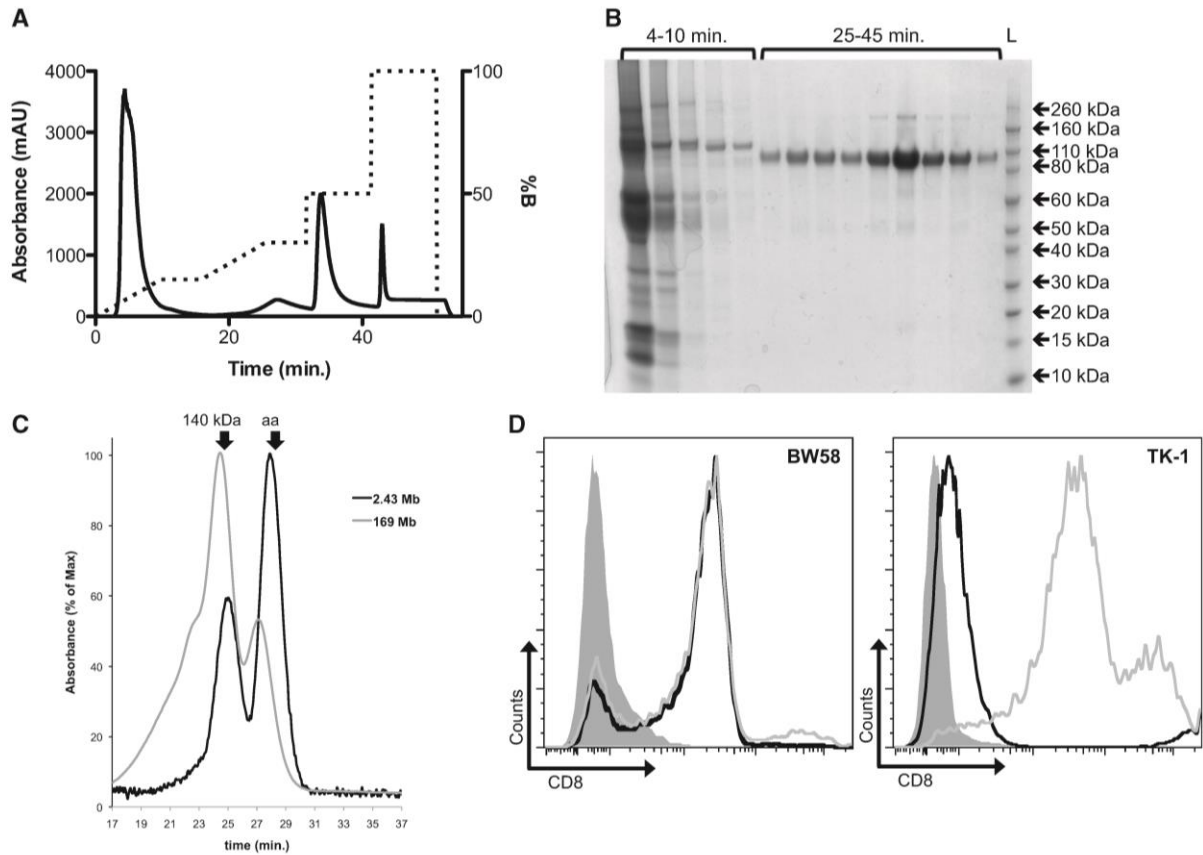


**Fig. S1.** Purification and characterization of 2.43 and YTS169 Mbs are shown. Mbs were purified from NS0 supernatant in one step using Ni-NTA immobilized metal affinity chromatography using imidazole elution (A) as shown by SDS/PAGE (B). mAU, milli-absorbance units. (C) SEC shows the presence of 81% ~80-kDa Mb for the 2.43 Mb and 23% ~80-kDa Mb for the YTS169 Mb. Max, maximum. (D, Left) Both the 2.43 Mb (black line) and YTS169 Mb (gray line) bind CD8 expressed on the Lyt2.2<sup>+</sup> BW58 murine thymoma cell line. (D, Right) Only the YTS169 Mb binds CD8 expressed on the Lyt2.1<sup>+</sup> TK-1 murine lymphoma cell line, however. The solid gray peak is cells only.

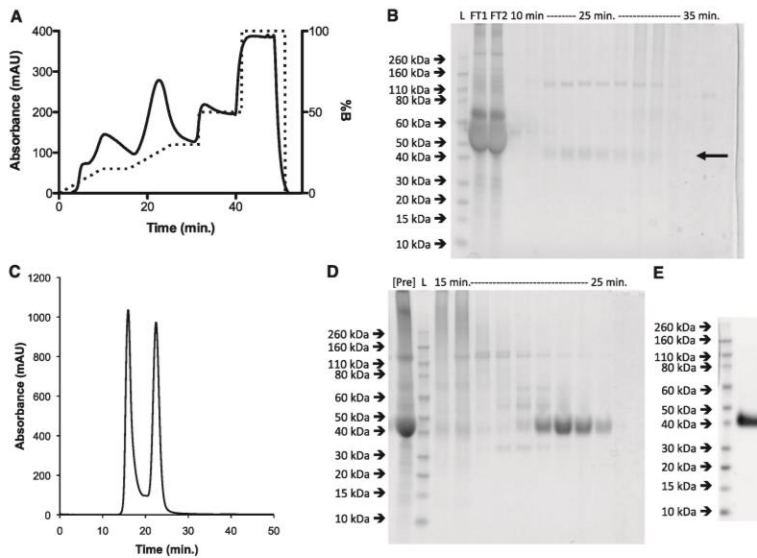


**Fig. S2.** Purification of the sCD8 $\alpha\beta$  antigen in two steps. First, Ni-NTA immobilized metal affinity chromatography using imidazole elution (A) purified the sCD8 $\alpha\beta$  and some higher molecular-weight contaminants, as shown by SDS/PAGE (B). Second, SEC (C) was used to remove contaminants, as shown by SDS/PAGE (D). (E) Purified antigen is shown.

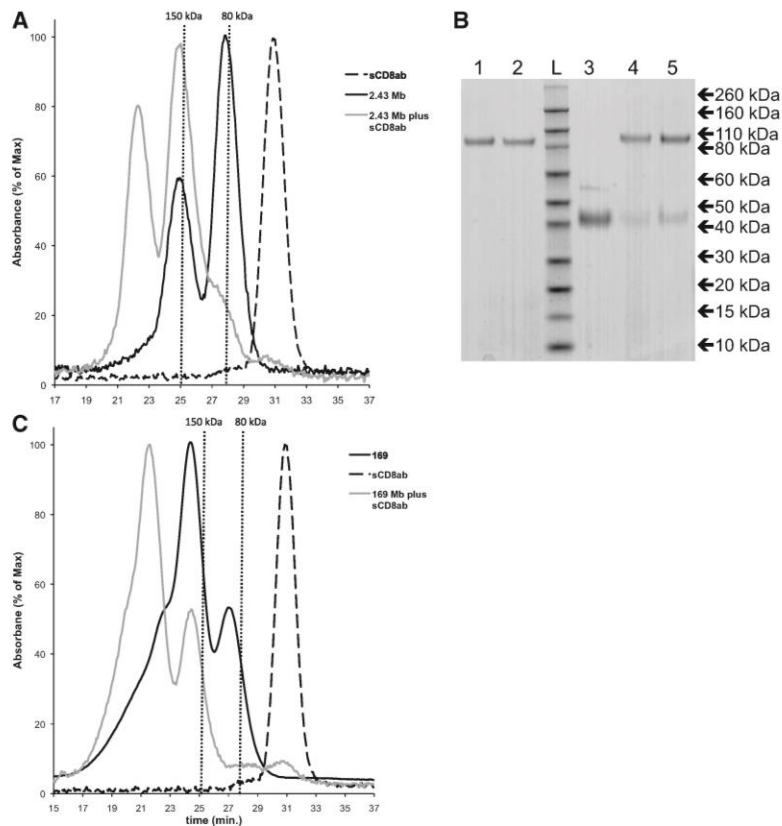
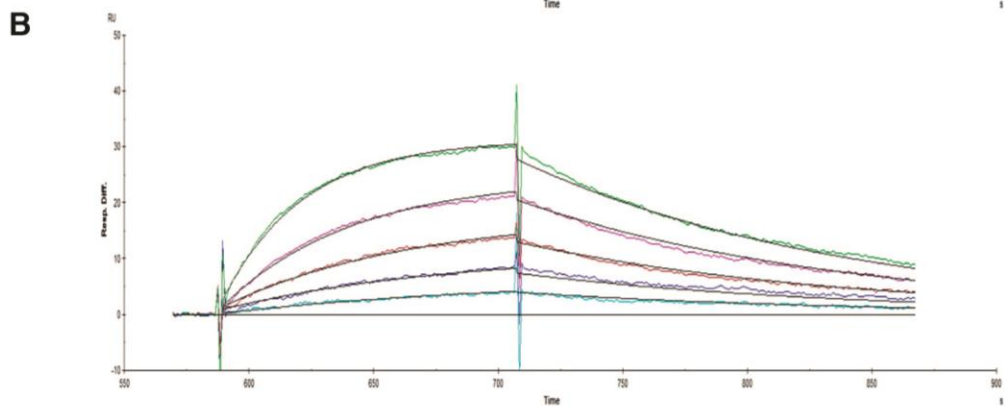
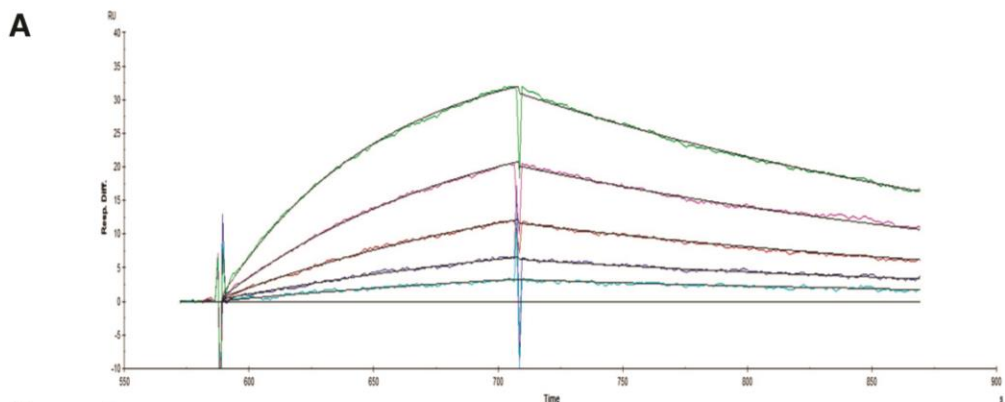


**Fig. S3.** Solution phase binding of 2.43 and YTS169 Mbs to sCD8 $\alpha\beta$  is demonstrated by SEC. The 2.43 Mb (A) or the YTS169 Mb (C) was mixed with equimolar amounts of sCD8 $\alpha\beta$  for 5 min before SEC analysis. (B) SDS/PAGE analysis of SEC elutions of 2.43 Mb alone at 25 and 27.5 min (lanes 1 and 2), sCD8 $\alpha\beta$  alone at 31 min (lane 3), and 2.43 Mb plus sCD8 $\alpha\beta$  at 22 and 25 min (lanes 4 and 5). Binding of 2.43 Mb to sCD8 $\alpha\beta$  is confirmed for both the 80-kDa Mb and the ~160-kDa multimer in lanes 4 and 5.



**C**

Ligand	Analyte	$k_a$ (1/Ms)	$k_d$ (1/s)	$R_{max}$ (RU)	[analyte]	$K_A$ (1/M)	$K_D$ (M)	$\chi^2$
2.43	sCD8 $\alpha\beta$	$1.2 \times 10^5$	$4.1 \times 10^{-3}$	48.9	0-100 nM	$3.0 \times 10^7$	$3.4 \times 10^{-8}$	0.05
YTS 169	sCD8 $\alpha\beta$	$2.3 \times 10^5$	$7.6 \times 10^{-3}$	37.9	0-100 nM	$3.0 \times 10^7$	$3.3 \times 10^{-8}$	0.17

**Fig. S4.** Kinetic analysis of Mb binding to sCD8 $\alpha\beta$  antigen using SPR Biacore 3000 is shown. The 2.43 (A) or YTS169 (B) Mb was immobilized using goat anti-mouse IgG Fc capture. Soluble monovalent antigen was then flowed over the chip at 100 (green), 50 (magenta), 25 (red), 12.5 (dark blue), 6.25 (light blue), and 0 (black) nM. (C) Full kinetic analysis is shown.  $k_a$ , association rate constant;  $K_A$ , equilibrium association constant;  $k_d$ , dissociation rate constant;  $K_D$ , equilibrium dissociation constant; Resp. Diff., response difference;  $R_{max}$ , maximum resonance units.; RU, resonance units.

## **CHAPTER 7:**

Conclusion and Future Studies

The primary goal of the research presented here is to develop non-invasive imaging strategies for tracking immune cell populations in vivo. In the previous five chapters, we have performed a series of studies that utilize positron emission tomography (PET) as a non-invasive imaging tool for tracking hematopoietic cells in vivo (1-5). Hematopoietic cells genetically engineered to express a PET reporter gene allowed for serial tracking of hematopoietic stem cell (HSC) transplant and engraftment (4), the trafficking of engineered T cells to the tumor of interest(3), and monitoring the ablation of reporter/suicide-gene labeled cells (2). For detecting endogenous CD8 cells, engineered antibody fragments were developed and imaged by immunoPET techniques (5). These pre-clinical studies establish multiple PET imaging strategies that can be directly translated for clinical use in monitoring immune cell populations.

PET reporter imaging has had limited clinical translation to date. In clinical studies, herpes simplex virus thymidine kinase 1 (HSV-TK) expressing lymphocytes were transferred into patients and a rapid immune response was detected against the cells (6). The adaptive immune response was determined to be CD8 cells directed against the HSV-TK transgene (6, 7). This immunogenicity has precluded the use of HSV-TK PET reporter gene imaging in a number of clinical studies that would greatly benefit from the non-invasive tracking of transplanted engineered cells. PET reporter imaging could provide a method to simultaneously detect transplanted cells throughout the whole body non-invasively. For adoptive cell therapies, imaging could be used to determine whether lymphocytes have trafficked to the tumor of interest or whether cells have migrated to alternate tissue or lymphoid organs.

As described in chapters 3-4, we developed and tested a human based PET reporter gene that is thought to be non-immunogenic (3, 4). Human deoxycytidine kinase with three point

mutations within the active site (hdCK3mut), when probed with [<sup>18</sup>F]-L-FMAU, was approximately two-fold more sensitive than HSV-TK as a PET reporter gene (1). Expression of hdCK3mut was inert, and HSCs were capable of long-term engraftment, expansion and differentiation with no diminution in quantity of reporter cells. In hdCK3mut expressing T cells, no defect in function was observed. PET reporter imaging detected the homing of hdCK3mut engineered T cells to the HLA matched tumor, providing a non-invasive tracking method.

### **Unanswered questions and future studies:**

#### **Can hdCK3mut be used as a suicide gene in vivo?**

Recombinant enzyme studies have demonstrated that hdCK3mut has a lower  $K_m$  for several chemotherapeutic agents in comparison to WT hdCK (8-10). Our work has demonstrated that cell lines expressing hdCK3mut were approximately 10 times more sensitive to Gemcitabine than cells expressing wild-type dCK (data not shown). Additional nucleoside analog compounds were tested with no difference in viability. Further in vitro and in vivo studies will need to be completed to identify potential drugs that selectively kill hdCK3mut expressing cells.

#### **Can memory T cells be detected by hdCK3mut?**

Our studies have demonstrated that hdCK3mut causes no defects in immune cell development or during a primary immune response (3). One question to be addressed is whether the expression of hdCK3mut alters memory T cell development or if these residual memory T cells can be detected by PET reporter imaging. Memory T cells are usually quiescent and their metabolic



state is different than activated T cells (11). This change in metabolism may alter the nucleoside transporter levels that transport [<sup>18</sup>F]-L-FMAU into cells and prevent the detection of reporter-labeled memory T cells.

### **Challenges for PET reporter applications in clinical therapies:**

To include PET reporter gene imaging into clinical applications, an argument must provide reasons why PET reporter imaging is needed and superior to current methods of monitoring.

Unlike biopsies which provide tissue-specific information at a static time point, serial reporter scans can track transplants long-term and non-invasively. Biopsies are biased based on the small sample size and selected location. The biopsy can damage surrounding tissue or potentially introduce an infection (12). Reporter imaging can be substituted as a method to detect transplant viability, and, if needed, provide information on a location to biopsy that contains transplanted cells.

Continuous expression of a transgene needs to be demonstrated as safe and inert in labeled cells prior to clinical translation. hdCK3mut causes no defect on hematopoietic cell function and is hypothesized to be non-immunogenic in clinical applications (4). Experiments in Chapter 4 demonstrated that the expression of hdCK3mut in antigen presenting cells did not induce T cell activation (3). There is still a risk of immunogenicity once cells expressing hdCK3mut are used clinically, but there are no further pre-clinical tests to completely disprove this.

Total radiation dose from the administered probe is a limitation in all PET imaging studies. [ $^{18}\text{F}$ ]-L-FMAU is cleared through renal filtration. This clearance exposes the highest dose of radiation to the bladder and also residual dose in the liver, kidneys, gall bladder, GI tract and myocardium (13). Pre-clinical biodistribution and a small clinical safety study has demonstrated the safety of [ $^{18}\text{F}$ ]-L-FMAU as a probe for clinical imaging (13).

### **Applications of PET reporter imaging in stem cell based therapies:**

As confirmed in Chapters 3-5, PET reporter imaging can monitor the engraftment and expansion of human stem and progenitor cells after HSC transplant (2-4). PET reporter genes can be applied to monitor the kinetics of clinical HSC transplants after gene therapy. In severe combined immunodeficiency (SCID) caused by a genetic loss of adenosine deaminase (ADA), gene therapy has corrected the enzyme deficiency and has been successful in clinical applications (14, 15). These transplants utilize genetically modified autologous HSCs, and inclusion of a PET reporter gene could allow serial measurements of the engraftment kinetics prior to peripheral T and B cell detection.

In stem cell based therapies that cannot be measured by peripheral blood or when biopsies are not possible, the inclusion of a PET reporter gene can solve an unmet need in tracking transplants (16). Examples could include stem cell therapies for replacing cardiomyocytes or pancreatic beta islet cells (16-19). Scans can determine the location and intensity of PET reporter expression, and provide a method to track the relative quantity and long-term engraftment of these transplanted cells in vivo.

### **PET reporter applications in immunotherapy:**

Engineered T cell therapies are expanding their clinical applications. Clinical trials with T cells engineered to express a chimeric antigen receptor (CAR) against CD19 have obtained complete remission and are believed to have cured patients with relapsed B cell acute lymphoblastic leukemia (B-ALL) (20). Investigators are hopeful that these engineered killer T cells will provide treatments for previously incurable cancers (21, 22). Although these cells have been highly effective, they have also been lethal in cases of on-target/off-tumor effects (23).

A major limitation of this approach is the lack of in vivo methods to determine off-target locations of engineered T cells. Co-expression of a PET reporter gene can allow for tracking T cells systemically (3). For pre-clinical models of engineered HLA-A2 TCRs the transgenic HLA-A2.1 SCID mouse can be used as a model system capable of carrying a xenograft test tumor. These mice will express HLA-A2.1 MHC class 1 and will present endogenous peptides systemically as well (24). Transplanted engineered T cells can be monitored for tumor homing, and to detect off-target T cell locations. The similarity between mouse and human proteins can identify off-target locations, and can predict complications in future human applications. Differences between species may not detect all potential complications due to alternate protein expression or sequences but can be used as a primary screening method.

### **Impact of hdCK3mut on PET reporter imaging:**

PET reporter imaging has been applied to pre-clinical studies for almost 20 years (25). Multiple PET reporter genes have been developed to optimize reporter expression and

sensitivity. Our work in Chapter 2 applies a standard imaging platform to compare different PET reporter genes sensitivity by comparing the vector copies per cell to the percent injected dose per gram (%ID/g) (1). As alternative PET reporter genes are developed, a standard comparison in the sensitivity to hdCK3mut or other previous PET reporter genes should be done. This assay can also be applied to testing novel PET probes for reporter detection. [<sup>18</sup>F]-L-FMAU has liver and myocardium uptake in healthy human scans (13). Identifying a different PET reporter probe that has lower background accumulation in humans may improve the range of applications for hdCK3mut reporter detection. A direct comparison of [<sup>18</sup>F]-L-FMAU and alternative probes can determine if there is a difference in signal accumulation. This will identify the optimal PET probe for each PET reporter gene.

The studies in chapter 3-5 demonstrate that PET reporter genes can be used for serial tracking of hematopoietic cells in vivo. hdCK3mut is the first PET reporter gene that has been tested for the long-term HSC reporter capacity (4). Engrafted cells were detected up to 32 weeks post bone marrow transplantation, with no counter selection of cells. Hematopoietic cells are continuously dividing and differentiating to supply a constant source of new blood cells. The hdCK3mut stem and progenitor population was not counter selected, and progeny cells expressed the PET reporter. Based on our studies in the hematopoietic system, we believe that expression of hdCK3mut will also be inert and maintained in other stem cell based therapies.

## **REFERENCES:**

1. Gil JS, Machado HB, Campbell DO, McCracken M, Radu C, Witte ON, and Herschman HR. Application of a rapid, simple, and accurate adenovirus-based method to compare PET reporter gene/PET reporter probe systems. *Mol Imaging Biol.* 2013;15(3):273-81.
2. Gschweng EH, McCracken, M.N., Kaufman, M.L., Ho, M., Hollis, R.P., Wang, X., Saini, N., Koya, R., Chodon, T., Ribas, A., Witte, O.N., Kohn, D.B. . In vivo HSV-sr39TK positron emission tomography and suicide gene elimination of human hematopoietic stem cells and their progeny in humanized mice. *Cancer Res.* 2014; Submitted
3. McCracken MN, Vatakis, D.N., Dhaval, D., McLaughlin, J., Zack, J.A., Witte, O.N. . Non-invasive detection of tumor infiltrating engineered T cells by human PET reporter imaging. *J Clin Invest.* 2014; Submitted
4. McCracken MN, Gschweng EH, Nair-Gill E, McLaughlin J, Cooper AR, Riedinger M, Cheng D, Nosala C, Kohn DB, and Witte ON. Long-term in vivo monitoring of mouse and human hematopoietic stem cell engraftment with a human positron emission tomography reporter gene. *Proc Natl Acad Sci U S A.* 2013;110(5):1857-62.
5. Tavare R, McCracken MN, Zettlitz KA, Knowles SM, Salazar FB, Olafsen T, Witte ON, and Wu AM. Engineered antibody fragments for immuno-PET imaging of endogenous CD8+ T cells in vivo. *Proc Natl Acad Sci U S A.* 2014;111(3):1108-13.
6. Berger C, Flowers ME, Warren EH, and Riddell SR. Analysis of transgene-specific immune responses that limit the in vivo persistence of adoptively transferred HSV-TK-modified donor T cells after allogeneic hematopoietic cell transplantation. *Blood.* 2006;107(6):2294-302.

7. Traversari C, Markt S, Magnani Z, Mangia P, Russo V, Ciceri F, Bonini C, and Bordignon C. The potential immunogenicity of the TK suicide gene does not prevent full clinical benefit associated with the use of TK-transduced donor lymphocytes in HSCT for hematologic malignancies. *Blood*. 2007;109(11):4708-15.
8. Hazra S, Sabini E, Ort S, Konrad M, and Lavie A. Extending thymidine kinase activity to the catalytic repertoire of human deoxycytidine kinase. *Biochemistry*. 2009;48(6):1256-63.
9. Iyidogan P, and Lutz S. Systematic exploration of active site mutations on human deoxycytidine kinase substrate specificity. *Biochemistry*. 2008;47(16):4711-20.
10. Sabini E, Ort S, Monnerjahn C, Konrad M, and Lavie A. Structure of human dCK suggests strategies to improve anticancer and antiviral therapy. *Nat Struct Biol*. 2003;10(7):513-9.
11. Fox CJ, Hammerman PS, and Thompson CB. Fuel feeds function: energy metabolism and the T-cell response. *Nat Rev Immunol*. 2005;5(11):844-52.
12. Ehdaie B, Vertosick E, Spaliviero M, Giallo-Uvino A, Taur Y, O'Sullivan M, Livingston J, Sogani P, Eastham J, Scardino P, et al. The impact of repeat biopsies on infectious complications in men with prostate cancer on active surveillance. *J Urol*. 2014;191(3):660-4.
13. Campbell DO, Yaghoubi SS, Su Y, Lee JT, Auerbach MS, Herschman H, Satyamurthy N, Czernin J, Lavie A, and Radu CG. Structure-guided engineering of human thymidine kinase 2 as a positron emission tomography reporter gene for enhanced phosphorylation of non-natural thymidine analog reporter probe. *J Biol Chem*. 2012;287(1):446-54.

14. Aiuti A, Slavin S, Aker M, Ficara F, Deola S, Mortellaro A, Morecki S, Andolfi G, Tabucchi A, Carlucci F, et al. Correction of ADA-SCID by stem cell gene therapy combined with nonmyeloablative conditioning. *Science*. 2002;296(5577):2410-3.
15. Fischer A, Hacein-Bey-Abina S, and Cavazzana-Calvo M. 20 years of gene therapy for SCID. *Nat Immunol*. 2010;11(6):457-60.
16. Paty BW, Bonner-Weir S, Laughlin MR, McEwan AJ, and Shapiro AM. Toward development of imaging modalities for islets after transplantation: insights from the National Institutes of Health Workshop on Beta Cell Imaging. *Transplantation*. 2004;77(8):1133-7.
17. Dimmeler S, Zeiher AM, and Schneider MD. Unchain my heart: the scientific foundations of cardiac repair. *J Clin Invest*. 2005;115(3):572-83.
18. Evgenov NV, Medarova Z, Dai G, Bonner-Weir S, and Moore A. In vivo imaging of islet transplantation. *Nat Med*. 2006;12(1):144-8.
19. Segers VF, and Lee RT. Stem-cell therapy for cardiac disease. *Nature*. 2008;451(7181):937-42.
20. Brentjens RJ, Davila ML, Riviere I, Park J, Wang X, Cowell LG, Bartido S, Stefanski J, Taylor C, Olszewska M, et al. CD19-targeted T cells rapidly induce molecular remissions in adults with chemotherapy-refractory acute lymphoblastic leukemia. *Science translational medicine*. 2013;5(177):177ra38.
21. Hinrichs CS, and Rosenberg SA. Exploiting the curative potential of adoptive T-cell therapy for cancer. *Immunol Rev*. 2014;257(1):56-71.

22. Tran E, Turcotte S, Gros A, Robbins PF, Lu YC, Dudley ME, Wunderlich JR, Somerville RP, Hogan K, Hinrichs CS, et al. Cancer immunotherapy based on mutation-specific CD4+ T cells in a patient with epithelial cancer. *Science*. 2014;344(6184):641-5.
23. Morgan RA, Yang JC, Kitano M, Dudley ME, Laurencot CM, and Rosenberg SA. Case report of a serious adverse event following the administration of T cells transduced with a chimeric antigen receptor recognizing ERBB2. *Mol Ther*. 2010;18(4):843-51.
24. Shultz LD, Saito Y, Najima Y, Tanaka S, Ochi T, Tomizawa M, Doi T, Sone A, Suzuki N, Fujiwara H, et al. Generation of functional human T-cell subsets with HLA-restricted immune responses in HLA class I expressing NOD/SCID/IL2r gamma(null) humanized mice. *Proc Natl Acad Sci U S A*. 2010;107(29):13022-7.
25. Yaghoubi SS, Campbell DO, Radu CG, and Czernin J. Positron emission tomography reporter genes and reporter probes: gene and cell therapy applications. *Theranostics*. 2012;2(4):374-91.